

NEA/CSNI/R(93)17  
GRS-106  
KfK 5287  
General Distribution

OECD  
NEA

ISP-31

OECD/NEA-CSNI  
International Standard Problem No. 31

CORA-13 EXPERIMENT  
ON SEVERE FUEL DAMAGE

Comparison Report

July 1993



**COMMITTEE ON THE SAFETY OF NUCLEAR INSTALLATIONS  
OECD NUCLEAR ENERGY AGENCY**

Le Seine Saint Germain - 12 Boulevard des Iles  
F-92130 Issy-les-Moulineaux (France)



Gesellschaft für Anlagen-  
und Reaktorsicherheit  
(GRS) mbH

ISP - 31  
OECD / NEA - CSNI  
International Standard Problem  
No. 31

CORA-13 EXPERIMENT ON  
SEVERE FUEL DAMAGE

Comparison Report

M. Firnhaber <sup>1)</sup>  
K. Trambauer <sup>1)</sup>  
S. Hagen <sup>2)</sup>  
P. Hofmann <sup>2)</sup>

in collaboration with G. Schanz <sup>2)</sup>,  
L. Sepold <sup>2)</sup>

- <sup>1)</sup> Gesellschaft für Anlagen- und  
Reaktorsicherheit, Köln und  
München, Germany  
<sup>2)</sup> Kernforschungszentrum Karls-  
ruhe, Karlsruhe, Germany

July 1993

GRS - 106  
KfK 5287  
NEA/CSNI/R (93) 17  
ISBN 3-923875-67-8

**Deskriptoren:**

Druckwasserreaktor, International Standard Problem, ISP31, CORA13, Severe Fuel Damage, Core Degradation, Melt Relocation, Zircaloy Oxidation, Hydrogen Generation,  $\text{UO}_2$ , Liquefaction, Material Interactions ( $\text{UO}_2$ , Zircaloy, Inconel, AgInCd, SS), Quench Phenomena

## **ORGANISATION FOR ECONOMIC CO-OPERATION AND DEVELOPMENT**

*Pursuant to Article 1 of the Convention signed in Paris on December 14th, 1960, and which came into force on September 30th, 1961, the Organisation for Economic Co-Operation and Development (OECD) shall promote policies designed:*

- *to achieve the highest sustainable economic growth and employment and a rising standard of living in Member countries, while maintaining financial stability, and thus to contribute to the development of the world economy;*
- *to contribute to sound economic expansion in Member as well as non-member countries in the process of economic development; and*
- *to contribute to the expansion of world trade on a multilateral, non-discriminatory basis in accordance with international obligations.*

*The original Member countries of the OECD are Austria, Belgium, Canada, Denmark, France, Germany, Greece, Iceland, Ireland, Italy, Luxembourg, the Netherlands, Norway, Portugal, Spain, Sweden, Switzerland, Turkey, the United Kingdom and the United States. The following countries became Members subsequently through accession at the dates indicated hereafter: Japan (April 28th, 1964), Finland (January 28th, 1969), Australia (June 7th, 1971) and New Zealand (May 29th, 1973). The Commission of the European Communities takes part in the work of the OECD (Article 13 of the OECD Convention).*

## **NUCLEAR ENERGY AGENCY**

*The OECD Nuclear Energy Agency (NEA) was established on 1st February 1958 under the name of the OEEC European Nuclear Energy Agency. It received its present designation on April 20th, 1972, when Japan became its first non-European full Member. NEA membership today consists of all European Member countries of OECD as well as Australia, Canada, Japan, the Republic of Korea and the United States. The Commission of the European Communities takes part in the work of the Agency.*

*The primary objective of NEA is to promote co-operation among the government of its participating countries in furthering the development of nuclear power as a safe, environmentally acceptable and economic energy source.*

*This is achieved by:*

- *encouraging harmonization of national regulatory policies and practices, with particular reference to the safety of nuclear installations, protection of man against ionising radiation and preservation of the environment, radioactive waste management, and nuclear third party liability and insurance;*
- *assessing the contribution of nuclear power to the overall energy supply by keeping under review the technical and economic aspects of nuclear power growth and forecasting demand and supply for the different phases of the nuclear fuel cycle;*
- *developing exchanges of scientific and technical information particularly through participation in common services;*
- *setting up international research and development programmes and joint undertakings.*

*In these and related tasks, NEA works in close collaboration with the International Atomic Energy Agency in Vienna, with which it has concluded a Co-operation Agreement, as well as with other international organisations in the nuclear field.*

## CSNI

The NEA Committee on the Safety of Nuclear Installations (CSNI) is an international committee made up of scientists and engineers. It was set up in 1973 to develop and coordinate the activities of the Nuclear Energy Agency concerning the technical aspects of the design, construction and operation of nuclear installations insofar as they affect the safety of such installations. The Committee's purpose is to foster international co-operation in nuclear safety amongst the OECD Member countries.

CSNI constitutes a forum for the exchange of technical information and for collaboration between organisations which can contribute, from their respective backgrounds in research, development, engineering or regulation, to these activities and to the definition of its programme of work. It also reviews the state of knowledge on selected topics of nuclear safety technology and safety assessment, including operating experience. It initiates and conducts programmes identified by these reviews and assessments in order to overcome discrepancies, develop improvements and reach international consensus on technical issues of common interest. It promotes the coordination of work in different Member countries including the establishment of co-operative research projects and international standard problems, and assists in the feedback of the results to participating organisations. Full use is also made of traditional methods of co-operation, such as information exchanges, establishment of working groups, and organisation of conferences and specialist meeting.

The greater part of CSNI's current programme of work is concerned with safety technology of water reactors. The principal areas covered are operating experience and the human factor, reactor coolant system behaviour, various aspects of reactor component integrity, the phenomenology of radioactive releases in reactor accidents and their confinement, containment performance, risk assessment, and severe accidents. The Committee also studies the safety of the fuel cycle, conducts periodic surveys of reactor safety research programmes and operates an international mechanism for exchanging reports on nuclear power plant incidents.

In implementing its programme CSNI establishes co-operative mechanisms with NEA's Committee on Nuclear Regulatory Activities (CNRA), responsible for the activities of the Agency concerning the regulation, licensing and inspection of nuclear installations with regard to safety. It also co-operates with NEA's Committee on Radiation Protection and Public Health and NEA's Radioactive Waste Management Committee on matters of common interest.

## Contents

## Page

<b>1.</b>	<b>Introduction</b> .....	<b>1</b>
<b>2.</b>	<b>Objectives of the International Standard Problem No. 31</b> .....	<b>2</b>
<b>3.</b>	<b>Description and Results of Experiment CORA 13</b> .....	<b>3</b>
3.1	Description of the CORA Test Facility .....	3
3.2	Test Conduct and Initial and Boundary Conditions .....	5
3.3	Temperature Response .....	7
3.4	Hydrogen Generation .....	8
3.5	Posttest Appearance of the Bundle and of Cross Sections .....	9
3.6	Mass Distribution and Blockage Formation .....	12
3.7	Estimation of Additional Boundary Conditions .....	13
3.7.1	ATHLET-CD .....	14
3.7.2	Computational Model .....	15
3.7.3	Comparison of Analytical and Experimental Results .....	15
<b>4.</b>	<b>Calculations by the Participants</b> .....	<b>18</b>
4.1	Selection of Variables to be Calculated .....	18
4.2	Participants and Codes .....	19
4.2.1	FRAS-SFD .....	20
4.2.2	ICARE2 .....	20
4.2.3	KESS-III .....	21
4.2.4	MELCOR .....	22
4.2.5	SCDAP/RELAP5 .....	22
4.3	Computational Model .....	23
4.3.1	AEA .....	23
4.3.2	CEA .....	23
4.3.3	ECN .....	24
4.3.4	IKE .....	24
4.3.5	JAE .....	25
4.3.6	KAE .....	25
4.3.7	NRI .....	25
4.3.8	SNL .....	26

4.3.9	VTT .....	26
4.4	Comparison of Analytical and Experimental Results .....	26
4.4.1	Initial and Boundary Conditions .....	27
4.4.2	Temperature .....	28
4.4.3	Core Degradation Variables .....	30
4.4.4	Hydrogen Generation .....	33
<b>5.</b>	<b>Summary and Assessment .....</b>	<b>34</b>
<b>6.</b>	<b>References .....</b>	<b>38</b>
<b>7.</b>	<b>Tables .....</b>	<b>41</b>
<b>8.</b>	<b>Figures .....</b>	<b>48</b>
<b>9.</b>	<b>Appendix</b>	

## Abstract

The severe fuel damage experiment CORA-13 has been offered as CSNI-International Standard Problem (ISP) No. 31 to the OECD member countries as well as to non-OECD countries. The out-of-pile experiment CORA-13 was executed in November 1990 at Kernforschungszentrum Karlsruhe. The major objectives of this experiment were to investigate the behavior of PWR fuel elements during early core degradation and fast cooldown due to refill. Measured quantities are boundary conditions, bundle temperatures, hydrogen generation and the final bundle configuration. The ISP was conducted as a blind exercise. Boundary conditions which could not be measured, but which are necessary for simplified test simulation (axial power profile, shroud insulation temperature, bundle refill flow) were estimated using ATHLET-CD. Results to the ISP were submitted by 9 participants.

Five participants used different versions of SCDAP/RELAP5, the other employed codes are FRAS-SFD, ICARE2, KESS-III, MELCOR. In five calculations only the bundle and shroud have been simulated, the other four comprised the bypass and cross flows, too. Five calculations included the refill phase. The thermal behavior up to significant oxidation has been predicted quite well by most of the codes. Larger deviations have been observed for the oxidation-induced temperature escalation. Some codes simulated clad ballooning. The hydrogen generation early in the transient has been overpredicted, but it has been underpredicted in the later prequench phase. None of the codes could predict the intensive hydrogen generation during refill. The simulation of material interactions was restricted to the dissolution of fuel by molten Zircaloy, except for one code which has taken into account the dissolution of oxidized cladding by molten Zircaloy, too.

In general, the capability of the codes in calculating the main degradation phenomena has been clearly illustrated and weaknesses concerning the modelling of some degradation processes have been identified. Among the degradation phenomena involved in the test, the more severe limitations concern the  $\text{UO}_2\text{-ZrO}_2$  dissolution by molten Zr, the solubility limits in the resulting U-Zr-O mixture and the cladding failure by the molten mixture. There is a lack concerning the Inconel spacer-grid interactions with the rods, the material interaction between control rod material and fuel rods, and in the modelling of hydrogen generation during cooldown.

Verification of reactor codes on small-scale experiments needs more code versatility, concerning power profile evolution, surrounding structures with imposed boundary conditions, more output conveniences. More verification and validation activities remain necessary for severe fuel damage codes.

Furthermore, this exercise illustrates the importance of the code user, the need for improved user guidelines with more detailed information and recommendations, and the need for user expertise on core degradation phenomena, to make more effective the use of the codes in this field.

## 1 Introduction

Following a recommendation of the OECD-CSNI<sup>1</sup>, International Standard Problem (ISP) Exercises are performed in the field of nuclear safety research and development. These exercises are defined as comparative exercises in which predictions of different computer codes for a given physical problem are compared with each other or with the results of a carefully controlled experimental study. The main goal of ISPs is comparing and evaluating the validity and accuracy of tools which are used in assessing the safety of nuclear installations /1/. In addition to that it enables the code user in gaining experience and proving his competence.

ISPs are performed as "open" or "blind" exercises. In an open ISP the results of the experiment are available to the participants before their evaluation and in a blind ISP the results are blocked until the delivery of the calculated results. Preferably, ISPs should be blind.

Suggested by the Federal Republic of Germany, the Principal Working Group (PWG) No. 2 of CSNI agreed on its meeting in 1990 to offer the experiment CORA-13 on severe fuel damage as International Standard Problem No.31 to its member countries and in addition to some non-OECD countries. The experiment CORA-13 is one out of a large number of severe fuel damage (SFD) experiments conducted at Kernforschungszentrum Karlsruhe /2/. The experiment and the conduct of the ISP were sponsored by the German Ministry of Research and Technology. The ISP was conducted as a blind exercise, i. e. only the initial and boundary conditions were given to the participants prior to performing the calculations.

The CORA-13 severe fuel damage experiment was executed on November 15th, 1990. The major objectives of this experiment were to investigate the behavior of PWR fuel elements under severe fuel damage accident conditions, including liquefaction, melting and relocation, as well as fast cooldown and quenching due to refill.

At the preparatory meeting, held at Karlsruhe on June 13, 1991, delegates from 15 countries participated; results to the ISP were submitted by 9 participants including one from a non-OECD country.

---

<sup>1</sup> Organization for Economic Cooperation and Development -Committee on the Safety of Nuclear Installations

The International Standard Problem No. 31 is the second ISP on severe fuel damage aspects. The first one (ISP28 /3/) was performed in 1990/91 using the PHEBUS-SFD B9+ experiment as basis for the data comparison /4/. Compared with this in-pile experiment, the CORA-13 electrically heated out-of-pile test bundle contained two absorber rods and was quenched from the bottom, simulating a rising water level during flooding of the core.

## **2 Objectives of the Standard Problem No. 31**

During an unmitigated severe LWR accident the core material reaches temperatures significantly higher than 1500 K. This causes core damages in a large variety of forms, i. e. chemical interactions of the different materials, melting, relocation and blockage formation during heatup, embrittlement and fragmentation of the cladding on cool-down and quenching, and hydrogen generation. At the early stage of the accident the core is still coolable, but to mitigate the accident a detailed knowledge of the core meltdown behavior and a possibility to predict the course of the accident are necessary. Experimental results and code predictions can be used to quantify the safety margins presently existing in the safety systems of operating reactors, and to explore possibilities of ending a high temperature transient before it can lead to an uncontrolled core meltdown. For demonstrating the capability of current computer codes to model and to calculate the core meltdown phase of a severe accident with sufficient accuracy, the OECD-CSNI decided to propose fuel element meltdown standard problems.

The general objectives of the International Standard Problem No. 31 (ISP31) are to analyze the heatup and meltdown phase of a PWR-type fuel element in the CORA test facility at Karlsruhe and to examine the reliability and accuracy of the severe accident computer codes used.

In more detail the objectives of ISP31 are the comparison and investigation of the following physical variables and phenomena:

- Temperature of selected fuel and absorber rods,
- Onset of temperature escalation as a result of the exothermic zirconium/steam interaction,

- Extent of Zircaloy cladding oxidation,
- Liquefaction temperature of Inconel spacers and (Ag, In, Cd) absorber rods,
- Relocation temperature of liquid phases,
- Extent of  $\text{UO}_2$  and  $\text{ZrO}_2$  dissolution by molten Zircaloy,
- Oxidation of metallic melt containing zirconium,
- Formation of blockages, extent and location,
- Timing and magnitude of hydrogen generation, especially during quenching,
- Fragmentation of embrittled fuel rods, particularly during quenching.

### **3 Description and Results of Experiment CORA-13**

The CORA-facility, the conduct of test CORA-13 and the results of this test are described in detail in /2/. For the convenience of the reader the information necessary for the comparison with the calculations is given here in summary form.

#### **3.1 Description of the CORA Test Facility**

The CORA out-of-pile facility is designed to investigate the behavior of LWR fuel elements under severe fuel damage accident conditions. In the experiments the decay heat is simulated by electrical heating. Great emphasis is given to the fact that the test bundles contain all materials used in light-water reactor fuel elements, to investigate the different material interactions. Pellets, cladding, grid spacers, absorber rods and the pertinent guide tubes are typical of those of commercial LWRs with respect to their compositions and radial dimensions.

The CORA facility is situated within the reactor hall of the now disused FR2 reactor at Kernforschungszentrum Karlsruhe (KfK). Figure 3.1 gives a simplified flow diagram of the facility. The geometrical arrangement of the different CORA components is given in Figure 3.2.

The central part of the facility is the fuel rod bundle. The bundle is enclosed in a Zry-4 shroud with  $ZrO_2$  fibre insulation. A high temperature radiation shield surrounds the bundle, leaving an annular space. The bundle is connected to the power supply system at the upper and lower ends.

Below the bundle is the quench unit with a water-filled quench cylinder, which can be raised towards the bundle with a controlled speed. The cylinder is guided by three rods, which also connect the electric power supply to the bundle lower end. At the beginning of the test the water level is 220 mm below the "zero elevation" of the bundle. The "zero elevation" corresponds to the lower end of the pellets in the heated rods.

The steam is produced in the steam generator, superheated and guided to the lower end of the bundle, entering at "zero elevation". The steam not consumed within the bundle is condensed in two parallel condensers and the hydrogen produced is fed to the off-gas system after dilution with air to obtain a low hydrogen concentration.

- Bundle Design

The location of the bundle within the high temperature shield is shown in Figures 3.3 and 3.4. The arrangement of the fuel rod simulators within the bundle is given in Figure 3.5. Figure 3.6 presents the individual main components of the bundle; i.e. the heated and unheated fuel rods and the (Ag, In, Cd) absorber rods. Characteristic data of the bundle are given in Tables 3.1 to 3.3.

Two types of fuel rod simulators are used: electrically heated rods and unheated solid rods. Altogether 25 rods made up of 16 heated rods, 7 unheated rods and 2 absorber rods have been used. Vertical cross-sections of the rods are shown in Figure 3.6. The heated fuel rod simulator is sheathed with standard PWR Zircaloy cladding tube. The central part of the internal heater consists of a 6 mm diameter tungsten rod surrounded by  $UO_2$  annular pellets. The tungsten heater has an effective length of 1024 mm. The unheated fuel rod simulator has the same configuration as the fuel rods in PWR-type reactors: solid  $UO_2$  pellets inside the original Zry-4 cladding.

The two absorber rods are also made from original components. The (Ag80, In15, Cd5) absorber material is sheathed in stainless steel and this rod is surrounded by a

Zry-4 guide tube. Three spacers are used in the bundle to maintain the positions of the rods. Original PWR-type spacers have been used. The material of the middle spacer is Inconel 718. The upper and lower spacer are made of Zircaloy-4. The distances from the top end of the spacers to "zero elevation" are +880 mm, +496 mm and -5 mm respectively.

The bundle is surrounded by a Zry-4 shroud of 1.2 mm thickness (Figure 3.5). The shroud conducts the steam through the bundle. The steam enters at 180° into the lower end (0 mm). To minimize the heat losses, the shroud is surrounded by an insulating layer of ZrO<sub>2</sub> fibre of 19 mm (0.75 inch) thickness. Due to the low heat conductivity and heat capacity of the fibre insulation, the shroud temperature can follow the bundle temperature closely. Since the Zry-4 shroud participates in the interaction with steam, the resulting oxidation energy contributes substantially to the bundle heat-up.

- High-temperature Shield

To keep the heat losses as low as possible, the bundle is surrounded by a high temperature shield (HTS), as shown in Figure 3.4. The high temperature shield consists mainly of ceramic fibre plates (114 mm thickness).

The high temperature shield is located within the pressure tube. In the pressure tube a large number of openings allow access to the bundle. Through these holes and their extensions in the temperature shield, the bundle can be inspected during the test with the help of the videoscope systems. In test CORA-13 three windows were used: in the 120° direction at the 390, 590 and 790 mm elevations. The size of the windows was 30 mm high and 40 mm wide.

- Power Supply

In CORA-13 16 rods out of 25 were heated. The power input is controlled by computer and programmed before the test. The power is controlled by measuring the current and setting the voltage necessary to obtain the desired power.

### 3.2 Test Conduct and Initial Boundary Conditions

The test sequence can be divided into three phases (Figure 3.7):

1. 0 - 3000 s: gas preheat phase;
2. 3000 - 4900 s: transient phase;
3. 4900 s onwards: cooling phase.

During the gas preheat phase there is a flow of 8 g/s preheated argon and a low constant electric power input of about 0.65 kW. During this period the temperature in the insulation reaches a level which is high enough to avoid steam condensation. To keep the videoscope windows clear, a total flow of 1 g/s argon is directed to the front of the windows of the videoscopes. The pressure in the system is maintained at 0.22 MPa.

During the transient phase the temperature increase is initiated by raising the electric power input from 6 to 27 kW at a constant rate (Figure 3.7). At 3300 s a steam flow of 6 g/s is introduced into the system. The cooling phase is initiated by the rise of the quench cylinder at 4870 s and the shut down of the electric power at 4900 s. The average velocity of the rising quench cylinder was 1 cm/s (Figure 3.11).

Figure 3.8 gives the "gas" temperature measured at the entrance of the bundle. For experimental reasons the steam superheater has to be slowly heated up in flowing argon, which only can be released through the facility. In consequence, at the starting point of the test, the entering gas has already a temperature of 525 °C, and the bundle has already been heated up by the passing gas. The increase in temperature at about 3400 s shows the influence of the steam addition. The steam heats up the connecting tube from the steam superheater.

The steam flow in the bundle is shown in Figure 3.9. These values are determined from the steam concentration measured at the 700 mm elevation during a pre-test under identical conditions. For comparison the evaporation from the quench cylinder is given in Figure 3.10.

The movement of the water level during the quench phase is given in Figure 3.11. Here the positions of the upper edge of the quench cylinder and of the water level in the cylinder are shown. For experimental reasons the quench cylinder was not raised with a constant velocity, but in steps. The average velocity was 1 cm/s.

To quench the bundle at a high temperature, the movement of the quench cylinder was started 30 s before the shutdown of the electrical power. The time histories of the power shut down and quench cylinder movement are given in Figure 3.12. During the shutdown of the power the water level of the quench cylinder was moved to 150 mm elevation. In about 90 s after shutdown of the electrical power, the quench cylinder was raised gradually to 1100 mm elevation. The water level rose during the same time to 950 mm elevation. To compensate for the evaporation a constant water flow was added to the quench cylinder.

It is assumed that the water disappearing from the quench cylinder was evaporated. Then the amount of evaporated water can be calculated from the difference of the water level to the upper edge of the quench cylinder taking into account the feed water (Figure 3.13). In Figure 3.14 the difference of the water level change corrected for the additional water input is given.

### 3.3 Temperature Response

The temperatures in the bundle were measured with high-temperature thermocouples (WRe5/WRe26 wire and HfO<sub>2</sub> insulating material), sheathed with tantalum and Zircaloy. Thermocouples with "Ker" in the name were additionally shielded with ZrO<sub>2</sub> tubes.

Test CORA-13 was terminated by quenching. Therefore, it was necessary to move the quench cylinder filled with water over the bundle. In consequence, all thermocouples had to be introduced from the top. Unfortunately this resulted in a strong attack on the compensation cable in the upper part of the bundle after the beginning of the escalation. This is the reason for the irregular behavior of temperature traces after 4200 s.

The temperatures are measured on the different components of the bundle at different elevations. In this paper only the measurements in the unheated rods are given, as a very flat radial profile was found. The complete measurements are discussed in /2/.

The temperatures in the unheated rods are shown in Figure 3.15. The temperature rise shows the same general features already found in earlier tests. With the increase of the electrical power input, first the temperature rises proportional to the power. Having reached about 1000 °C, the Zr/steam reaction adds an increasing contribution to the energy input, resulting in a temperature escalation. The escalation starts at 850 mm elevation, followed by 950 mm and 750 mm with not much delay. About 100 s later the escalation at 650 mm and at 550 mm of rod 6.6 can be seen. The thermocouple at 550 mm elevation in rod 4.2 (in the neighborhood of a window) shows the escalation, analogous to that at 420 mm, 300 s later.

The temperature measurements at the 1050 mm and 1150 mm elevations, where thermocouples survived up to the end of the test, suggest that there seems to be a plateau in the temperature history, before the final rise due to quenching. Also for the temperature at 1350 mm a plateau is indicated between 4500 s and the quench rise. The temperature value of this plateau (1000 °C) is in good agreement with the measurement on the heated rods at this elevation. Also the rise of the temperature at the beginning of the quench process is in good agreement with the temperature measurements on the heated rods.

The "gas" temperature of the surface of the bundle is given on Figure 3.16 and Figure 3.17 at the elevations 1350 mm and 1250 mm. The thermocouples, introduced through the bundle head plate, survived the test. Both measurements show the strong increase of the temperature during the quench process: 800 K at 1350 mm and 600 K at 1250 mm elevation.

In Figure 3.18 best estimated temperatures in the bundle are given. The upward movement of the quench cylinder from the lower end of the test section made it necessary to introduce all thermocouples from the upper end. In consequence most of the thermocouples failed around 4500 s. As the measurements during the initial phase show that the temperatures on the different components at the same elevation can be found within a temperatures interval of  $\pm 100$  K, we have determined best estimated temperatures for the different elevations of the bundle. In these graphs the measurements for heated rods to shroud are considered. Also the comparison of the axial neighbors are included. For 350 mm elevation it could not be decided whether there was a temperature increase before the final temperature decrease due to the quench process.

### 3.4 Hydrogen Generation

The hydrogen produced during the test by the steam/Zr reaction is usually measured at two different positions, i.e. above the test section and in the mixing chamber (see Figure 3.1). The mixture which contains hydrogen among other gases is transported to the spectrometer via capillary tubes. It is analyzed by quadrupole mass spectrometers. The ion currents representing the concentrations of the respective gases are determined. From these data the mass production rate of hydrogen as well as of the other gases is calculated with the ratio of the partial pressure of the particular gas and that of argon (the carrier gas) and multiplied by the argon flow rate through the test bundle.

The measured hydrogen data for test CORA-13 are given in Figure 3.19. The hydrogen production is correlated to the accelerated temperature increase in the bundle. (Figure 3.14). The Zry/steam reaction which increases to remarkable values beyond 1000 °C after 4000 s produces the hydrogen and due to its exothermic nature also extra chemical energy, which accelerates the temperature increase. The strong hydrogen spike after 4900 s is related to the quench process. The protecting oxide layers formed during the initial heatup process are cracked due to thermal stress, so that the steam has access to the metallic Zry-4 at high temperatures, which results in a strong Zr/steam reaction producing the hydrogen spike and the temperature peak.

After covering the bundle with water no further hydrogen can be produced. The tail in Figure 19 after the quench peak is due to transport phenomena. If we correct the hydrogen generation curve in a way that the hydrogen generation indicated after quench is added to the initial phase of steam-zirconium reaction, we obtain the initial increase of hydrogen production as shown in Figure 3.19a by the dashed line. The amount of hydrogen which had to be shifted to the initial slope was 30 g. Scooping experiments in which a definite hydrogen flow was input into the CORA bundle showed that the tail of measured hydrogen production that appeared after cut off of hydrogen input has to be added to the initial slope of the measured curve. This justifies the correction of the measured curve which is shown as a best estimate in Figure 3.19a. According to the best estimate curve in Figure 3.19a the percentage of hydrogen generation before quench amounts to 63% of the total hydrogen generation.

### 3.5 Posttest Appearance of the Bundle and of Cross Sections

The post-test appearance of the CORA-13 bundle is shown in Figure 3.20. The appearance of the four sides of the bundles shows that the interaction between the components is the predominant damage mechanism. The Zircaloy cladding liquefied by the absorber material has started to dissolve the  $\text{UO}_2$ -pellets. The relocated melt has glued together the remnants of the fuel rods. Also, melt newly formed during the quench process dominates the appearance of the bundle. An appreciable oxide layer is seen on the fuel rods only in regions not influenced by the interaction.

For the preparation of metallurgical cross-sections the bundle was filled with epoxy and sectioned with a diamond saw. The microphotographs of the cross sections are presented in Figure 3.21. The destructive post-test examinations of the bundle showed strong chemical interactions over the whole bundle length. In the upper half of the bundle the (Ag,In,Cd) absorber rods and Zircaloy guide tubes as well as a great part of the Zircaloy cladding of the fuel rods have been removed by melting. The relocated materials solidified, according to their solidification temperatures, at different axial elevations. The maximum blockage is reached just below 500 mm elevation. This may be influenced by the former Inconel grid spacer at this elevation.

As a result of the high temperatures in the upper part of the bundle the interactions of the materials with steam are very fast and the resulting reaction products and melts are all ceramic in nature. In the bundle cross-section elevation 848 mm one can still recognize a part of completely oxidized upper Zircaloy grid spacer. A great part of the Zircaloy cladding and  $\text{UO}_2$  pellets have disappeared; only in the outer ring of the fuel rods some oxidized cladding remnants are still present.

The solidified material at the bundle cross-section elevation of 498 mm (Inconel grid spacer location) is mainly ceramic. On solidification large pores have formed. The cladding of nearly all fuel rod simulators was melted off or dissolved by the (Ag, In, Cd) absorber alloy. Also the  $\text{UO}_2$  fuel has been chemically attacked and partially dissolved (liquefied). At some locations a pronounced cracking of the ceramic material occurred during quenching of the bundle. The resulting unusual crack pattern is similar to those observed in in-pile quench tests.

The two absorber rods are present below 250-300 mm elevation. The gap between the Zircaloy guide tube and stainless steel cladding of the absorber rods has been filled with the relocated absorber alloy. The damage of the fuel rods in the vicinity of the absorber rods is stronger than further away. The Ag of the absorber alloy attacks the Zircaloy cladding and dissolves it very quickly above about 1250 °C. The composition of the melts at this elevation is rather homogeneous; the high Zr content of about 52 wt.% reflects the strong interactions between the absorber alloy and Zircaloy.

The chemical compositions of the various melts at different cross-section elevations have been quantitatively determined by SEM/EDX<sup>2</sup> examinations and are listed in Table 3.4 and plotted in Figure 3.22 as a function of the axial bundle elevation. The results indicate that below 400 mm all melts are metallic in nature. Sometimes the solidified melts contain small quantities of ceramic phases. Above 500 mm all melts are ceramic in nature. In-between (400 - 500 mm) both types of melts can be detected.

Figure 3.22 shows the variation in the composition of the metallic and ceramic melts as function of the bundle elevation. One can recognize the strong decrease of U and strong increase of Ag in the solidified melts going from the top to the bottom of the bundle. No stainless steel or absorber alloy elements or corresponding reaction products are present in the upper half of the bundle, but U, Zr and oxygen are observed.

The measurements described above are the basis for the determination of the axial distribution of UO<sub>2</sub>, Zry-4 and mass as they are given in the next section in Figures 4.31, 4.32 and 4.35 for comparison with the calculations. In Figure 4.35 in addition the experimental values of the mass distribution as determined by weighing of the bundle segments are given (see Figure 3.27).

The measured ZrO<sub>2</sub> scale thickness increases from a few μm at 148 mm elevation to an order of 100 μm at 248 mm, but at 348 mm complete conversion of the cladding has occurred locally. At higher elevations the destructive mechanical consequences of severe cladding oxidation and the competing degradation processes restrict the respective evaluation: On the basis of a Pilling-Bedworth factor of 1.5 to 1.56 the 725 μm original cladding wall would convert to roughly 1100 μm of ZrO<sub>2</sub>. The measured values, however, cannot be used to confirm this more precisely. Lower values

---

<sup>2</sup> Scanning Electron Microscope / Energy Dispersive X-Ray Spectroscopy

observed can easily be explained by spalling of partial layers or tube wall thinning during melt agglomeration at the respective side of the cladding periphery.

In Figure 3.23 the axial distribution of the measured  $ZrO_2$  scale thickness is drawn. Broad scatter bands for the lower elevations indicate considerable local variations. For the upper half of the bundle the presence of any residual metallic cladding can be excluded, although the obtainable data are scarce.

The axial distribution of peak temperatures in the bundle, measured during the transient and the quenching phase is included in Figure 3.23. The temperatures and the availability of steam were high enough for dramatic additional oxidation to occur, if residual metallic material were available in the upper bundle half. Even above the heated zone, up to roughly 1300 mm elevation, no metallic cladding residues are expected.

On the other hand the completeness of the oxidation over an axial range of roughly 1000 mm together with the integral value of hydrogen generation allows to estimate the percentage of cladding which has relocated as or contributed to metallic melt. The steam oxidation of such a melt has to be neglected in this estimation, since it cannot be quantified. This is justified because the specific surface and the temperatures at the final location of melts are both reduced. The described estimation gives a value of ca. 28 % of relocated and of ca. 72 % of in situ oxidized cladding and shroud material.

The axial distribution of  $ZrO_2$  determined by the above mentioned measurements and considerations is given in Figure 4.33 for comparison with the code results. This curve is determined as mean value for all rods of the bundle. The same curve is used for comparison also in Figures 4.24 and 4.25, as the accuracy of the measurement does not justify a separation between the first and second ring of rods.

### **3.6 Mass Distribution and Blockage Formation**

An axial profile of the volume distribution can be obtained by using the epoxying process. The epoxy resin is introduced into the bundle from the bottom end. By weighing the resin left in the supply container after each step, i.e. when the resin has raised in the bundle by 1 cm, the difference of mass allows the calculation of the void volume of the bundle as a function of axial height. The filling process is slow enough so that

the reading at the scale can be taken per cm. The result of the specific mass (g/cm) in Figure 3.24 shows the axial distribution of the voids, because a higher amount of resin is equivalent to a larger void volume. The smoothed solid-line curve in Figure 3.24 was obtained from the data (crosses) by filtering, i.e. by using a Fourier transformation where higher frequencies were cut off by a low-pass filter. The smoothed curve is used for further evaluation.

Figure 3.25 presents the axial distribution of the bundle material. For the evaluation of this profile the cut bundle segments were weighed. These data consist of the masses of the bundle and of the epoxy resin.

Figure 3.26 shows the axial blockage profile calculated from the epoxy distribution (Figure 3.24) relative to the inner surface of the shroud. For comparison the profile of the undisturbed bundle is given. Figure 3.27 presents the axial mass distribution after the test determined from the weight of the bundle segments corrected for the epoxy distribution. Again the mass distribution of the undisturbed bundle is given for comparison. The blockage and the mass distribution are used in Figures 4.36 and 4.35 for comparison with the calculated values.

By image processing of the pictures of the bundle cross sections the remaining  $\text{UO}_2$  of the single rods is determined. Taking into account the original cross section, in Figure 3.28 the axial distribution of the removed, i. e. dissolved and broken away  $\text{UO}_2$  for the whole bundle is given. Figures 3.29 and 3.30 show the analogue curves for the unheated rods and heated rods.

For the heated rods a much higher fraction is removed. The higher numbers are partially due to using relative values, as for the heated rods the reference annular cross section is smaller. (The center part of 61 mm diameter of the annular pellets is missing.) But there is additional dissolution on the inside surface due to melt - mainly Zircaloy - penetrated into the gap between heater rod and annular pellets.

The dissolution of the 4 heated rods (position 3.3, 3.5, 5.3, 5.5) of the first ring and of 6 unheated rods (position 2.2, 2.4, 2.6, 4.2, 6.4, 6.6) of the second ring are compared with the code calculations in Figures 4.26 and 4.27 in section 4.

### 3.7 Estimation of Additional Boundary Conditions

GRS analyzed the CORA 13 experiment with the code ATHLET-CD. The calculations were performed with the knowledge of the experimental temperature histories besides the boundary conditions. The aim of the analysis was to provide, for simplified simulations, additional boundary conditions, which could not be measured during the experiment, as

- axial power profile
- shroud insulation surface temperature
- refill mass flow rate for bundle

and to check the energy balance for the bundle heatup. The results of this open analysis have been submitted in the same format as those of the blind calculations, but they are presented separately in this chapter. The estimated boundary conditions are shown in the specifications /5/.

#### 3.7.1 ATHLET-CD

The system code ATHLET-CD (Analyses of Thermalhydraulics of LEaks and Transients with Core Degradation) /6/ is being developed by GRS in cooperation with Institut für Kernenergetik und Energiesysteme (IKE), Stuttgart. The field of application comprises the whole spectrum of leaks and large breaks, as well as operational and abnormal transients, for PWR's and BWR's. At present the analysis covers the in-vessel thermalhydraulics, the early phases of core degradation, fission product core release, and aerosol and fission product transport in the coolant system.

The core degradation module is coupled with the four equation thermodynamic non-equilibrium model, which allows multichannel geometry with cross flow and the simulation of a mixture level. The relative velocity between the steam and water phases is determined by the full-range drift-flux model. The code considers for the core region radial and axial heat conduction, convective heat exchange, and radiative heat transfer.

The core degradation module describes cladding deformation, oxidation, and melt relocation. Both the fission product core release, based on rate equations similar to CORSOR, and the aerosol and fission product transport module TRAPMELT are fully integrated in the system code.

The assessment of ATHLET-CD is being based on the analysis of separate effects tests, integral tests and plant events. Up to now, post-test calculations of CORA, PHEBUS; PBF and NRU experiments have been performed.

### **3.7.2 Computational Model**

The ATHLET-CD model represents the CORA test section from the lower end of the unheated rods up to the upper end of the shroud and from the bundle up to the outer surface of the high temperature shield (Figure 3.31). This includes three parallel flow channels, one for the bundle and two for the bypass. The bypass was subdivided into two flow channels with 11 cross flows to facilitate natural convection as well as the lifting of the quench cylinder, which covers only one part of the bypass with water. Five cross flows between bundle and bypass simulate the three windows and leakage paths at the lower and upper ends of the test section.

Six different components represent the bundle and the surroundings: the single central unheated rod, the first ring of four heated rods, the second ring of eight unheated rods, the third ring of twelve heated rods, the shroud including the  $ZrO_2$  insulation layer and the high temperature shield. Control rods and grid effects are not modeled. Cladding and shroud outer side oxidation are modeled by using the rate equation based on Cathcart, Urbanic, and Heidrick. Possible steam starvation is taken into account for the cladding but not for the shroud oxidation.

Liquefaction, melting and relocation are suppressed by high, constant, user-specified solidus and liquidus temperatures (2873 K, 3423 K), to concentrate on the thermal behavior of the bundle.

### 3.7.3 Comparison of Analytical and Experimental Results

This section gives, as in section 4.4 for the ISP participants, a comparison of the analytical with the experimental results with some additional observations and comments. The abbreviations used herein are equivalent to the plot identifier from /6/ Table 1 and 2.

- Initial and Boundary Conditions

Figure 3.32 and 3.33 show that the input data electrical bundle power, inlet vapor flow rate, and inlet temperature agree well with the given boundary condition. The power losses of the external resistance, of estimated  $0.5 \Omega$  per rod, ranges at about 1kW. The steam inlet flow results from water injection into the evaporator and superheater, which is shown as the experimental value. The input data take into account the time delay of the vapor flow with an estimated time lag of about 100 s.

The values of external resistance and vapor flow time lag (time constant) are roughly estimated and should be provided more precisely by the experimental team.

- Temperatures

The figures 3.34 to 3.37 indicate good agreement between calculated and measured data up to 4500 s in the lower bundle part and up to temperatures of about 2200 K in the upper part. The steep temperature increase in the lower bundle part results from melt relocation which was not modeled in the analysis.

The fuel rod temperature measurement in figure 3.36, curve "TU2R exp", might be either an erroneous temperature measurement or an indication of a strong local influence of the open windows, since the location of the thermocouple (550 U4.2) is close to one of them and cooler gases flow from the bypass into the bundle region through it. In the figures 3.36 and 3.37 the curves "TEI0 exp" increase sharply at 4250 s. This might result from melt relocation through the windows or melt penetration through the shroud insulation. These local effects are unique for the CORA test facility which makes special effort in modelling those very questionable.

In general the good agreement between calculated and measured temperature during heatup indicates that the energy balance for the bundle is fulfilled. No adequate measurements for the cooldown phase are available.

- Zirconium oxidation and hydrogen generation

Figures 3.38 to 3.41 show the hydrogen generation, as well as cladding and shroud oxidation. Though the temperature escalation - which indicates the onset of significant oxidation - starts at 4100 s, the measured hydrogen generation rate increases very slowly and reaches at 4700 s a plateau of 0.25 g/s. During the prequench phase, the generation rate never reaches the maximum possible value of about 0.7 g/s according to a steam flow of 6 g/s. This indicates two facts

- the hydrogen measurement seems to be delayed significantly compared with the hydrogen generation
- only a part of the steam available is consumed by the oxidation, due to local blockage or steam bypass flow.

The calculated values show strong oxidation of the shroud, where the steam starvation is not modeled in the high temperature region but steam starved conditions in the bundle after 4100 s, where due to an artificial overestimated "blockage" at the Inconel grid location only 10 % of the fluid flows through the upper bundle part (Figure 3.42). Through the windows at elevation 590 and 790 mm, steam reverses from the bypass into the bundle, which allows, due to higher partial vapor pressure, some oxidation downstream of it. This is shown in the Figures 3.40 and 3.43.

In general, compared with the hydrogen measurement, the oxidation before quenching is

- overpredicted during the temperature escalation phase and
- underpredicted during the high temperature phase.

During the refill phase the steam flow increases rapidly and the calculated hydrogen generation rate increases to 1.7 g/s (out of plot range) for a short time. Figure 3.40 indicates, that oxidation occurs in the previously steam starved upper bundle part. Any other effects as embrittlement or shattering were not modeled.

## 4 Calculations by the Participants

### 4.1 Selection of Variables to be Calculated

The selection of variables to be calculated was done in order to meet the objectives of the ISP. The variables to be calculated comprise global parameters, temperatures at different locations and core degradation variables indicating the state of the bundle /6/.

The global variables are needed mainly for the energy balance, e. g. heat fluxes including losses and storage and power generation by oxidation and hydrogen generation. The temperature variables indicate the thermal behavior of the bundle including shroud, shroud insulation and high temperature shield. They consist of

- Fluid temperature
- Fuel temperature
- Cladding temperature
- Absorber temperature
- Guide tube temperature
- Shroud liner temperature
- Insulation temperature
- High temperature shield (HTS) temperature

The bundle degradation variables represent the damage to the bundle and give the fraction or percentage of

- Zr oxidized
- $\text{UO}_2$  dissolved
- $\text{ZrO}_2$  dissolved
- Zr dissolved by AIC<sup>3</sup>

---

<sup>3</sup> AIC = Ag, In, Cd absorber material

- Molten Zircaloy
- AIC liquefied
- Total mass (UO<sub>2</sub>, ZrO<sub>2</sub>, Zr, AIC)
- Bundle blockage

All mass fractions are defined by

$$100x \frac{M_i(t)}{M_i(0)}$$

with  $M_i(t)$  = amount of mass at level i and time t for each mass considered  
 $M_i(0)$  = initial amount of mass at level i for each mass considered

In the case of ZrO<sub>2</sub> dissolved  $M_i(0)$  refers to the theoretical mass of ZrO<sub>2</sub> if the initial mass of Zr is completely oxidized.

The core blockage is defined by

$$100x \frac{A_i(0) - A_i(t)}{A_i(0)}$$

with  $A_i(t)$  = Flow area available for the fluid at level i and time t  
 $A_i(0)$  = Initial flow area available for the fluid at level i

#### 4.2 Participants and Codes

Representatives of nine organizations participated in the International Standard Problem No. 31 (ISP31) based on the CORA-13 experiment on severe fuel damage. Five different codes were used, i.e. FRAS-SFD, ICARE2, KESS-III, MELCOR and SCDAP/RELAP5. Table 4.1 summarizes the analysts, the participating organizations and the codes used.

In addition two further contributions were delivered out of the time schedule. Their results are added in the Appendix.

#### 4.2.1 FRAS-SFD

The FRAS-SFD /7/ code is being developed in the Nuclear Research Institute at Rez near Prague (Czechoslovakia) since early 1990. The main goal of the development is to provide a suitable tool for evaluation of particular phenomena occurring during a severe accident in a PWR; especially modelling of the oxidation and dissolution processes at elevated temperatures. Principally it is based on the FRAS-SFD code originally developed for the modelling of fuel thermomechanical behavior under LOCA and RIA conditions.

The FRAS-SFD code describes the behavior of a single PWR fuel rod including:

- heat transfer in the fuel rod,
- one and two-phase thermalhydraulics in a single channel without reflood,
- high-temperature oxidation by steam,
- $\text{UO}_2$ /Zircaloy chemical interaction at high temperatures,
- $\text{UO}_2$  and  $\text{ZrO}_2$  dissolution in molten Zircaloy,
- deformations of the fuel rod.

However, in the present version of the FRAS-SFD the module for molten material relocation is not included so that the calculations can be performed only for the intact geometry.

#### 4.2.2 ICARE2

The ICARE2 computer code, developed at the Institut de Protection et de Surete Nucleaire (IPSN), is a mechanistic computer code which models all the main phenomena occurring during a severe PWR accident /8/. It works as a stand-alone code to describe both experimental facilities and reactor cores. The present version is the preliminary ICARE2V2mod1 version running on a SUN station.

The thermalhydraulic model is derived from the one-dimensional, two phase flow model of the CATHARE code /9/ without liquid phase available. Only one noncondensable gas is taken into account. So, the gas phase flowing into a channel is a mixture

of the steam and of the non-condensable gas chosen (hydrogen, argon or helium). To better fit the radial temperature gradients a multichannel modelling without cross-flow is possible. Changes in the geometry as a consequence of the relocation of molten materials are taken into account.

The code considers radial and axial heat conduction, various convective heat exchange modes and radiative heat transfer.

Three states of material are defined in the mechanical model: compact (generally the initial state), cracked (internal oxidation and release of fission products are allowed) and dislocated (material is able to flow down). A special module is implemented to calculate the ballooning and the burst of the cladding. Melting, down flow and refreezing of materials are described.

The following chemical reactions are considered in the code: Zircaloy and stainless steel oxidation by steam as well as fuel and  $ZrO_2$  dissolution by molten Zircaloy. The dissolution of Zircaloy by molten AIC is not modeled. Only an instantaneous dissolution of Zircaloy is assumed when in contact with AIC.

#### **4.2.3 KESS-III**

The KESS-III code, being developed at IKE Stuttgart, addresses major in-vessel severe accident phenomena in a LWR /10/. The physical and chemical processes are modeled by means of independent modules with data exchange through a common data base.

The thermalhydraulic model is a 1-D steady state channel model for a gas mixture with mono- or multi-channel geometry but without cross-flow. In the present version the gas mixture flow was extended to steam-water mixture flow by using a drift flux model. For most of the quenching mode a film boiling mode, e. g. inverted annular flow, has been considered.

KESS treats chemical reactions between steam and Zircaloy (oxidation) as well as between Zircaloy and  $UO_2$  (dissolution). Oxidation of stainless steel and Inconel is not considered. No interaction between cladding and spacer grids is considered. The

dissolution of Zircaloy by molten AIC as well as the dissolution of  $ZrO_2$  by molten metallic Zircaloy is not taken into account.

Cladding deformation is described by means of pellet-cladding contact and ballooning. If the maximum stress or strain exceeds given limits cladding rupture is assumed. Fragmentation of oxidized cladding is considered, using empirically derived embrittlement criteria.

#### **4.2.4 MELCOR**

MELCOR is an integrated computer code for modelling of severe accidents in nuclear power plants through all stages of the accident. It is being developed at Sandia National Laboratory for the USNRC /11/. The governing equations for the thermalhydraulic behavior are the two-fluid conservation equation of mass, momentum and energy. Control volumes are connected through flow paths without restrictions regarding the network. For the reactor core a separate heat transfer package was developed. It treats all important modes of heat transfer within the core as well as fission power generation, metal oxidation, debris formation, and relocation.

MELCOR contains a model to calculate the downward flow of molten material and the subsequent refreezing, the so-called "candling" process. It is based on thermalhydraulic principles incorporating user-specified refreezing heat transfer coefficients. No explicit model for clad ballooning is incorporated. Cladding rupture is deemed to occur when a given threshold temperature is exceeded.

#### **4.2.5 SCDAP/RELAP5**

The SCDAP/RELAP5 code is being developed by Idaho National Engineering Laboratory for the USNRC to provide a predictive capability of the state in LWR reactor coolant systems during severe accidents and other transients /12/. The thermalhydraulic model uses six basic conservation equations together with the state equations.

The meltdown and fuel relocation process is calculated in 3 steps: determination of locations where the cladding and fuel have been liquefied, determination of locations where the cladding oxide shell is breached and calculation of the movement of

liquefied cladding and fuel material, including freezing and blockage formation. The failure criterion for the oxide shell is defined by a user supplied failure temperature.

The chemical reaction model calculates Zircaloy and stainless steel oxidation and dissolution of  $\text{UO}_2$  and  $\text{ZrO}_2$  by molten Zircaloy. Cladding mechanical deformation is calculated for both axisymmetric and local asymmetric ballooning and collapse rupture of fuel rods.

### **4.3 Computational Model**

This section gives a short overview of the important input features of the computational model used by the participants as far as described in the submitted reports/13-21/. User-specified input parameters are given in Table 4.2.

#### **4.3.1 AEA**

The SCDAP/RELAP5 model represents the CORA test rig up to the outer boundary of the high temperature shield. These include two parallel flow channels (bundle and by-pass flow channel), the rods, the shroud and the high temperature shield. The bundle and by-pass flow channel are connected by three cross-flow junctions .

Six SCDAP component groups represent the rods and the shroud: the single central unheated rod, the first ring of four heated rods, the second ring of six unheated rods, and two control rods, the third ring of twelve heated rods, and the shroud including the  $\text{ZrO}_2$  insulation layer. There is a simple model of melt hold-up on spacer grids, which themselves are assumed to disappear if their melting temperature is reached. The ballooning is modeled by using a internal rod pressure similar to the specified pressure history.

#### **4.3.2 CEA**

The ICARE2 model uses a single channel to describe the thermal hydraulic flow conditions.

The test bundle is represented by seven rods (3 heated rods, 3 unheated rods, 1 absorber rod), a cylinder for the shroud liner and the shroud insulation. Not modeled are the high temperature shield (HTS), the open windows, the by-pass flow and the spacer grids. The temperature history at the external surface of the shroud insulation is imposed as a boundary condition.

The following chemical reactions are considered: zirconium oxidation and the dissolution of  $\text{UO}_2$  and  $\text{ZrO}_2$  by molten Zircaloy. The dissolution is stopped according to the liquidus temperature of the ternary phase diagram U-Zr-O. After cladding burst time a 250 mm high cracked zone is supposed to appear allowing double side oxidation.

The  $\text{ZrO}_2$  layers are deemed to fail if one of the two following sets of criteria is fulfilled:

- $\text{ZrO}_2$  thickness < 0.3 mm and temperature > 2 250 K
- temperature > 2 500 K

Failure of the control rod guide tube occurs as soon as the melting temperature of stainless steel is reached (1 730 K).

#### 4.3.3 ECN

The SCDAP/RELAP5 nodalization of the hydraulic system and boundary conditions is given in Figure 4.1. The bundle itself is represented by one flow channel divided into 15 axial zones without a by-pass channel and cross flow. The heated and unheated rods, the absorber rods and the shroud are modeled by 6 components. The temperature outside the shroud insulation is imposed as a boundary condition, as given in the specification.

#### 4.3.4 IKE

The bundle section is modeled by only one fluid channel due to the narrow radial dimensions. Four zones were adopted (central rod, first, second and third ring) for the radial discretization and 18 axial levels with equal mesh dimension for the axial discretization. The shroud region was simulated using 2 cylindrical layers of different materials ( $\text{Zry-4}$ ,  $\text{ZrO}_2$ ).

The oxidation of Zry-4 was considered. A temperature of 2 250 K was specified for the onset of fuel dissolution by molten Zircaloy. The failure criterion of the cladding is assumed to be an oxidized thickness of less than 300  $\mu\text{m}$  and the cladding temperature greater than 2250 K or the cladding temperature greater than 2600 K. The relocation velocity is set to 0.3 m/s.

#### **4.3.5 JAE**

For the hydraulic simulation a single channel model is used (see Figure 4.2). Six components according to the specification represent the bundle and the shroud. Failure of the cladding is assumed to occur at  $\text{ZrO}_2$  thickness  $< 0.6$  mm and temperature  $> 2\ 500$  K. Chemical reactions considered are the oxidation of Zry-4 and the dissolution of  $\text{UO}_2$  and  $\text{ZrO}_2$  by molten Zry-4.

#### **4.3.6 KAE**

For modelling the thermalhydraulic conditions a parallel channel model with cross flow junctions is adopted (Figure 4.3). The bundle itself is treated with six SCDAP components for two unheated rods, two heated rods, one control rod and one shroud component.

#### **4.3.7 NRI**

Since the FRAS-SFD can simulate only one single fuel rod the following simplifications have to be made:

- only one rod is chosen (heated rod in the first ring),
- only the fuel stack is considered,
- influence of control rods and shroud is neglected,
- a "fictive" shroud temperature was calculated,
- the calculation is valid only up to the onset of material relocation since cladding failure was disabled in the code by input parameters.

#### **4.3.8 SNL**

The nodalization diagram of the flow paths and control volumes is shown in Figure 4.4. The model consists of twelve control volumes and seventeen flow paths which basically are grouped into two parallel channels (bundle, by-pass) and the temperature boundary condition (pressure tube). The MELCOR core model contains four radial rings representing the central rod and the three radial rings. All four radial rings communicate to one hydro-dynamic control volume appropriate for the height. The shroud insulation and the high temperature shield are represented by heat structures. The quench water source was split into two volumes, one for the bundle flow and one for the by-pass flow. The flow rates of the two flows were adjusted to approximate as closely as possible the experimental conditions. The cross flow connections were closed during quenching.

#### **4.3.9 VTT**

For thermal hydraulic modelling a parallel channel model with cross-flow is used. Four SCDAP components are used for the bundle, one component each for the heated fuel rods, the unheated fuel rods, the absorber rods and the shroud. Therefore, the calculated value for the central rod and second ring and for the first and third ring are equal as well.

The cladding failure criteria are as follows: temperature  $> 2\ 500\ \text{K}$  and  $\text{ZrO}_2$  thickness  $< 0.6\ \text{mm}$ .

### **4.4 Comparison of Analytical and Experimental Results**

This section gives a comparison of the experimental results with the results as provided by the participants, with some additional observations and comments. From the list of variables given in the specification, only the important ones are discussed. In order to associate the different curves with the organizations, each curve is labeled with a three-letter code according to Table 4.1.

#### 4.4.1 Initial and Boundary Conditions

Some initial and boundary conditions measured in the test facility are compared with those actually used by the participants. This facilitates the evaluation of the calculational results.

- Bundle Power

The measured bundle power and the data calculated by the participants are given in Fig 4.5. Between  $t = 3\ 000\ \text{s}$  and  $t = 4\ 800\ \text{s}$  the measured power increases steadily from 6 kW to 27 kW. This includes the power loss of the external resistance in the electrical connection which decreases from about 14 to 4 % and the heating power of the copper and molybdenum electrodes which amounts to about 9 %. Some data include the external resistance (ECN, IKE, SNL), one curve shows only the heating power of the 1 m long system electrode (JAE). While five of the calculations (AEA, ECN, IKE, NRI, SNL) follow the measured data quite well, one of them (JAE) uses a lower estimate of the heating power, due to a higher external resistance (1 m $\Omega$ /rod), and two of them (KAE, VTT) deviate considerably and reveal a power shut off at an earlier time than specified. The CEA curve only shows the thermal power generated in the tungsten heater and part of the molybdenum electrodes.

- Steam Inlet Flow

Steam inlet flow (Figure 4.6) during prequench results from a water feed flow of 6 g/s between 3300 and 4900 s with a time constant of about 100 s. This value was used by NRI. Five participants (AEA, IKE, JAE, KAE, SNL) have chosen a shorter and three (CEA, ECN, VTT) estimated a much larger time constant which results in an underestimated steam flow. CEA has added the evaporation rate from the quench cylinder to the inlet flow.

- Inlet Temperature

The given inlet temperature (Figure 4.7) was correctly put in by all but one (ECN) participant.

#### 4.4.2 Temperature

The calculated and measured temperatures indicate the thermal behavior of the bundle including the shroud and high temperature shield. To give a complete picture of the thermal behavior, many temperatures are calculated and plotted in the report, though only a few of them are recorded experimentally and discussed here.

- Fuel Temperature

Figure 4.8 shows the fuel temperature of a heated rod (first ring) in the upper part of the bundle (location 750 mm). In general, the experiment is quite well predicted during the heat up period. After the onset of the zirconium oxidation, the fuel temperature is strongly influenced by that phenomenon. Therefore, this period is discussed with the cladding temperature figures. Figure 4.9 to 4.12 show further fuel temperatures at different locations of the bundle. A comparison of Figures 4.8 and 4.12 shows that ECN and JAE calculate large differences between heated and unheated rod temperatures (350 K at 4000 s) while the other codes predict temperature differences of about 100 K, which is in the order of measured temperature differences. The under-prediction of rod temperatures by KAE and VTT might result from the underpredicted bundle power. The other curves (AEA, CEA, IKE, NRI, SNL) are in good agreement with the experimental data, except for the temperature excursion indicated by CEA at level 050, which results from melt relocation.

- Cladding Temperature

The cladding temperature in the upper part of the bundle (elevation 750 mm) of a heated rod (first ring) is plotted in Figure 4.13. Since no cladding temperature was measured and fuel and cladding temperature are fairly close, the measured fuel temperature at this location is added to the plot for comparison purpose.

Again during the heat up phase between 3 000 and about 4 000 s the temperature behavior is quite well calculated with a spread of about 150 K. But this temperature spread results in a larger spread in time of the onset of the temperature escalation. The onset spans over 400 s, beginning at about 4 050 s. The onset of the fuel temperature escalation lies at about 4 100 s. While the time values of the onset show considerable differences the temperature values are very close together (1800 K)

except CEA which indicates like the experimental data, the onset at 1500 K, and IKE which shows a continuous increase of heatup rate.

At 4 900 s quenching occurs as measured in the experiment and given as boundary conditions.

Cladding temperatures at other locations throughout the bundle are given in Figures 4.14 to 4.17. They show that in four calculations the temperature is underpredicted and the temperature escalation is significantly delayed (ECN, JAE) or even not reached (KAE, VTT). On the other hand, CEA predicts in the lower bundle part a temperature escalation which is too early, induced by melt relocation.

- Absorber and Guide Tube Temperature  
Shroud Temperature

Apart from the temperature level the absorber and guide tube temperature (Figures 4.18 and 4.19) and the shroud temperature (Figure 4.20) show the same behavior as previously discussed for the fuel cladding.

A very tight coupling between fuel rod and absorber rod temperatures is seen in CEA and IKE calculations, temperature differences of about 100 K are predicted by SCDAP user. Similar statements are valid for the shroud temperature, except for JAE, KAE and VTT which did not simulate shroud oxidation. SNL shows somewhat larger temperature differences between fuel rods and shroud.

- Outer Insulation Temperature  
Inner HTS Temperature

An example of the shroud outer insulation temperature (location 750 mm) is given in Figure 4.21. CEA uses the recommended temperature history as a boundary condition (BC) while ECN and JAE use other estimates as BC. In the other calculations the same temperature trend is predicted, but with temperature differences up to  $\pm 300$  K compared with the recommended BC. The measured curve indicates a very strong temperature rise at about 4300 s. This might result from melt penetration through the shroud insulation, which is beyond the modelling capability of the codes used.

The inner HTS temperature at location 550 mm is given in Figure 4.22. Two calculations (IKE, SNL) follow the measured data quite well, while AEA and KAE do not show the temperature increase at 4 300 s.

- Fluid Temperature

The calculated fluid temperature at location 750 mm is given in Figure 4.23. Qualitatively, in four calculations (AEA, CEA, NRI, SNL) the fluid temperature follows the shroud temperature quite well, while the other (IKE, JAE, KAE, VTT) show much lower temperatures.

#### 4.4.3 Core Degradation Variables

The core degradation variables give a picture of core during the experiment. The data are plotted for a given time over the length of the core. For time  $t = 4\ 750$  s, just before quenching occurs, in some plots the experimental values are added, as they have been recorded after the test by analyzing the post-test state of the bundle.

a) Bundle State Before Relocation

- Zirconium Oxidation

Figures 4.24 and 4.25 show the percentage of  $ZrO_2$  for the first ring (heated rod). The post test examination (PTE) shows complete oxidation of all remaining Zircaloy in the upper bundle part. The estimated average of remaining Zircaloy-4 is about 72 %, above 450 mm the other 28 % are molten and relocated. This estimation was based on the measured total hydrogen evolution. Below 250 mm, no significant oxidation has been observed. At 4 250 s most of the calculations reveal an oxidation between 10 and 50 % except JAE and NRI. Here the amount of oxidized zirconium is up to 100 %. The situation at 4 750 s is more complex but basically the same as at 4 250 s. As it can be seen the estimated increase of  $ZrO_2$  between the elevations 250 mm and 450 mm is calculated by most of the codes. At other locations in the bundle or at the shroud the calculated general behavior is quite similar.

- UO<sub>2</sub> Dissolved

The amount of UO<sub>2</sub> dissolved by molten Zircaloy is plotted in Figures 4.26 and 4.27. The measured data show the UO<sub>2</sub> relocated, since no discrimination can be made between breakaway and dissolution. For the first ring (heated rod) at 4 750 s the dissolution reaches up to 20 % (except AEA which reaches 50 %) in the upper part of the bundle. For the second ring (unheated rod) the dissolution is considerably smaller. Experiment and calculation agree in the location of UO<sub>2</sub>-dissolution (400 mm to 1000 mm), but not in the actual percentage of dissolution.

It should be remarked, that the initial UO<sub>2</sub> mass of the heated rods (first ring) is only 57 % of the UO<sub>2</sub> mass of the unheated rods (second ring). This means, that for the same removed mass, the relative value for the heated rods is nearly twice as high as for the unheated rods. It is obvious that this has not been taken into account in the calculation results except for AEA. Breakaway and fuel dissolution by molten Zircaloy in the gap between heater and annular pellet has not been modeled by the codes.

- Zircaloy Molten

The amount of molten Zircaloy for the first ring (heated rod) is given in Figure 4.28. The estimated experimental value of molten Zircaloy is 28 % in the upper part above 450 mm. This value is understood to include the amount of Zircaloy having alloyed with absorber material and having dissolved fuel. Below 250 mm no significant melting has been observed. At 4 750 s the molten Zircaloy runs up to 60 % in the upper part of the bundle, except for CEA where up to 100 % is molten and SNL where the calculated molten Zircaloy is completely relocated to the lower part of the bundle. The second ring (unheated rod) reveals similar behavior (Figure 4.29).

- Absorber Material (AIC) Liquefied

Figure 4.30 illustrates the experimental amount of absorber material liquefied before relocation. The experimental data show that above location 350 all absorber material was liquefied and disappeared. The absorber materials remain in place below 250 mm. The VTT calculation shows only a partial liquefaction and disappearance. CEA and AEA calculated a complete liquefaction of the absorber material above location 50, and KAE above 650 mm. According to SNL calculation, above 50 mm all absorber

material liquefied, but stays in place up to 250 mm. At higher elevations the absorber material disappeared.

b) Bundle State After Relocation

- $\text{UO}_2$  Total Mass

Figure 4.31 gives the total mass of  $\text{UO}_2$  at 4 750 s. While three calculations (AEA, KAE, VTT) show a significant relocation or dissolution in the upper part of the bundle, the remaining ones reveal only a slight relocation or dissolution.

The measured amount of  $\text{UO}_2$  shows a pronounced peak of > 200 % at 500 mm close to the spacer grid location. This peak was not calculated, because the codes do not consider spacer grids in sufficient detail. AEA, KAE and VTT show a refreezing of  $\text{UO}_2$  at lower location over a wider range and lower maximum blockage values.

- Zr Total Mass

Figure 4.32 shows the total mass distribution of metallic zirconium. The measured data have, as can be seen for  $\text{UO}_2$ , also a pronounced peak at 500 mm elevation and a second refreezing at the lower end of the bundle. KAE calculates a similar distribution, the AEA and VTT results show less Zr accumulation in the lower bundle part. The other calculation shows only the remaining metallic Zr. In the CEA calculation all zirconium is relocated below elevation 250 mm. The complete relocation of the cladding and liner material took place while the metallic Zr content was still high.

- $\text{ZrO}_2$  Total Mass

The total mass of  $\text{ZrO}_2$  is given in Figure 4.33. The experimental data increase between elevation 250 and 450 mm from 0 to 72 % (see Figure 4.25). This estimation does not take into account the relocation of  $\text{ZrO}_2$  fragments and their accumulation as rubble at lower bundle elevations, since this process could not be quantified. The analytical data show, due to higher amount of Zr melting, less oxidation but a similar local distribution, except CEA which indicates the relocation of the oxide shell to a lower position.

- Absorber Material Total Mass

In Figure 4.34 the total mass of the absorber material is plotted. The data comply with the results in Figure 4.30, which shows the absorber material liquefied. Both in the experiment and in the calculation, the absorber material can be found in the lower part of the bundle. The experimental data show the accumulation of the absorber material between -100 and + 300 mm, while the analytical data reveal the remaining, not relocated material.

- Total Mass

The total mass (U - Zr - O - AIC) is plotted in Figure 4.35. Two experimental curves are added to the analytical ones. One was estimated from metallographic post-test analysis and the other from weight measurements of the sectioned bundle. Both curves give comparable results. From the analytical data it can be seen that AEA calculated the overall mass distribution fairly correctly, except the position of the maximum value of mass, which is at lower elevation than measured. The other curves are not comparable.

- Core Blockage

Core blockage at 4 750 s is plotted over the length of the bundle in Figure 4.36. The core blockage is comparable to the total mass (Figure 4.35). The experimental data vary between - 20 and + 40 % with a maximum of 40 % at elevation 480 mm and a second maximum of 20 % at location 200 mm. While four participants calculate a blockage between 10 % and 40 % between 50 and 450 mm, one calculates approximately 85 % (CEA) at a lower elevation. In general, the two different blockages formed are caused by different phenomena. The blockage at the elevations of 200 mm consists mainly of absorber rod material whereas the other blockage is composed of metallic Zr containing dissolved  $\text{UO}_2$  and  $\text{ZrO}_2$ .

The overall behavior of the analytical data compares quite well with the experimental data, though none of the calculations show two separated blockage zones.

#### 4.4.4 Hydrogen Generation

In Figure 4.37 and 4.38 the calculated hydrogen generation rate of the bundle and of the shroud is plotted. It can be seen that most of the calculated hydrogen is generated during the time of the temperature excursion and none during the quench phase. The maxima of the rate vary approximately between 0,1 and 0,4 g/s (bundle) and 0,1 and 0,3 g/s (shroud). The sum of both rates is given in Figure 4.39 together with the experimental data.

The accumulated hydrogen generation for the bundle plus shroud is given in Figure 4.40. The experimental value at the end of the experiment is 210 g.

The comparison between experimental data and calculated results indicates that all codes

- overpredict the oxidation during the temperature escalation phase
- underpredict the oxidation during the high temperature phase where melting and relocation occurs
- do not simulate oxidation during the quenching where embrittlement and fragmentation take place.

Nevertheless, the experimental data are affected by some uncertainties and delay in the measurement of partial pressure. It can be shown that during the prequench phase the maximal possible hydrogen generation rate of approximately 0.7 g/s is never reached which indicates that a significant amount of steam bypasses the bundle region.

## 5 Summary and Assessment

The International Standard Problem (ISP) No. 31 on severe fuel damage which has been proposed by OECD-CSNI was performed to improve the understanding of the physical phenomena involved and to assess the predictive ability of computer codes used in severe accident analyses. The experiment selected for this ISP was the CORA-13 experiment conducted at the Kernforschungszentrum Karlsruhe. CORA-13

was designed to investigate the behavior of PWR fuel elements under severe accident conditions, including liquefaction, melting and relocation, as well as during fast cool down due to refill.

To challenge the predictive capability of the codes as far as possible, the ISP was conducted as a blind exercise, i. e. only the initial and boundary conditions were provided to the participants for performing the calculation.

Nine organizations participated in the blind ISP using the codes FRAS-SFD, ICARE2, KESS-III, MELCOR and SCDAP/RELAP. In addition, an ATHLET-CD calculation was performed in order to produce some boundary conditions which could not be measured. For this ATHLET-CD calculation the measured temperature behavior was known.

The physical variables compared in the report are basically temperature histories at different locations in the bundle, hydrogen generation and core degradation variables of the final bundle state.

The following observations and conclusions have been drawn by the participants in the final workshop:

- Heat-up Phase

The thermal behavior up to significant oxidation has been predicted quite well by most of the codes. Larger deviations have been observed for the onset of the oxidation-induced temperature escalation ( $\Delta t = 400$  s). It was recommended to calculate the heat balance more accurately to get a better onset of the escalation.

- Material Interaction and Cladding Failure Criteria

The cladding failure criteria have a great influence on the bundle behavior by limiting the  $UO_2$  dissolution and Zr oxidation. The codes use cladding failure temperatures in the range 2250 to 2750 K which at least at the upper end is too high compared with the experiment. None of the codes was able to model the interaction between the control rod or grid spacer material with the fuel rod cladding which weakens the cladding and which leads to early melt relocations. To get a better agreement between

calculations and experiment, models for dissolution of  $\text{UO}_2$  and  $\text{ZrO}_2$  by liquid Zircaloy should be improved and cladding failure criteria should be derived mechanistically. Unfortunately, cladding failure mechanisms and temperatures cannot be quantified experimentally with the required precision.

- Refill

Six of the participants calculated the refill phase. The calculations only show a temperature decrease but no increase due to chemical reaction as measured just before the decrease. The temperature drop is too slow due to the underestimation of the heat transfer, which results in delayed quenching.

- Hydrogen Generation

While early in the transient the hydrogen generation has been overpredicted, it has been underpredicted in the later prequench phase. The overprediction might be due to unlimited oxidation in the calculation, which did not occur in the experiment because of shielding effects, diffusion limitation of vapor and bypass flow.

None of the codes except ATHLET-CD could predict the intensive hydrogen generation during refill. The reason for this is the lack of an appropriate model and the calculated oxidation of all Zr before the beginning of refill.

It was recommended to develop an embrittlement model for partially oxidized cladding.

- Core Blockage

The calculated main core blockage reproduces fairly well the experimental data despite the lack of correct modelling of the real bundle geometry.

- Oxidation Profile

The oxidation profile at the end of the experiment was adequately calculated though an overestimation in the prequench phase occurred. It was recommended to introduce a double-sided oxidation model into the codes which describes in addition the cladding deformation, the so-called "flowering".

- General Observation

The code user has a great influence on the calculated results, e. g. by setting up the correct heat balance of the system or by choosing the cladding failure criteria. For code development the modelling of more materials interactions was recommended.

Verification of reactor codes on small-scale experiments needs more code versatility, concerning power profile evolution, surrounding structures with imposed boundary conditions, more output conveniences. More verification and validation activities remain necessary for severe fuel damage codes.

Furthermore, the exercise illustrates the need for improved user guidelines with more detailed information and recommendations, and the need for user expertise on core degradation phenomena, to make more effective the use of the codes in this field.

#### Acknowledgment

The authors would like to acknowledge the financial support of the German Ministry for Research and Technology and the technical comments of the members of the OECD-CSNI. Thanks also to T.J. Haste for reviewing the report.

## 6 References

- /1/ CSNI  
Standard Problem Procedure  
CSNI Report No. 17, January 1984
- /2/ S. Hagen et al.  
Results of Severe Fuel Damage Experiment CORA-13  
KfK 5054, February 1993
- /3/ B. Adroguer, A. Commande, C. Rongier  
International Standard Problem ISP 28  
PHEBUS-SFD B9+ Experiment on the Degradation of a PWR Core Type  
Preliminary Comparison Report, DRS/SEMAR 16/91, May 1991
- /4/ C. Gonnier, G. Geoffroy, B. Adroguer  
PHEBUS Severe Fuel Damage Programme  
ANS Meeting, Portland, July 1991
- /5/ M. Fimhaber, K. Trambauer, S. Hagen and P. Hofmann  
Specification of the International Standard Problem 31:  
CORA-13 Experiment on Severe Fuel Damage.  
GRS Cologne / KfK Karlsruhe, August 1991
- /6/ K. Trambauer  
The Code ATHLET-CD for the Simulation of Severe Accidents in Light Water  
Reactors  
NURETH5, Salt Lake City, 1992
- /7/ F. Pazdera et al.  
Test Calculations with Computer Code FRAS for Thermomechanical Calcula-  
tion of Light Water Reactor Fuel Rod Behavior under Accident Conditions  
UJV 7891-T, Rez near Prague, CSFR, 1987

- /8/ ICARE2 Version 2  
User's Manual and Physical Models  
To be published
- /9/ J. Micaelli et al.  
CATHARE Best-estimate Thermalhydraulic Code for Reactor Safety Studies.  
Last Developments.  
Int. Conf. Th. React. Safety, Avignon, France, October 1988
- /10/ K.-D. Hocke, M. Bürger, A. Schatz  
KESS-III, Ein Programmsystem zur Simulation auslegungsüberschreitender  
Störfälle in Leichtwasserreaktoren  
IKE2-93,  
Stuttgart, January 1991
- /11/ R. M. Summers et al.  
"MELCOR 1.8.0: A Computer Code for Severe Nuclear Reactor Accident  
Source Term and Risk Assessment Analysis"  
NUREG/CR-5531, SAND90-0364, Sandia National Laboratories, January  
1991
- /12/ C.M. Allison et al.  
SCDAP/RELAP5/MOD2 Code Manual  
NUREG/CR 5273, September 1989
- /13/ R.P. Hiles, T.J. Haste, L.M. Shirley  
International Standard Problem 31: Summary of UK Blind Calculations of the  
CORA-13 Melt Progression Experiment using the SCDAP/RELAP5 Code  
AEA Reactor Services, Winfrith Technology Centre  
AEA RS 5225, January 1992
- /14/ J.C. Crestia, R. Gonzalez  
International Standard Problem 31  
Results of ICARE2 Blind Calculations on the Severe Fuel Damage CORA-13  
Experiment  
CEA Report, January 1992

- /15/ H.A. Roodbergen  
International Standard Problem 31 (CORA-13 Experiment on Severe Fuel  
Damage)  
BU Nuclear Energy, (ECN), NP-R & V-92-01
- /16/ K. Müller, M. Bruder, K.-D. Hocke  
ISP-31: CORA Test 13  
Institut für Kernenergetik und Energiesysteme, January 1992
- /17/ K. Hashimoto, K. Soda, E. Matsumoto  
Description of the Analytical Model used for ISP-31  
Japan Atomic Energy Research Institute, May 1992
- /18/ H.-D. Kim  
KAE-Report, March 1992
- /19/ L. Belovsky, M. Valach  
Simulation of the CORA-13 Experiment by the FRAS-SFD Computer Code in  
Blind Conditions  
Nuclear Research Institute Rez, 1992
- /20/ R.J. Gross, S.L. Thompson, G.M. Martinez  
MELCOR Simulation of the International Standard Problem ISP-31  
Sandia National Laboratories, 1992
- /21/ E. Pekkarinen  
Technical Research Center of Finland  
Report, January 1992

## 7 Tables

**Table 3.1: Design characteristics of test bundle CORA-13**

Bundle type:	PWR
Bundle size:	25 rods
Number of heated rods:	16
Number of unheated rods:	7
Pitch:	14,3 mm
Rod outside diameter:	10,75 mm
Cladding material:	Zircaloy-4
Cladding thickness:	0,725 mm
Rod length:	<ul style="list-style-type: none"> <li>- heated rods: 1960 mm (elevation - 489 to 1471 mm)</li> <li>- unheated rods: 1672 mm (elevation - 201 to 1471 mm)</li> </ul>
Heated pellet stack:	1000 mm
Heater material:	Tungsten (W)
Heater	<ul style="list-style-type: none"> <li>- length</li> <li>- diameter</li> </ul>
Fuel pellets	<ul style="list-style-type: none"> <li>- heated rods: UO<sub>2</sub> annular pellets</li> <li>- unheated rods: UO<sub>2</sub> full pellets</li> </ul>
Pellet stack	<ul style="list-style-type: none"> <li>- heated rods: 0 to 1000 mm</li> <li>- unheated rods: - 199 to 1295 mm</li> </ul>
U-235 enrichment:	0,2 %
Pellet outer diameter (nominal):	9,1 mm
Grid spacer	<ul style="list-style-type: none"> <li>- material: Zircaloy-4, Inconel 718</li> <li>- length: Zry 42 mm Inc 38 mm</li> <li>- location: lower (Zry) - 5 mm center (Inc) + 496 mm top (Zry) + 880 mm</li> </ul>
Shroud	<ul style="list-style-type: none"> <li>- material: Zircaloy-4</li> <li>- wall thickness: 1,2 mm</li> <li>- outside dimensions: 89,4 x 90,4 mm</li> <li>- elevation: 36 mm to 1231 mm</li> </ul>
Shroud insulation	<ul style="list-style-type: none"> <li>- insulation thickness: ZRO<sub>2</sub> fibre 19 mm</li> <li>- elevation: 36 mm to 1036 mm</li> </ul>

**Table 3.1: (Continuation)**

Mo electrode	- length - diameter	300 mm 8,6 mm
Cu electrode	- length - length - diameter	189 mm (lower end) 669 mm (upper end) 8,6 mm
Absorber rod	- numer of rods - material and composition - cladding - cladding OD - cladding ID - length - absorber material	2 80Ag, 15In, 5Cd (wt. %) Stainless steel 11,2 mm 10,2 mm 1660 mm -189 mm to + 1300 mm
Absorber rod guide tube	- material - OD - wall thickness of tube	Zircaloy-4 13,8 mm 0,8 mm
Plenum Volume	- heated rods - unheated rods	$12 \times 10^{-6} \text{ m}^3$ $87 \times 10^{-6} \text{ m}^3$

**Table 3.2: Total specific mass data of bundle CORA-13**

Tungster heater elements	8,70 kg/m
UO <sub>2</sub>	11,24 kg/m
Zircaloy in rods	3,45 kg/m
Zircaloy in absorber rods	0,43 kg/m
Stainless steel in absorber rods	0,26 kg/m
Ag / In / Cd absorber	1,62 kg/m
Inconel grid spacer	0,11 kg
Zircaloy grid spacer	0,14 kg
Zircaloy of shroud	2,60 kg/m
Total zircaloy	6,48 kg/m

**Table 3.3: Areas of bundle CORA-13**

<u>Cross section areas [m<sup>2</sup>]</u>	
Tungsten	4,524 x 10 <sup>-4</sup>
UO <sub>2</sub>	1,077 x 10 <sup>-3</sup>
Zircaloy cladding	5,252 x 10 <sup>-4</sup>
Absorber (Ag / In / Cd)	1,634 x 10 <sup>-4</sup>
Stainless steel cladding	3,362 x 10 <sup>-5</sup>
Zircaloy guide tube	6,535 x 10 <sup>-5</sup>
Zircaloy shroud	3,888 x 10 <sup>-4</sup>
Total area inside the shroud	8,038 x 10 <sup>-3</sup>

Table 3.4: Average Chemical composition of various types of relocated melts at different CORA bundle 13 cross section elevations

CORA bundle 13; PWR quench test

Type of melt	Cross section	Zr	Fe	Cr	Ni	Ag	In	Cd	U
metallic	148 mm range	33 - 54	3 - 6	1 - 2	1 - 2	30 - 49	5 - 10	1 - 3	0 - 2
	average	44,5	4,4	1,3	1,8	37,8	7,1	2,2	< 1,0
metallic	248 mm range	47 - 61	7 - 8	2 - 3	2 - 3	16 - 32	4 - 6	1	3 - 4
	average	53	7,5	2,5	2,8	23	4,7	1	3,8
metallic	398 mm range	55 - 69	4 - 5	1 - 2	-	4 - 10	2 - 3	-	13 - 20
	average	62,8	4,2	1	-	6,8	2,2	-	17,5
ceramic	range	54 ± 1	-	-	-	-	-	-	46 ± 1
metallic	448 mm range	33 - 72	2 - 13	1 - 8	0 - 10	2 - 11	0 - 2	-	7 - 45
	average	50	5	3	5,5	5	0,5	-	22
ceramic	range	78 ± 3	-	-	-	-	-	-	22 ± 3
ceramic	498 mm range	12 - 50	1 - 2	0 - 1	0 - 1	1 - 3	-	-	43 - 72
	average	33	1	0	0	1	-	-	63

- compositions in wt.%  
- on average up to 10 different locations were analysed by SEM/EDX examinations

**Table 4.1** Analysts, Organizations and Codes Used

	<b>ANALYSTS</b>	<b>ORGANIZATIONS</b>	<b>COMPUTER CODE</b>
AEA	R. P. Hiles, T. J. Haste, L. M. Shirley	AEA Reactor Services UK	SCDAP/RELAP5/MOD2.5
CEA	J. Crestia, R. Gonzales	Commissariat à L'Energie Atomique, France	ICARE2/V2/MOD1
ECN	H. A. Roodbergen	Netherlands Energy Research Foundation	SCDAP/RELAP5/MOD3
IKE	K. Müller, M. Bruder, K.-D. Hocke	Institut für Kernenergetik und Energiesysteme, Stuttgart	KESS-III
JAE	K. Hashimoto, K. Soda, E. Matsumoto	Japan Atomic Energy Research Institute	SCDAP/RELAP5
KAE	Hee-dong Kim, Rae-Joon Park	Korea Atomic Energy Research Institute	SCDAP/RELAP5/MOD2.5
NRI	L. Belovsky, M. Valach	Nuclear Research Institute Rez	FRAS-SFD
SNL	R. J. Gross, S. L. Thompson, G. M. Martinez	Sandia National Laboratories	MELCOR 1.8.0
VTT	E. Pekkarinen	Technical Research Centre of Finland	SCDAP/RELAP5/MOD2.5

TABELLE 4.2

End of Calculation	Nodalization	Axial meshes in heated zone	Rod types	Axial Power Profile	Material Properties	Ballooning	Cladding Failure	Zr Oxid.	UO <sub>2</sub> -Zr diss.	ZrO <sub>2</sub> -Zr diss.	Relocation Velocity
AEA 5 050 s End of Cooling	2 Flow Channels 3 Cross Flows	10	4 + AIC	M	MATPRO	yes	> 2 500 K and < 60 % Oxidized	C/U/H 1-s	Hofmann U-O-Zr	no	
CEA 4 800 s No Quenching	1 Flow Channel	21	6 + AIC	M	MATPRO	yes	> 2 250 K and < 300 μ Oxidized or > 2 500 K	U/H 2-s	Kim U-O-Zr	Hofmann U-O-Zr	0.6 m/s
ECN 5 050 s End of Cooling	1 Flow Channel	10	4 + AIC	M	MATPRO					no	
IKE 5 000 s After Quenching	1 Flow Channel	10	4 + AIC	M	MATPRO	yes	< 300 μ Oxidized > 2 250 K or > 2 600 K	L	Kim U-O-Zr	no	0.3 m/s
JAE 5 050 s End of Cooling	1 Flow Channel	10	4 + AIC	M	MATPRO		> 2 500 K and < 60 % Oxidized			no	
KAE 4 900 s No Quenching	2 Flow Channels 5 Cross Flows	10	4 + AIC	M	MATPRO	no	> 2 500 K < 60 % Oxidized			no	
NRI 4 500 s	1 Flow Channel	10	1 BC	BC		no	/.	---		no	---
SNL 5 050 s End of Cooling	2 Flow Channels 4 Cross Flows	10	4 + AIC	M	MELCOR Material Properties	no	> T <sub>crit</sub> and < Oxid crit.			no	
VTT 5 050 s End of Cooling	2 Flow Channels 5 Cross Flows	10	2 + AIC	M			> 2 500 K < 60 % Oxidized			no	

C/U/H: Cathcart, Urbanic, Heidrick  
 U-O-Zr: Ternary Diagram Limitation  
 1/2-s: Outer/Outer and Inner Cladding Oxidation  
 L: Leistikow

M: Electrical Heater Model  
 BC: Boundary Condition  
 AIC: Silver-Indium-Cadmium Control Rod

## 8 Figures

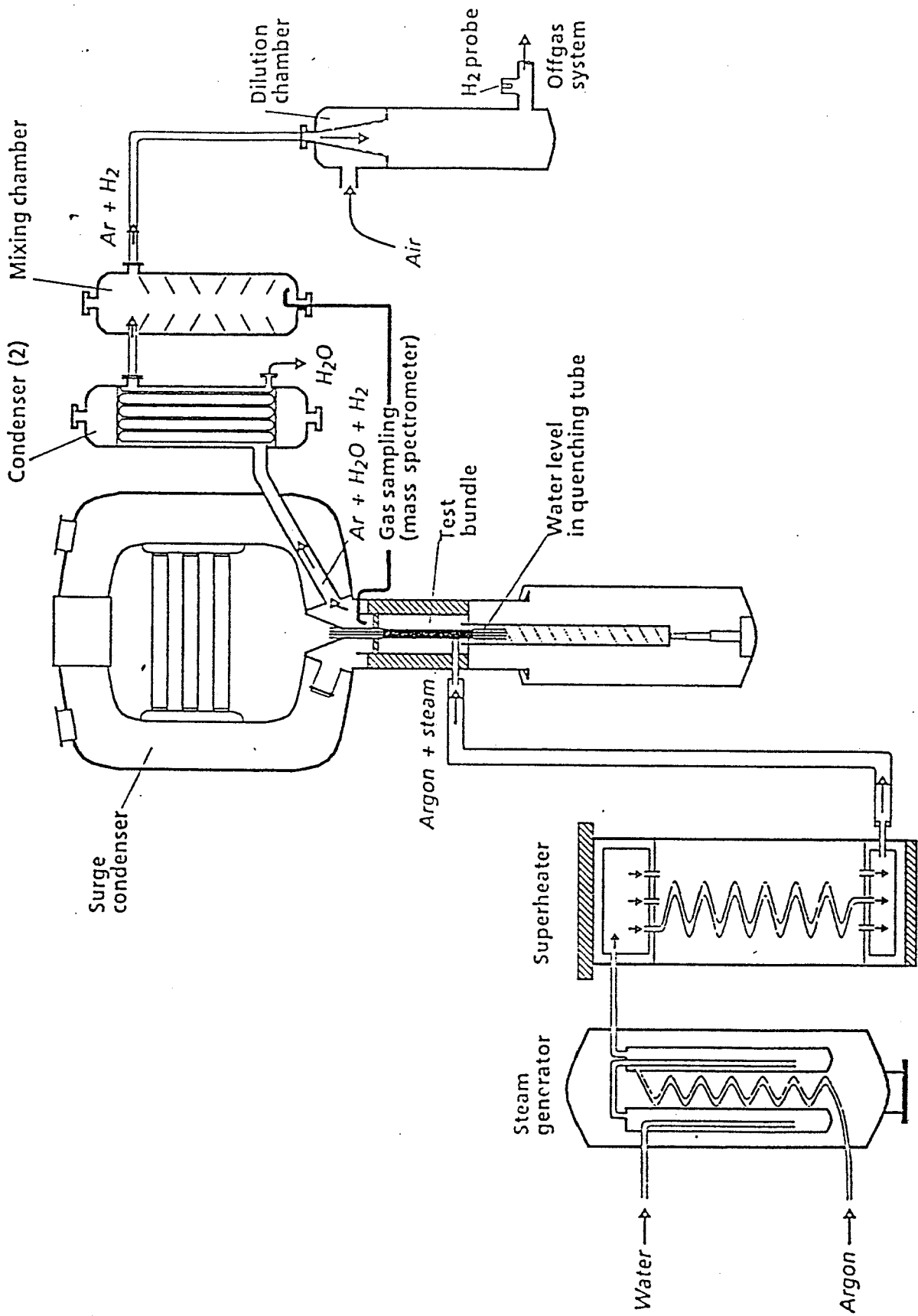


**Fig. 3.1: SFD Test Facility (Simplified flow diagram)**

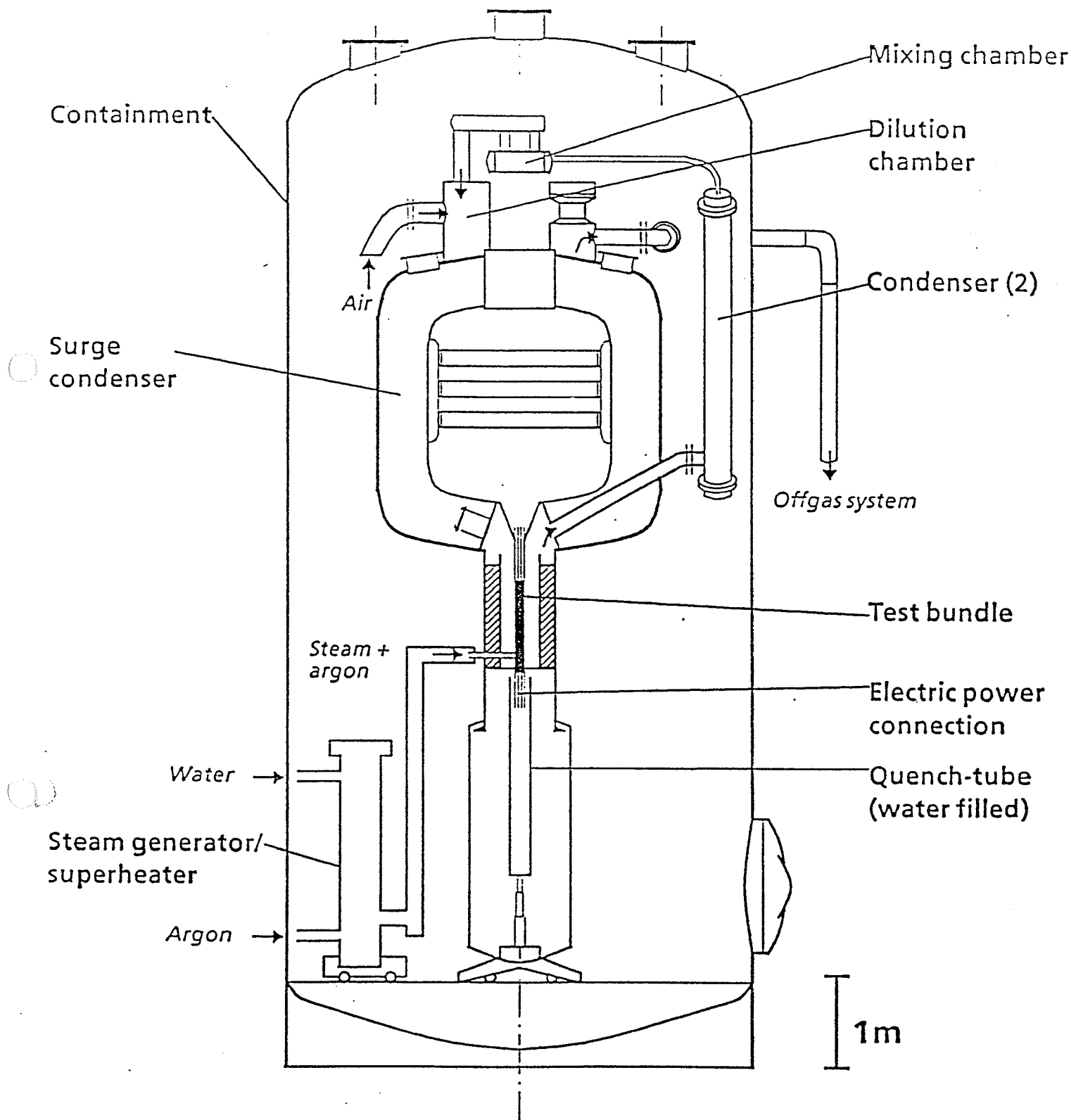


**Fig. 3.2: SFD Test Facility (Main components)**

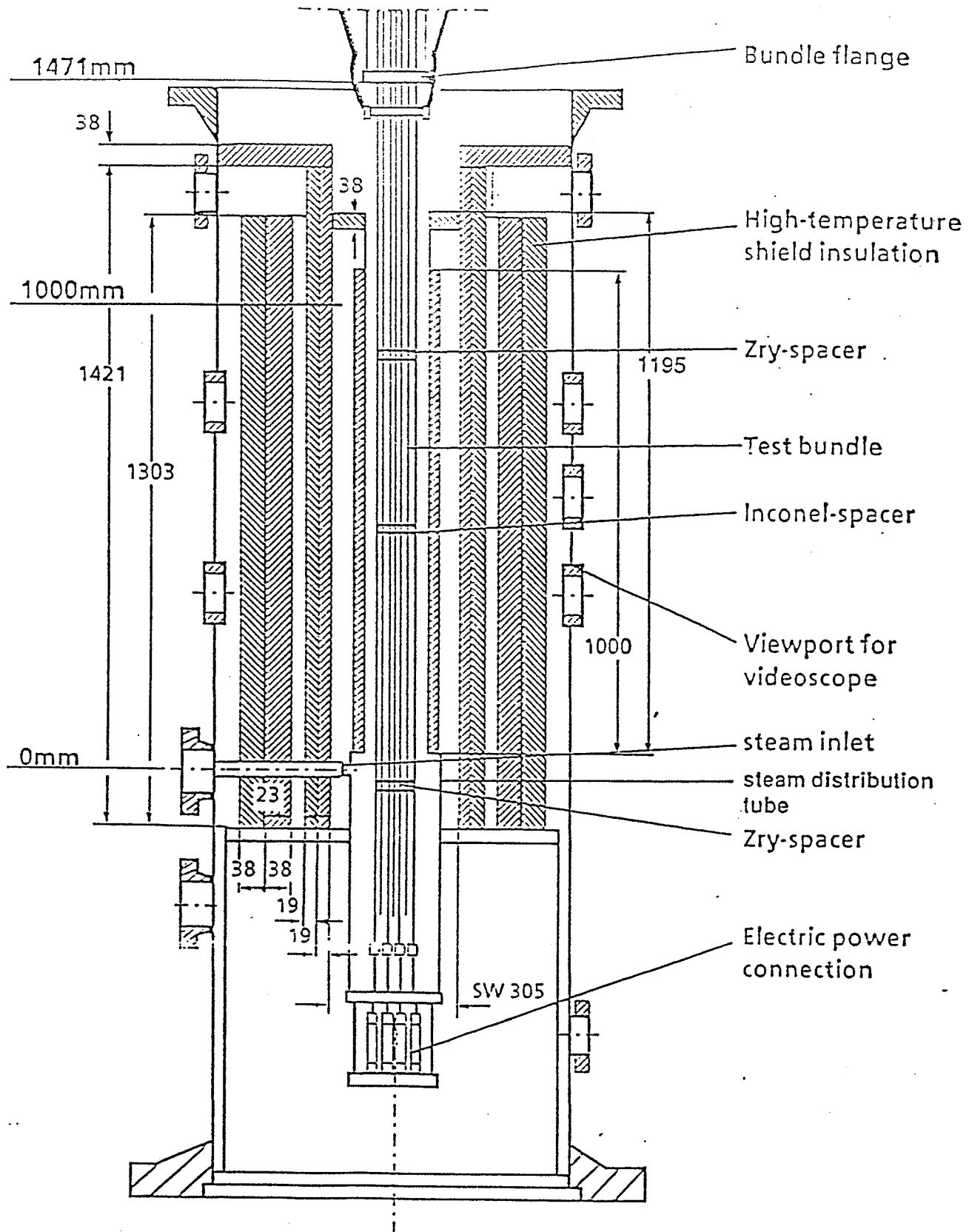


**Fig. 3.3: CORA bundle arrangement.**

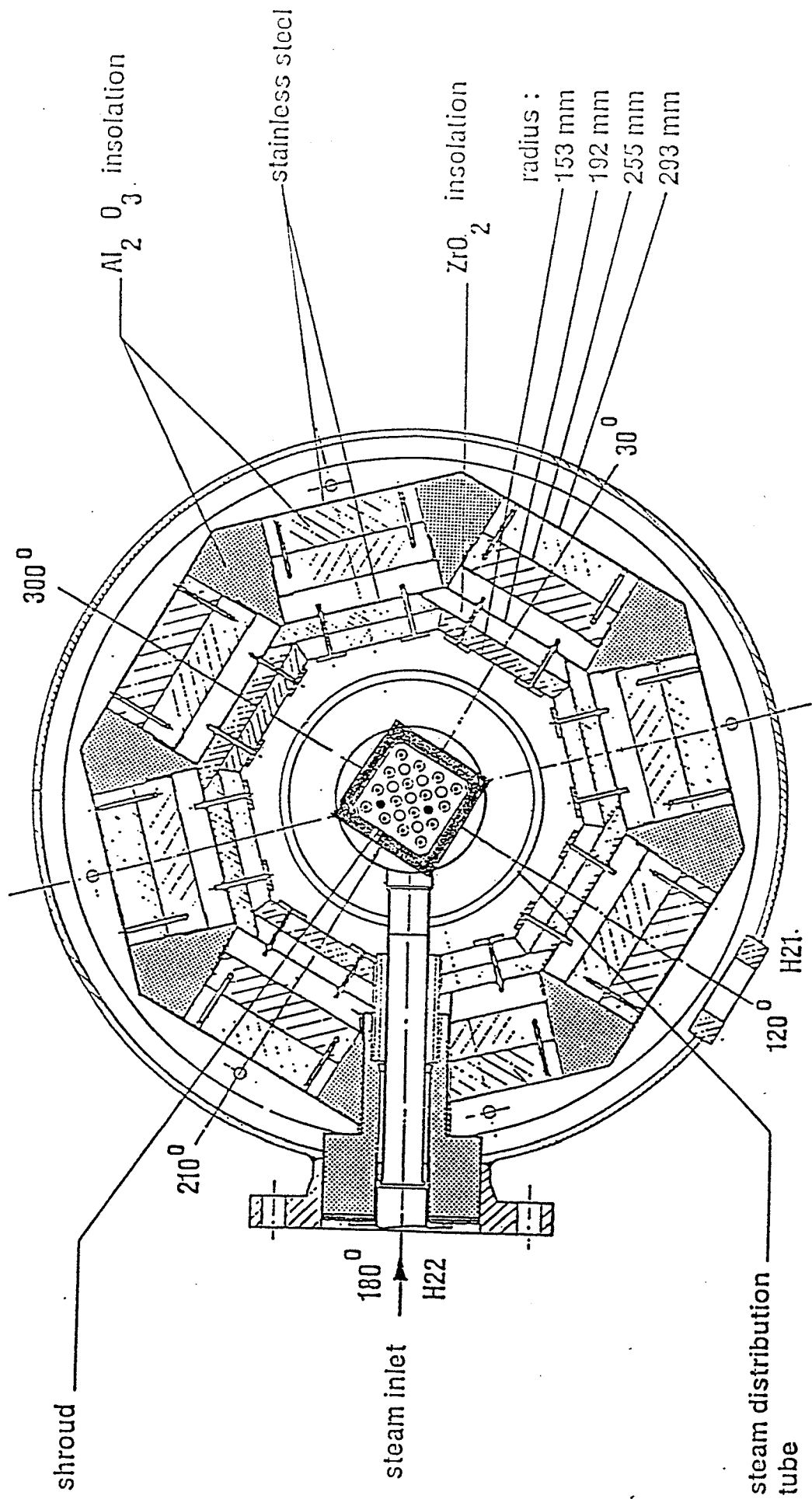


**Fig. 3.4: Horizontal cross section of the high temperature shield**

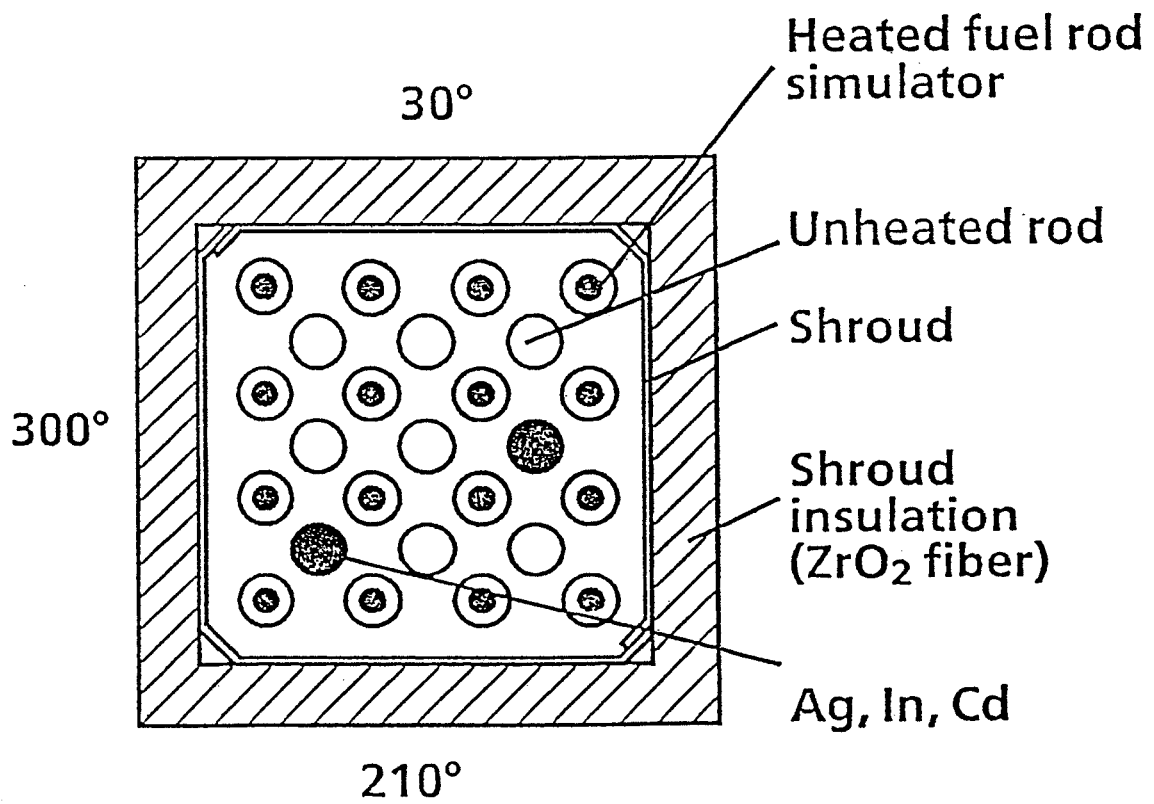
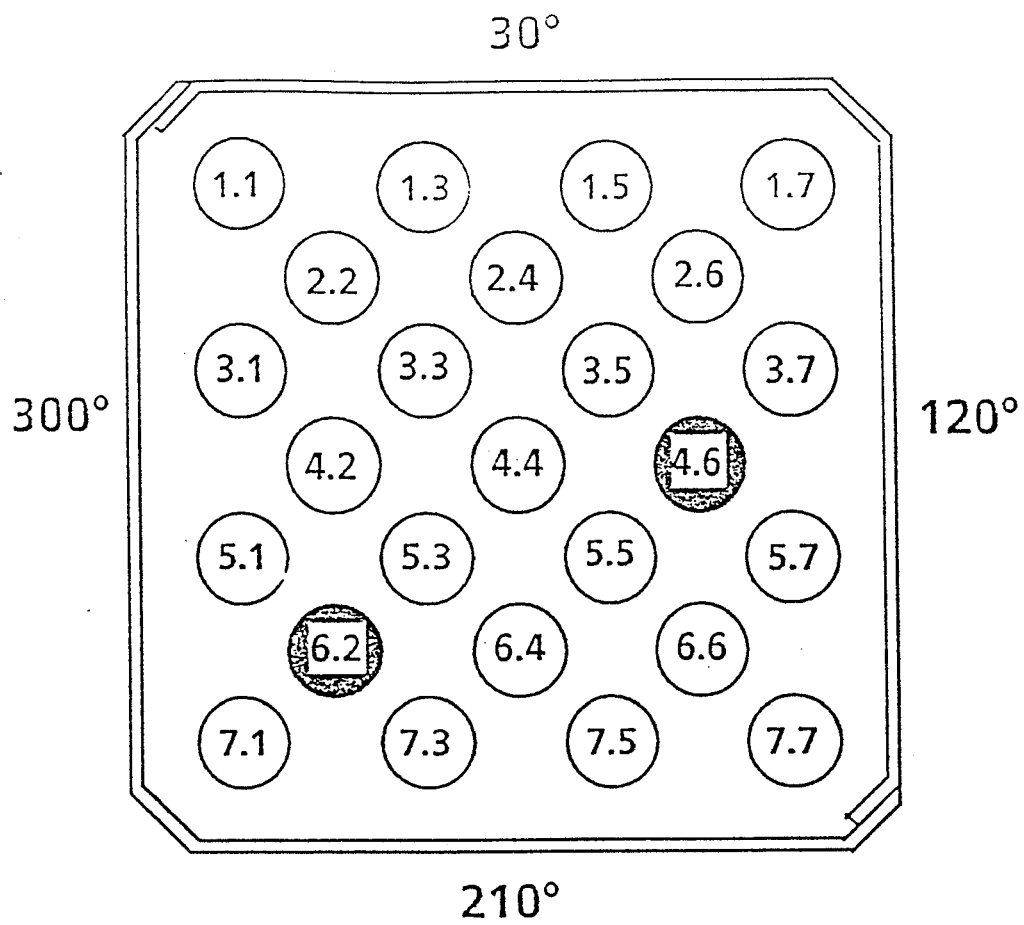


Fig. 3.5: Rod designation of the test bundle CORA-13

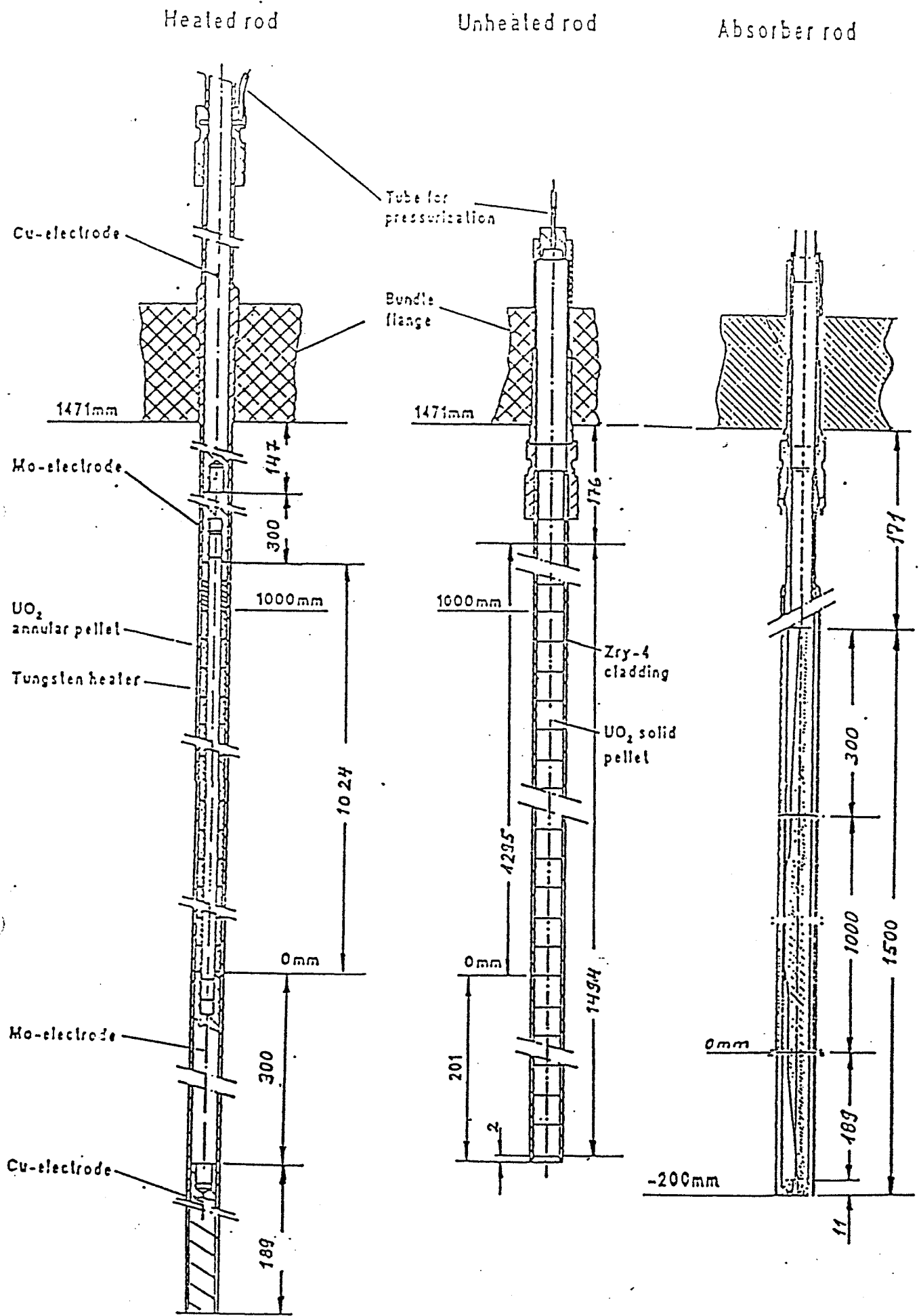
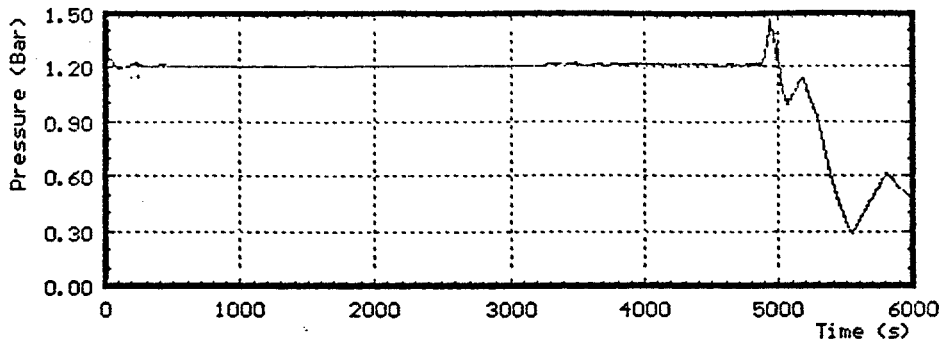
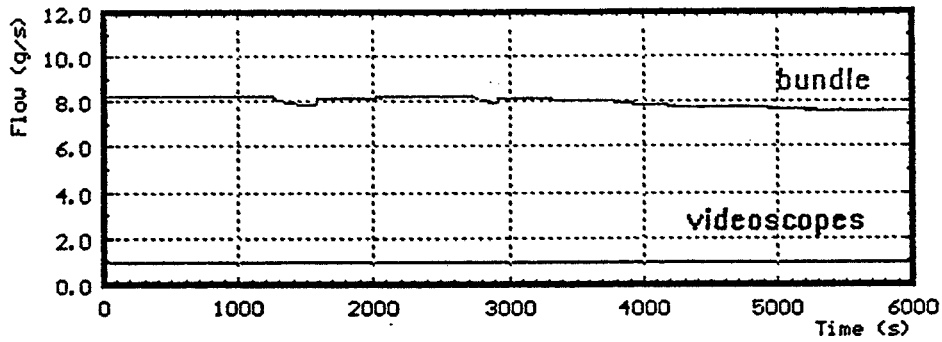


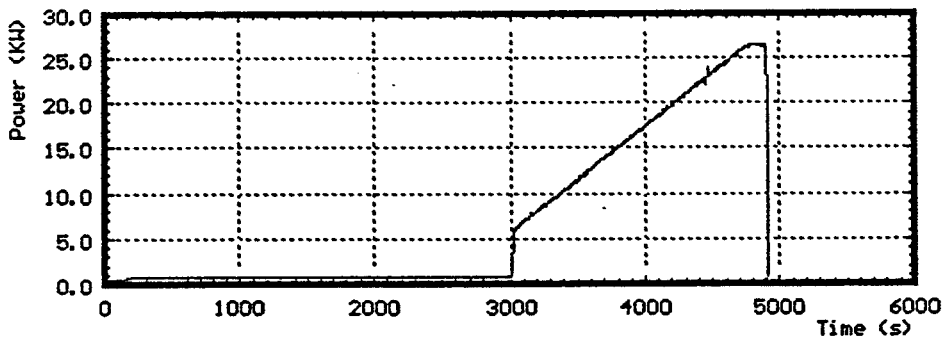
Fig. 3.6: Rod types used in the CORA experiments



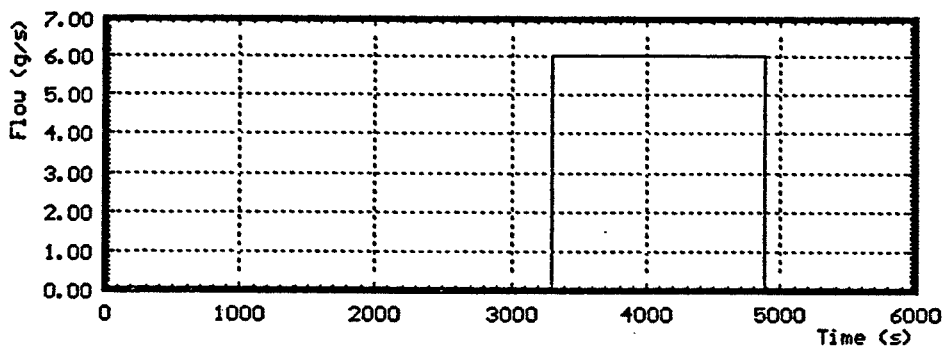
system  
overpressure



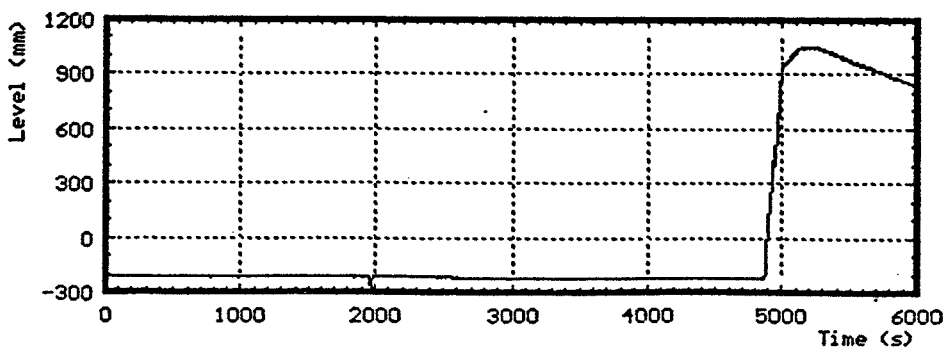
Argonflow



power



steam  
production



quench  
level

**Fig. 3.7: System pressure, argonflow, steam input, power and quench level during test CORA-13**

# CORA 13

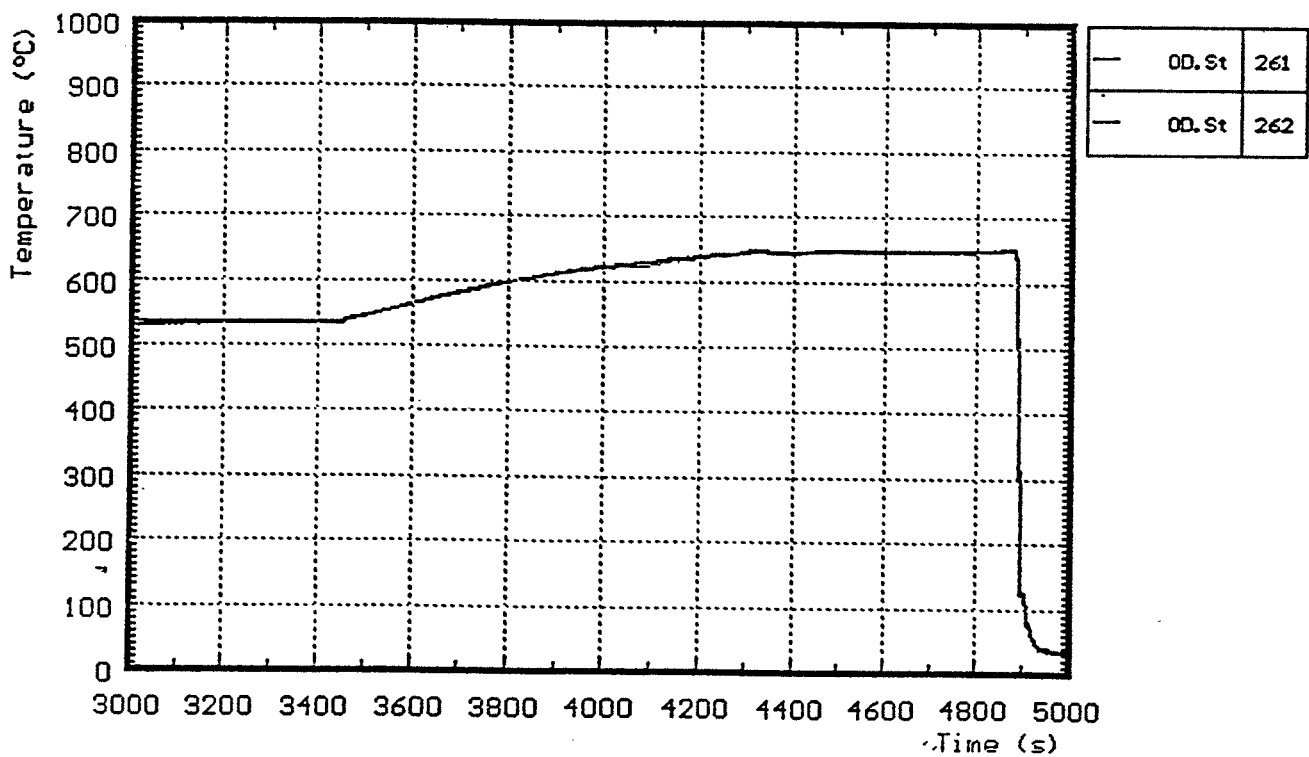
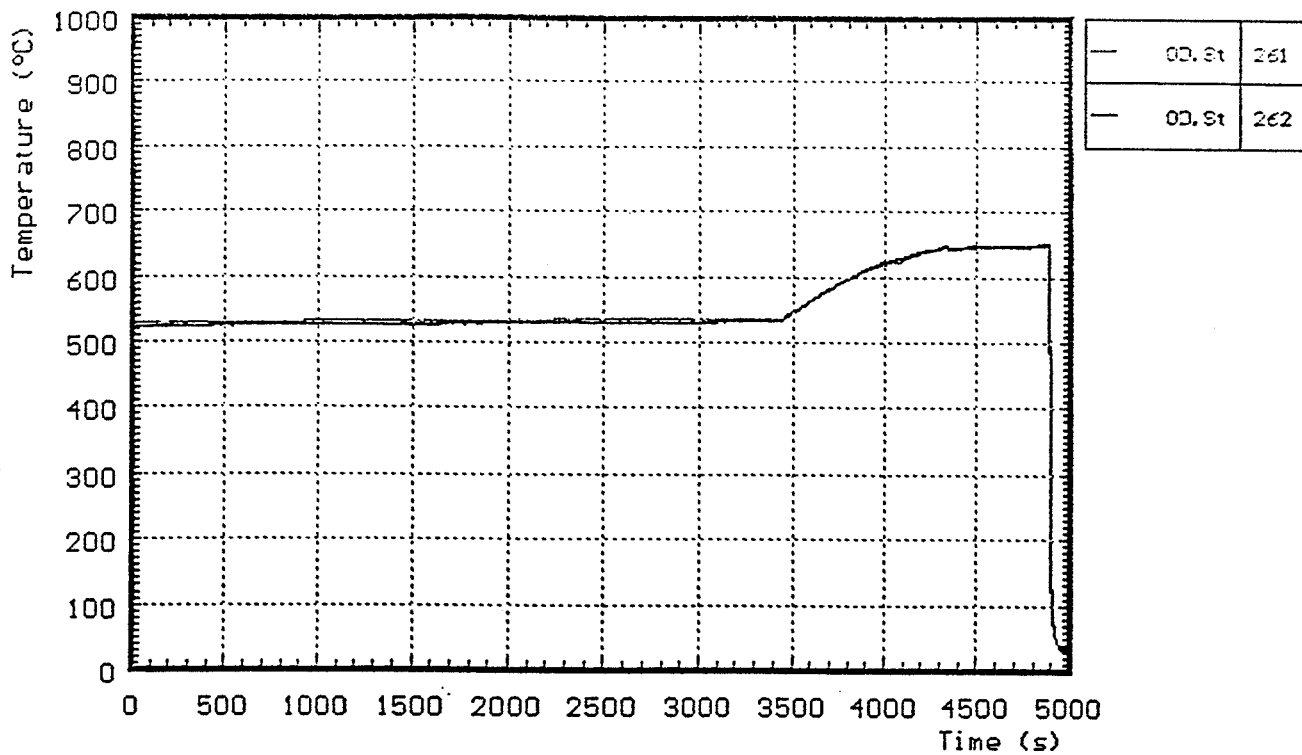


**Fig. 3.8: Temperatures at steam inlet (CORA-13)**

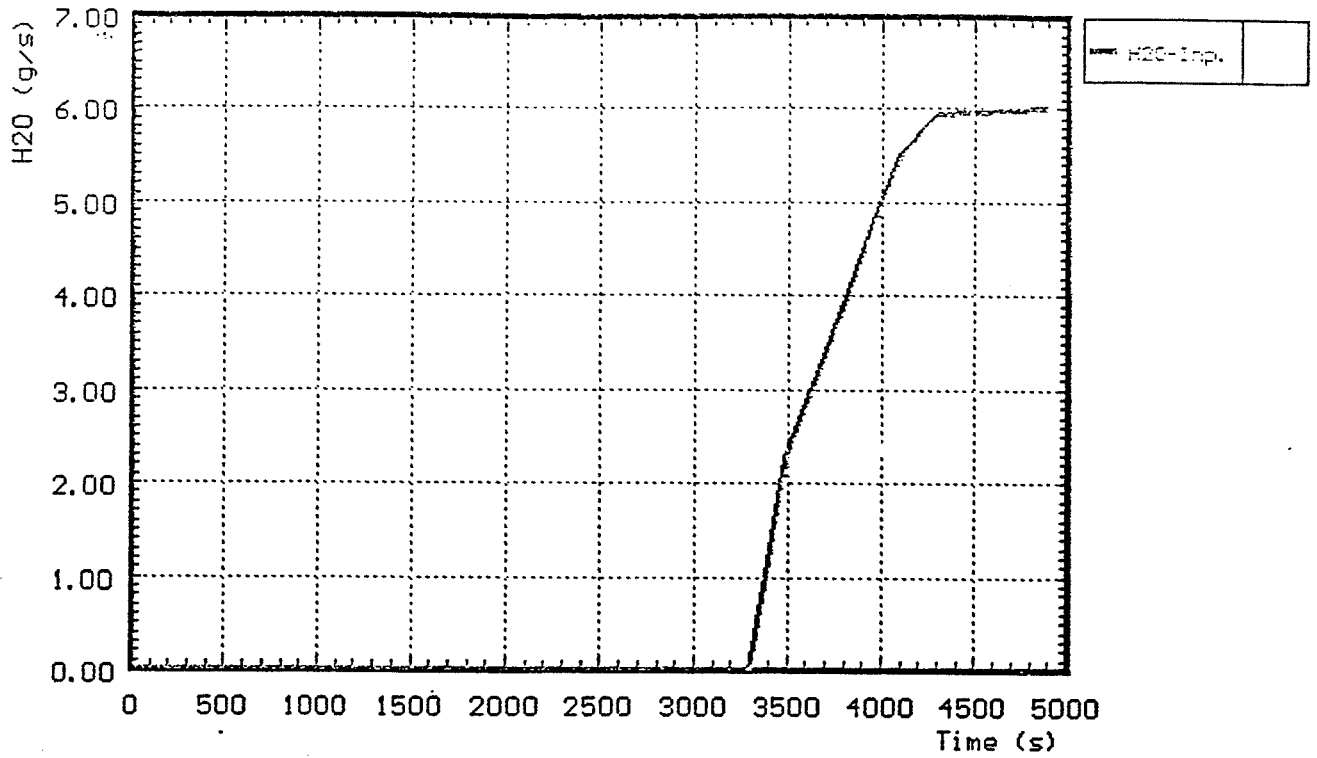


**Fig. 3.9: Steam input into bundle CORA-13**

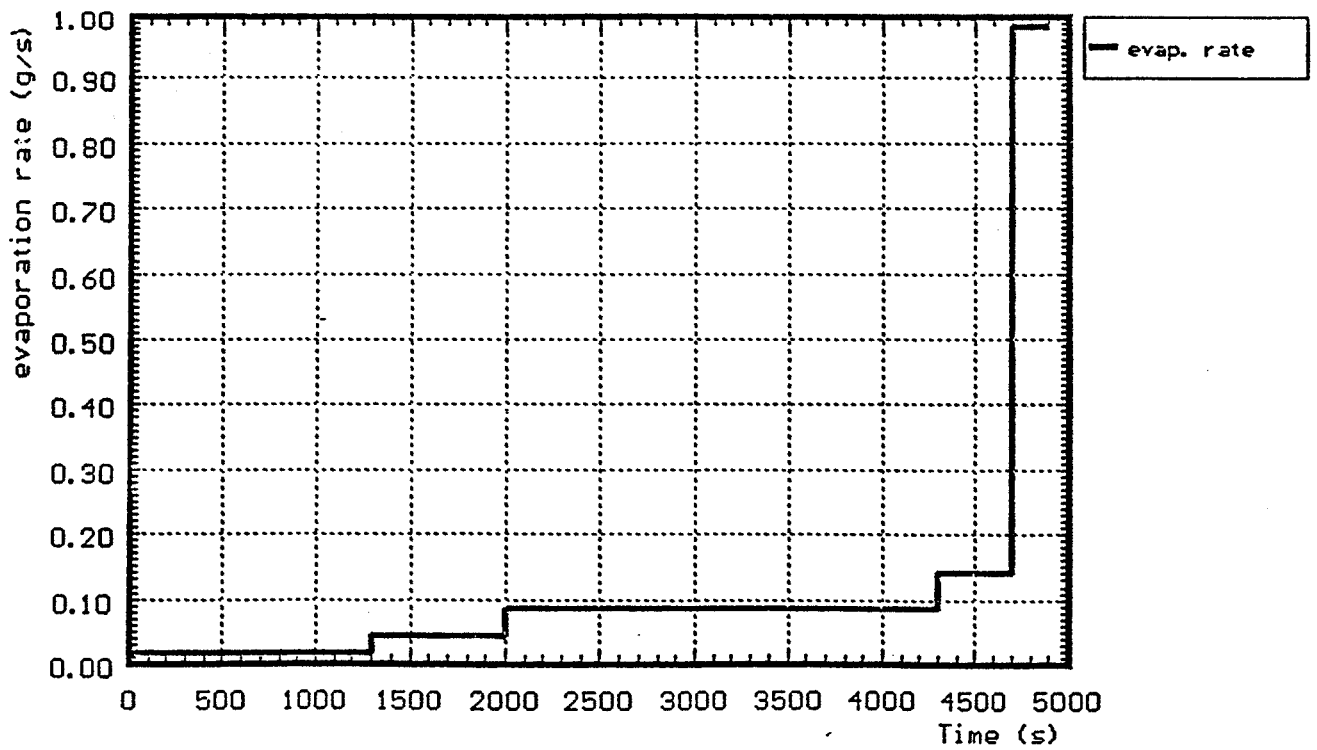


**Fig. 3.10: Evaporation rate during the transient of CORA-13**

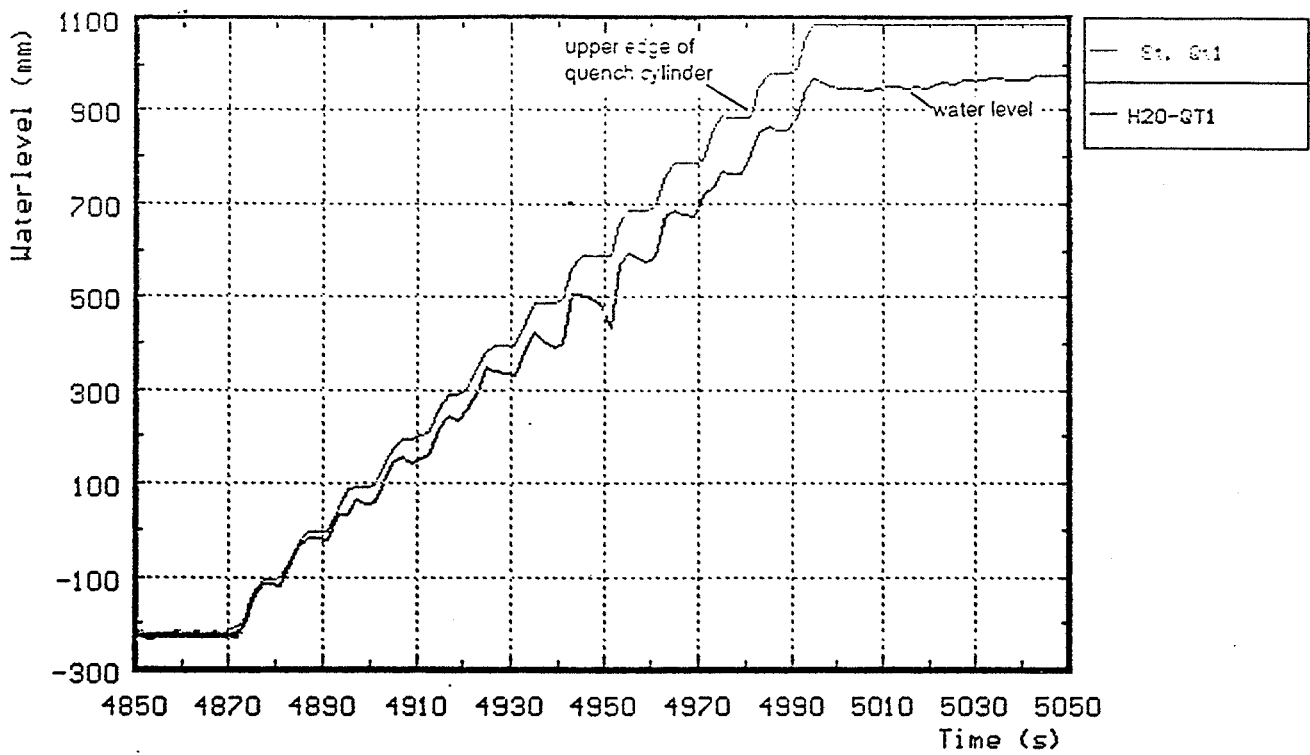


**Fig. 3.11: Position of upper edge and water level in the quench cylinder (CORA-13)**

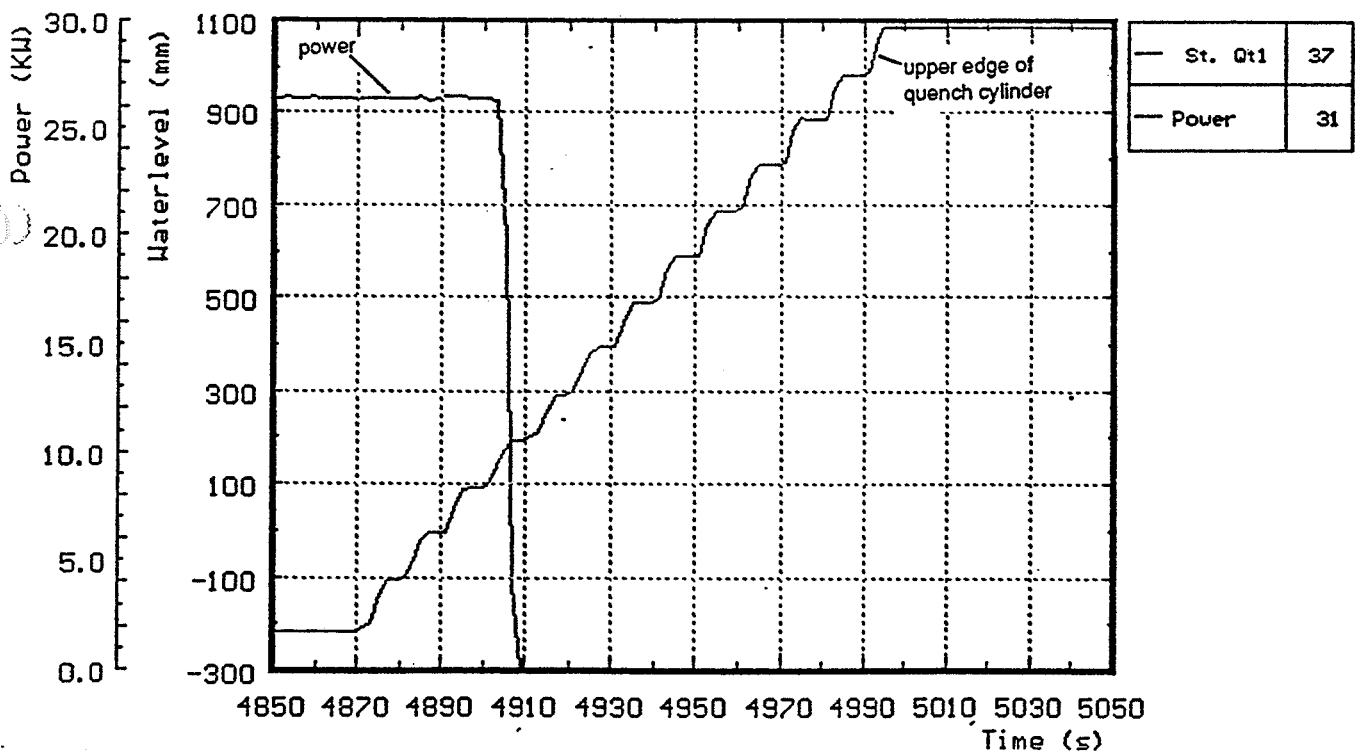


**Fig. 3.12: Movement of the quench cylinder compared to power input (CORA-13)**

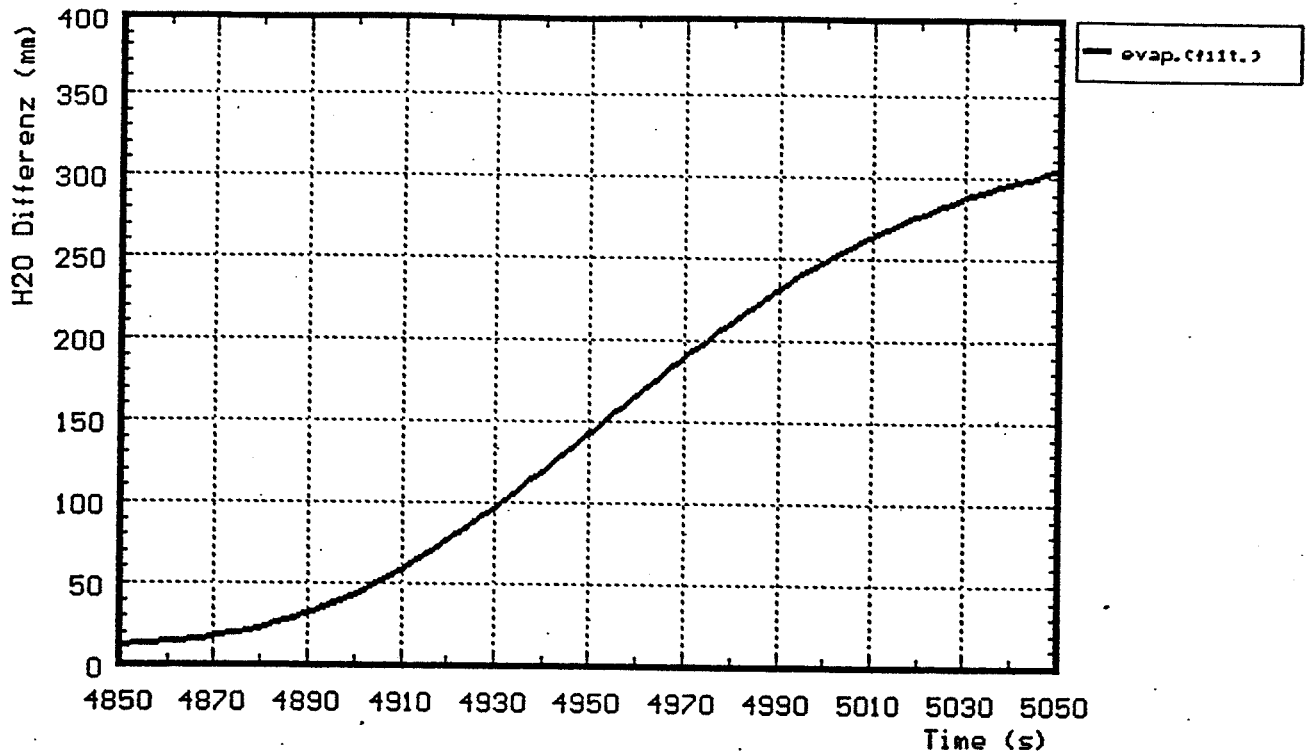


**Fig. 3.13:** Epavorated water from quench cylinder during the quench process (corrected for additional water input) (CORA-13)

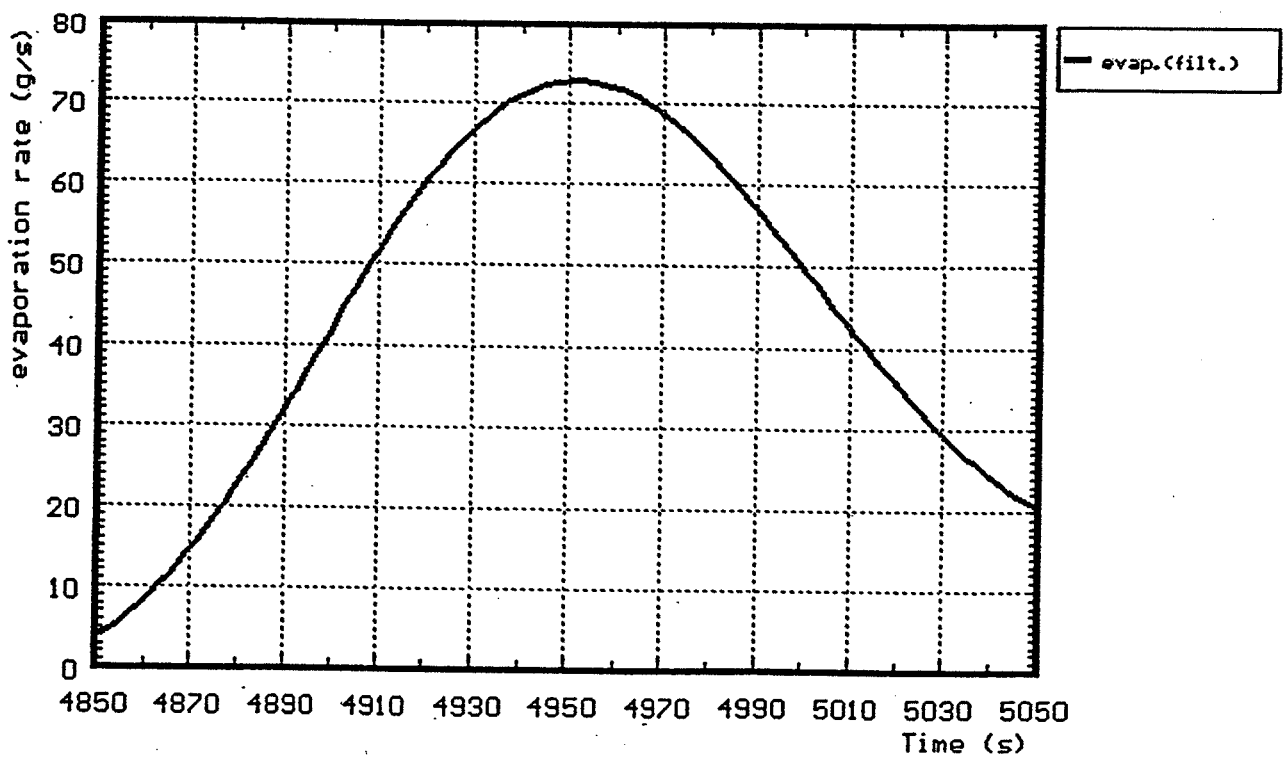


**Fig. 3.14:** Epavoration rate (g/s) during the quench process

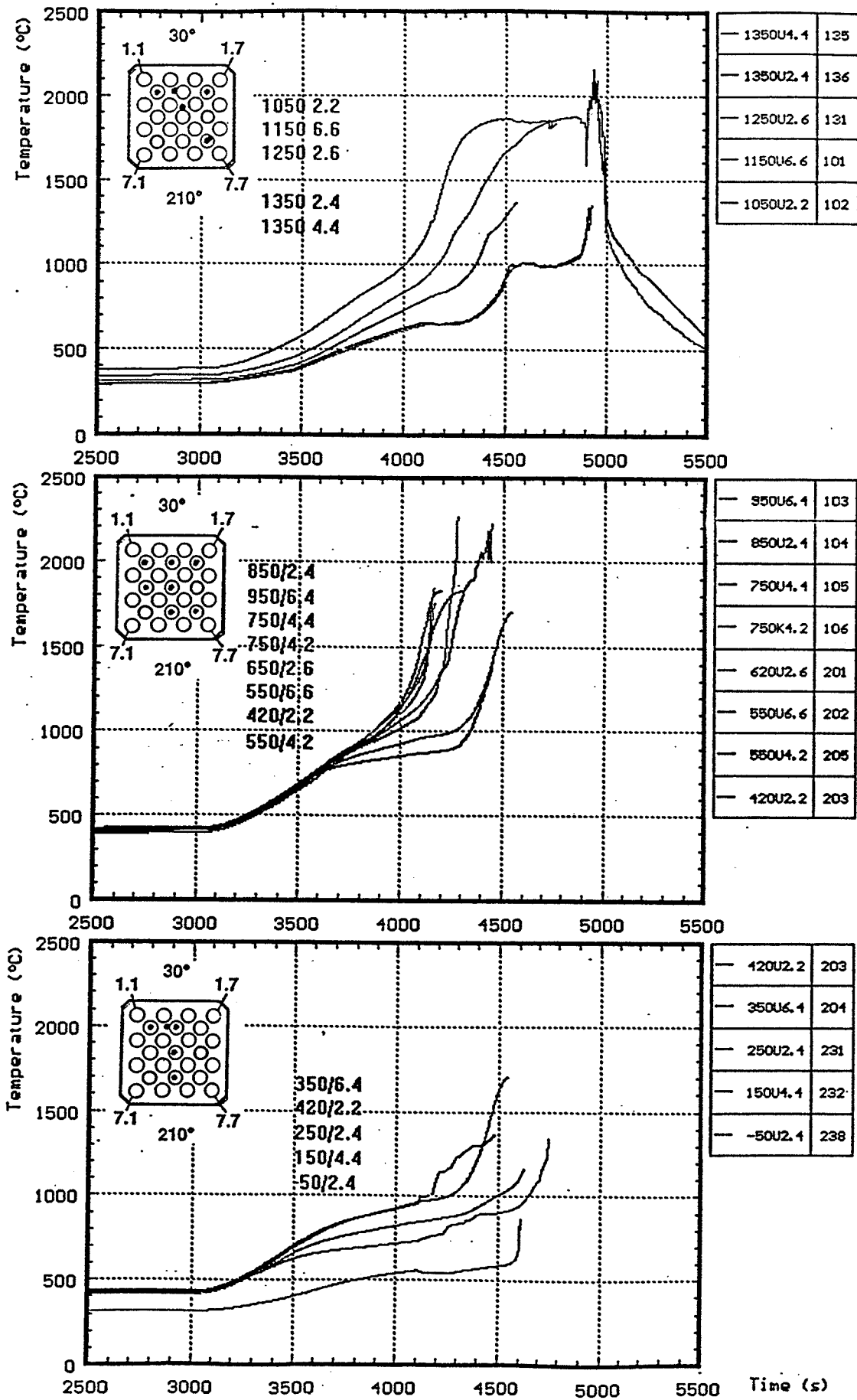
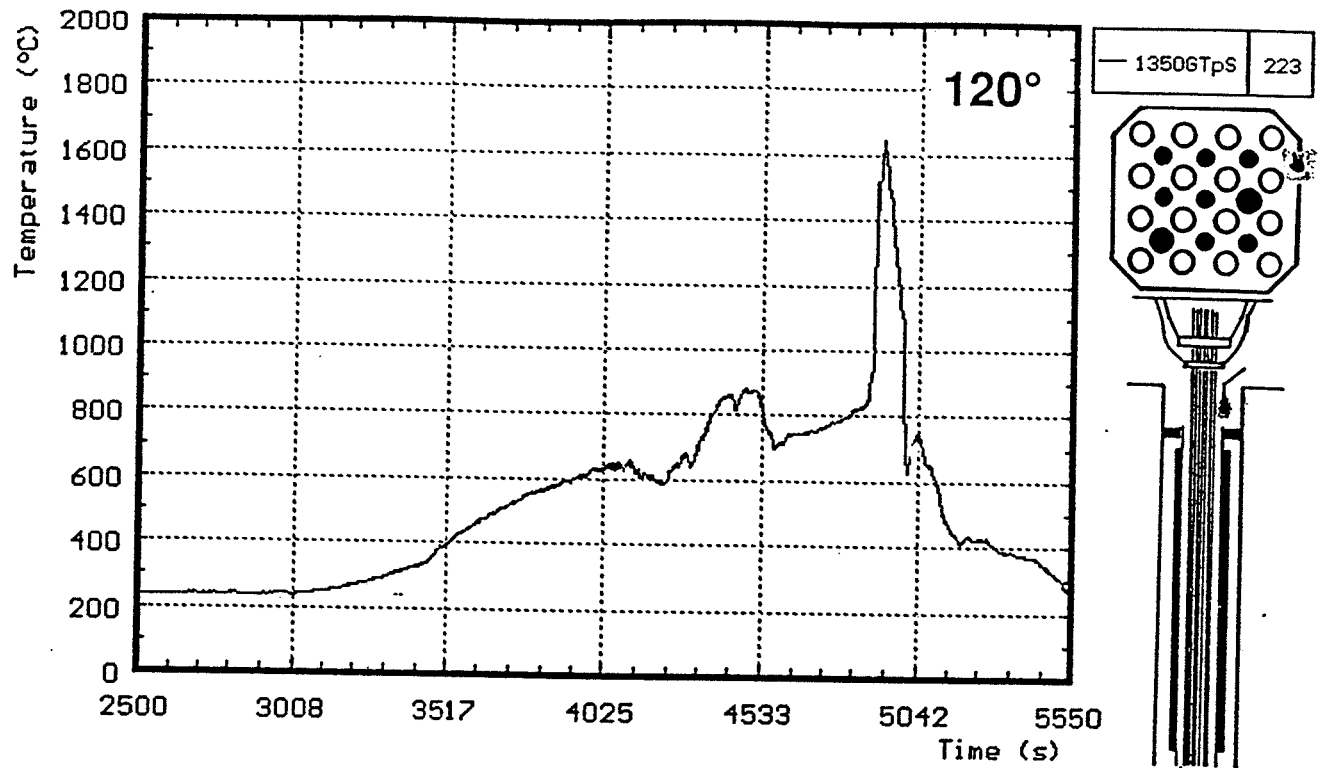
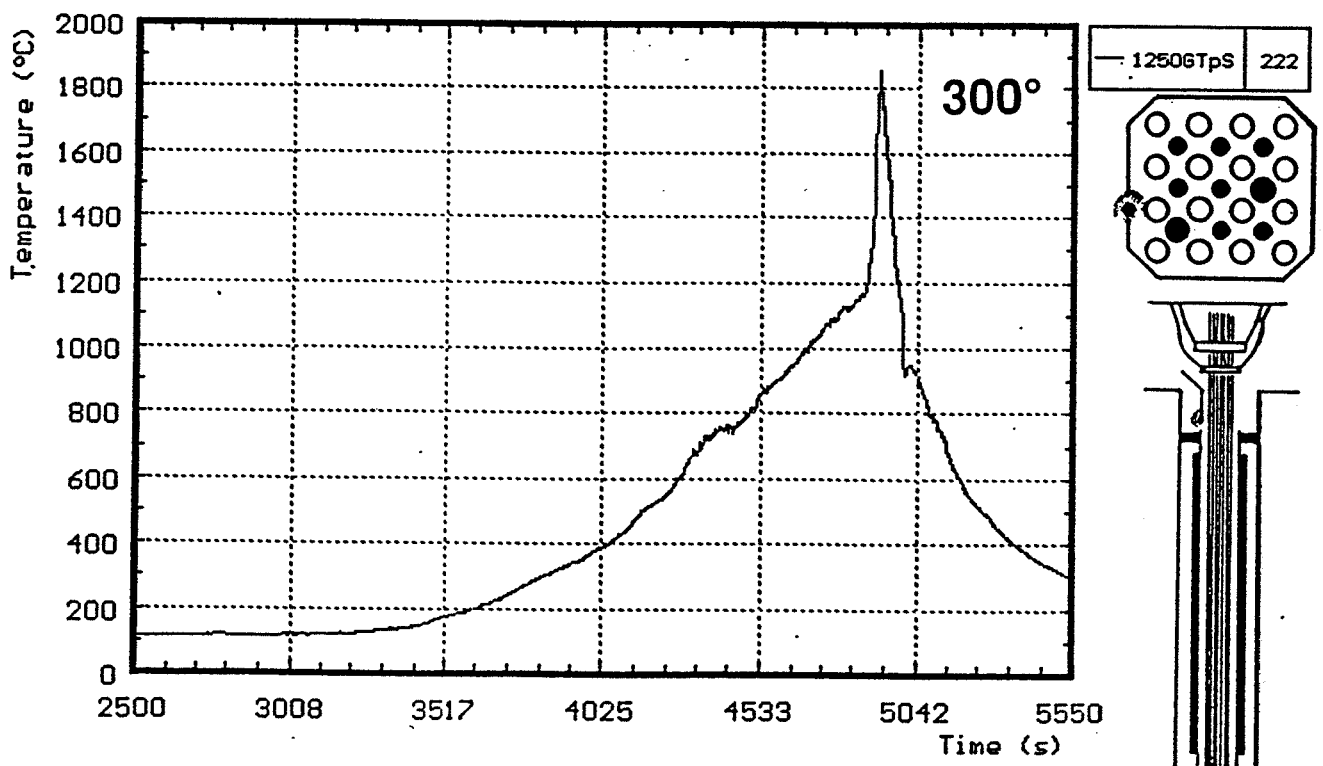


Fig. 3.15: Temperatures of the unheated rods (CORA-13)



**Fig. 3.16:** Gas temperature above the shroud at 1350 mm elevation (CORA-13)



**Fig. 3.17:** Gas temperature above the shroud at 1250 mm elevation (CORA-13)

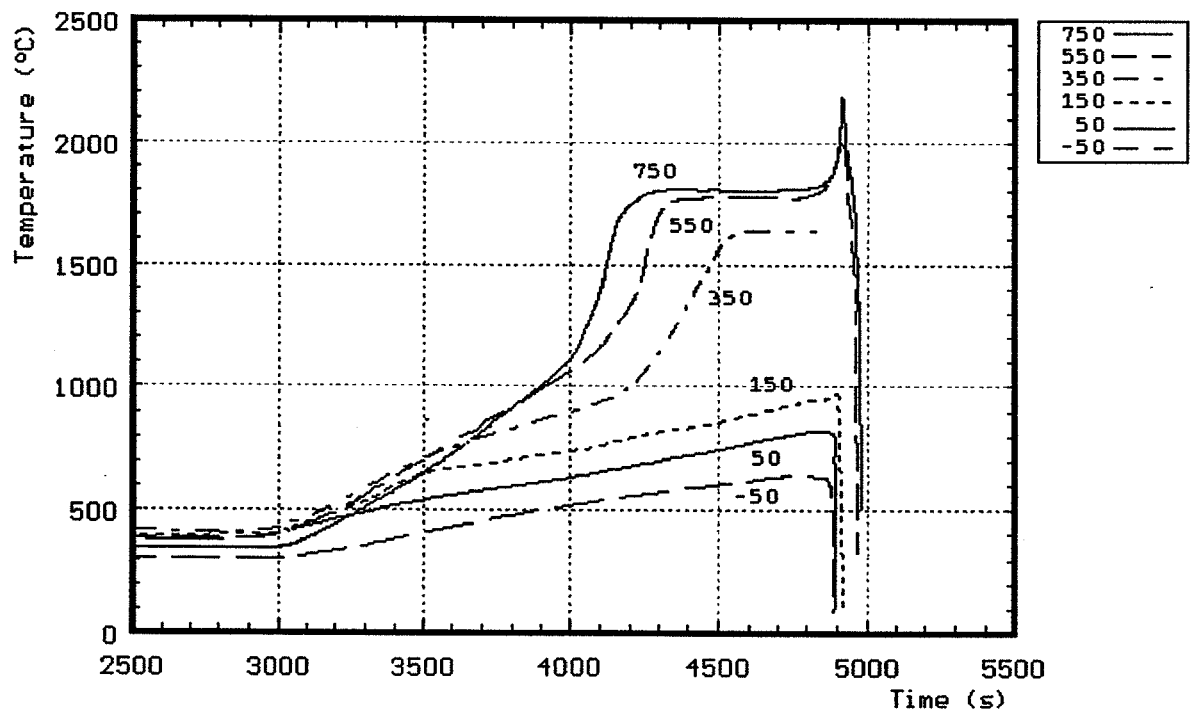
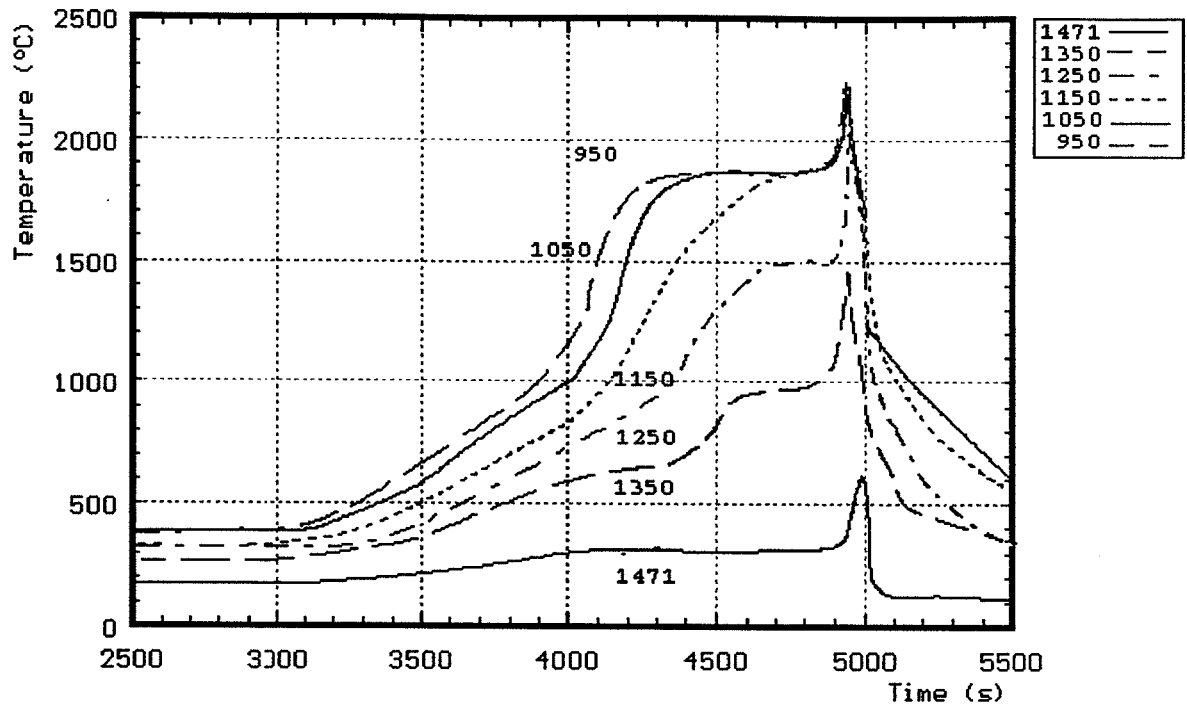


**Fig. 3.18: Best estimated temperatures in the bundle (CORA-13)**

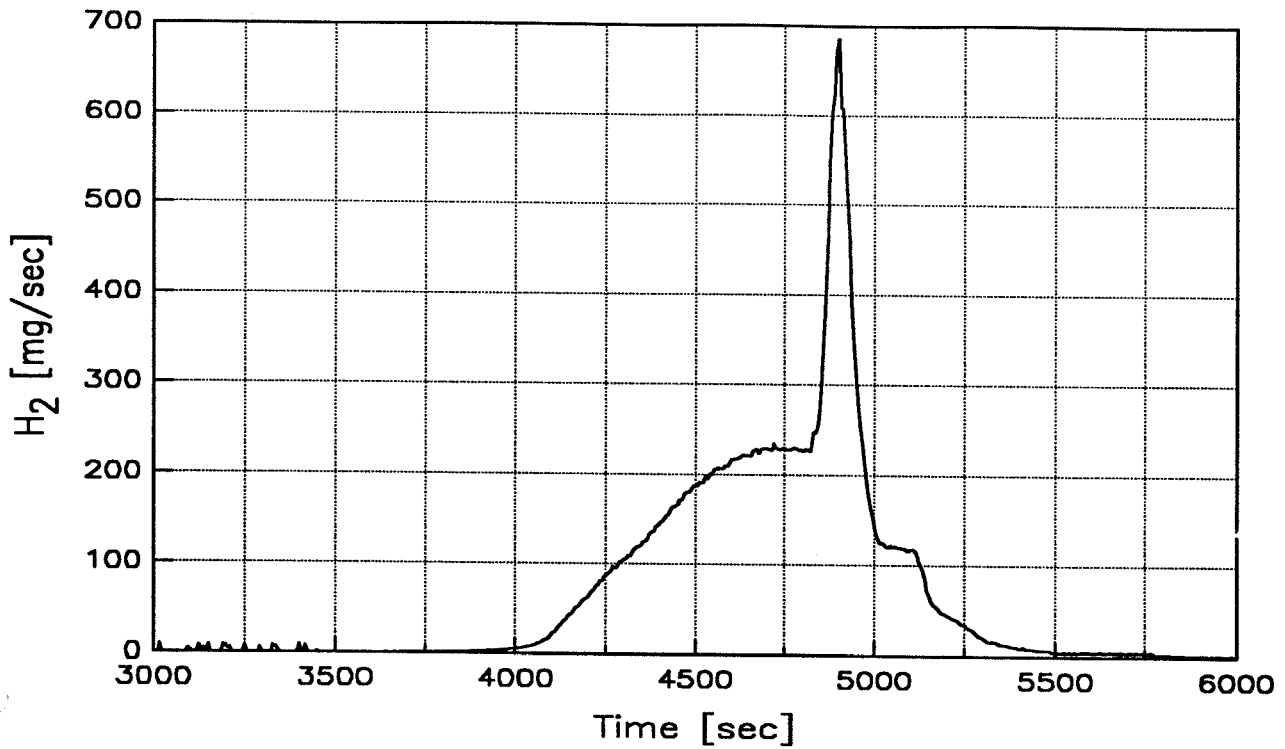


Fig. 3.19: Hydrogen generation during Test CORA-13 as measured

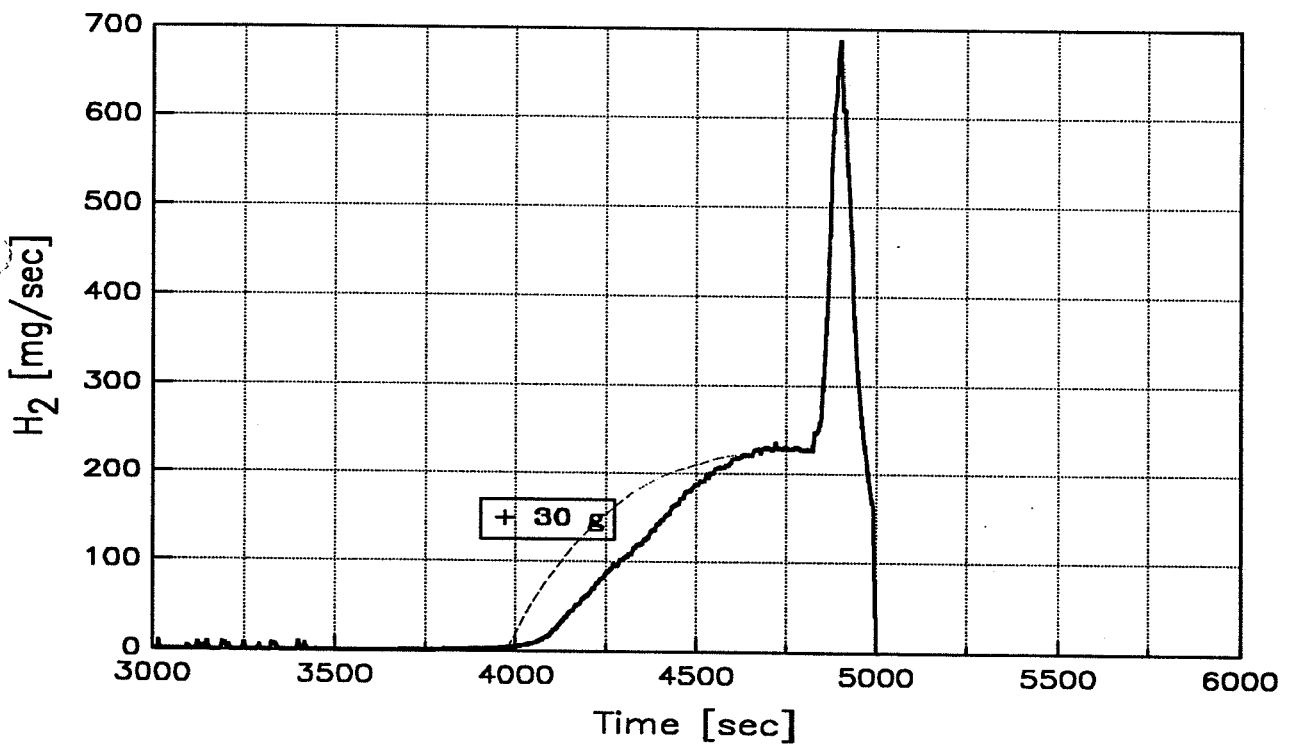


Fig. 3.19a: Hydrogen generation during Test CORA-13 Best estimate after adding of distributed hydrogen

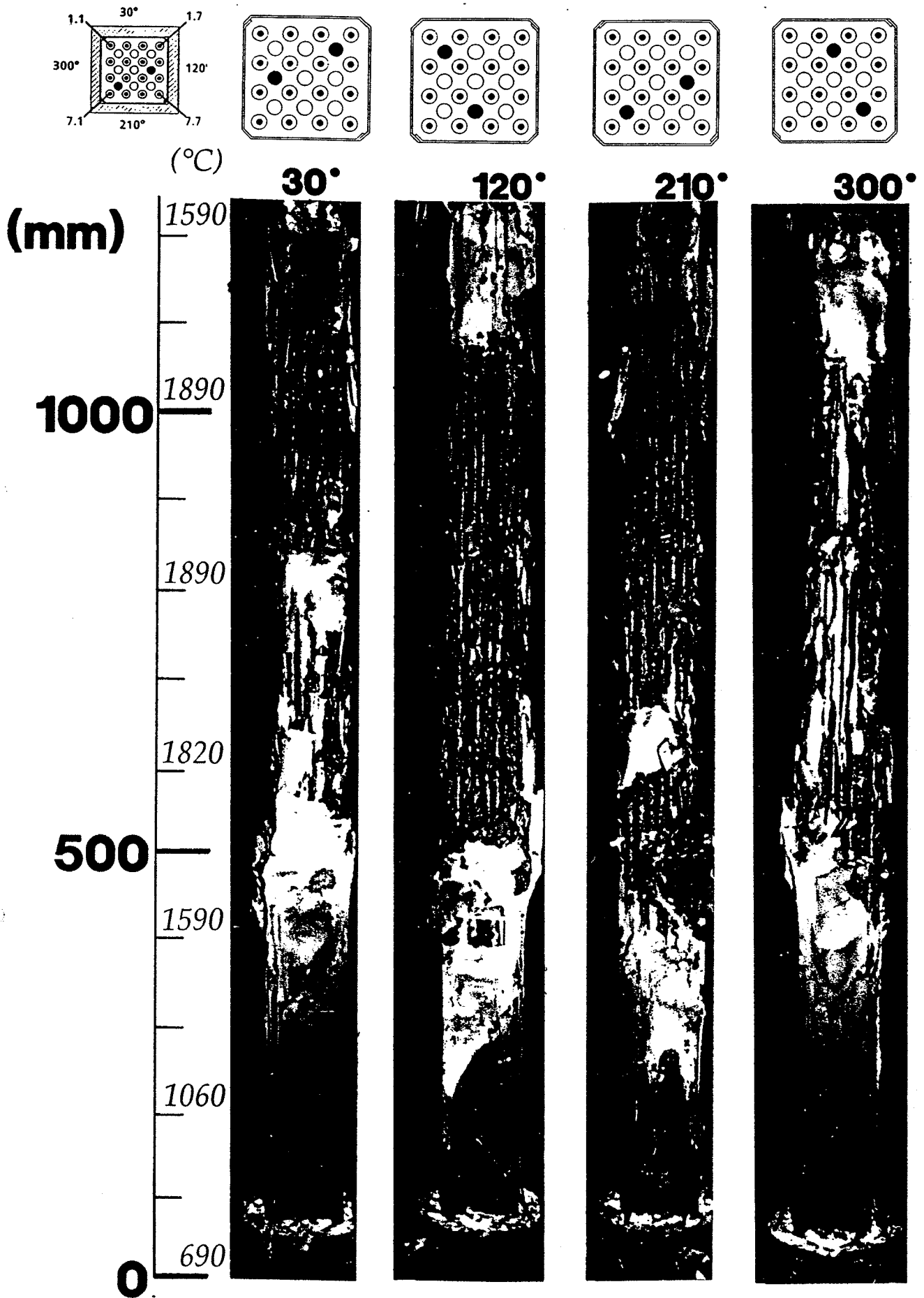


Fig. 3.20: Posttest view of bundle CORA-13 after partial removal of shroud

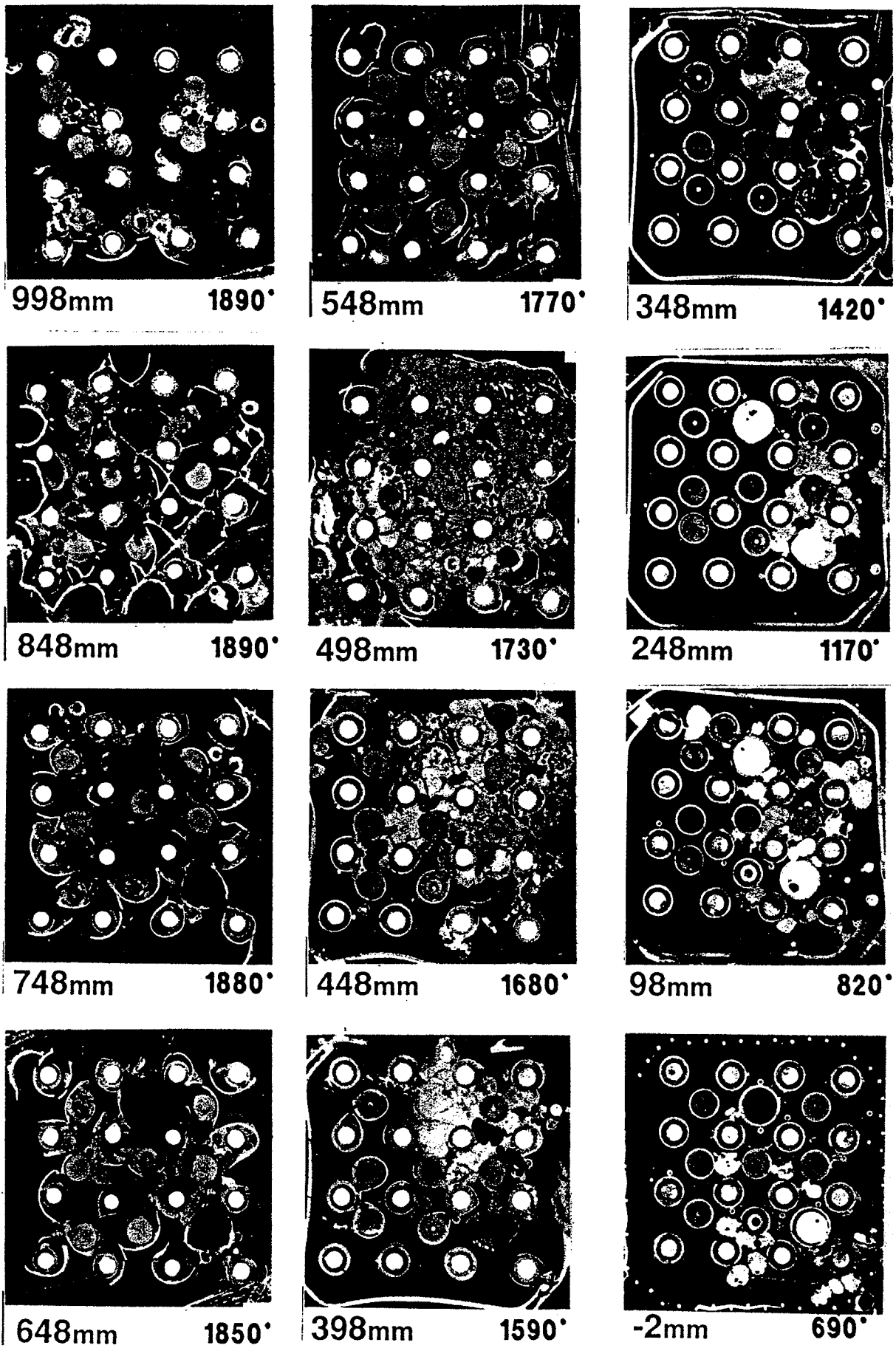
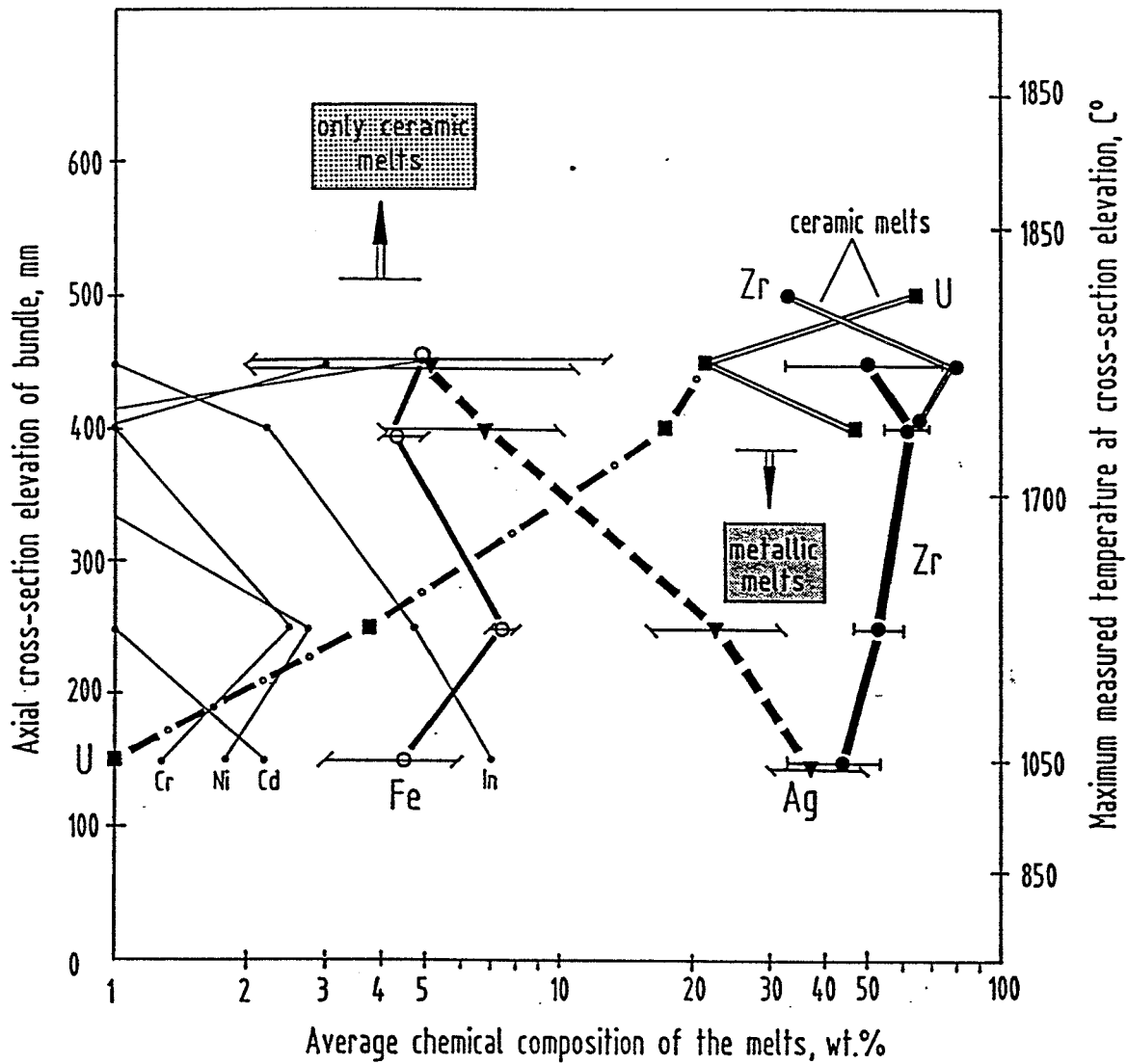


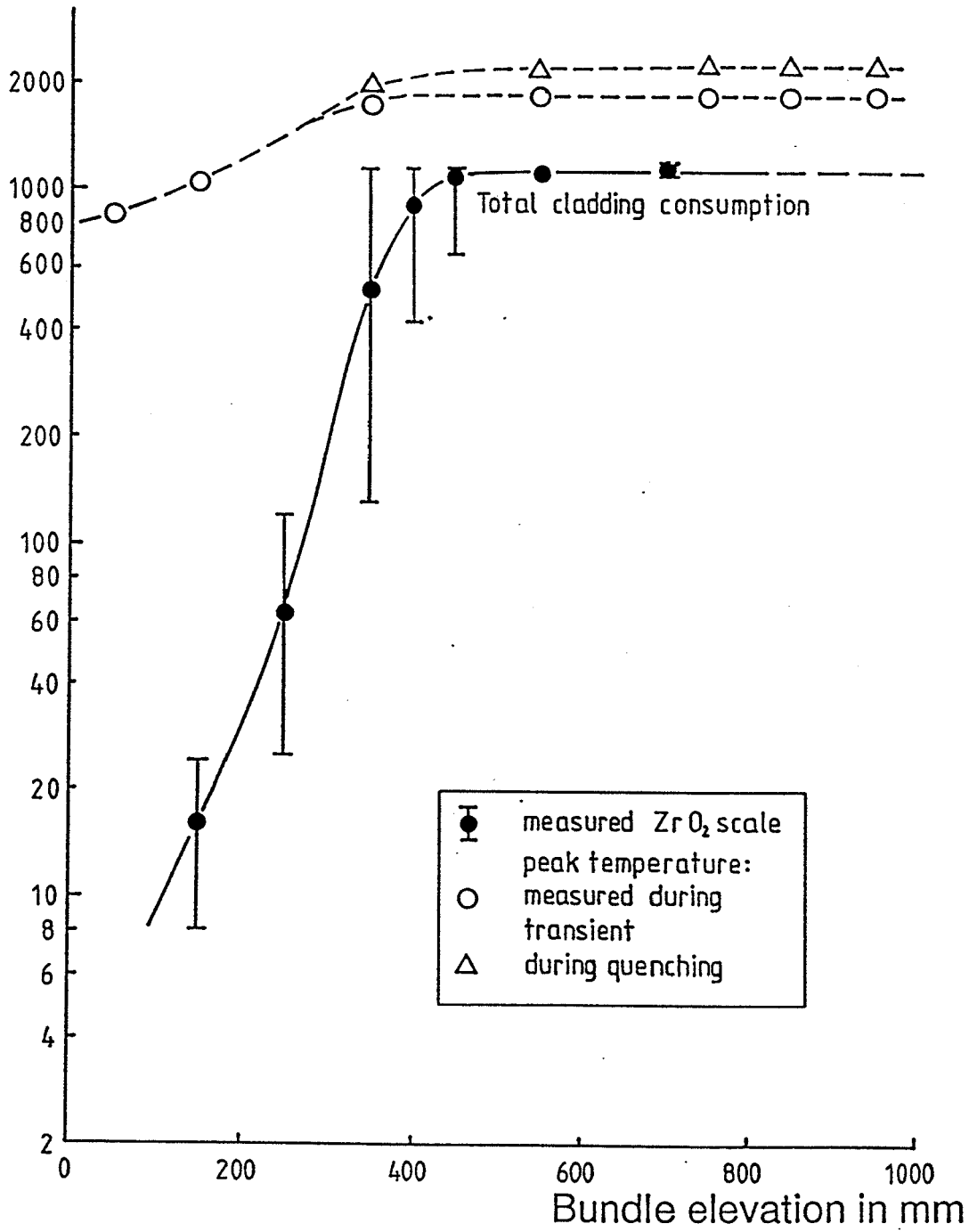
Fig. 3.21: Horizontal cross sections of bundle CORA-13  
(top view)



CORA bundle 13; PWR quench test

Fig. 3.22: Chemical composition of melts as function of cross-section elevation

ZrO<sub>2</sub> scale thickness in μm  
 Max. temperature in °C



KfK

Fig. 3.23: Axial distribution of ZrO<sub>2</sub> scale thickness of the CORA-13 fuel rods in comparison to maximum temperatures

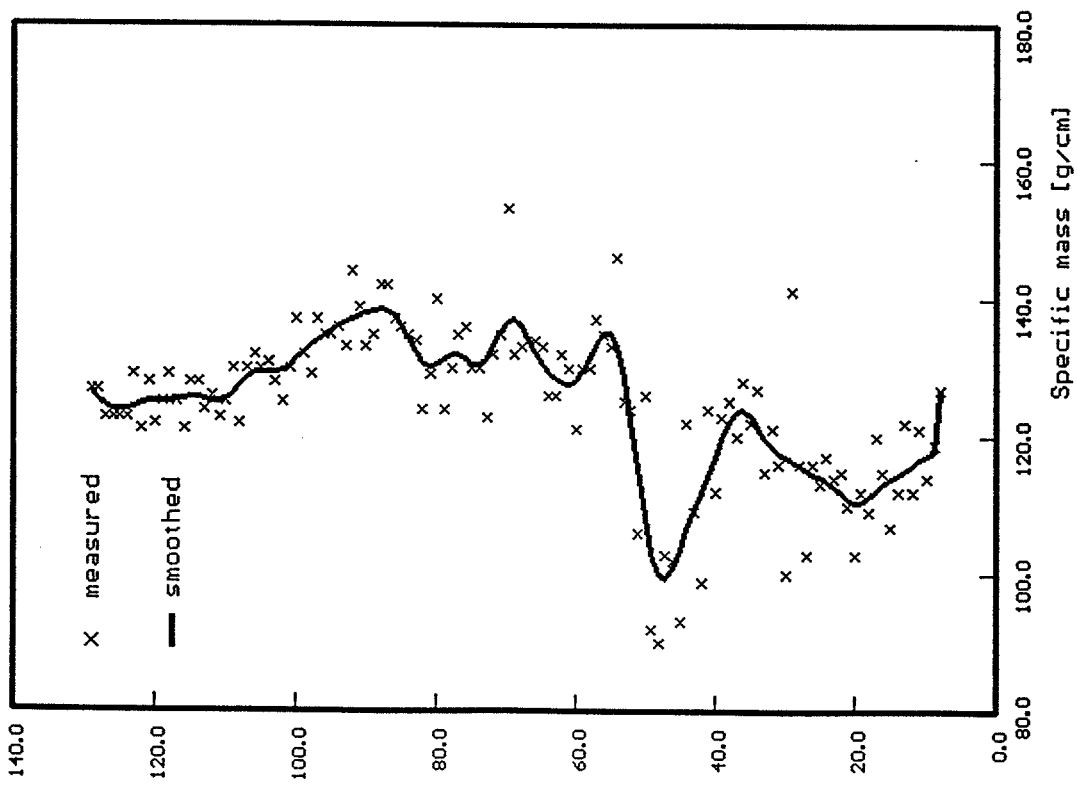


Fig. 3.24 : CORA 13: Axial distribution of epoxy bundle fill-up

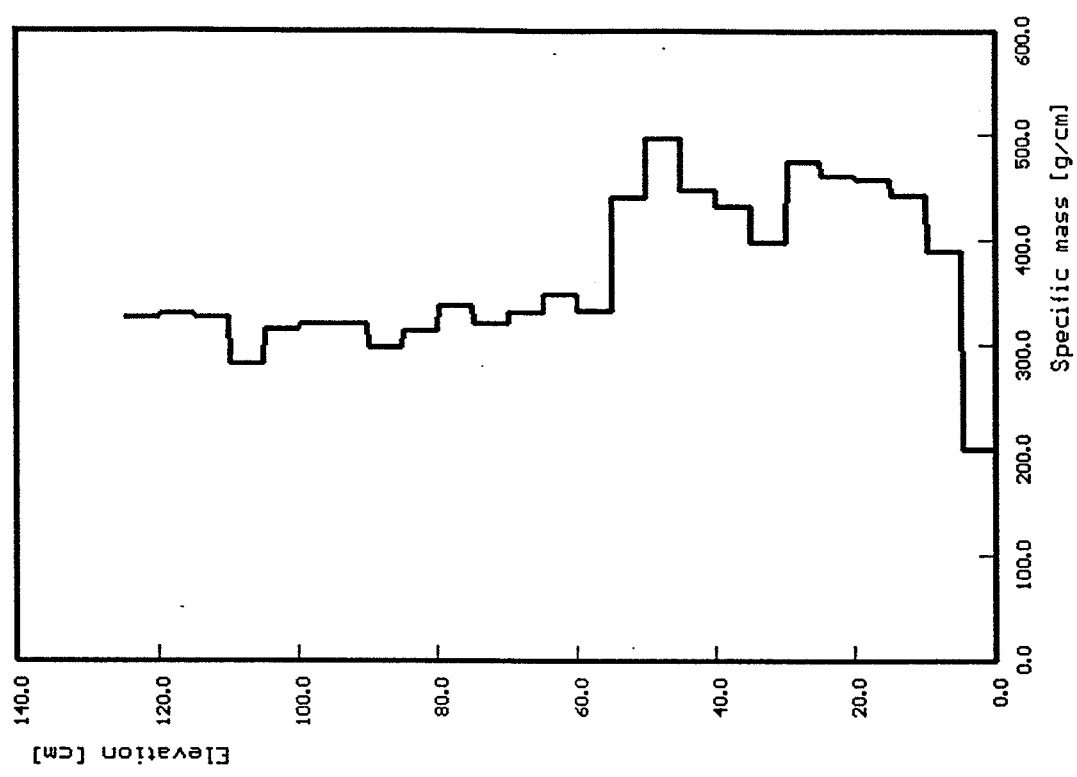


Fig. 3.25 : CORA 13: Axial distribution of bundle segments filled with epoxy

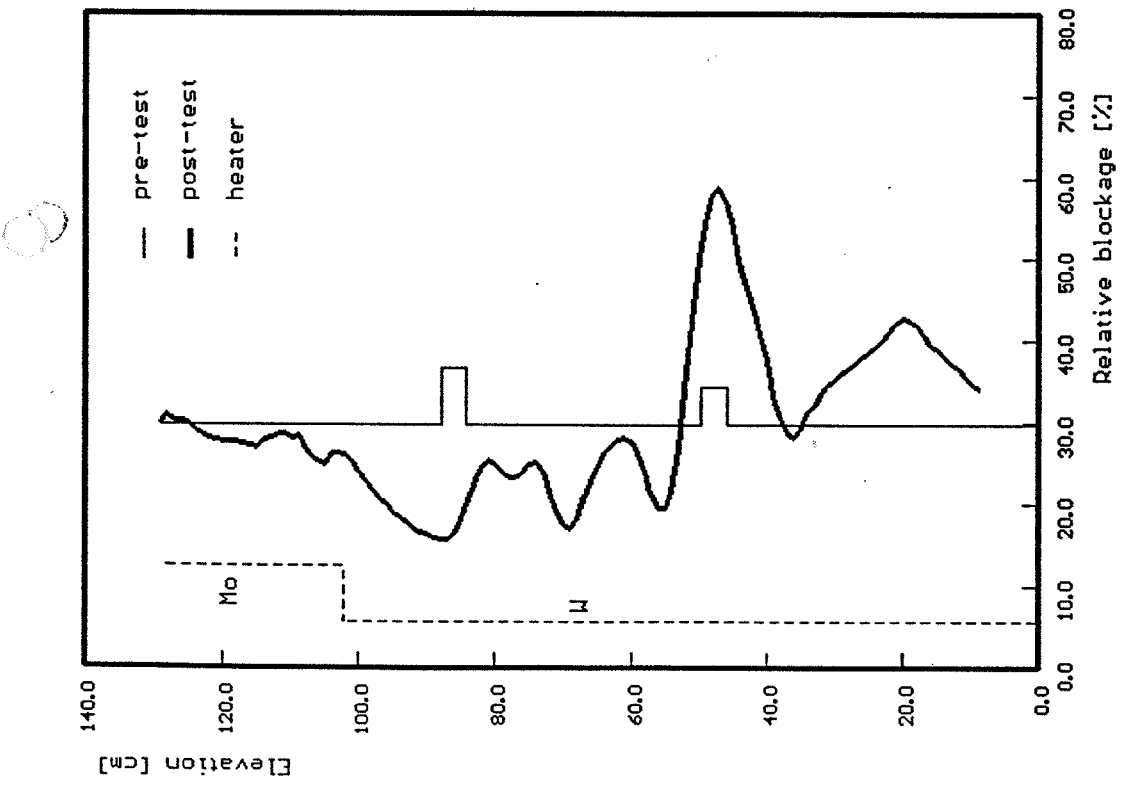


Fig. 3.26 : CORA 13: Axial distribution of blocked area inside the shroud

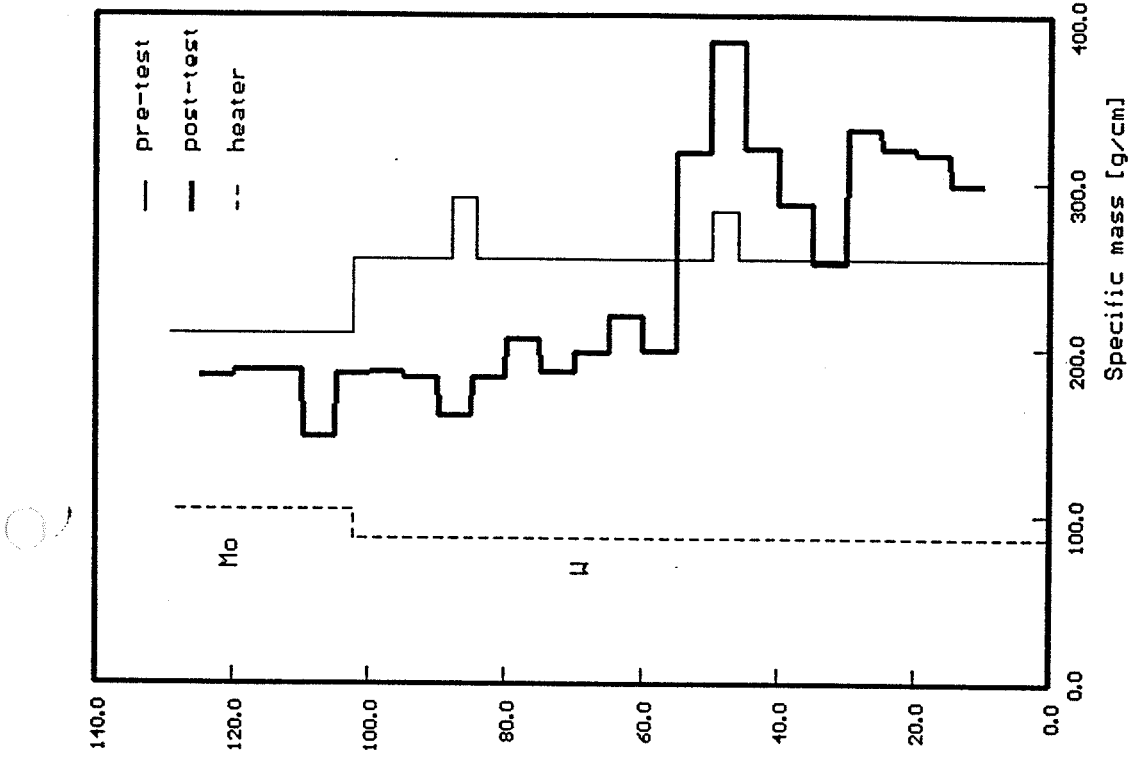
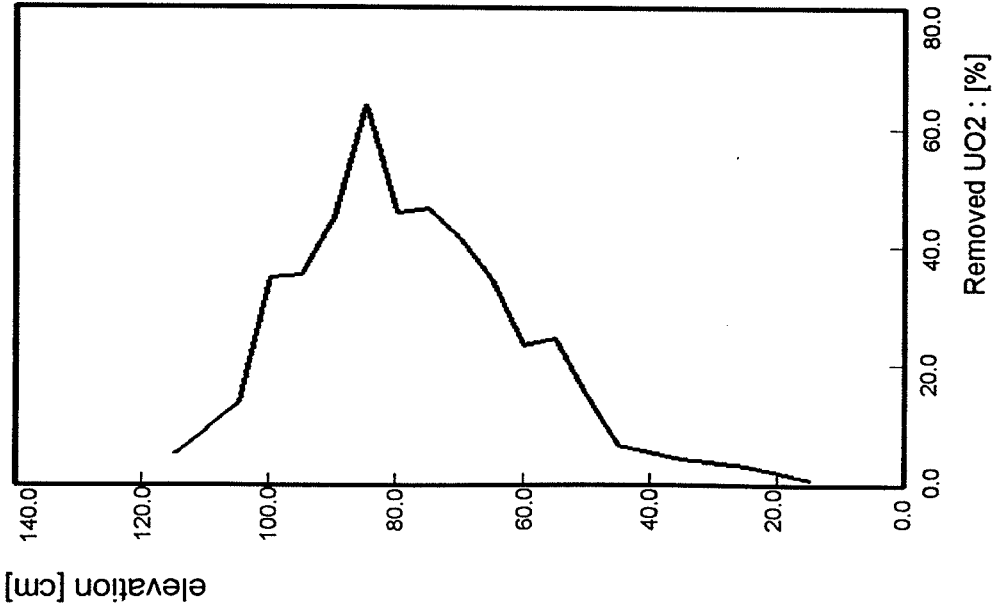
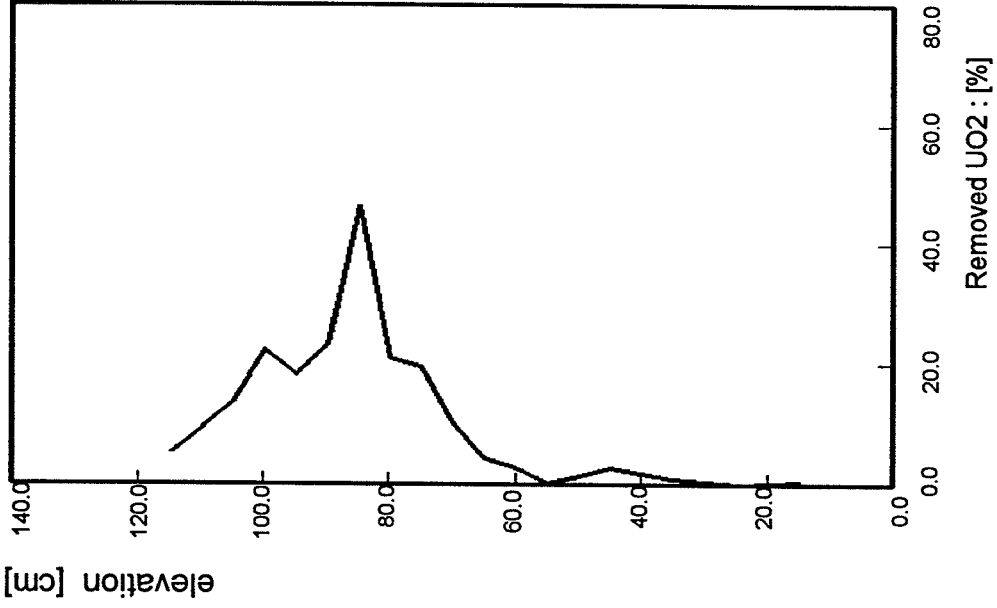


Fig. 3.27 : CORA 13: Axial mass distribution



**Fig. 3.28: Removed UO2:  
Total bundle  
(CORA-13)**



**Fig. 3.29: Removed UO2:  
unheated rods  
(CORA-13)**

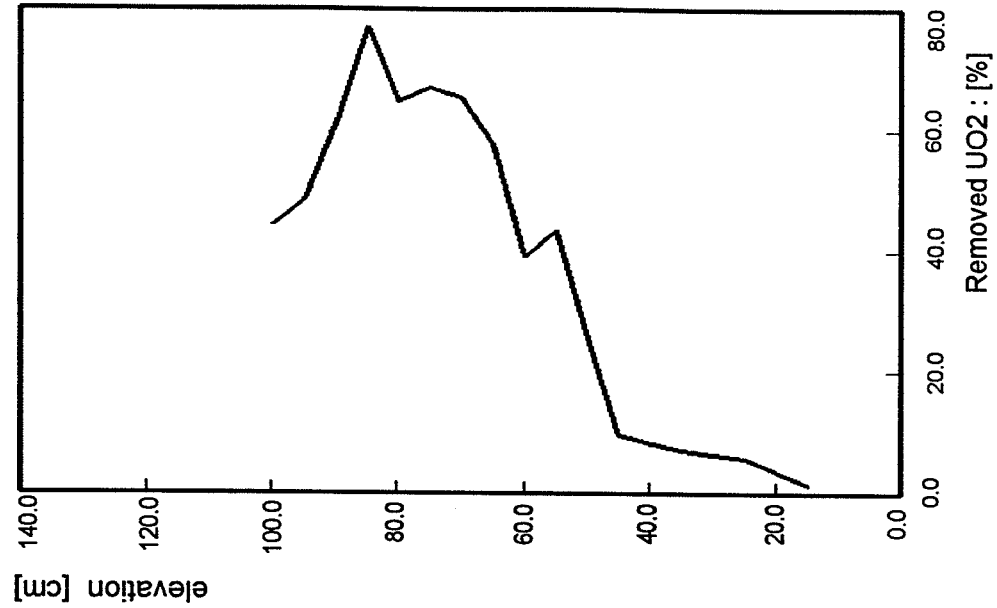
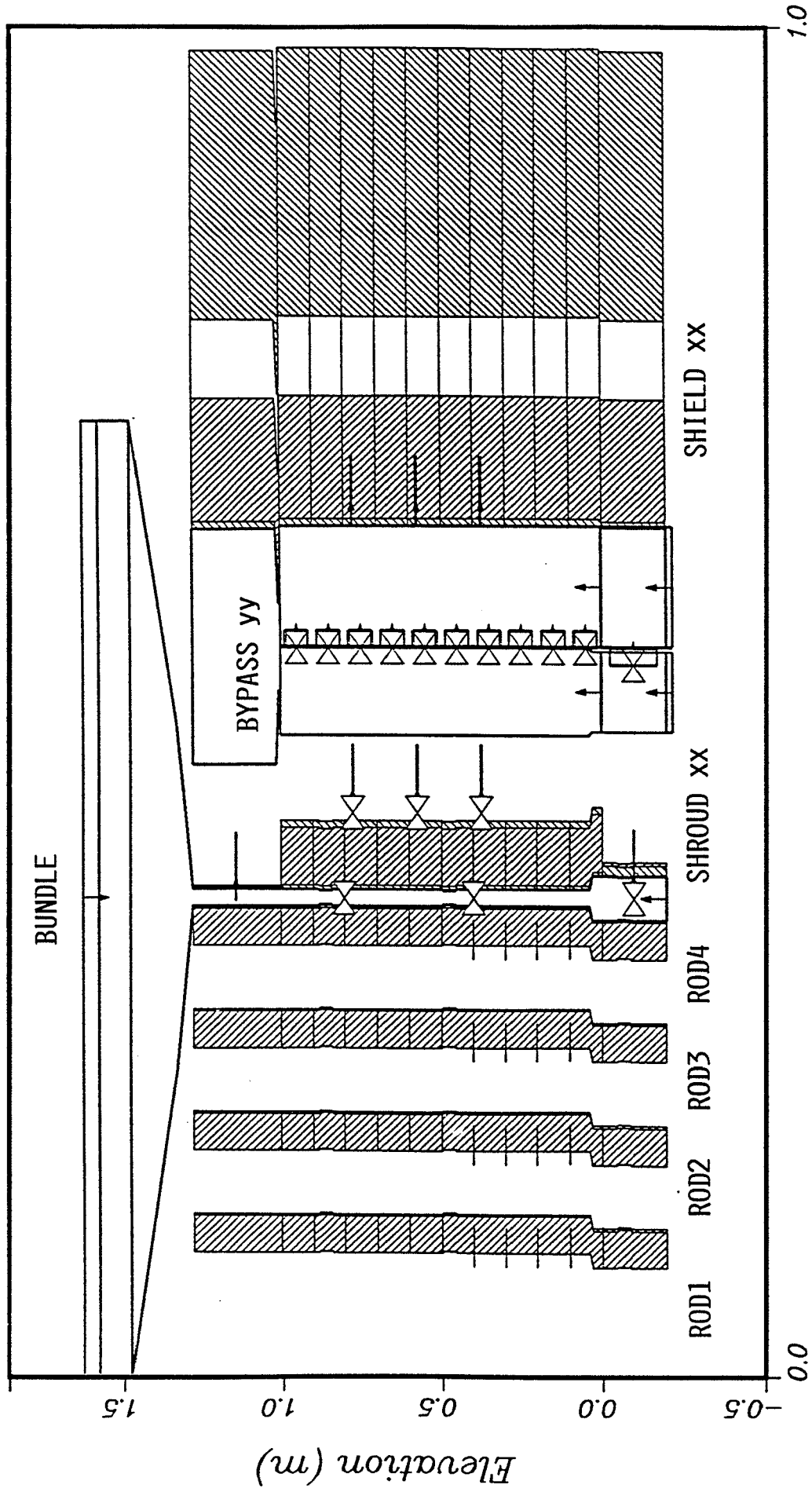


**Fig. 3.30: Removed UO2:  
Heated rods  
(CORA-13)**



Relative Cross Section Area  
Figure 3.31 : Nodalization Scheme

CORA13 Posttest Calculation with ATHLET-CD

GRS

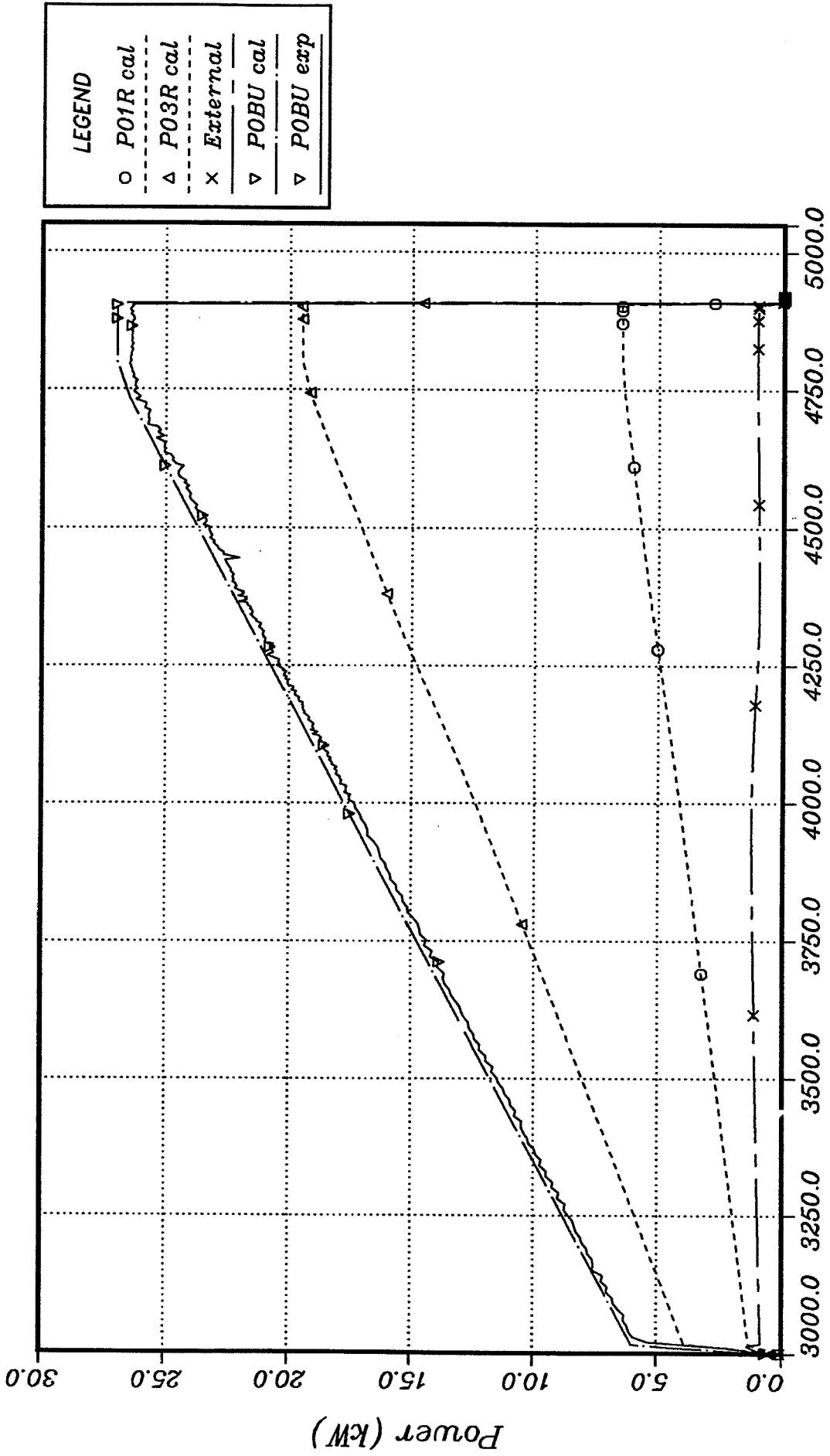


Figure 3.32 : Electrical Bundle Power

CORA13 Posttest Calculation with ATHLET-CD

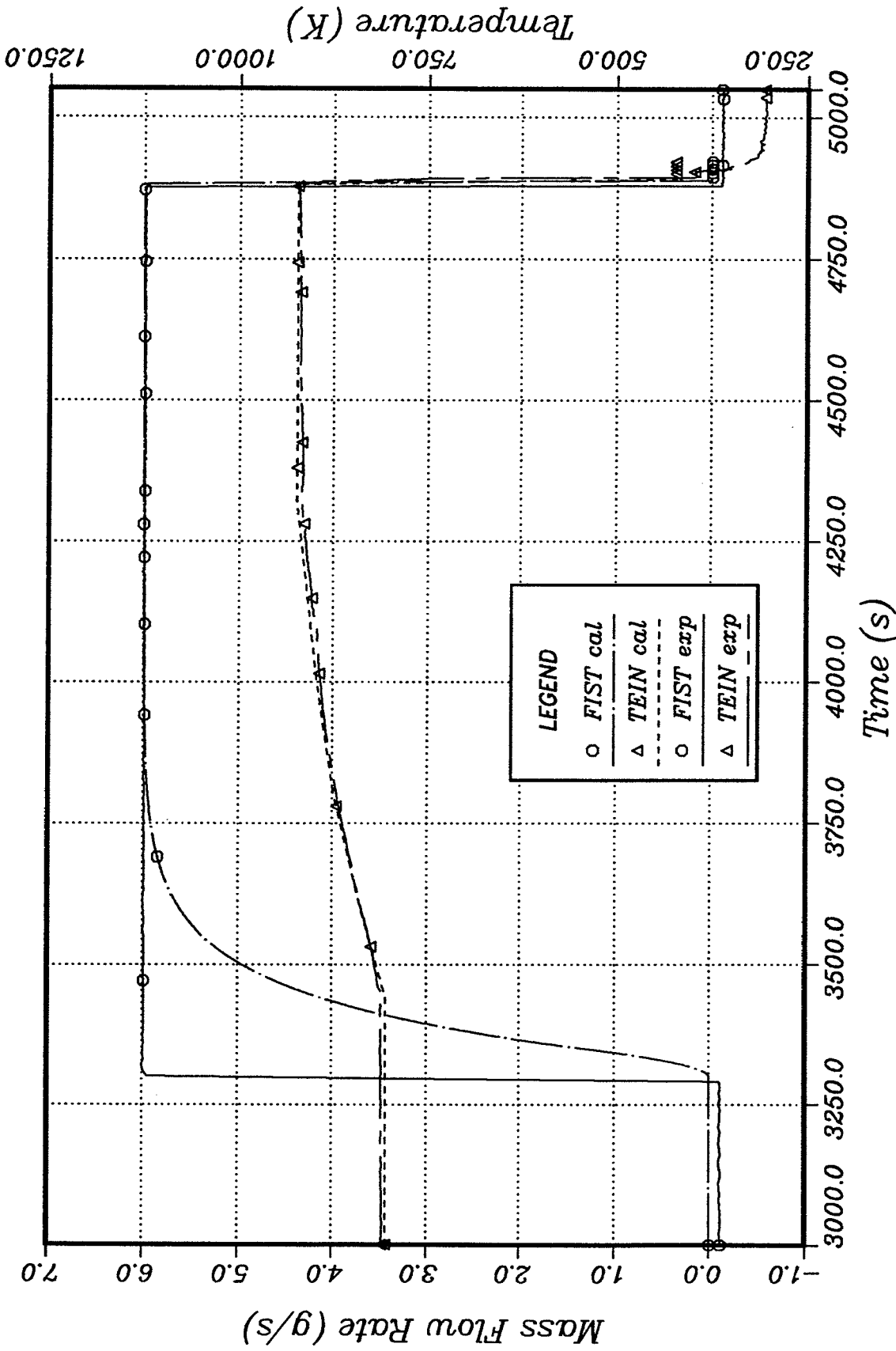


Figure 3.33 : Inlet Vapor Flow Rate and Temperature

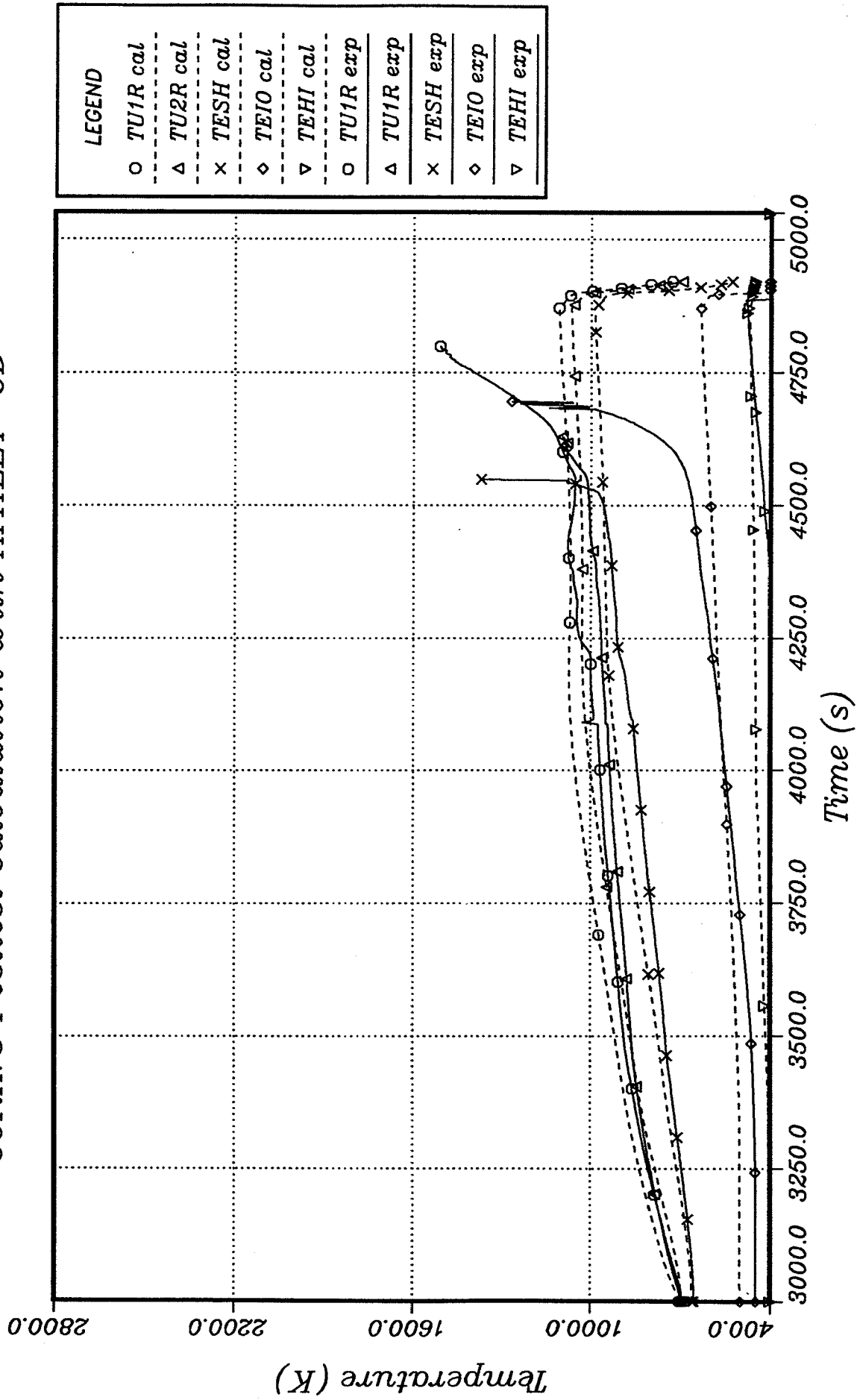


Figure 3.34 : Temperatures at Elevation 50 mm

CORA13 Posttest Calculation with ATHLET-CD

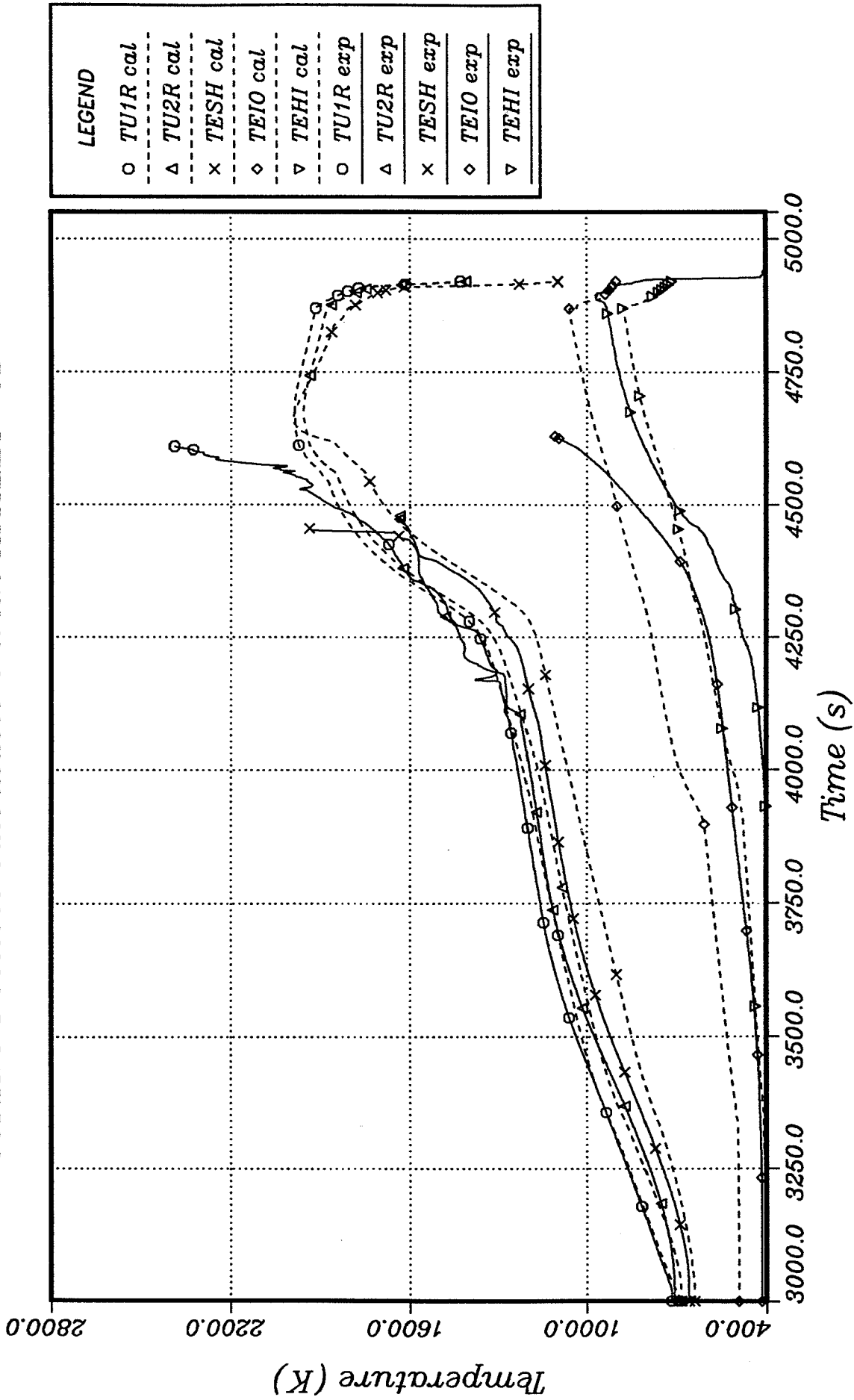


Figure 3.35 : Temperatures at Elevation 350 mm

CORA13 Posttest Calculation with ATHLET-CD

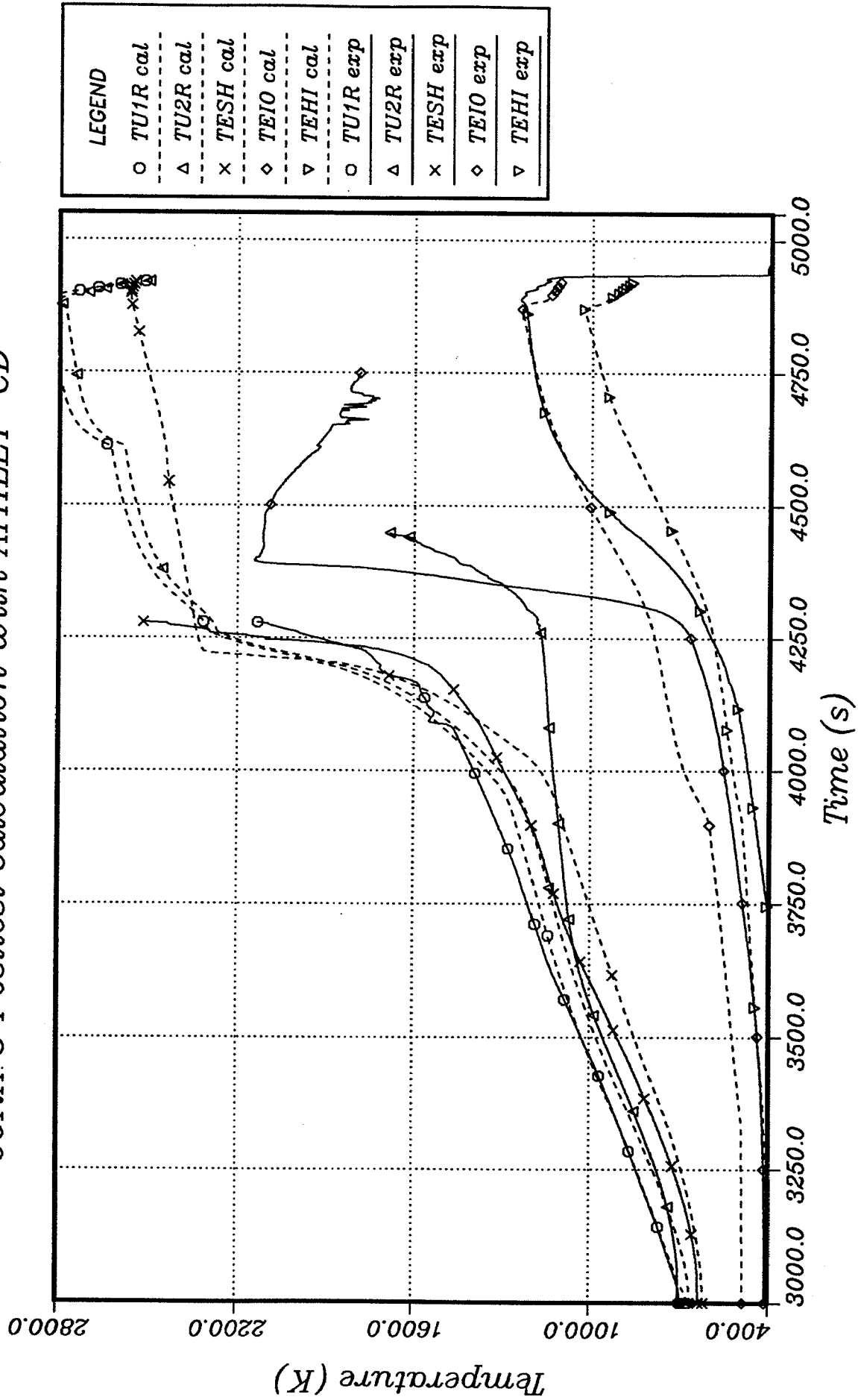


Figure 3.36 : Temperatures at Elevation 550 mm

CORA13 Posttest Calculation with ATHLET-CD

GRS

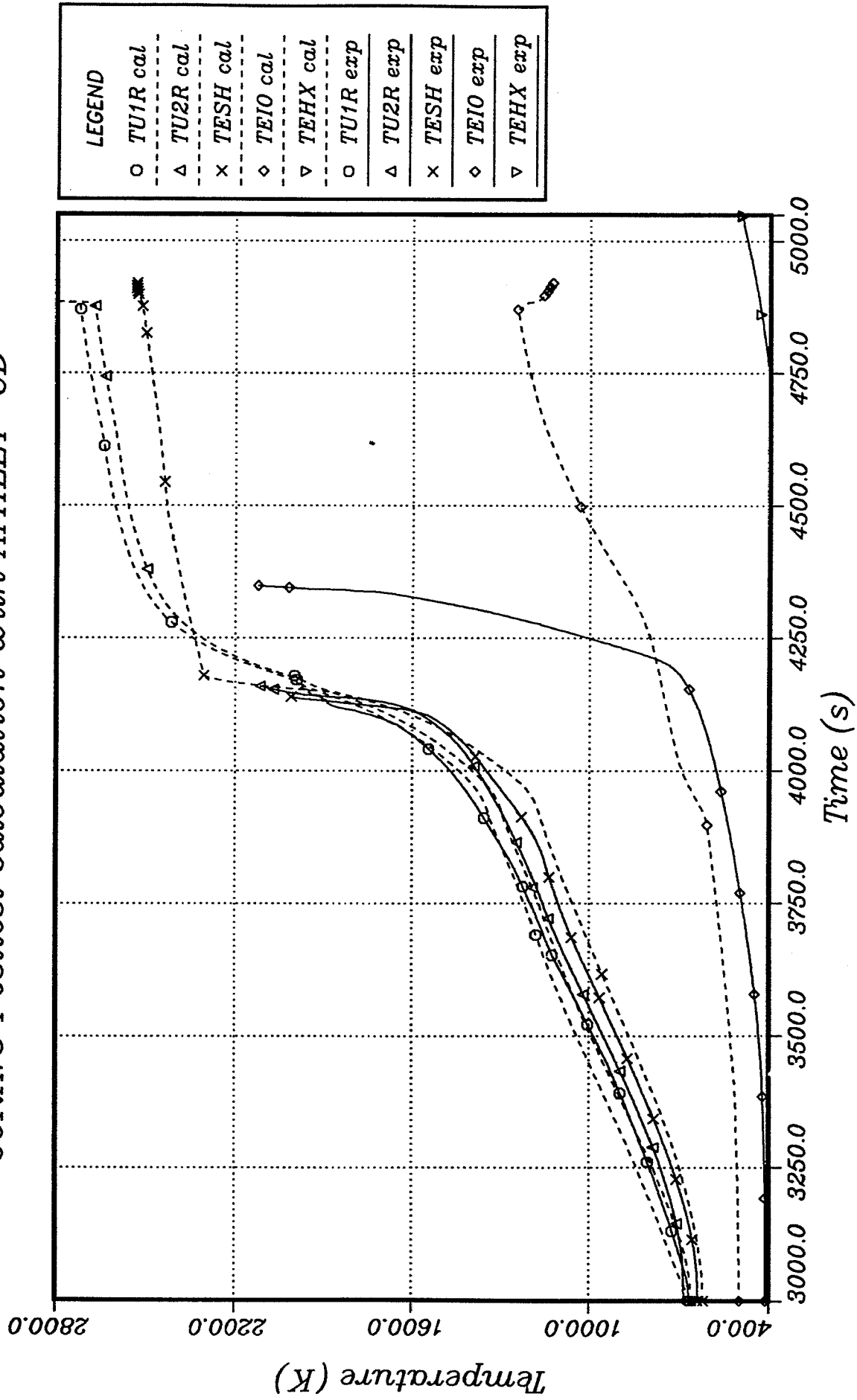


Figure 3.37 : Temperatures at Elevation 750 mm

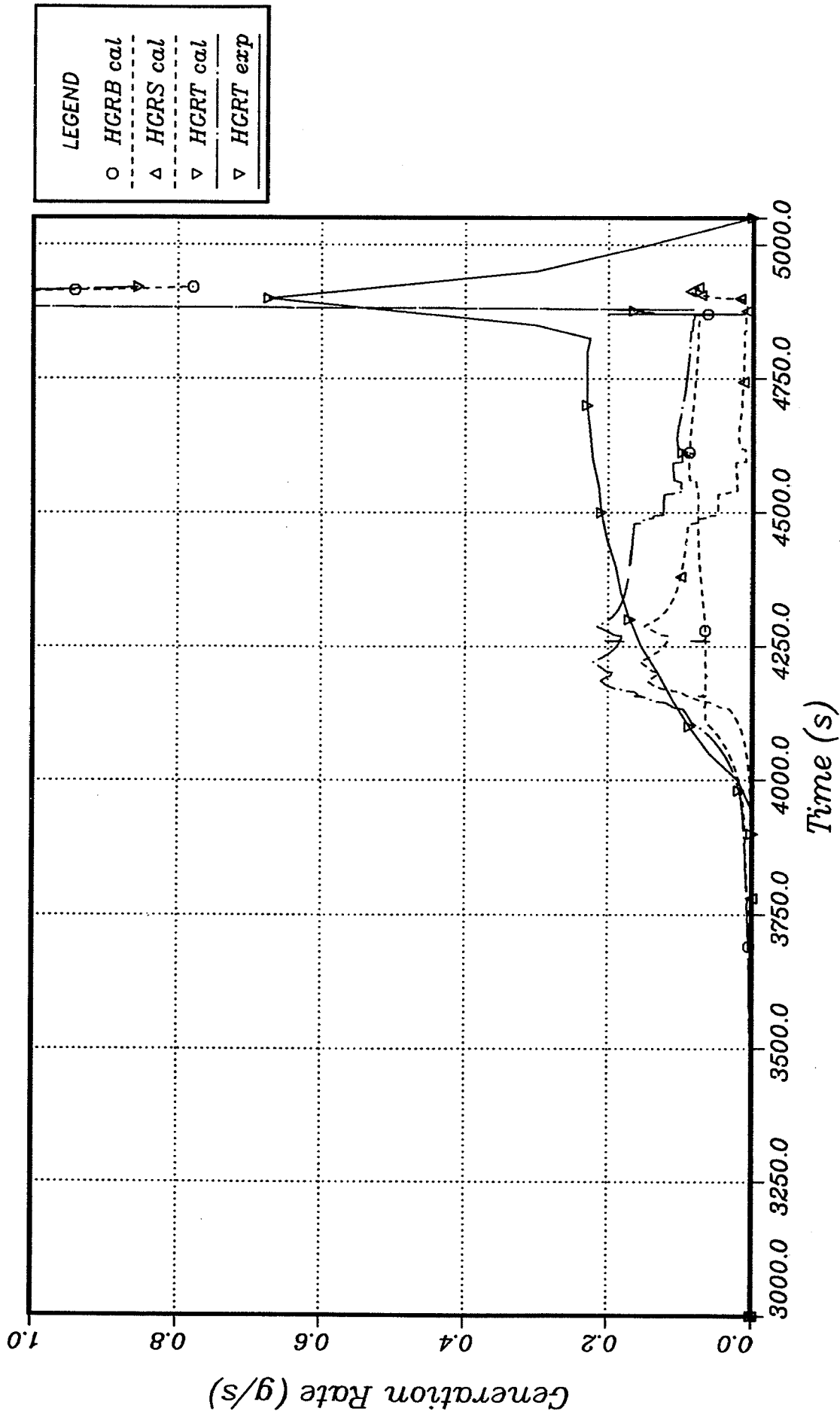


Figure 3.38 : Hydrogen Generation Rate



CORA13 Posttest Calculation with ATHLET-CD

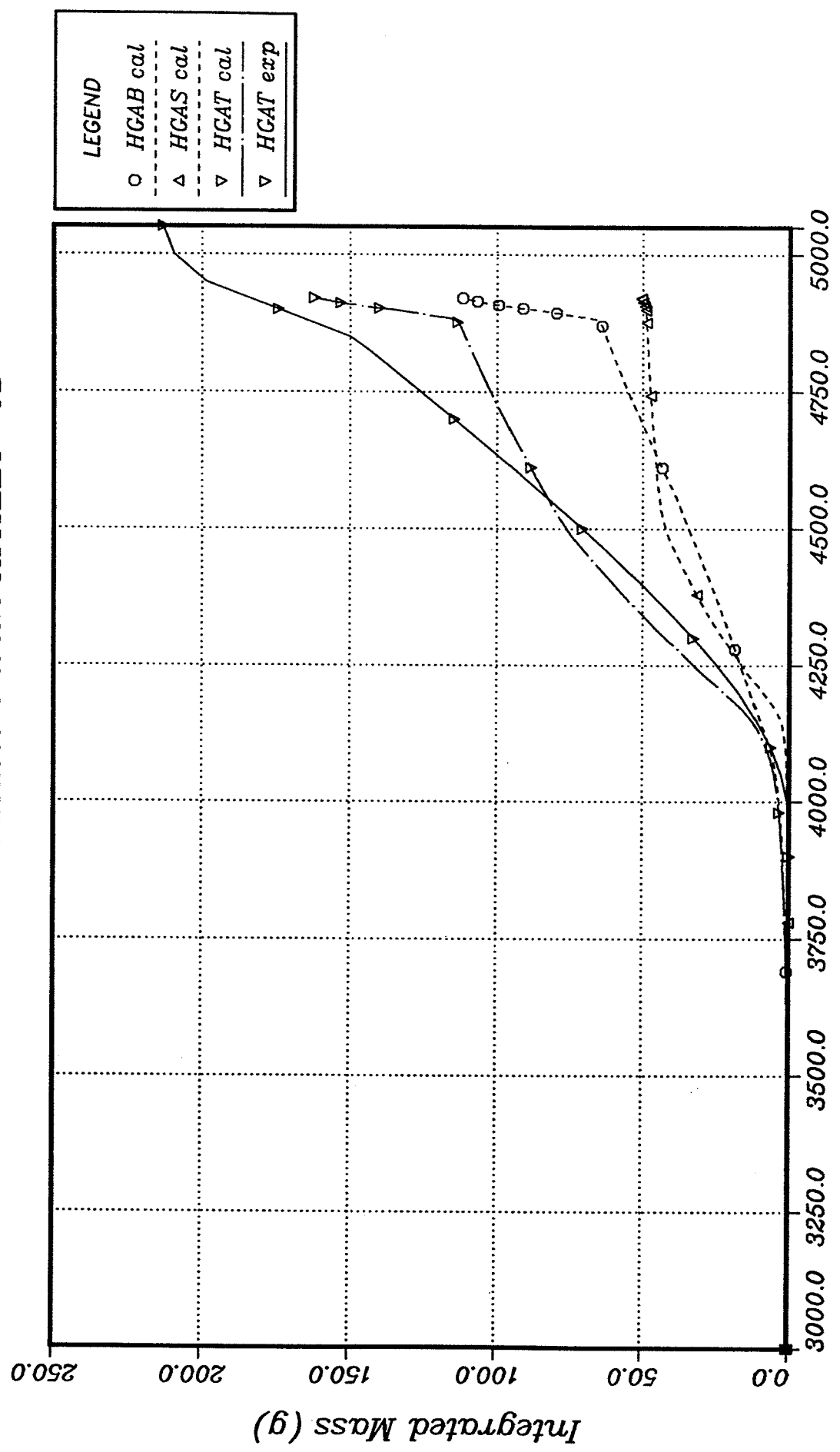


Figure 3.39 : Accumulated Hydrogen Generation

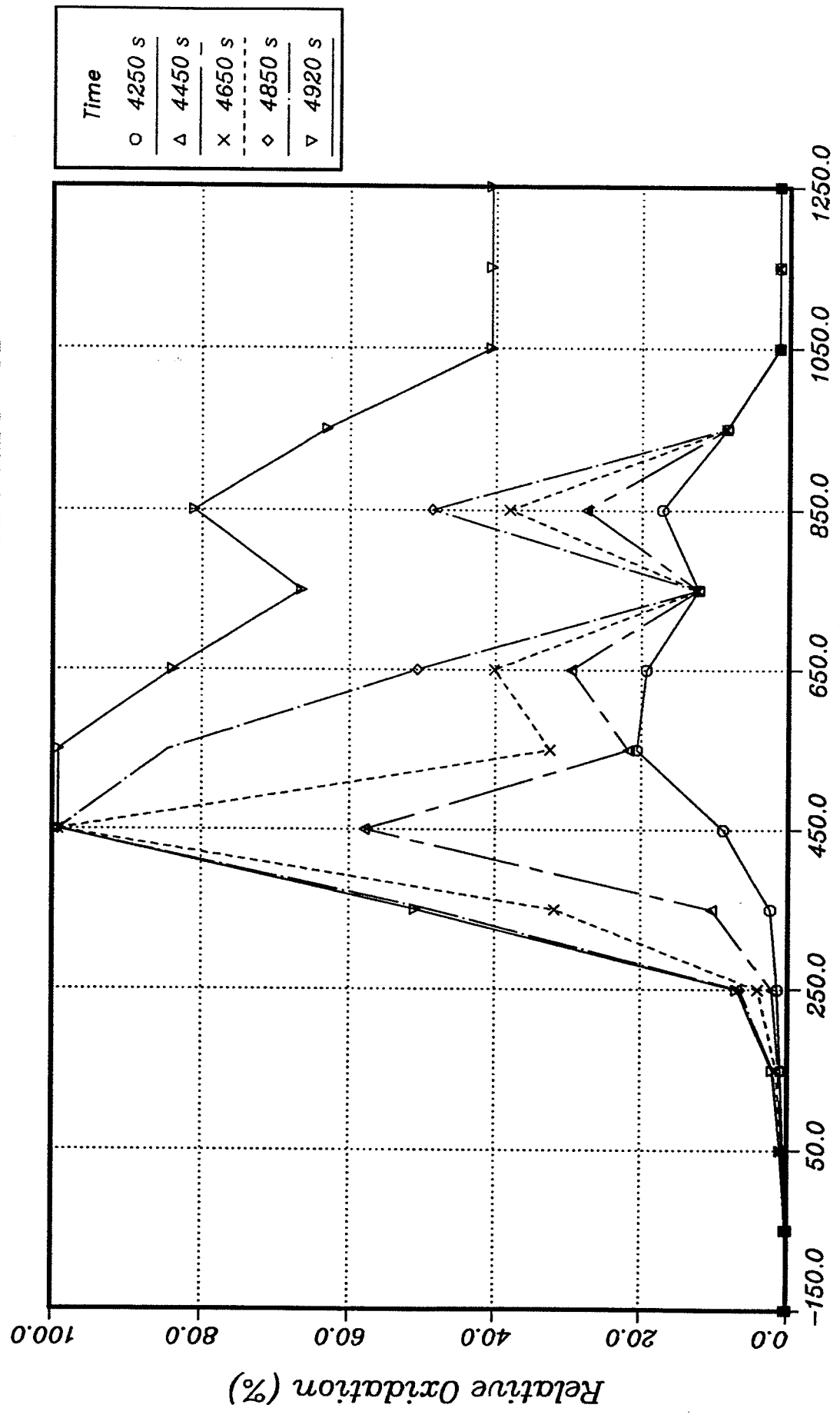


Figure 3.40: Zr Oxidation, First Ring (Z01R)

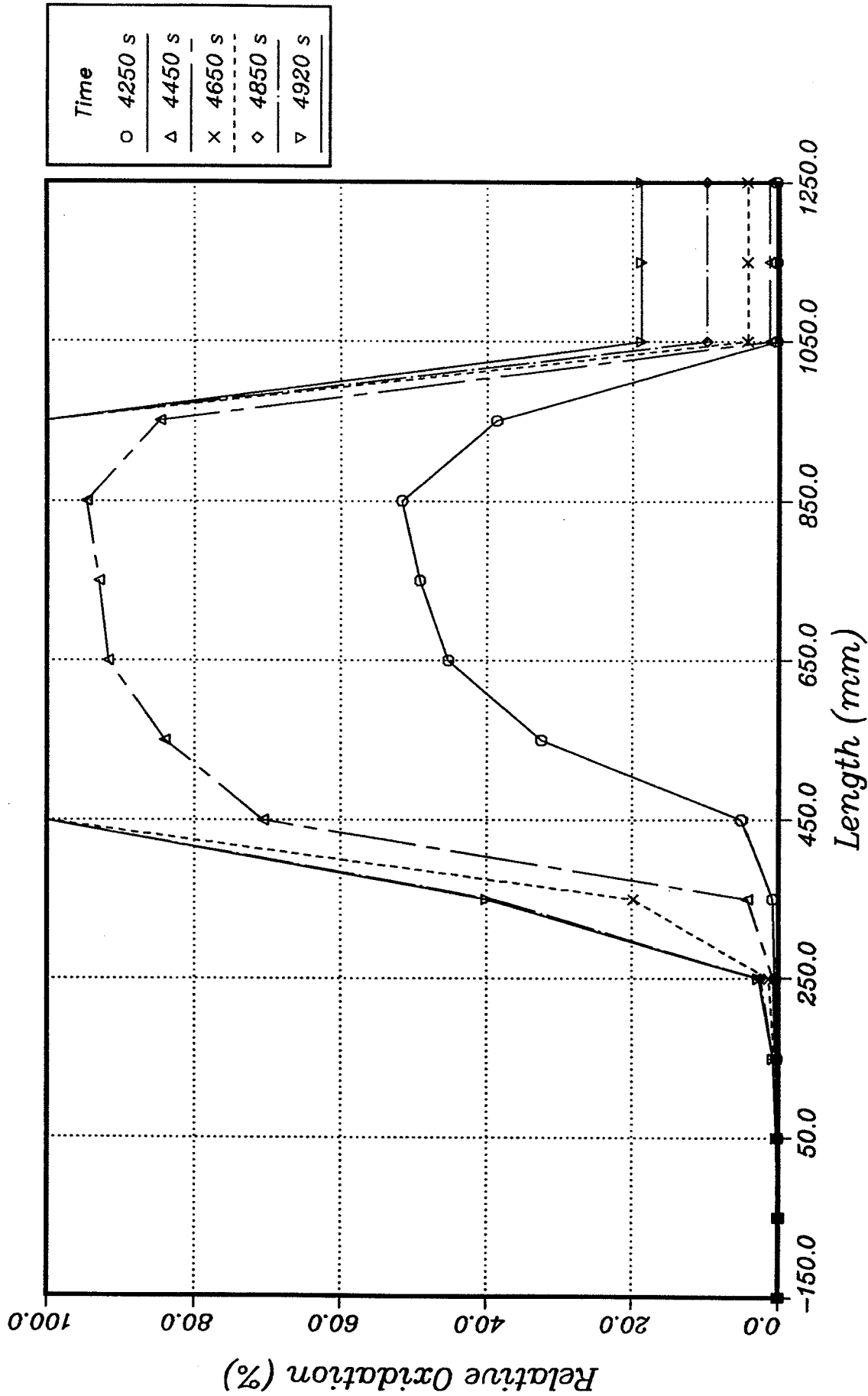
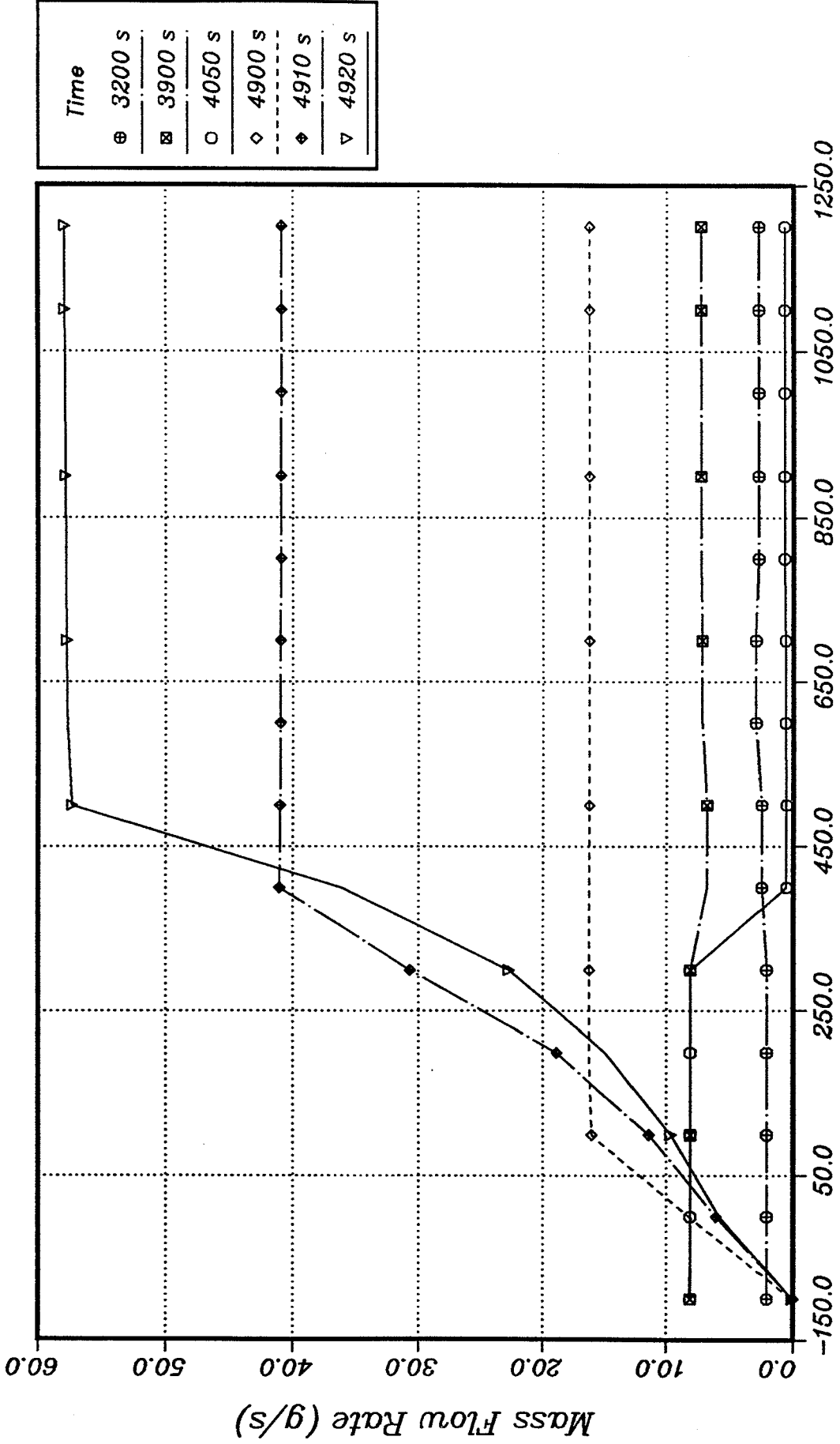


Figure 3.41: Zr Oxidation, Shroud (ZOSH)

GRS

CORA13 Posttest Calculation with ATHLET-CD



Length (mm)

Figure 3.42: Vapor + 1/4 Argon Mass Flow Rate

GRS

CORA13 Posttest Calculation with ATHLET-CD

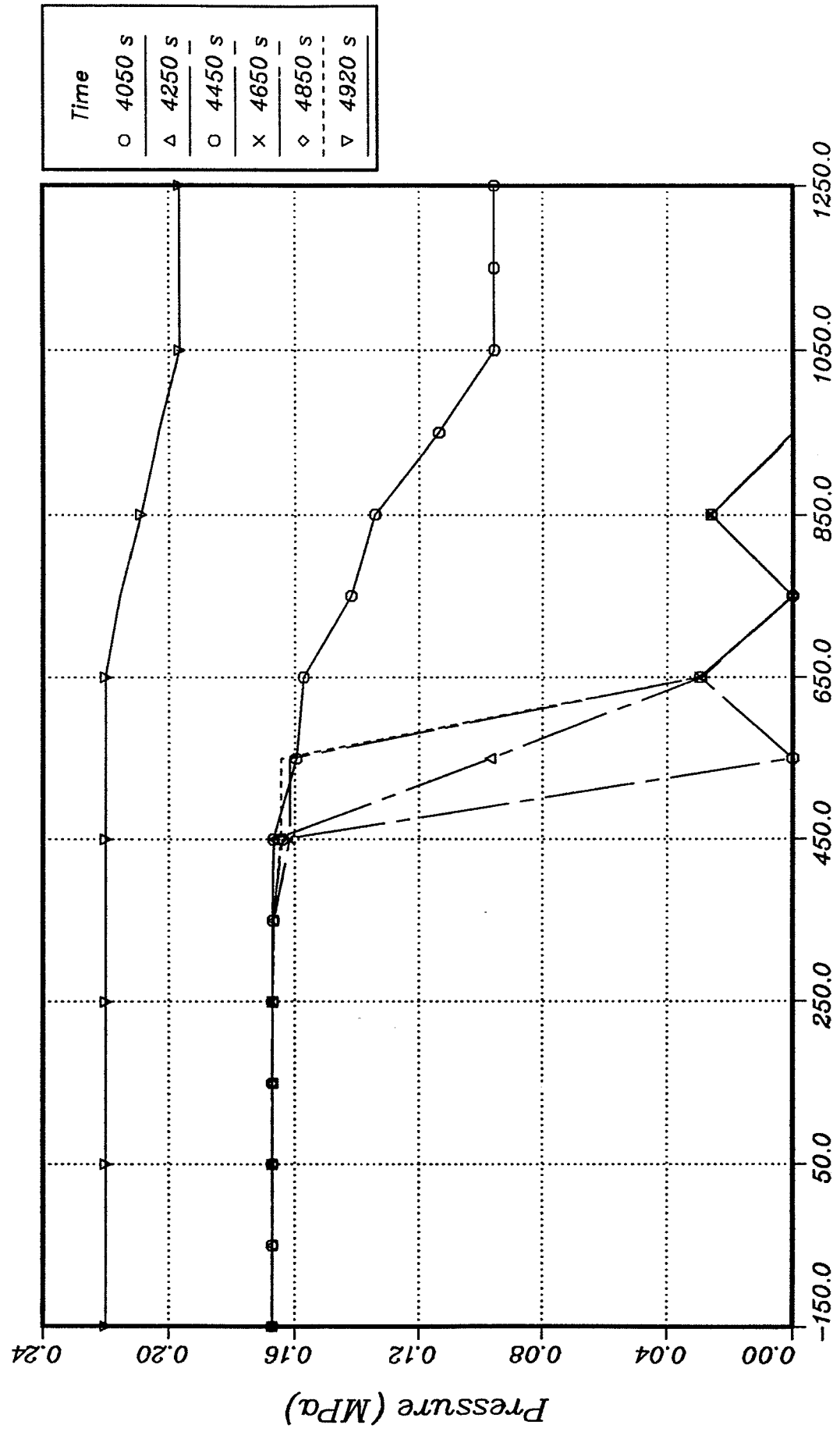


Figure 3.43: Partial Vapor Pressure

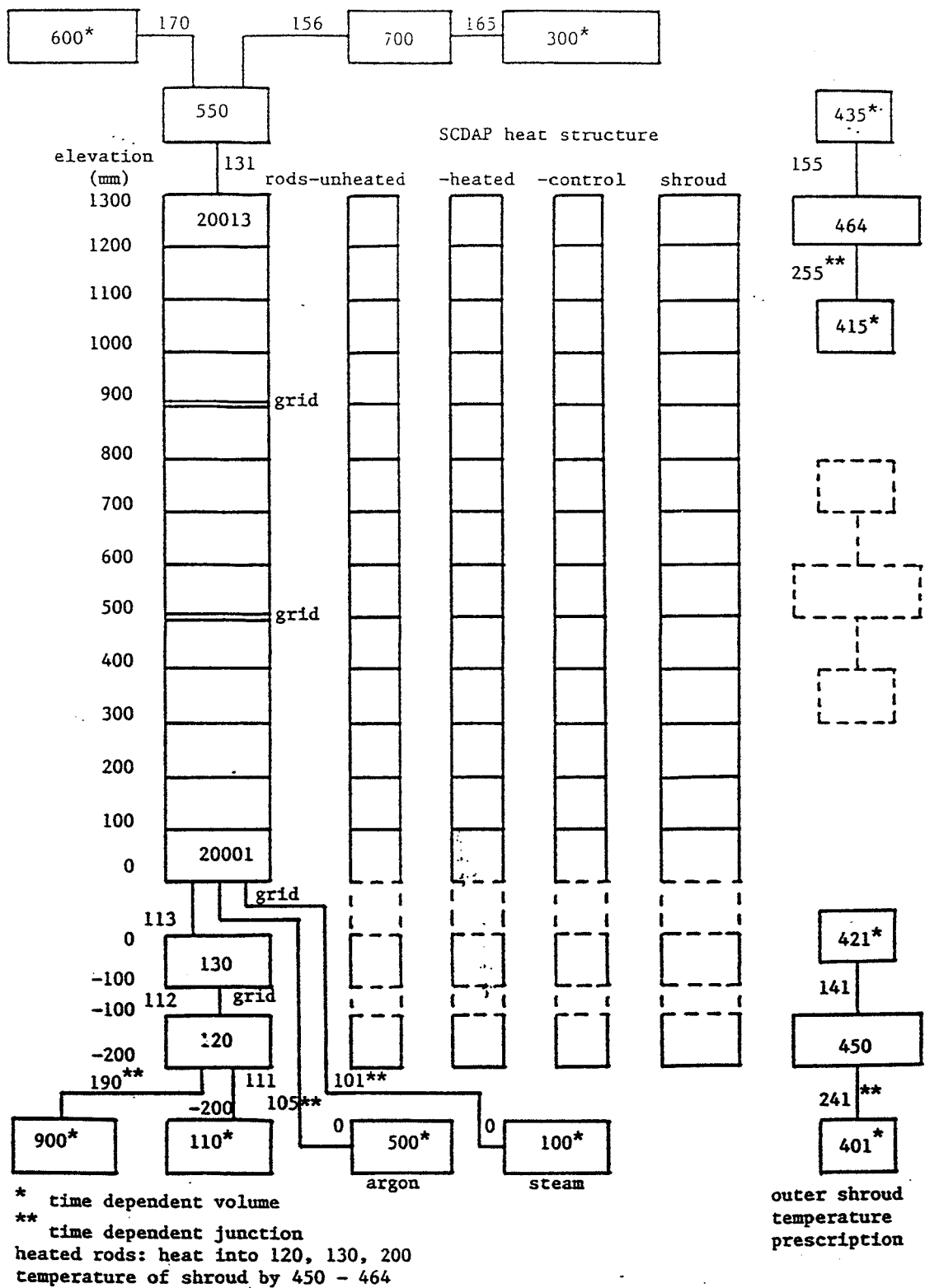


Figure 4.01 ECN - Nodalization Scheme



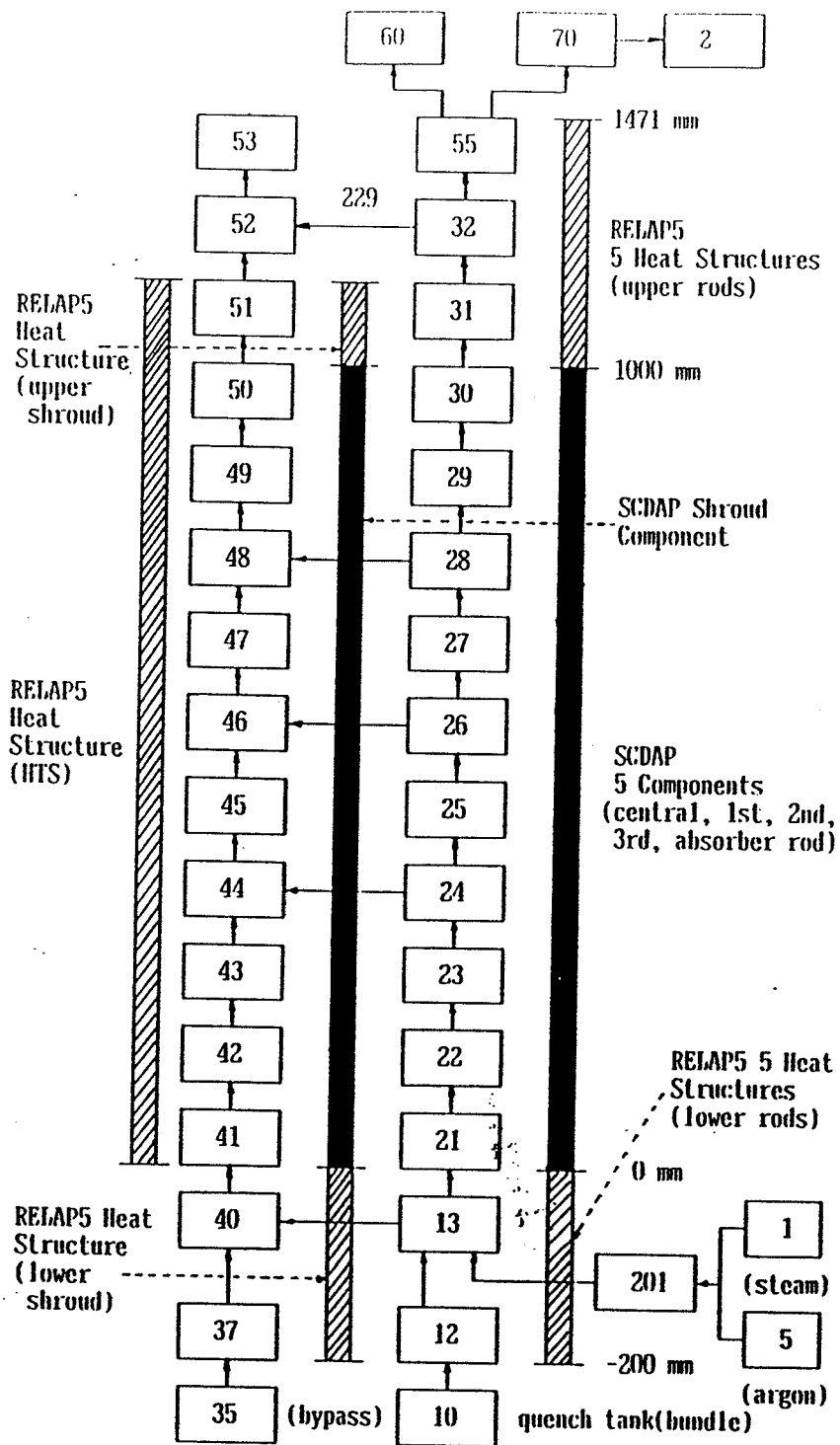


Figure 4.03 KAE - Nodalization Scheme

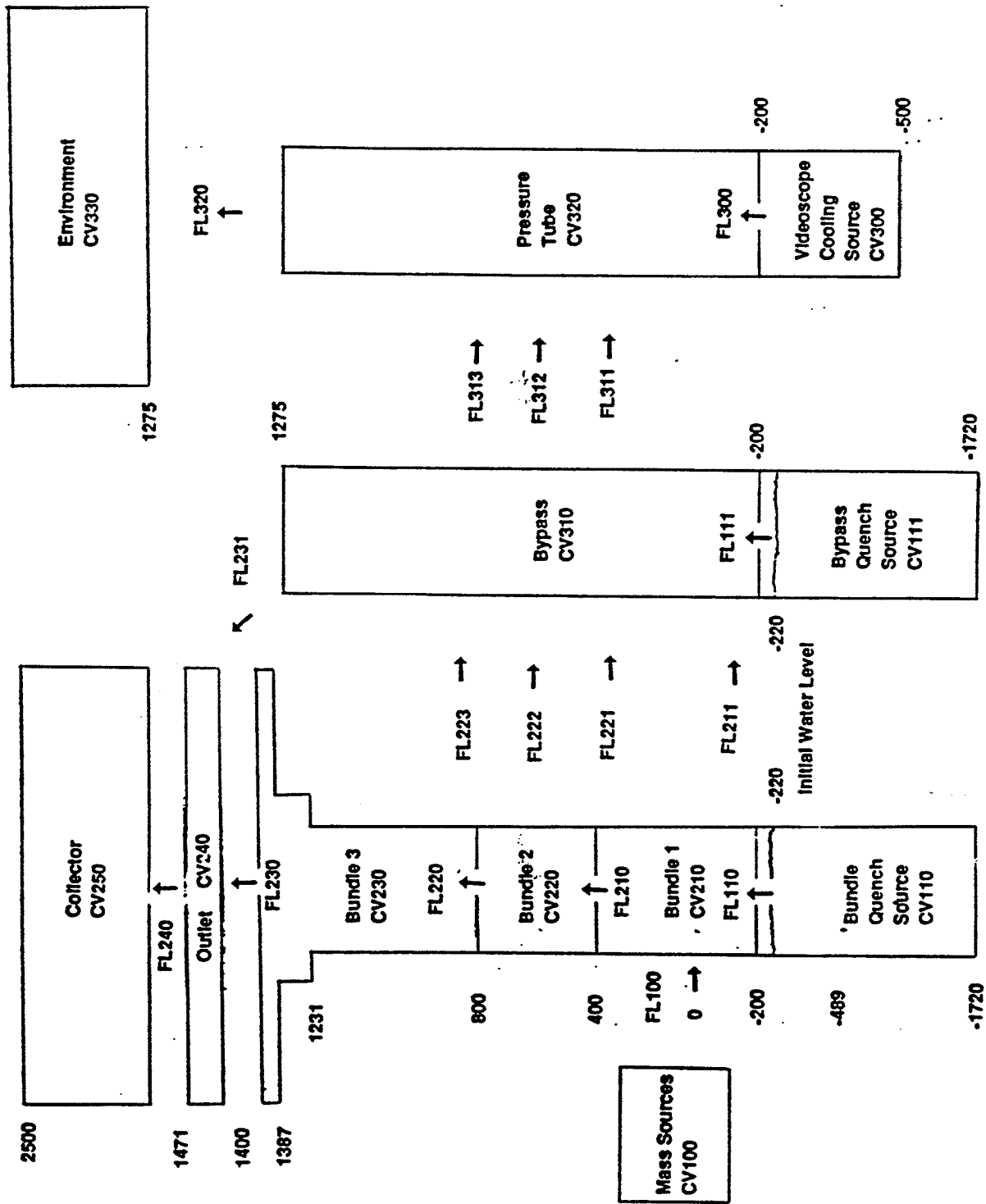


Figure 4.04 SNL - Nodalization Scheme

GRS

ISP 31

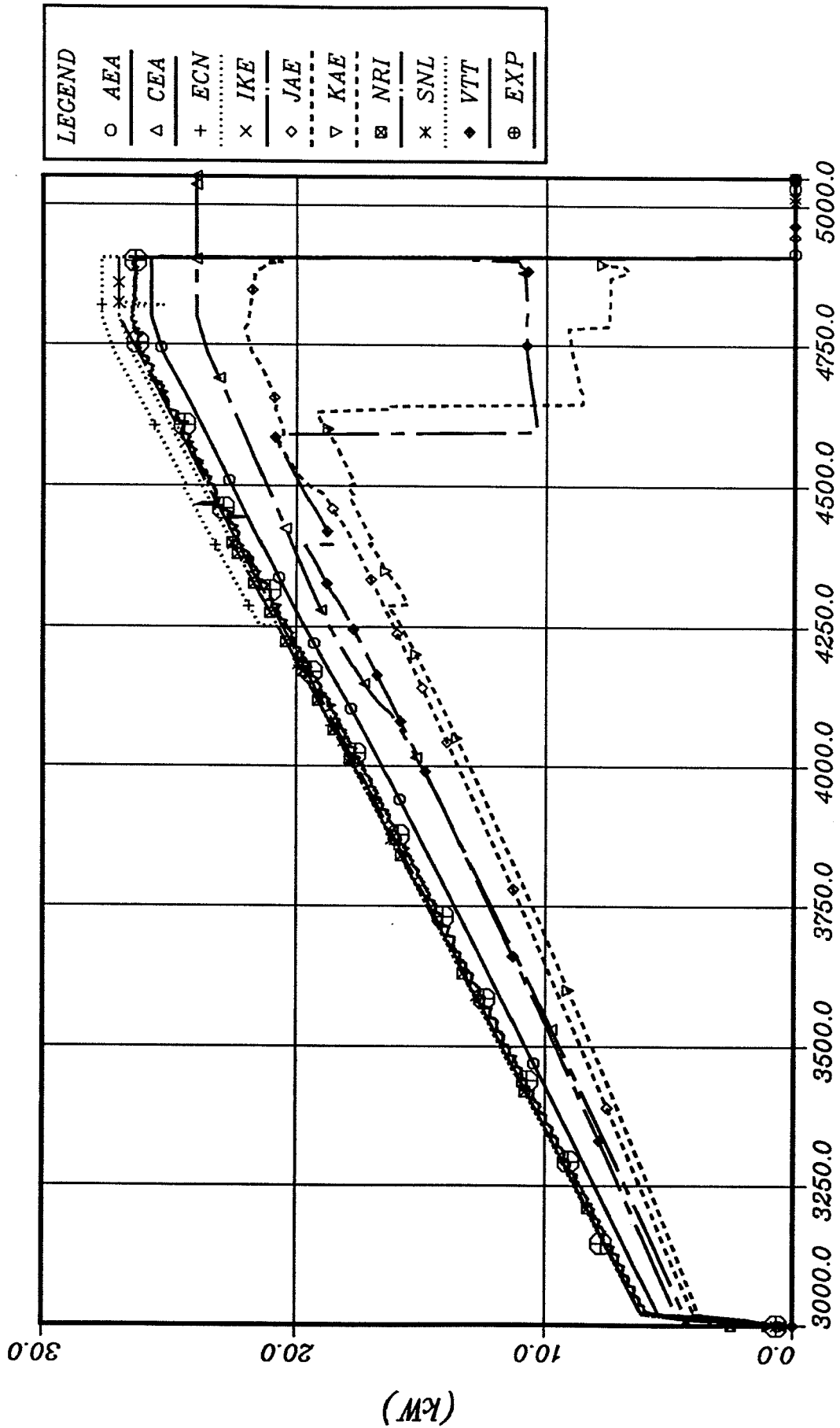


Figure 4.05: Bundle Power (POBU)

ISP 31

GRS

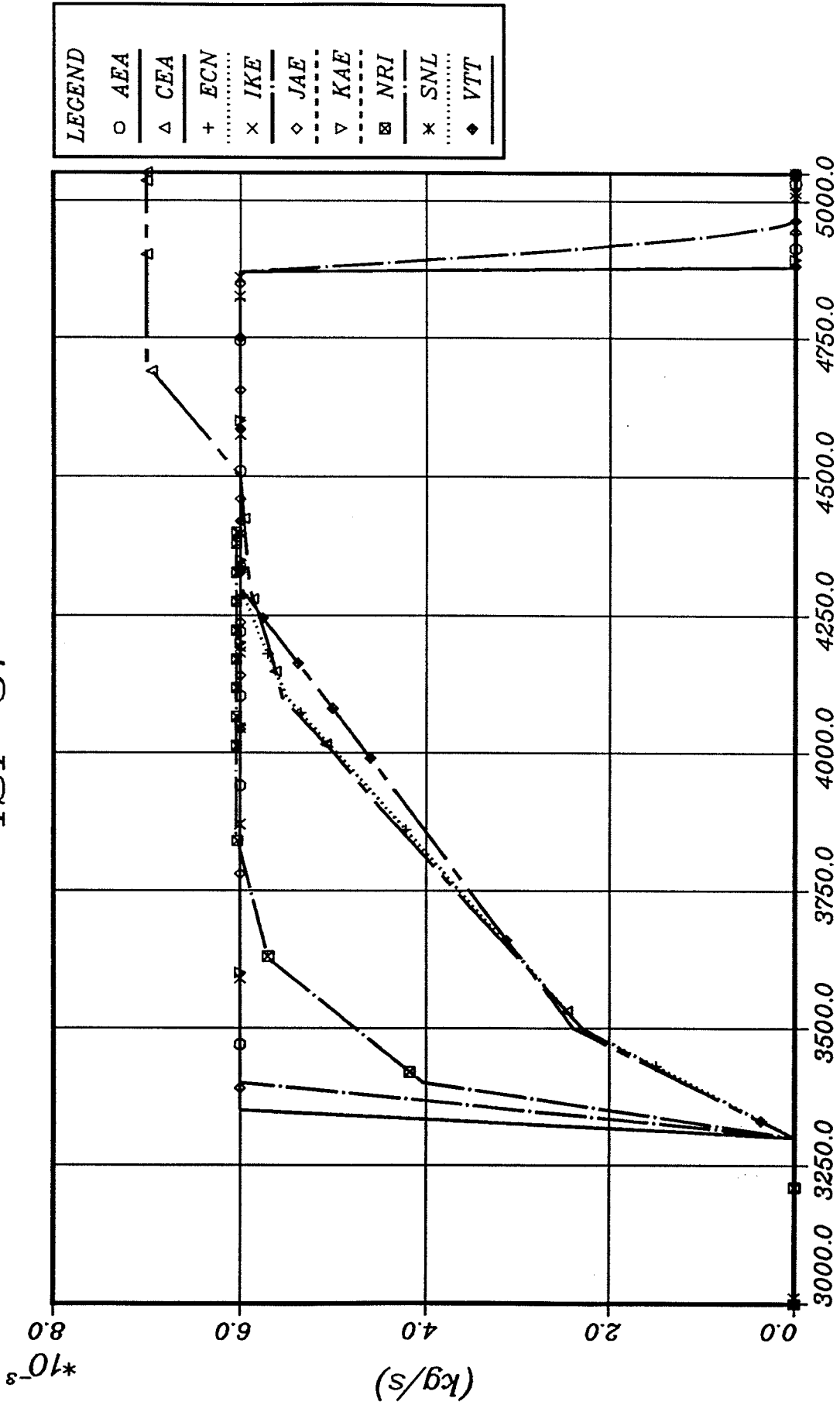


Figure 4.06: Steam Inlet Flow (FIST)

ISP 31

GRS

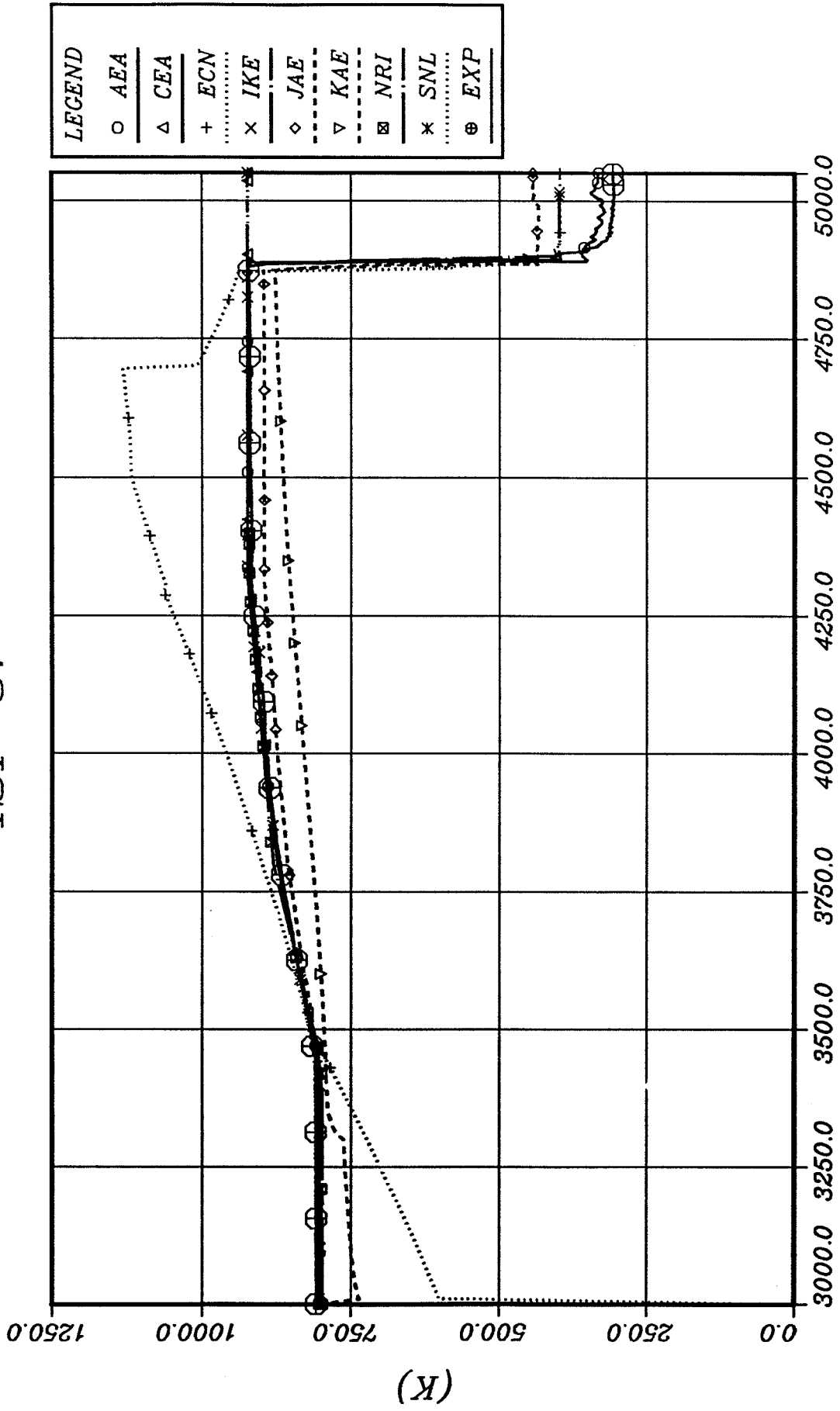
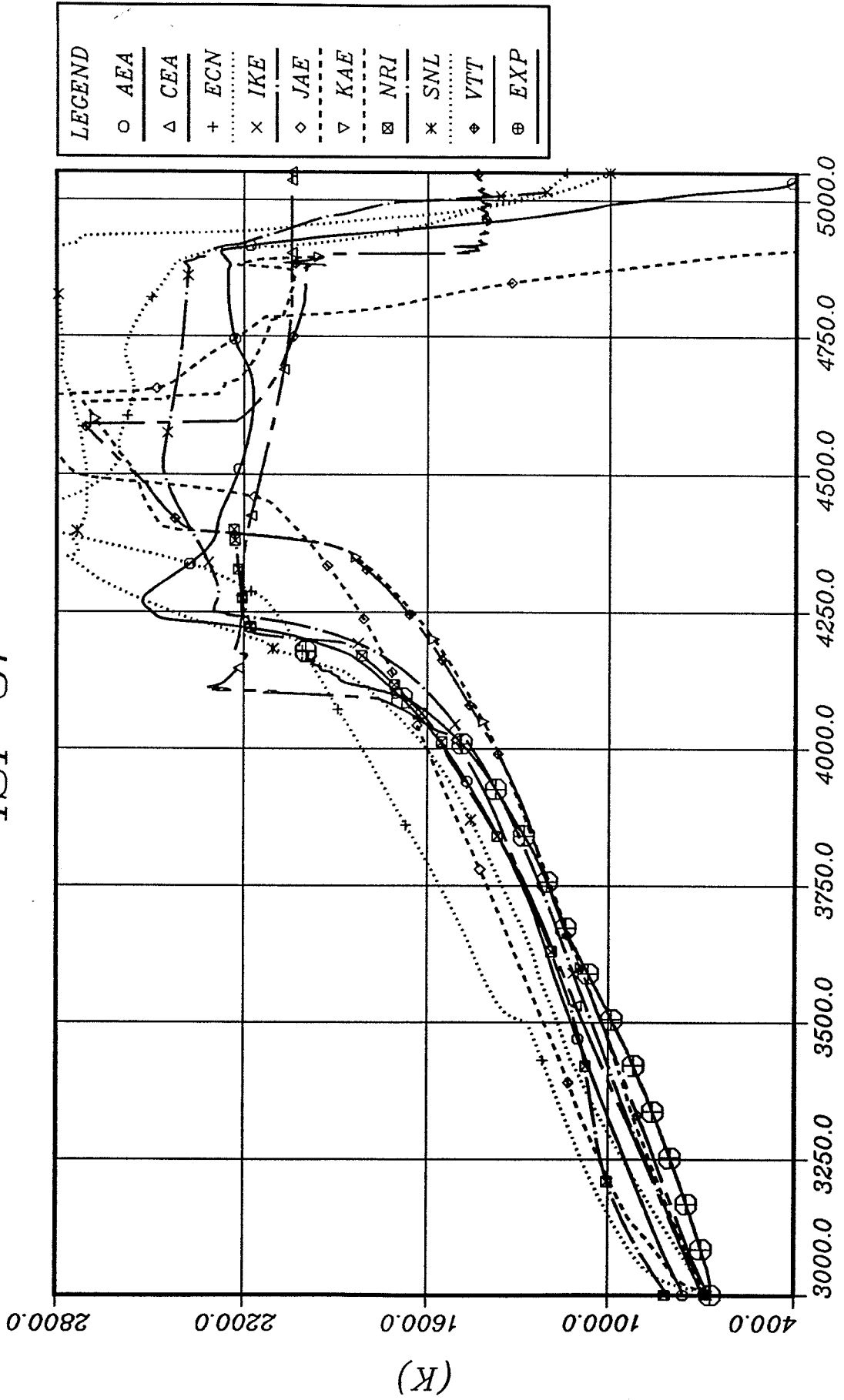


Figure 4.07: Inlet Temperature (TEIN)

ISP 31

GRS



LEGEND

○	AEA
△	CEA
+	ECN
×	IKE
◇	JAE
▽	KAE
⊠	NRI
*	SNL
◆	VTT
⊕	EXP

Figure 4.08: Fuel Temperature, First Ring (TU1R 0750)

ISP 31

GRS

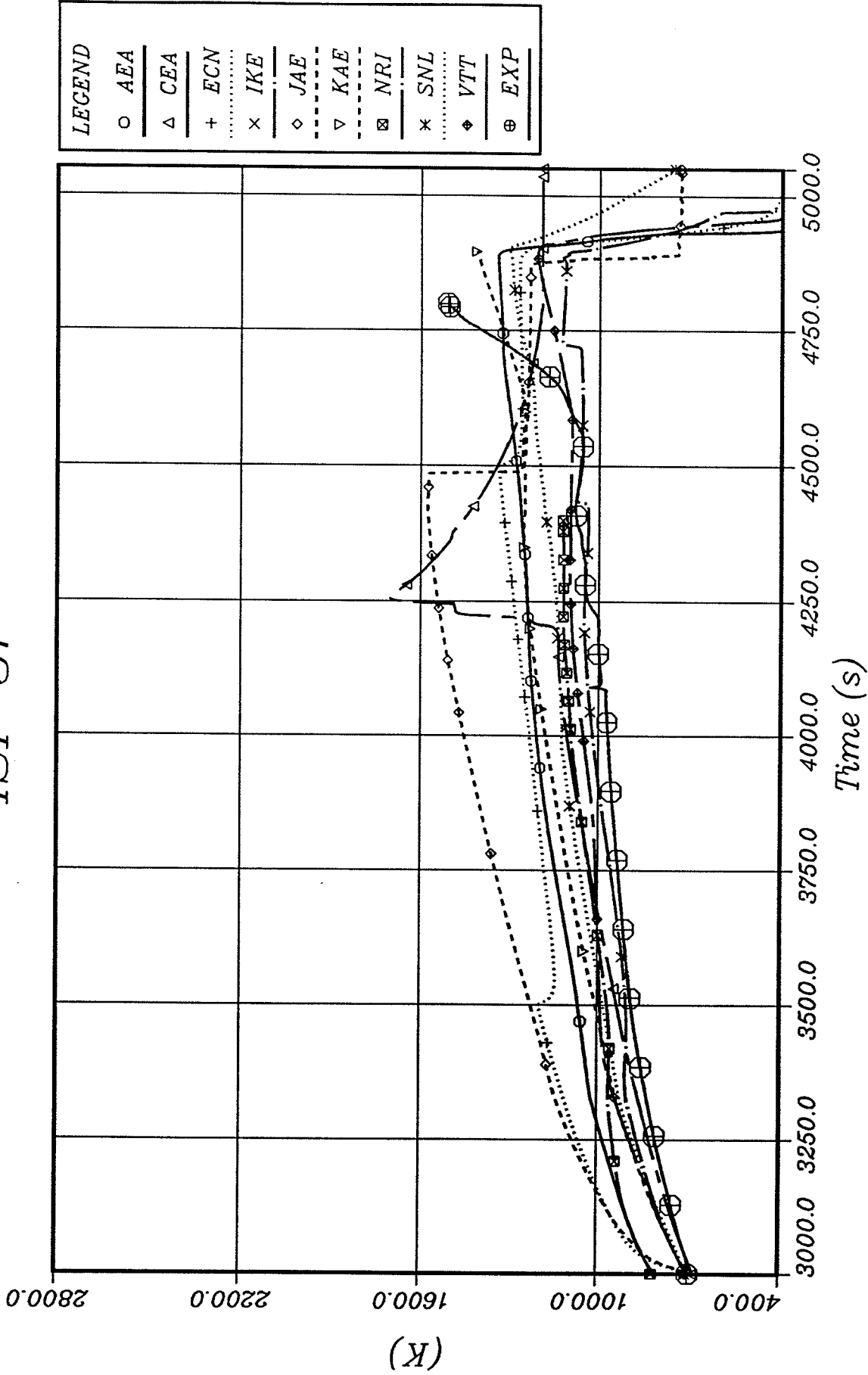
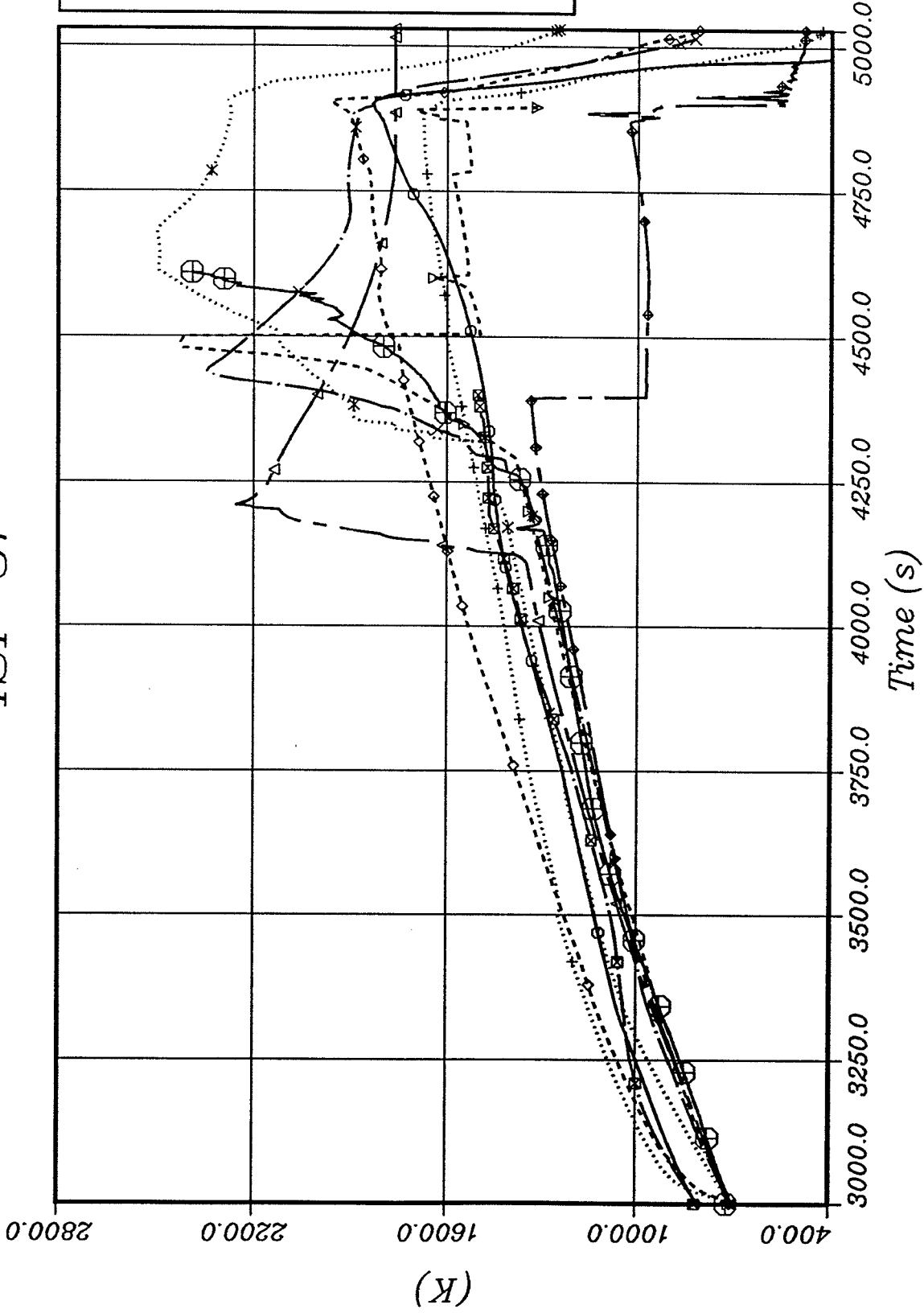


Figure 4.09: Fuel Temperature, First Ring (TU1R 0050)

ISP 31

GRS



LEGEND

○	AEA
△	CEA
+	ECN
×	IKE
◇	JAE
▽	KAE
⊠	NRI
*	SNL
◆	VTT
⊕	EXP

Figure 4.10: Fuel Temperature, First Ring (TU1R 0350)

ISP 31

GRS

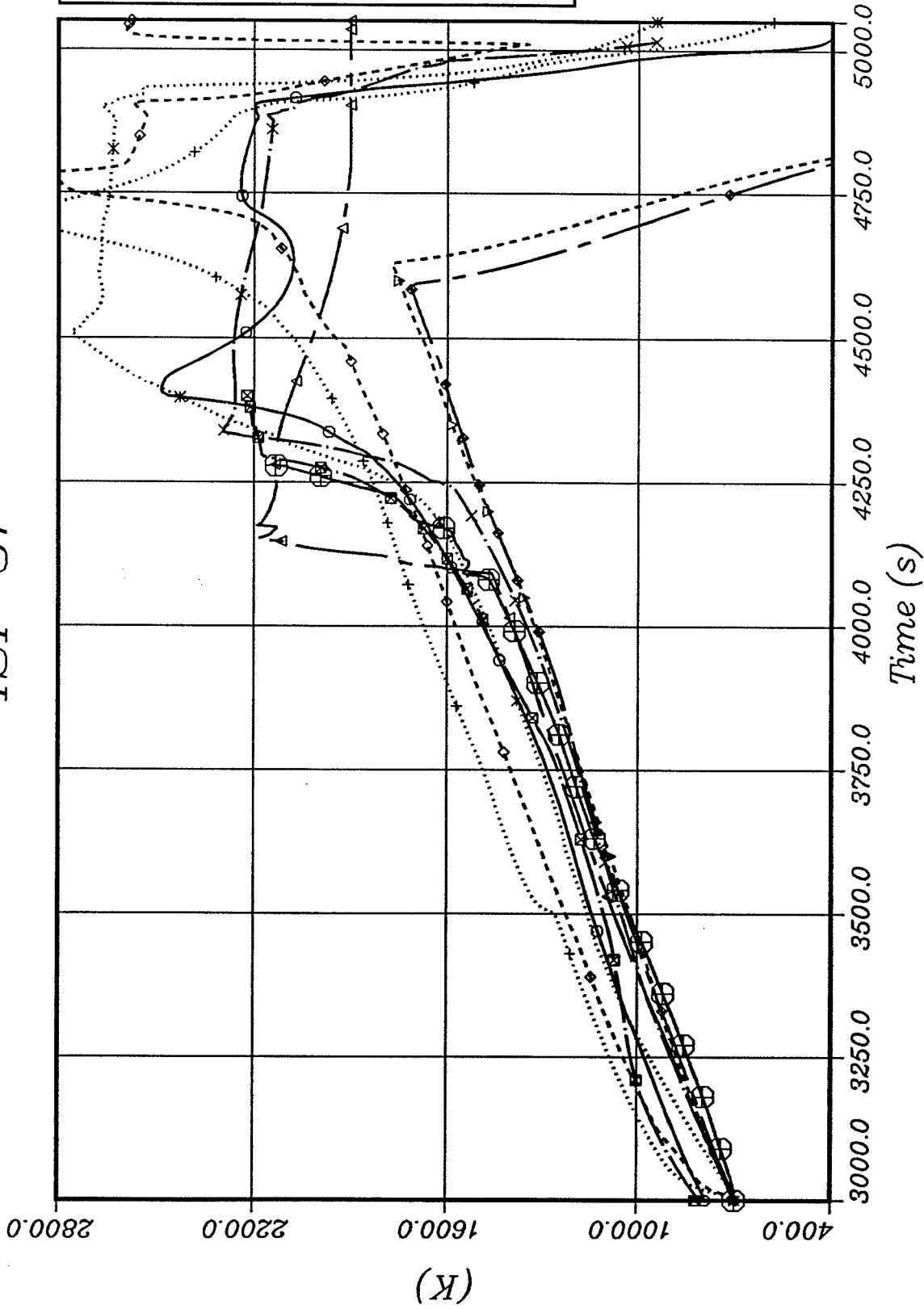
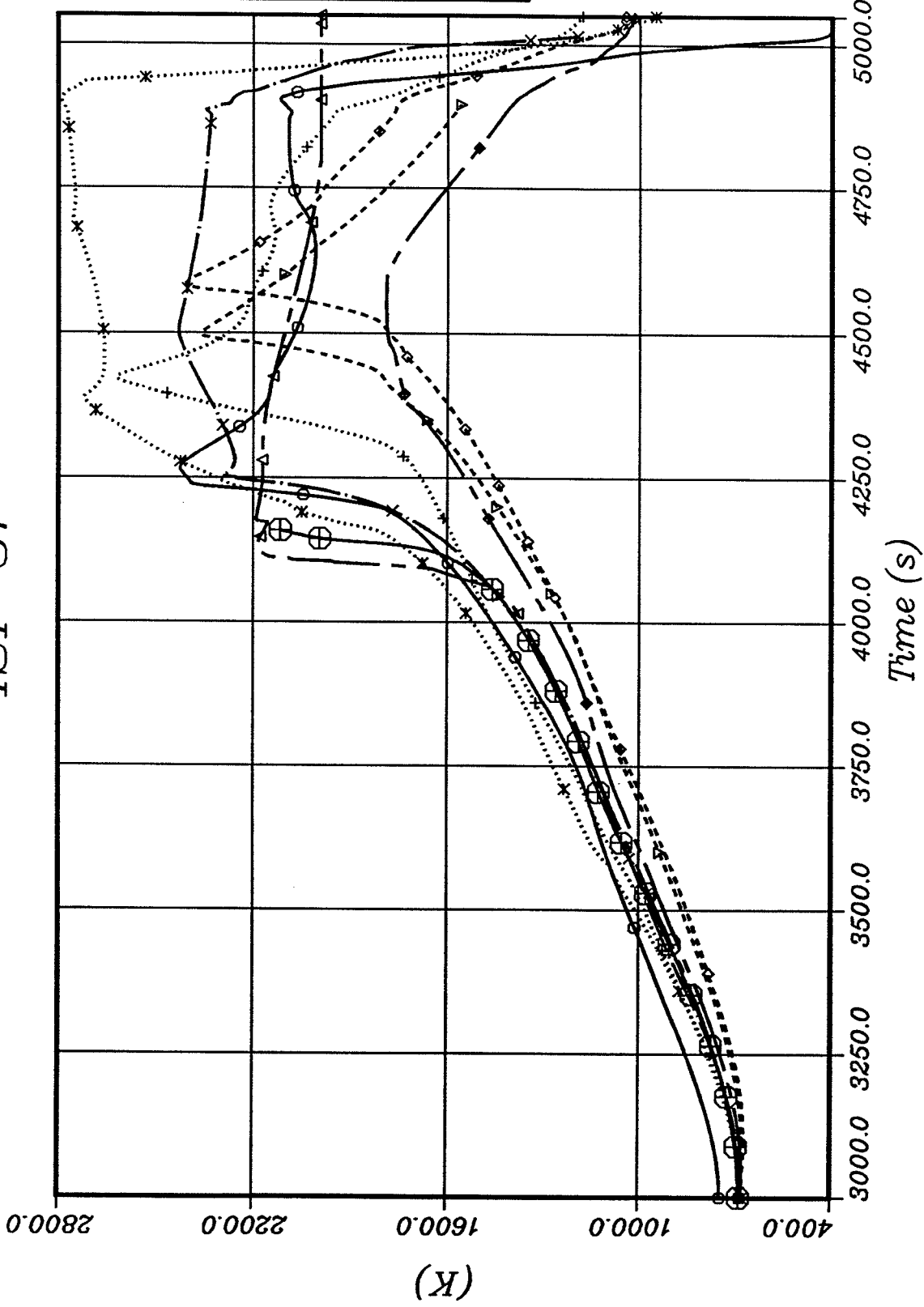


Figure 4.11: Fuel Temperature, First Ring (TU1R 0550)

GRS

ISP 31



LEGEND

○	AEA
△	CEA
+	ECN
×	IKE
◇	JAE
▽	KAE
*	SNL
◆	VTT
⊕	EXP

Figure 4.12: Fuel Temperature, Second Ring (TU2R 0750)

ISP 31

GRS

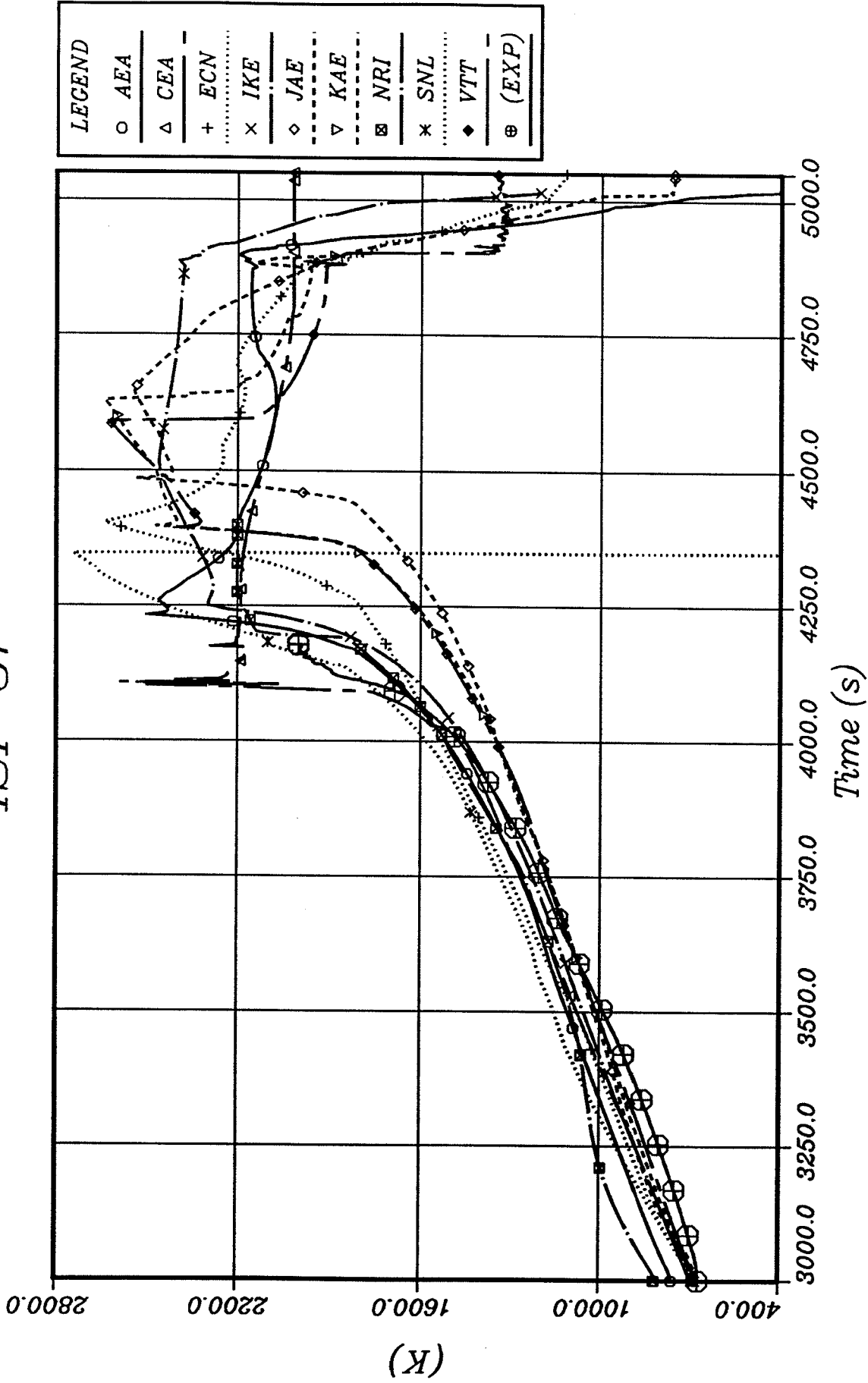


Figure 4.13: Cladding Temperature, First Ring (TC1R 0750)

ISP 31

GRS

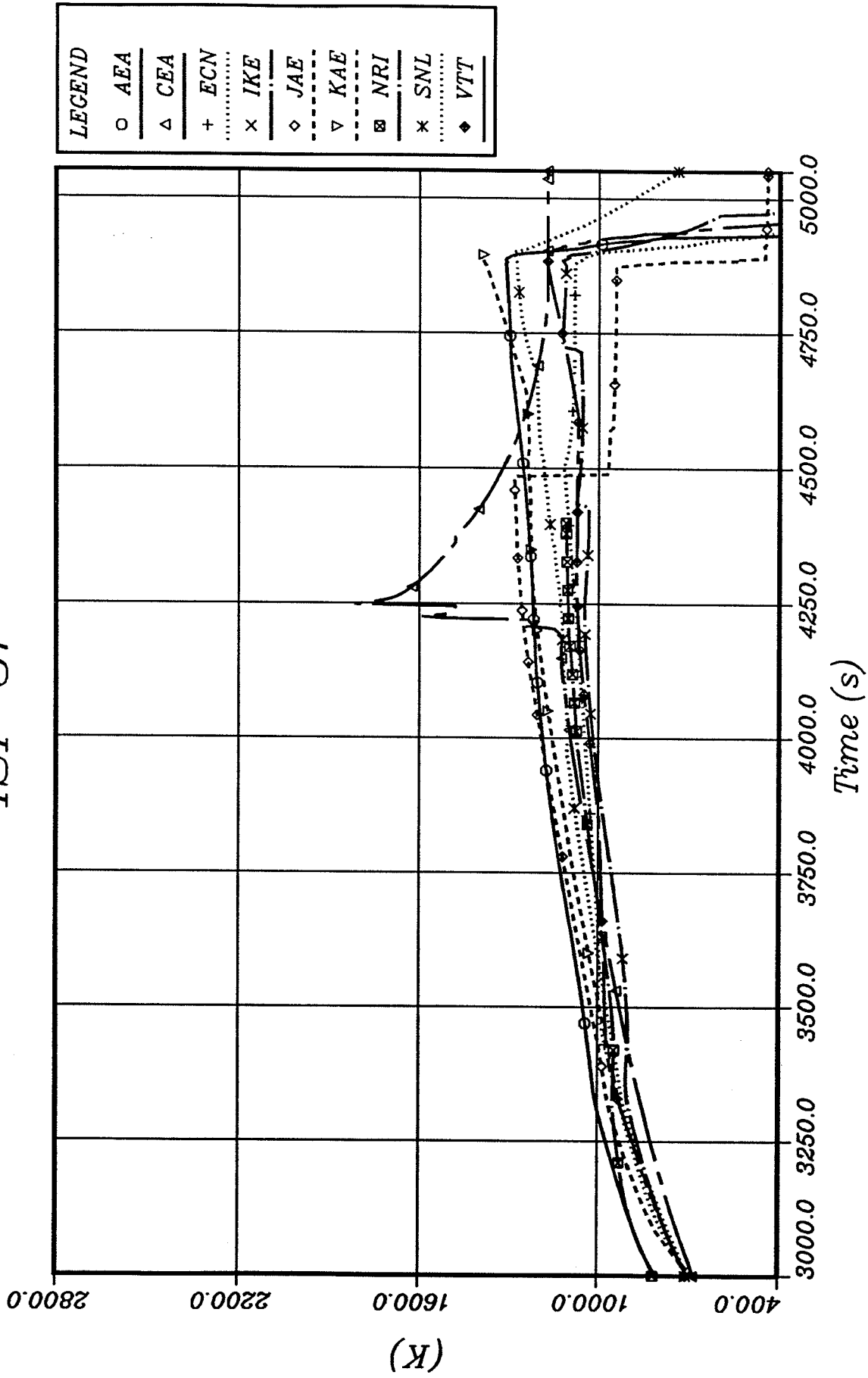
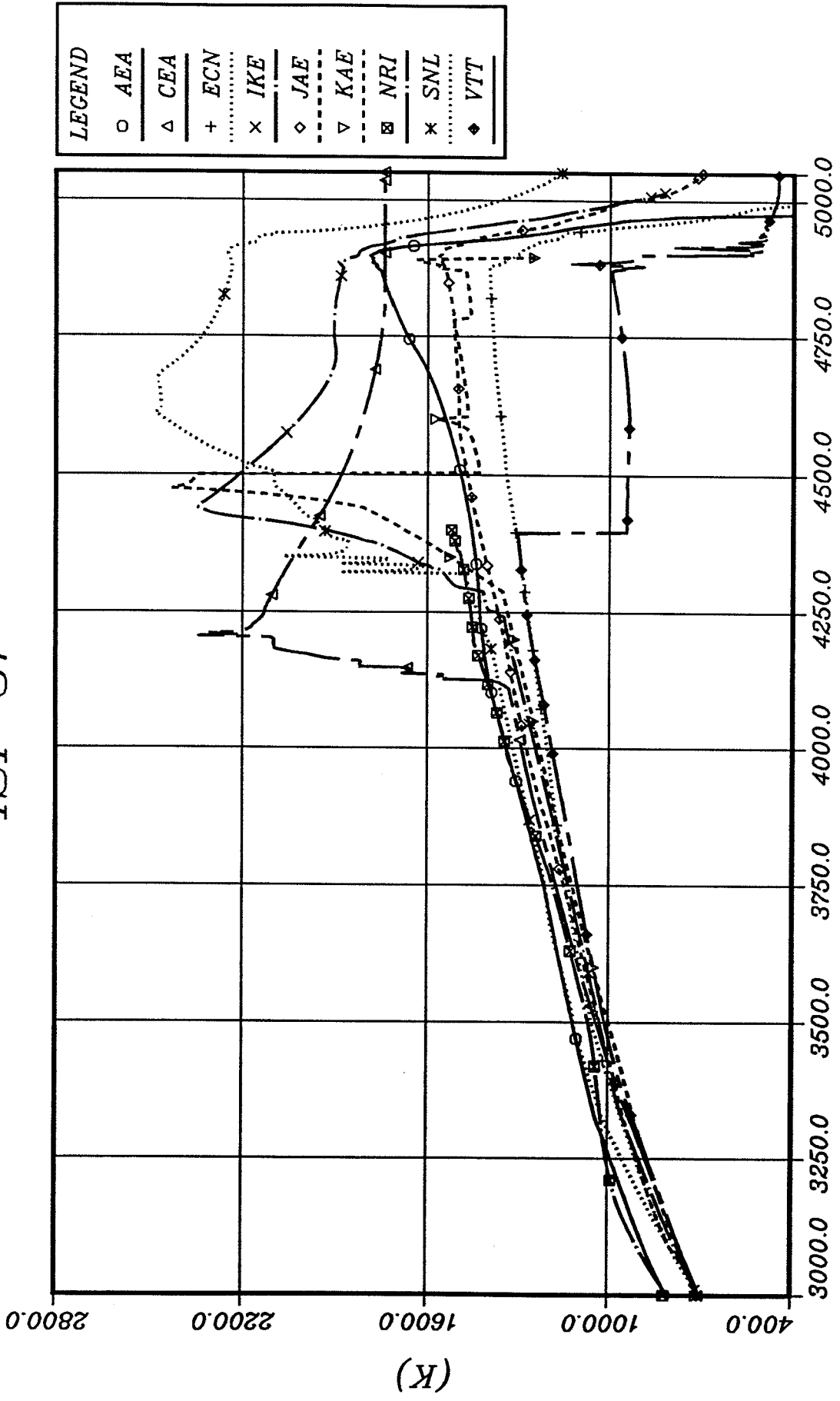


Figure 4.14: Cladding Temperature, First Ring (TC1R 0050)



LEGEND

○	AEA
△	CEA
+	ECN
×	IKE
◇	JAE
▽	KAE
⊠	NRI
*	SNL
◆	VTT

Figure 4.15: Cladding Temperature, First Ring (TC1R 0350)

ISP 31

GRS

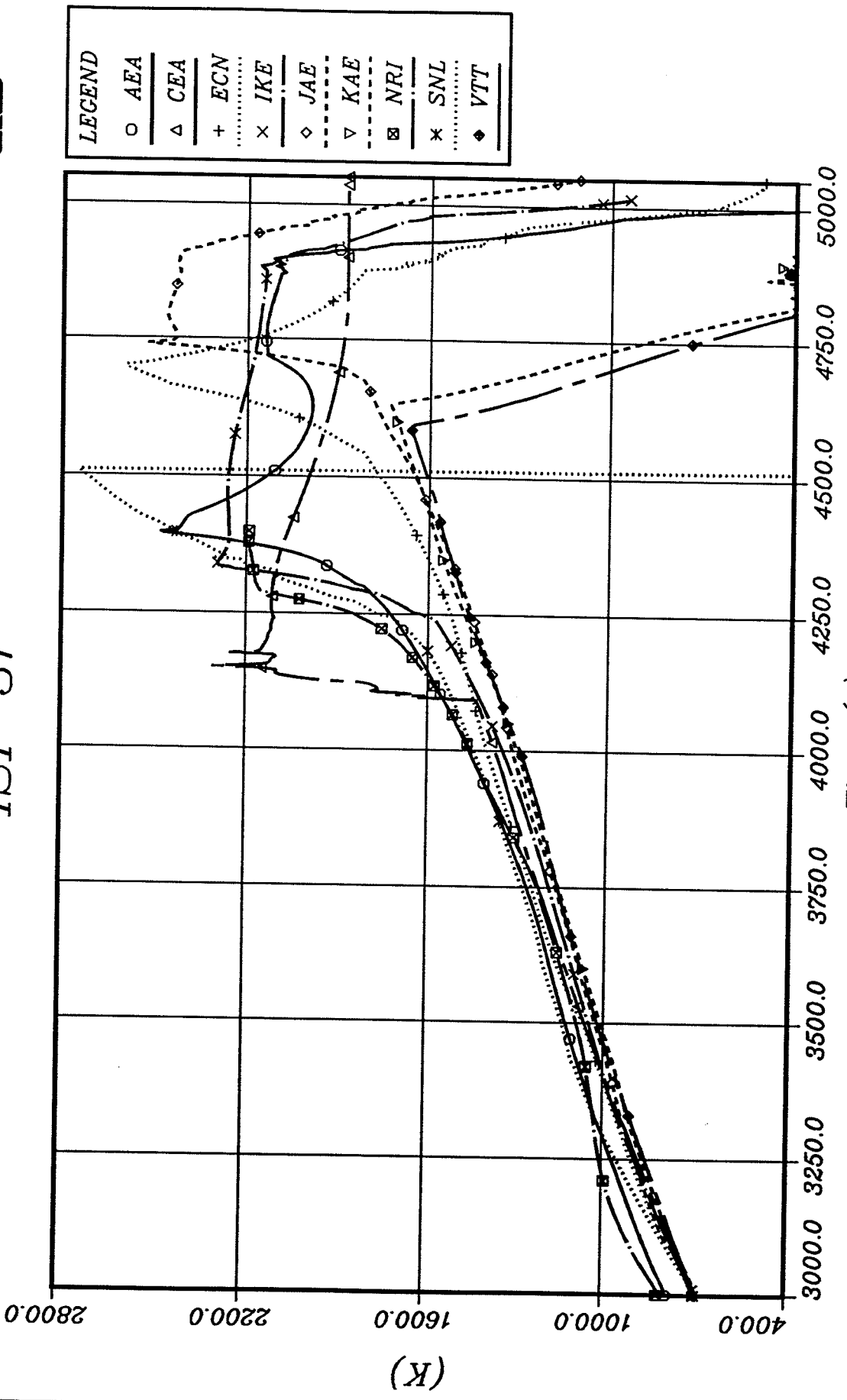


Figure 4.16: Cladding Temperature, First Ring (TC1R 0550)

ISP 31

GRS

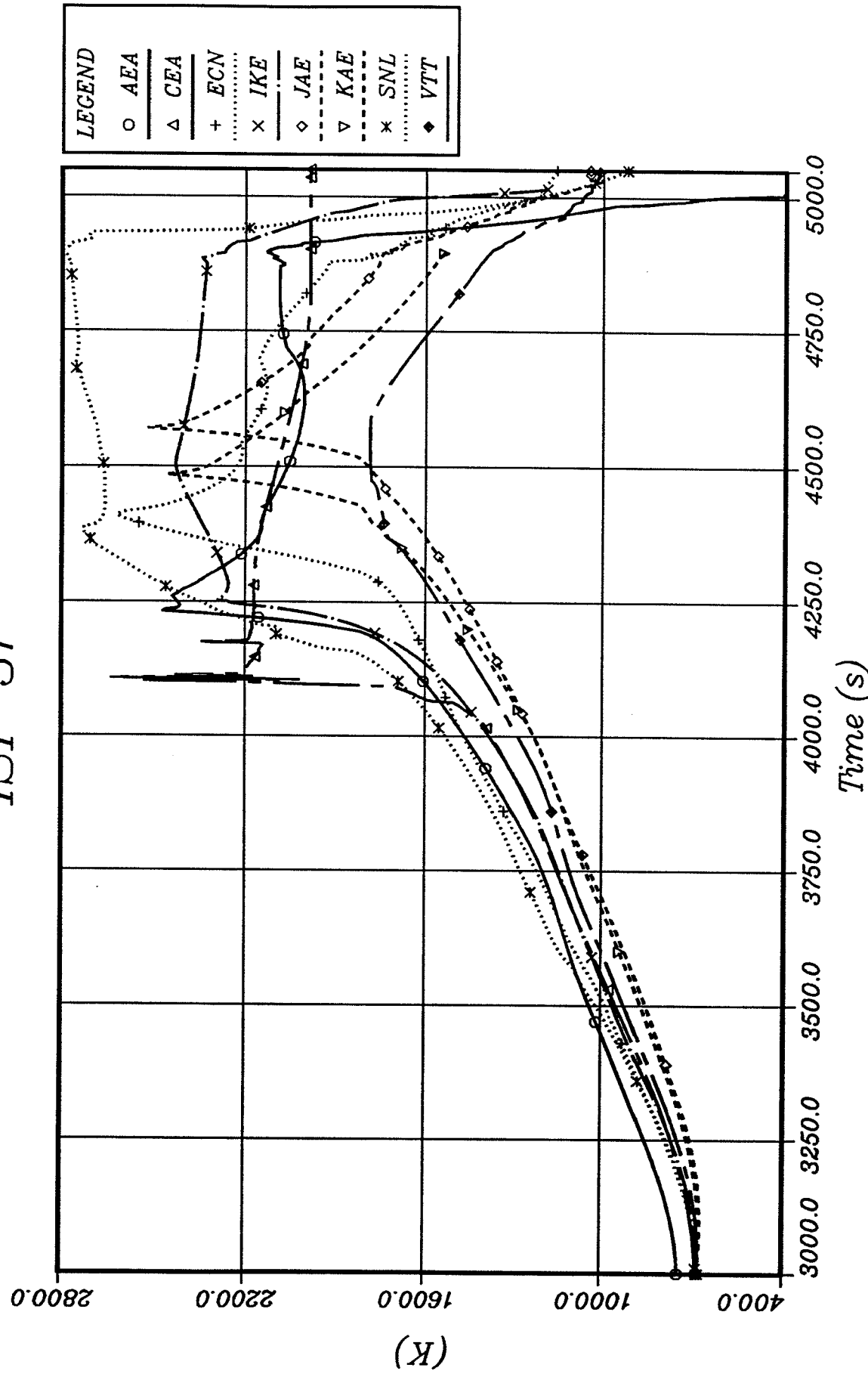


Figure 4.17: Cladding Temperature, Second Ring (TC2R 0750)

ISP 31

GRS

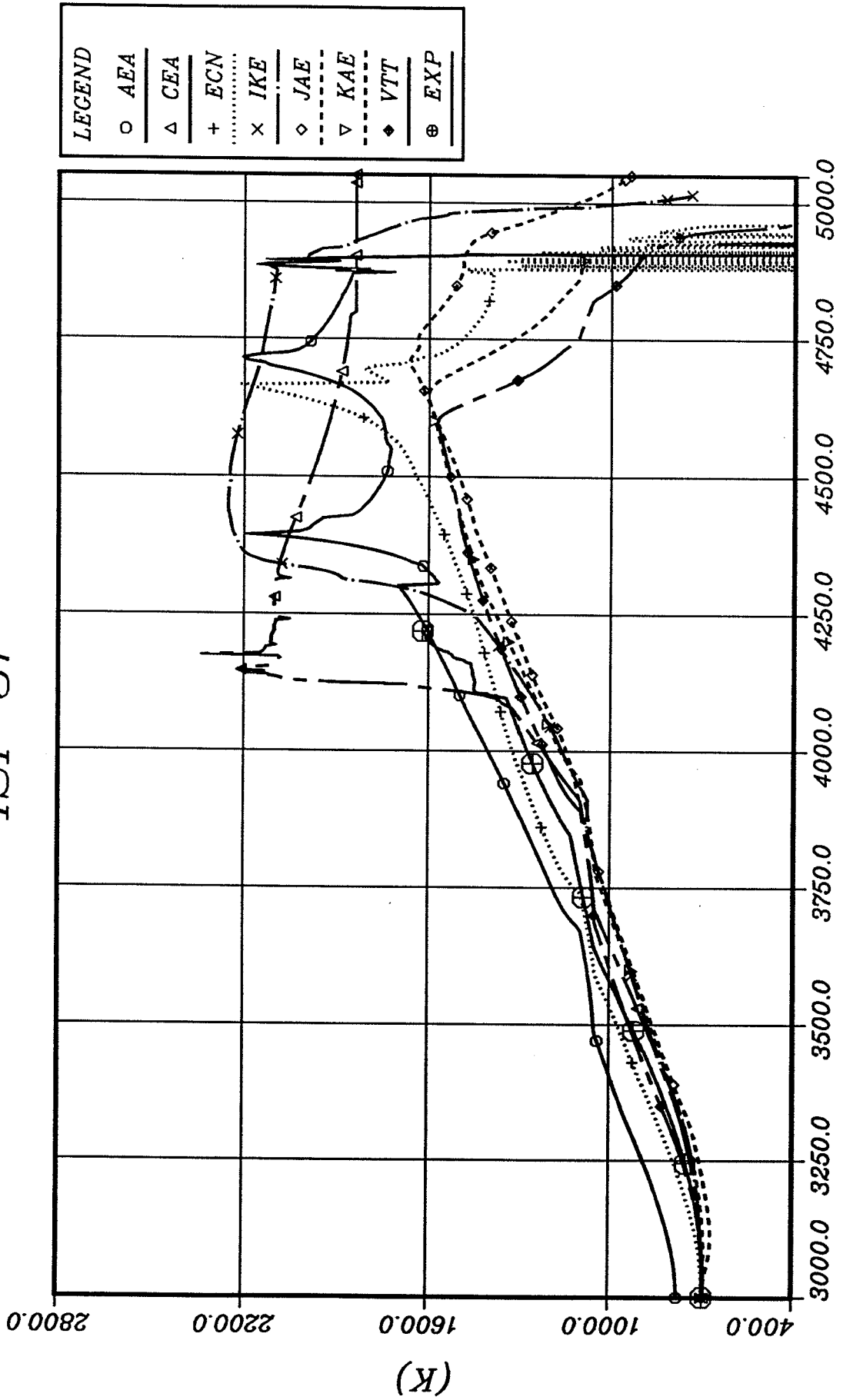


Figure 4.18: Absorber Temperature (TAIC 0550)

ISP 31

GRS

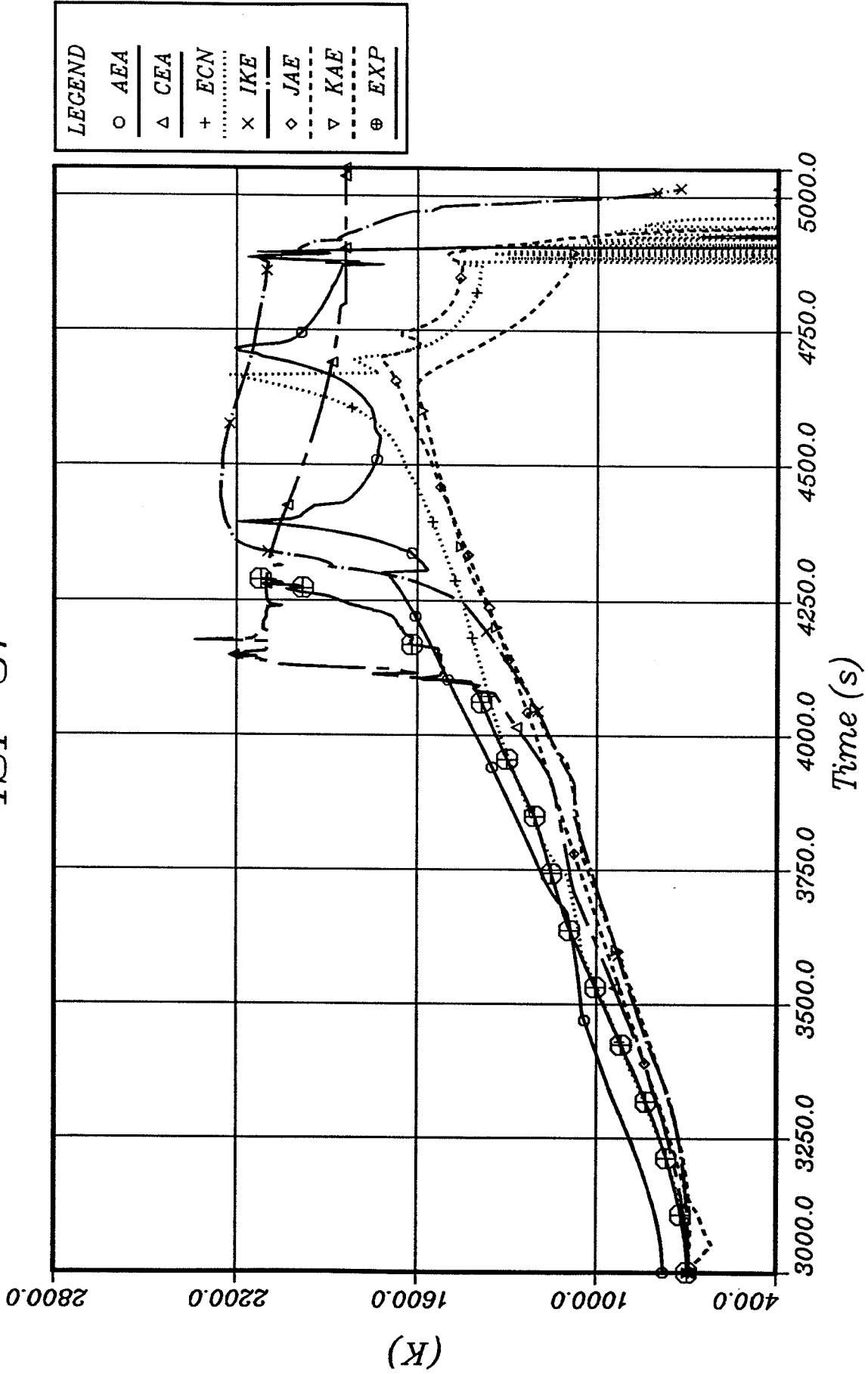


Figure 4.19: Guide Tube Temperature (TECT 0550)

GRS

ISP 31

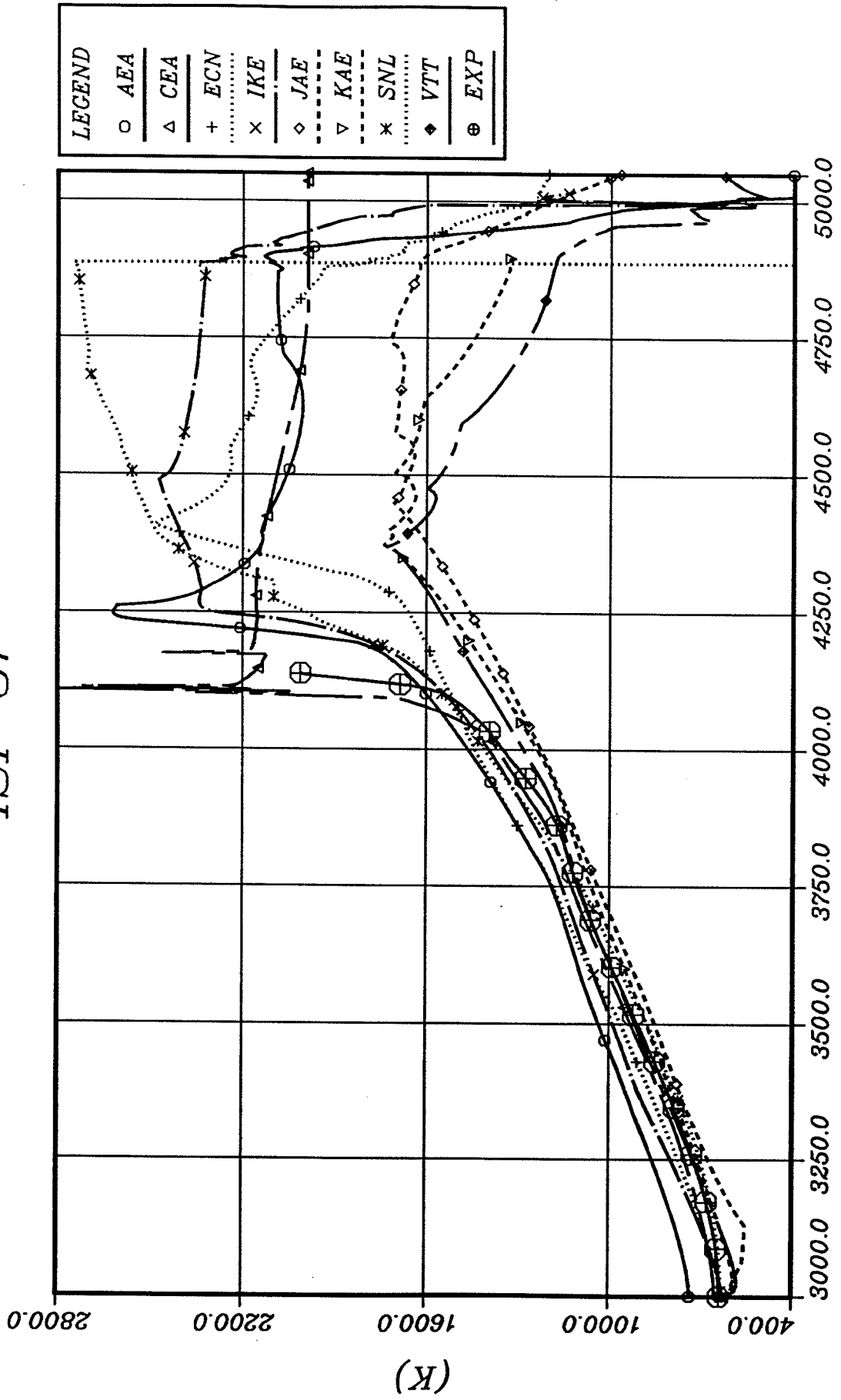


Figure 4.20: Shroud Temperature (TESH 0750)

ISP 31

GRS

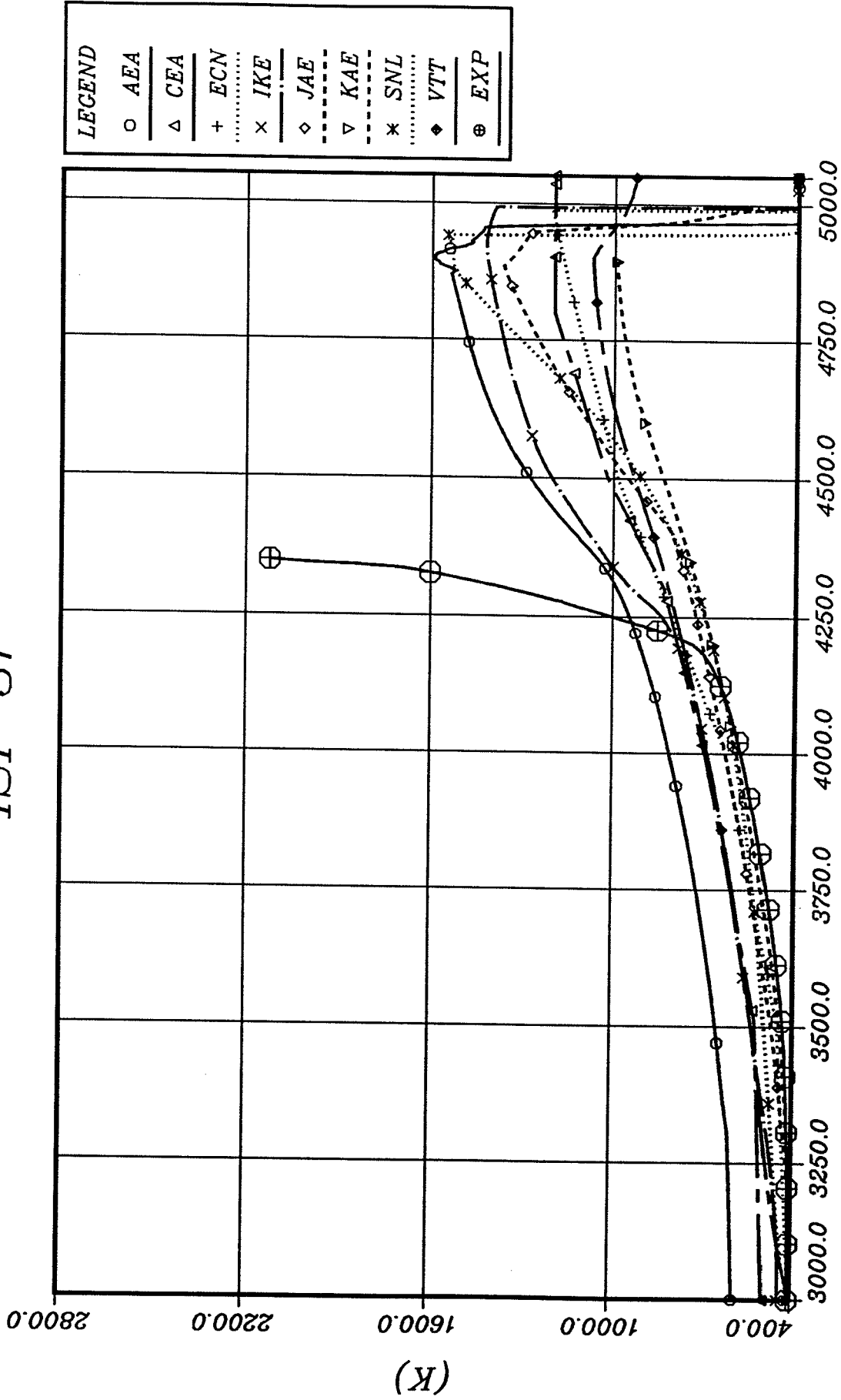


Figure 4.21: Outer Insulation Temperature (TEIO 0750)

ISP 31

GRS

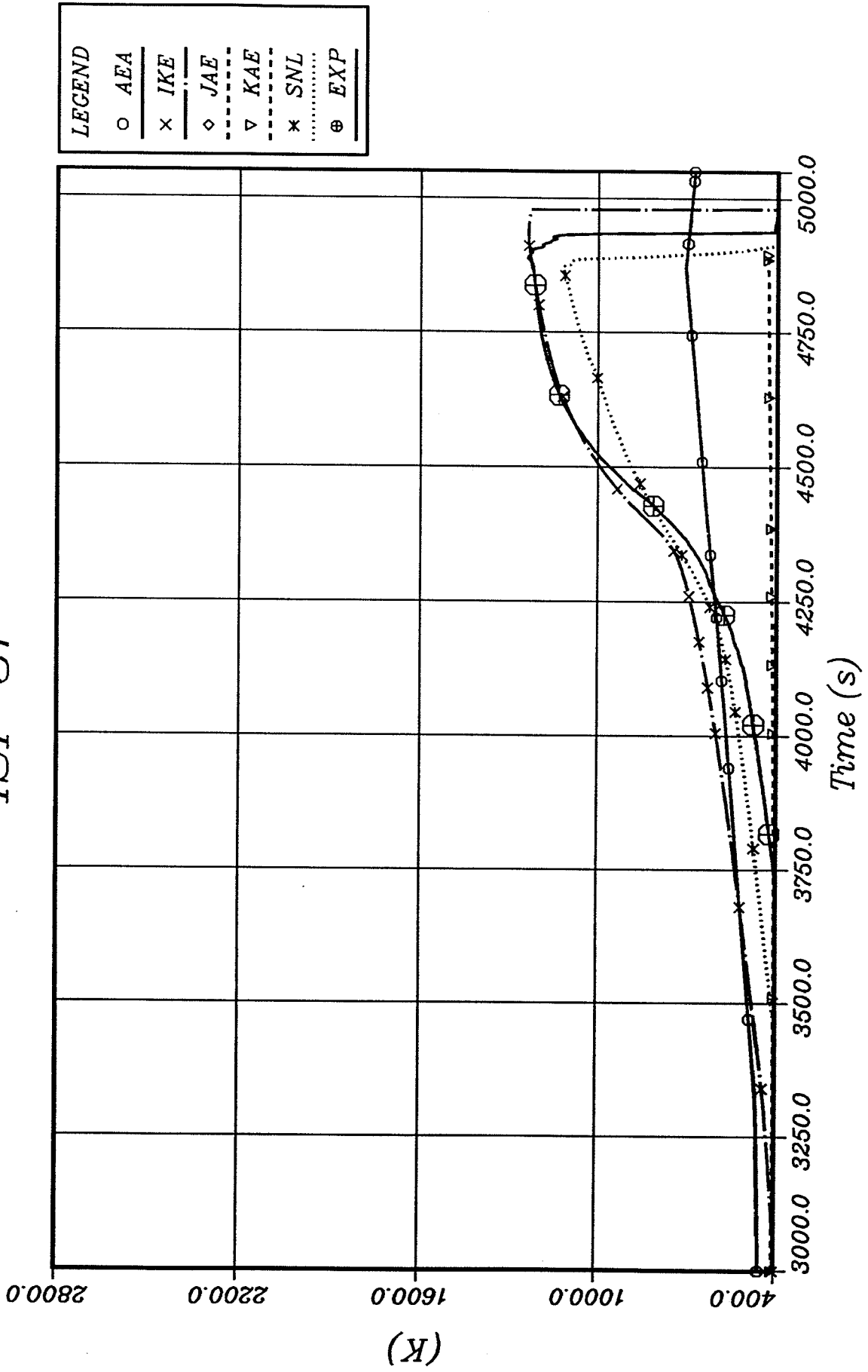


Figure 4.22: Inner HTS Temperature (TEHI 0550)

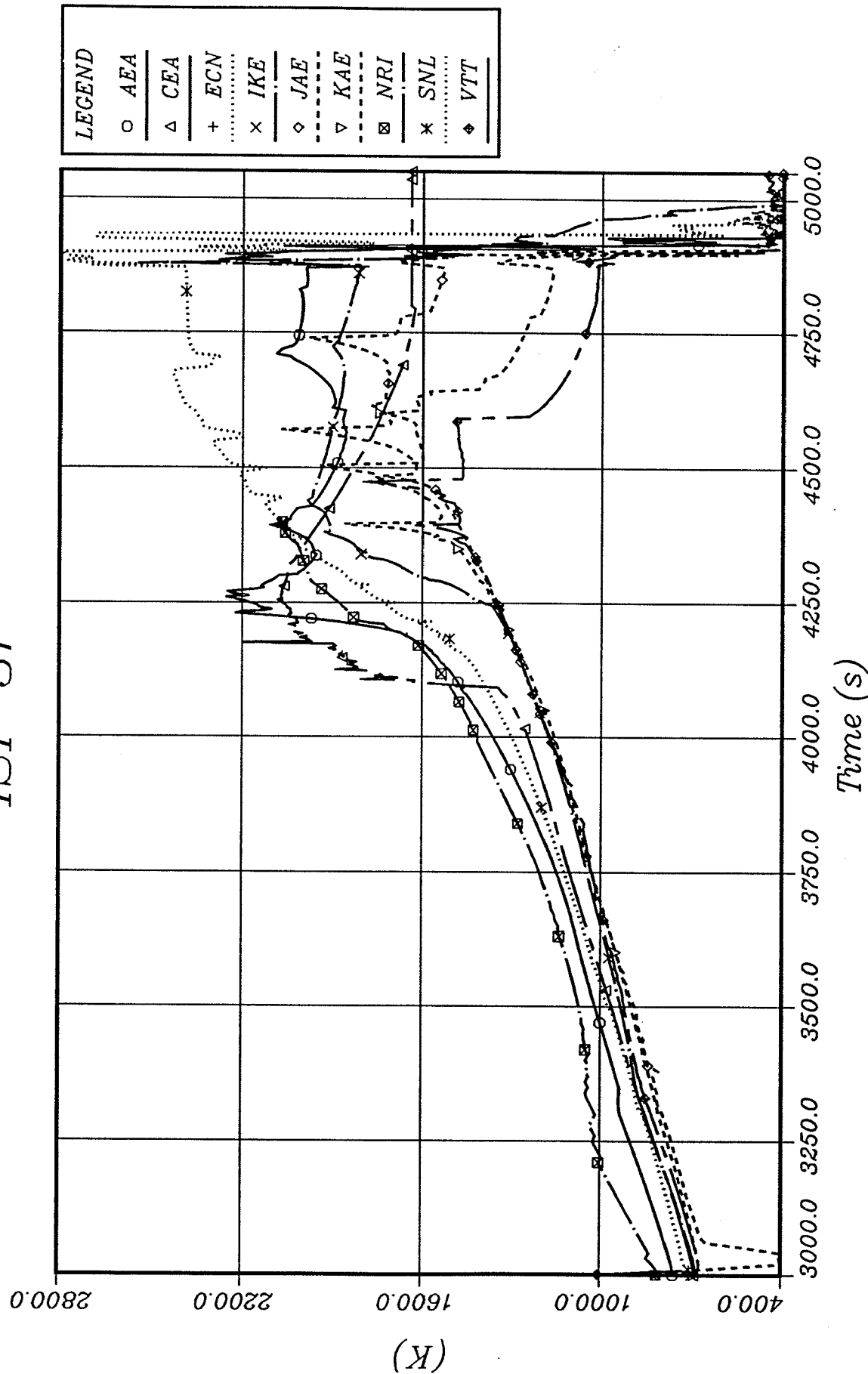


Figure 4.23: Fluid Temperature (TEFLO 0750)

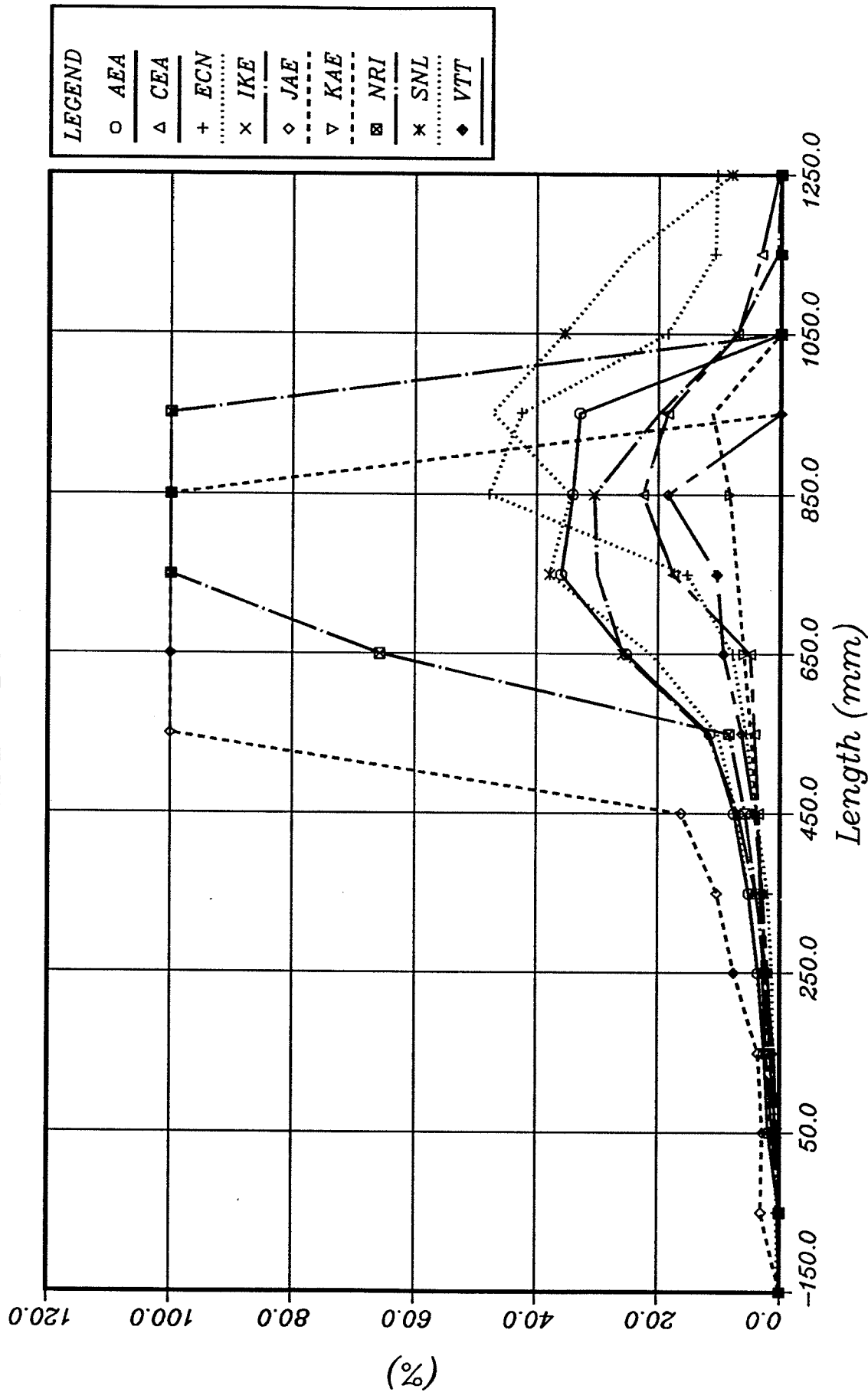


Figure 4.24: ZrO2, First Ring (Z01R 4250), t=4250 s

ISP 31

GRS

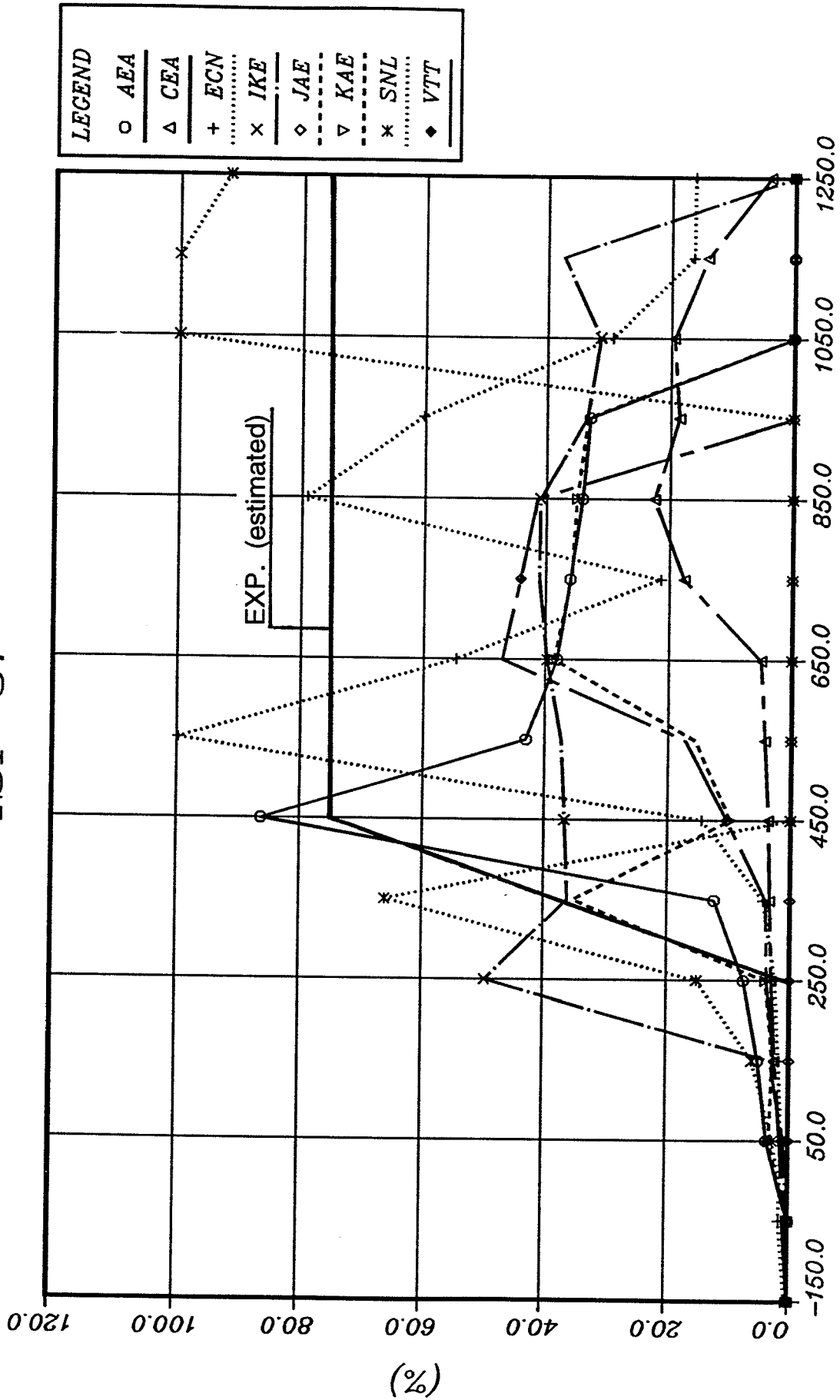


Figure 4.25: ZrO<sub>2</sub>, First Ring (Z01R 4750)

ISP 31

GRS

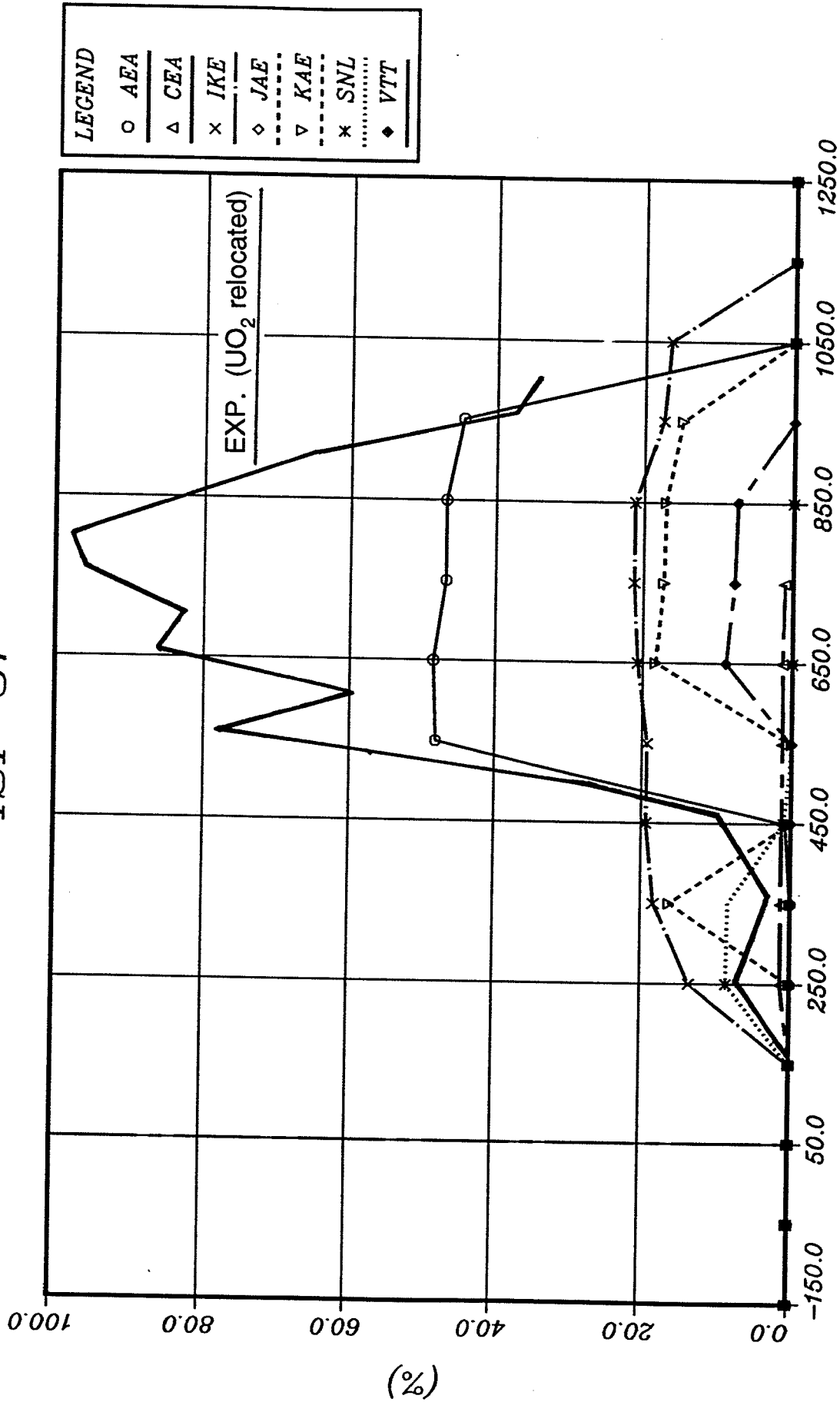


Figure 4.26: UO<sub>2</sub> Dissolved, First Ring (UD1R 4750)

ISP 31

GRS

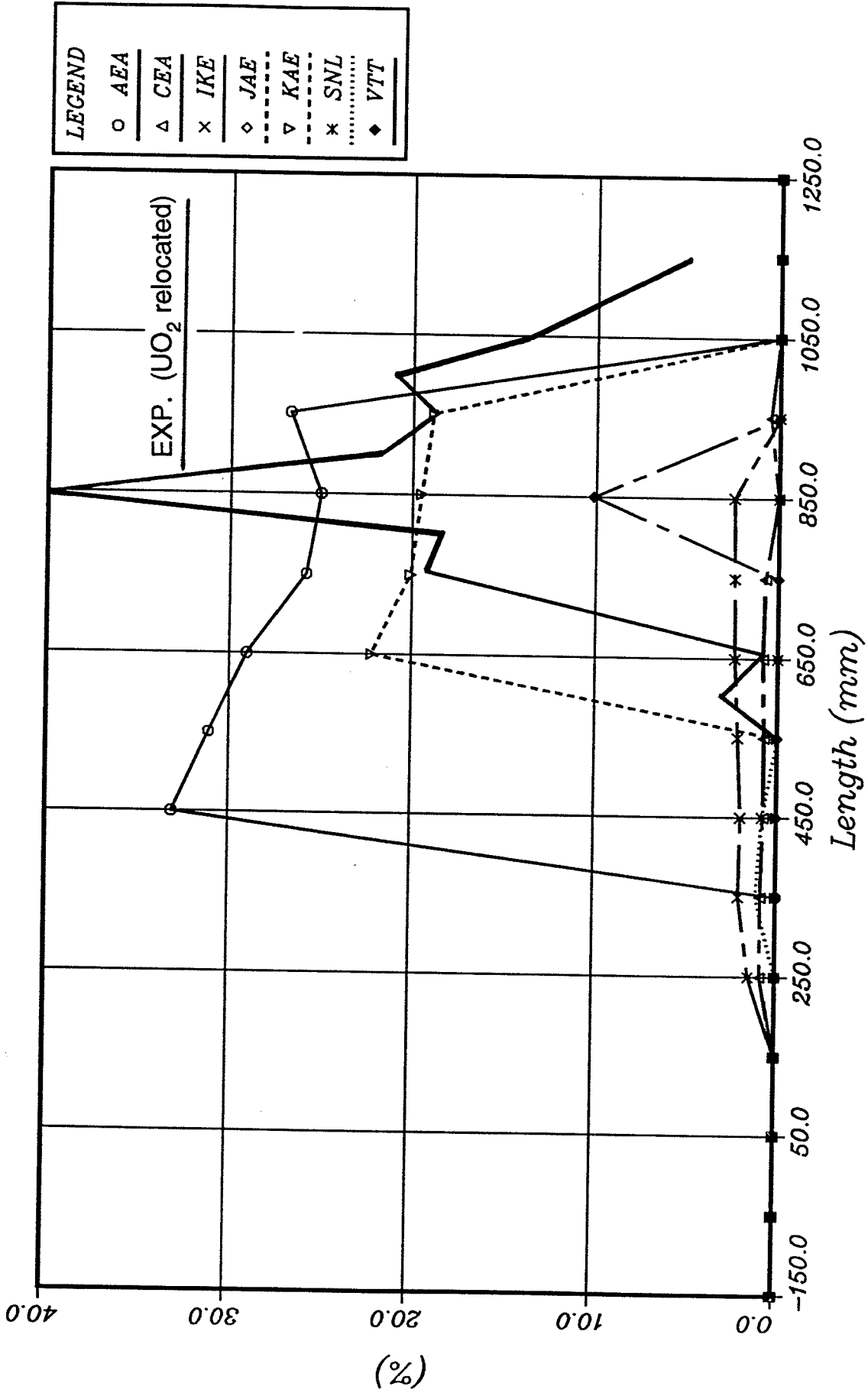


Figure 4.27: UO<sub>2</sub> Dissolved, Second Ring (UD2R 4750)

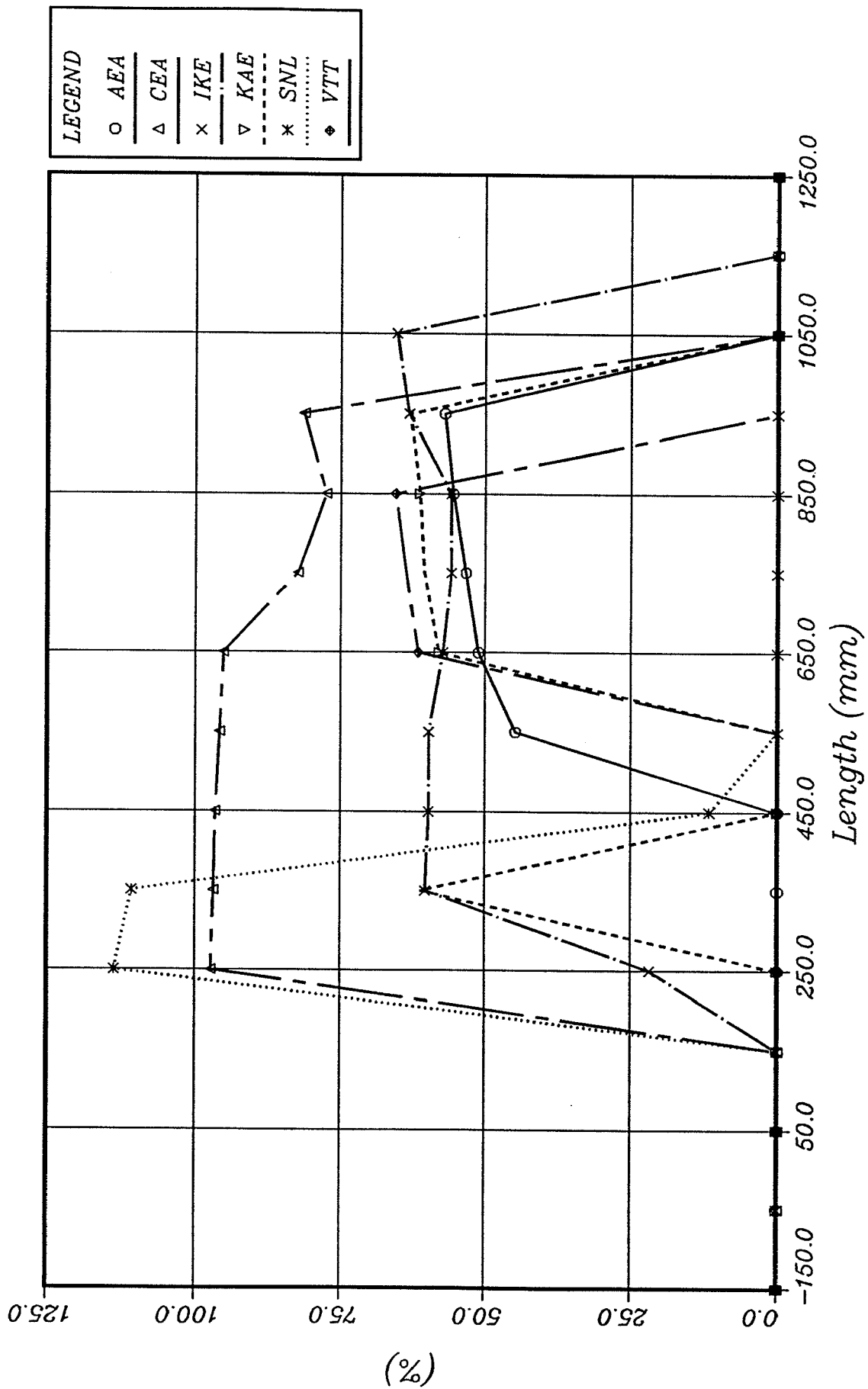


Figure 4.28: Zirkaloy Molten, First Ring (ZM1R 4750)

GRS

ISP 31

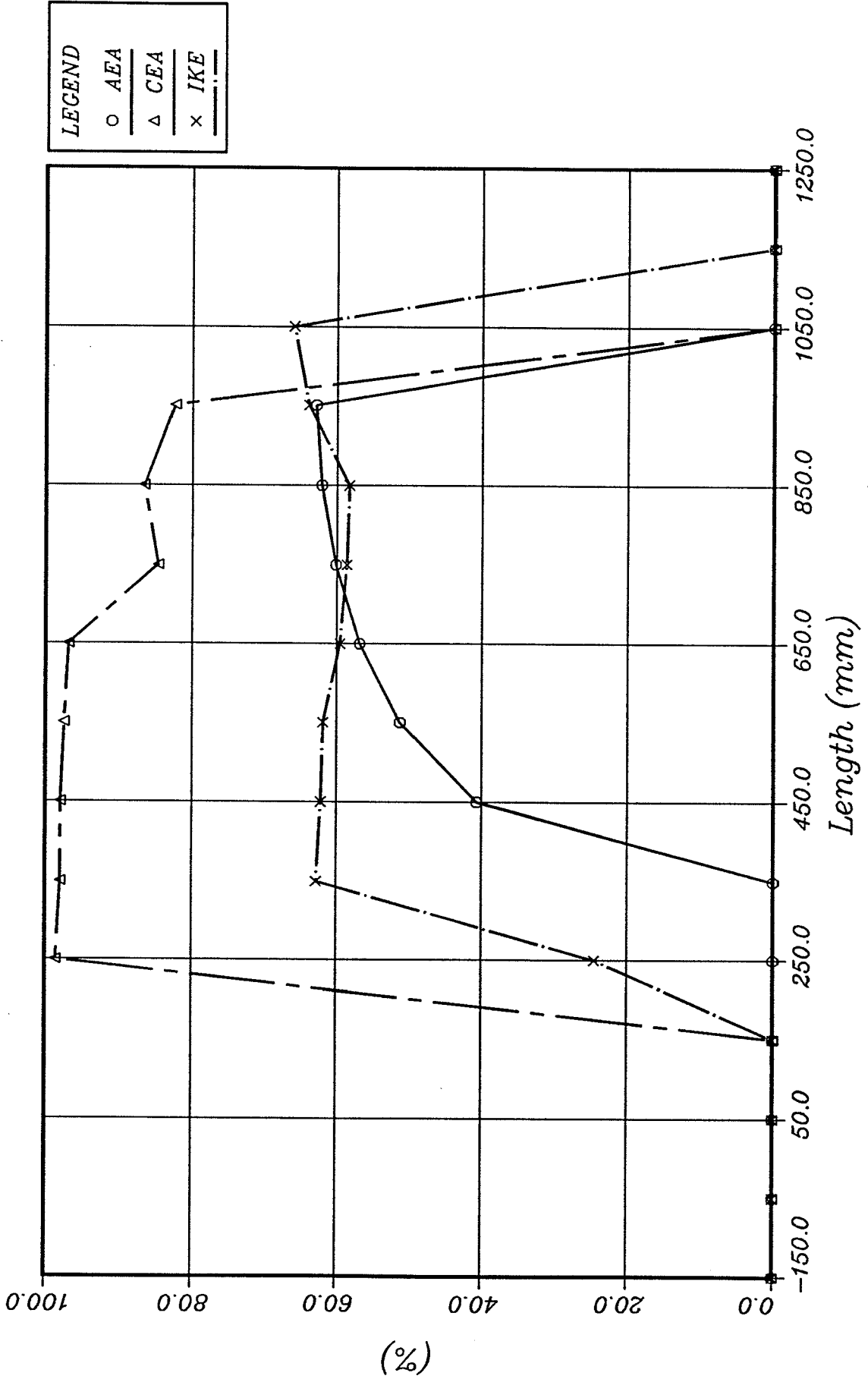


Figure 4.29: Zirkaloy Molten, Second Ring (ZM2R 4750)

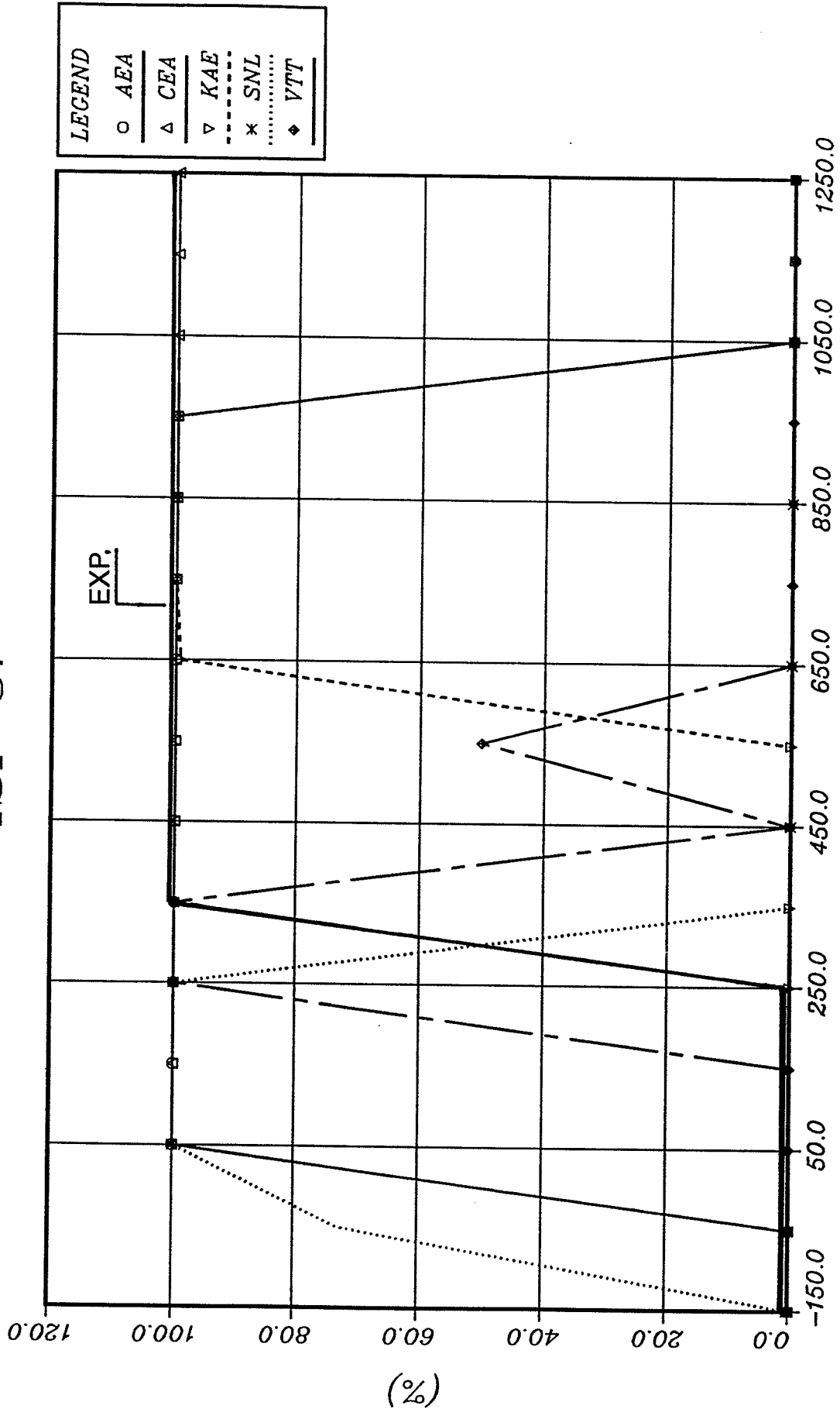
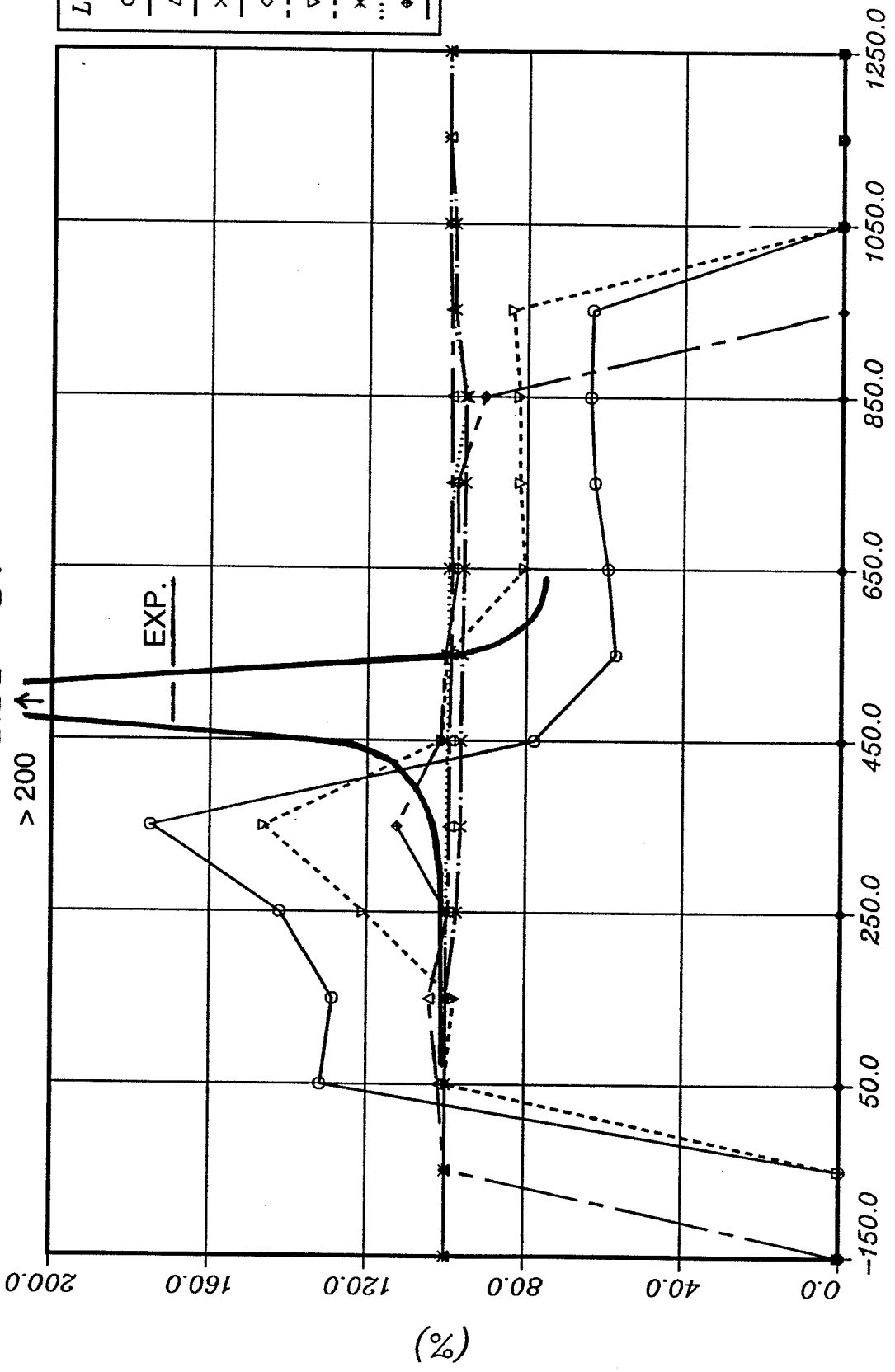


Figure 4.30: AIC Liquefied (AICL 4750)

GRS

ISP 31



LEGEND

○	AEA
△	CEA
×	IKE
◇	JAE
▽	KAE
*	SNL
◆	VTT

Figure 4.31: U02 Total Mass

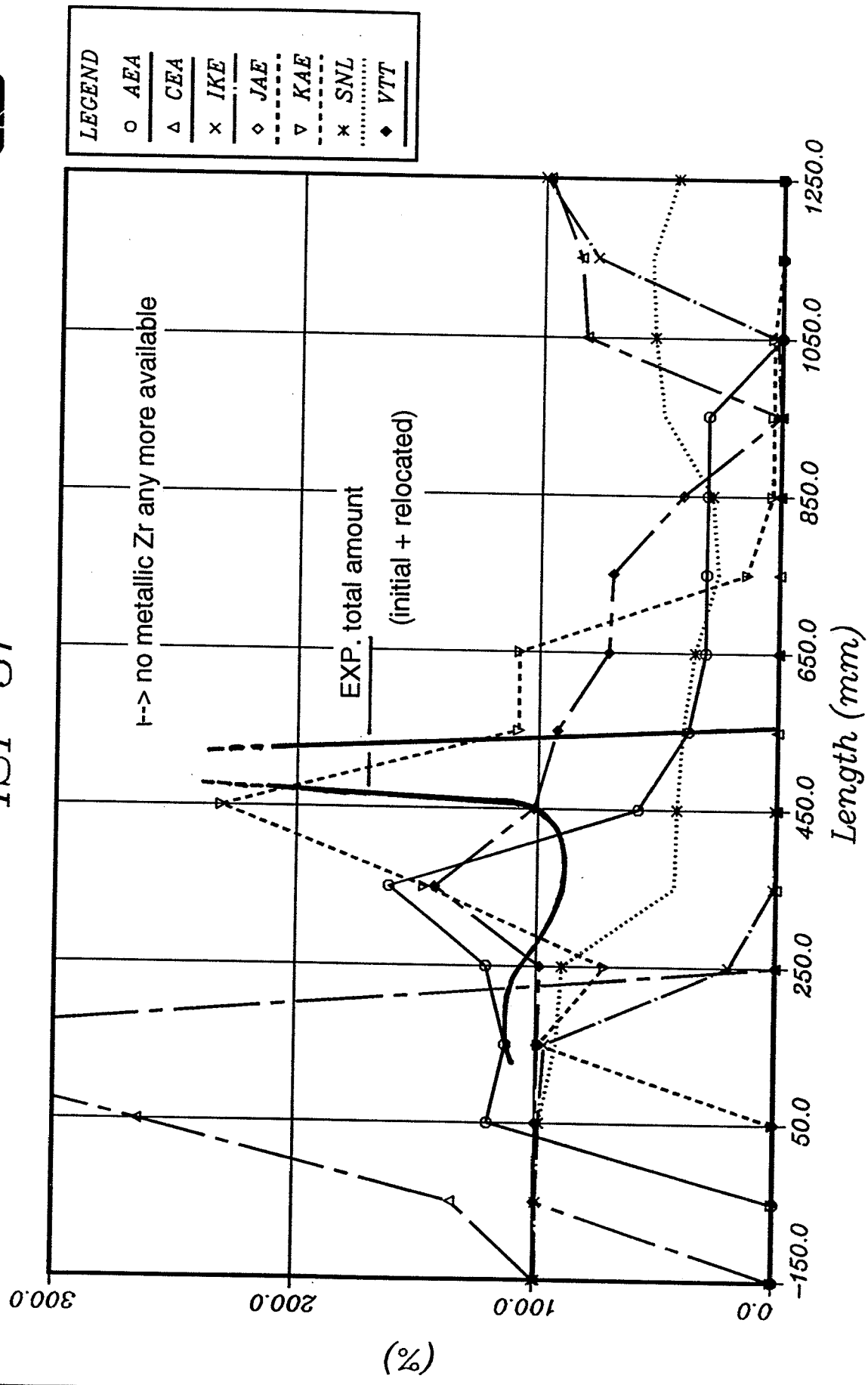


Figure 4.32: Metallic Zr Total Mass (ZRTM 4750)

ISP 31

GRS

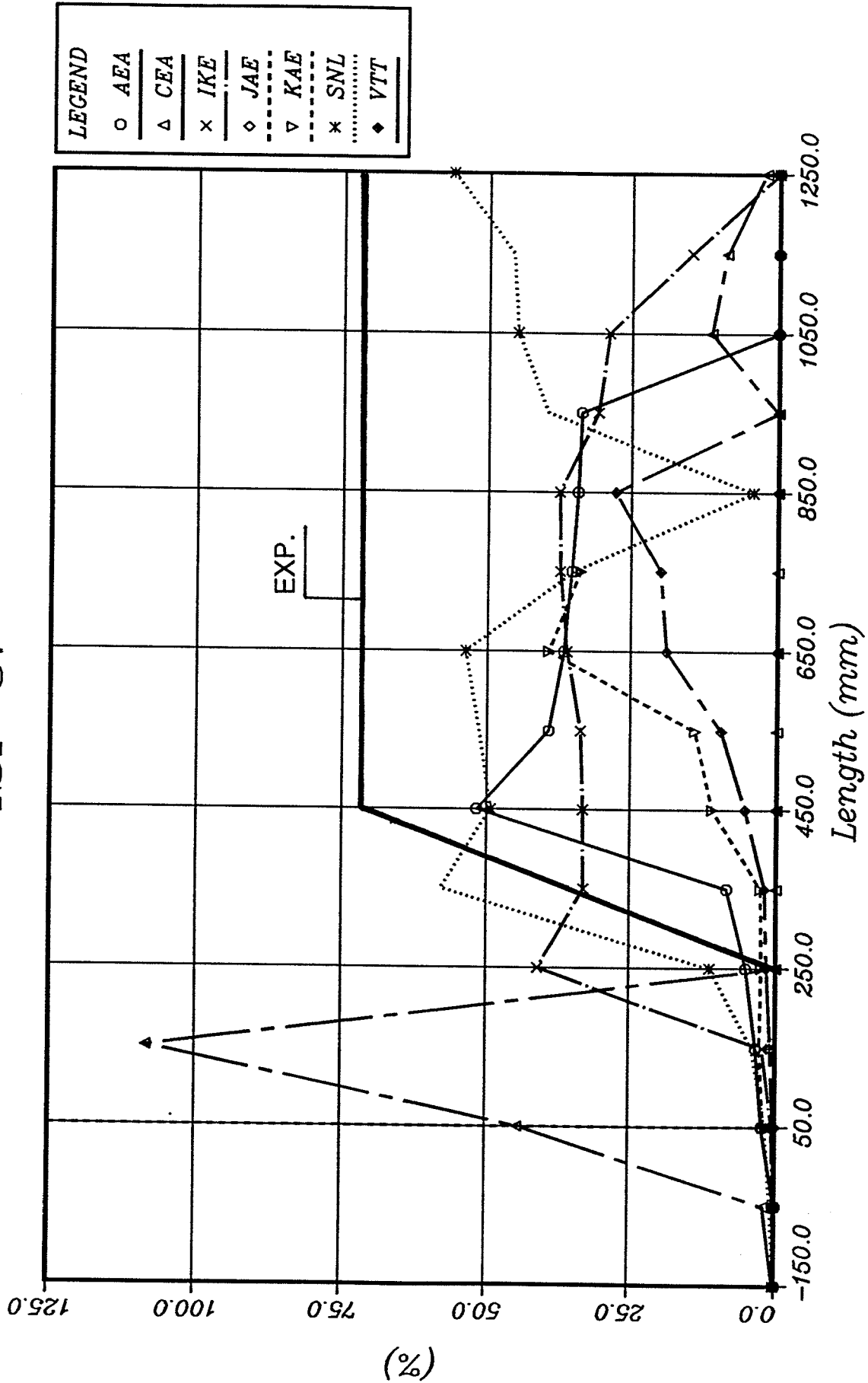


Figure 4.33: ZrO2 Total Mass (ZOTM 4750)

GRS

ISP 31

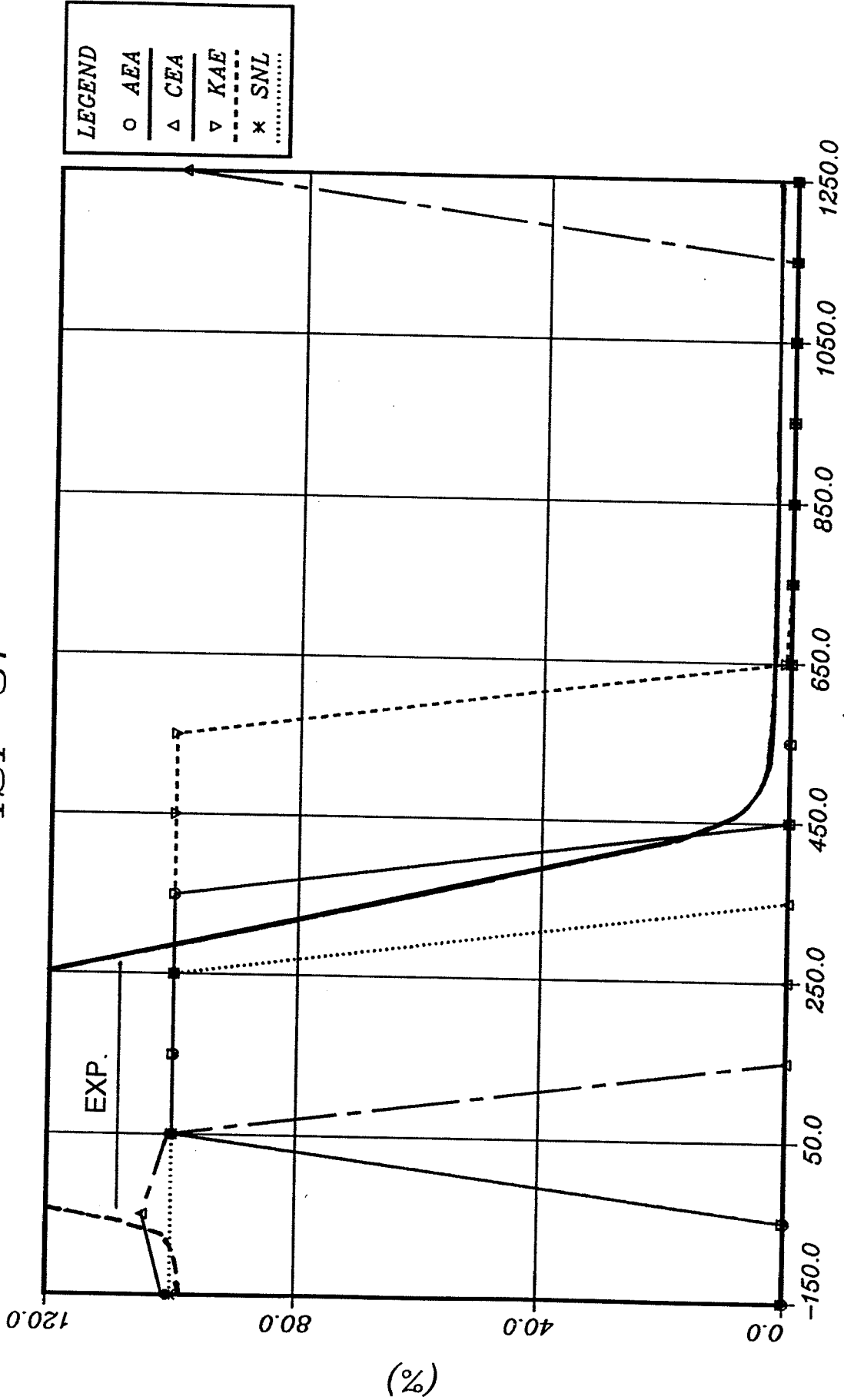
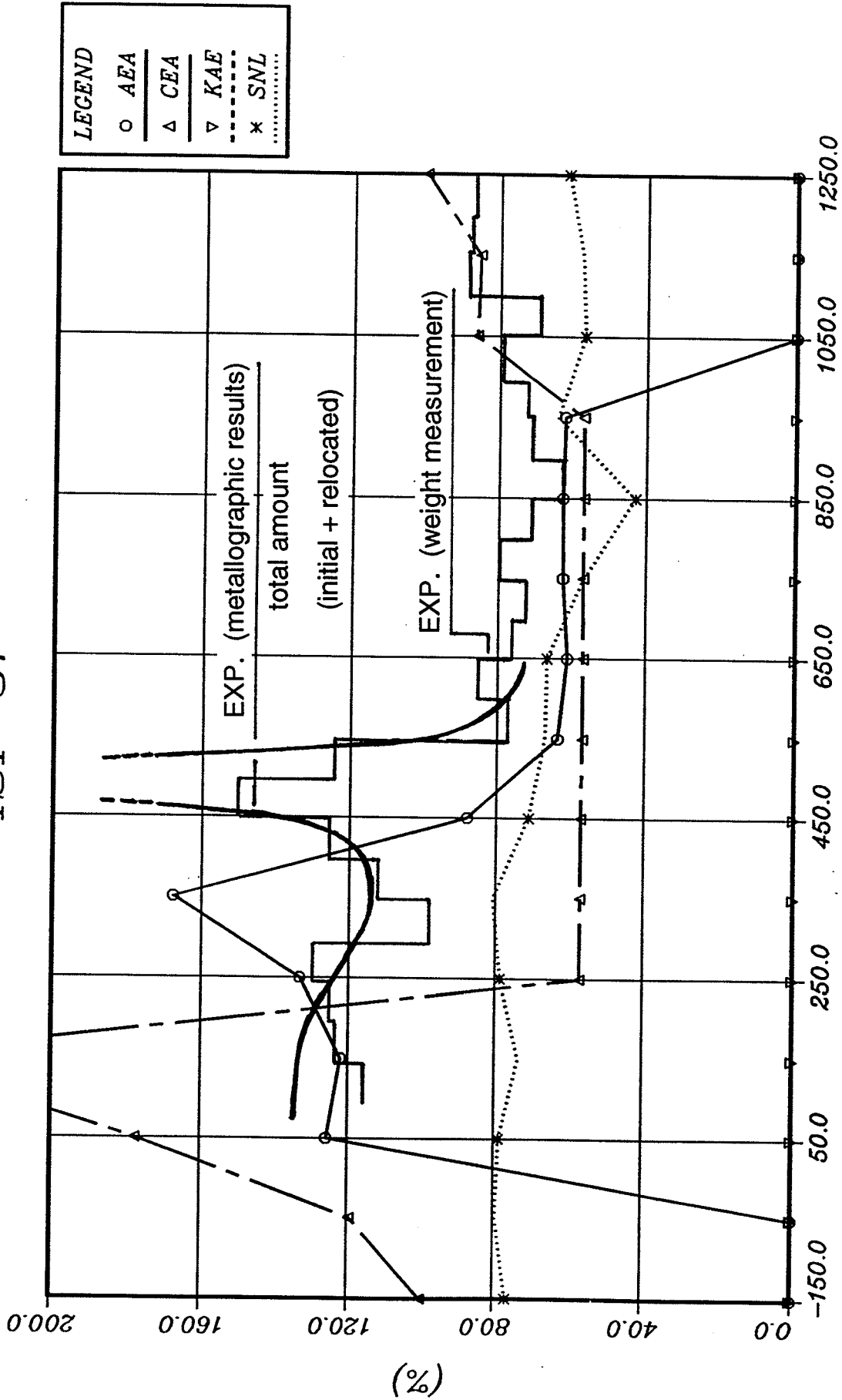


Figure 4.34: AIC Total Mass (AITM 4750)



Length (mm)  
Figure 4.35: Total Mass (UATM 4750)

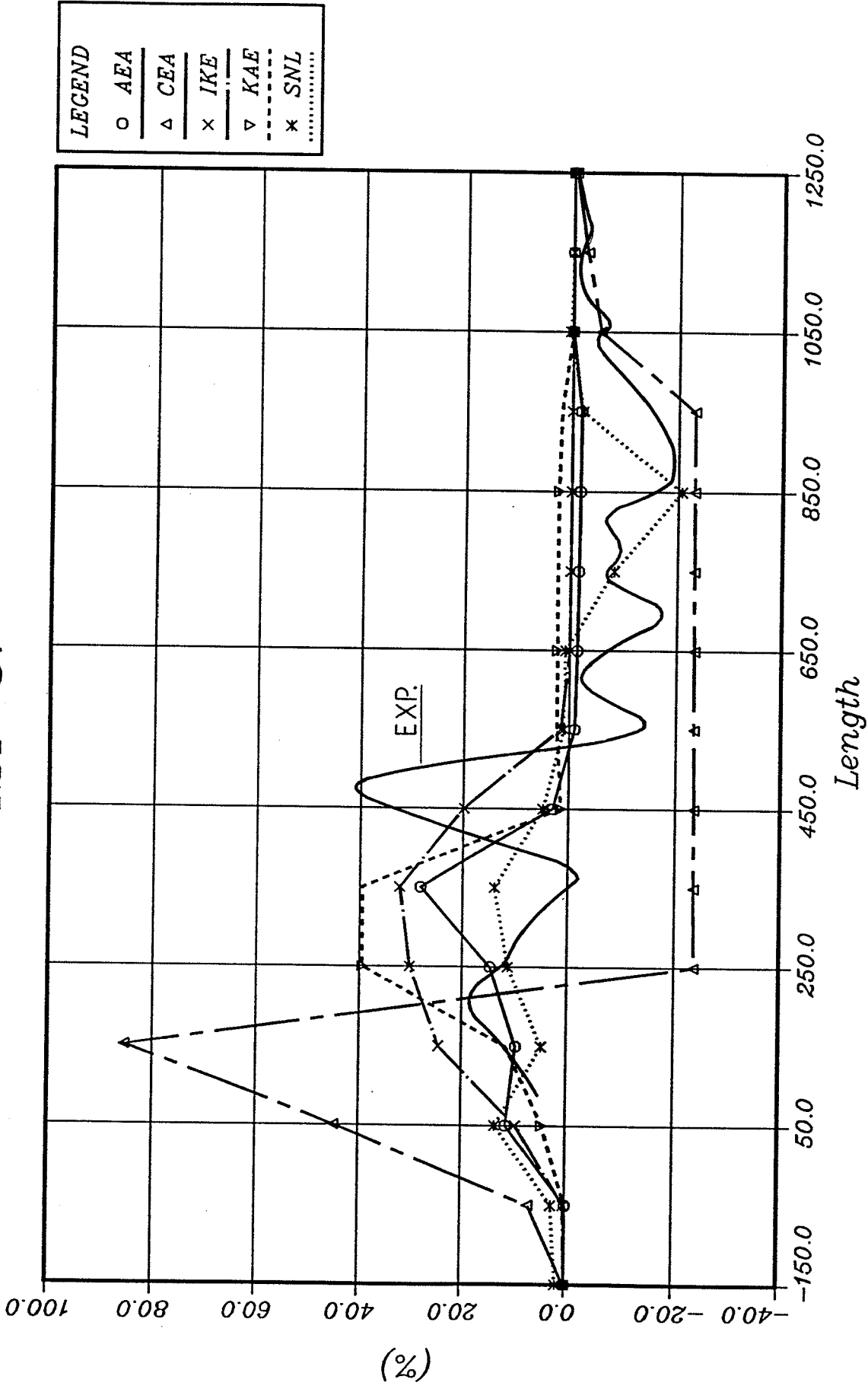


Figure 4.36: Core Blockage (COBK 4750)

ISP 31

GRS

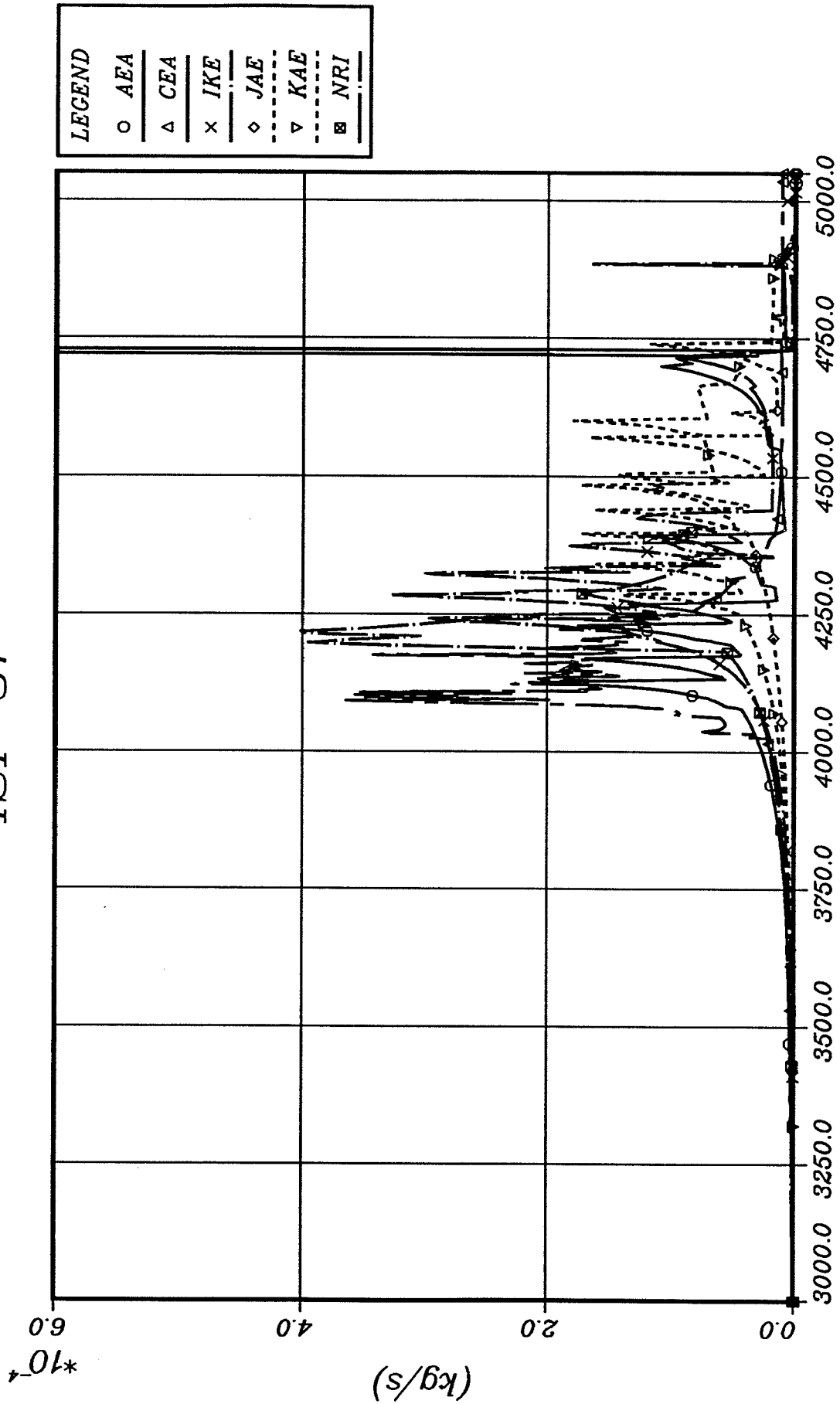


Figure 4.37: Hydrogen Generation Rate Bundle (HGRB)

ISP 31

GRS

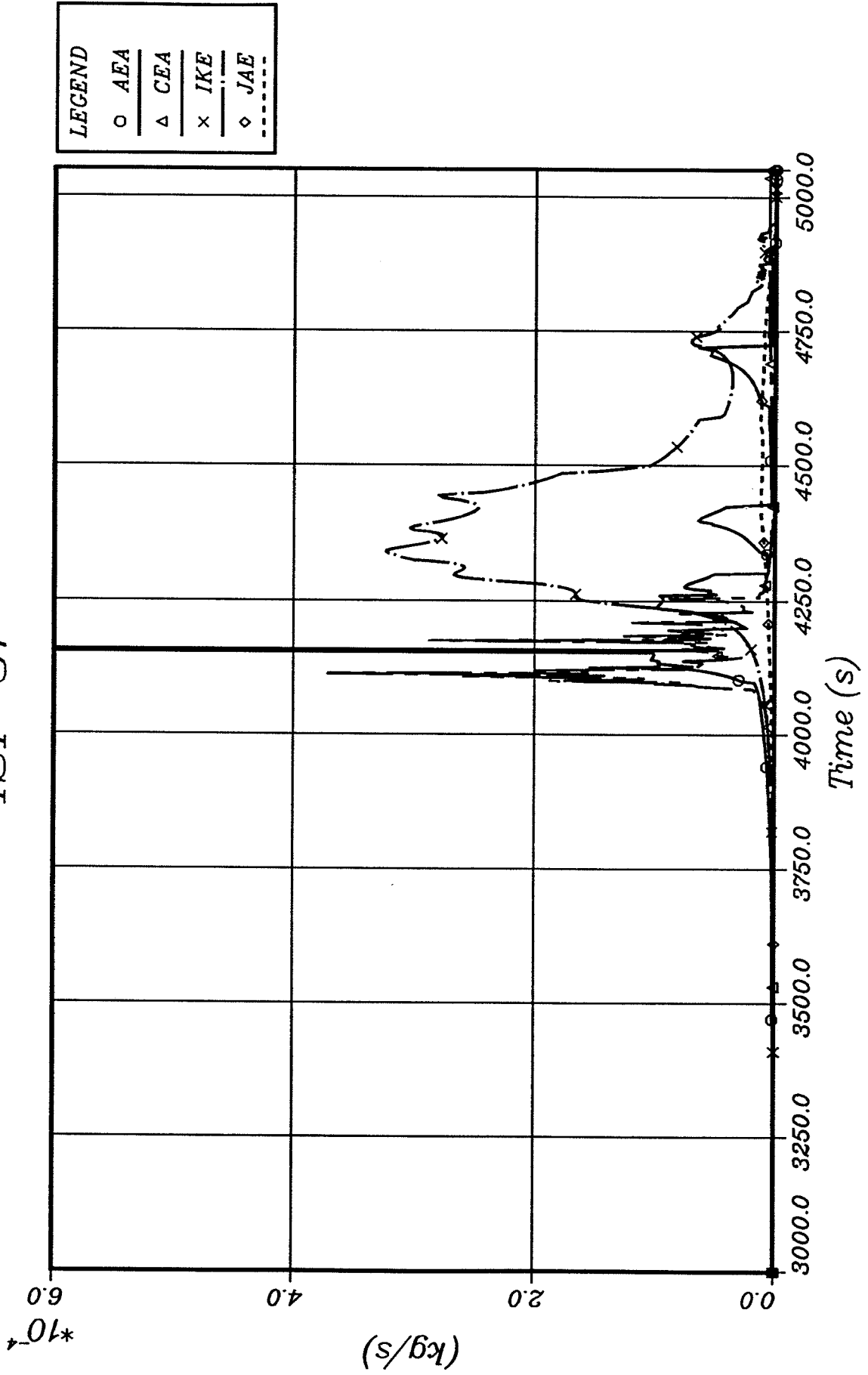


Figure 4.38: Hydrogen Generation Rate Shroud (HGRS)

ISP 31

GRS

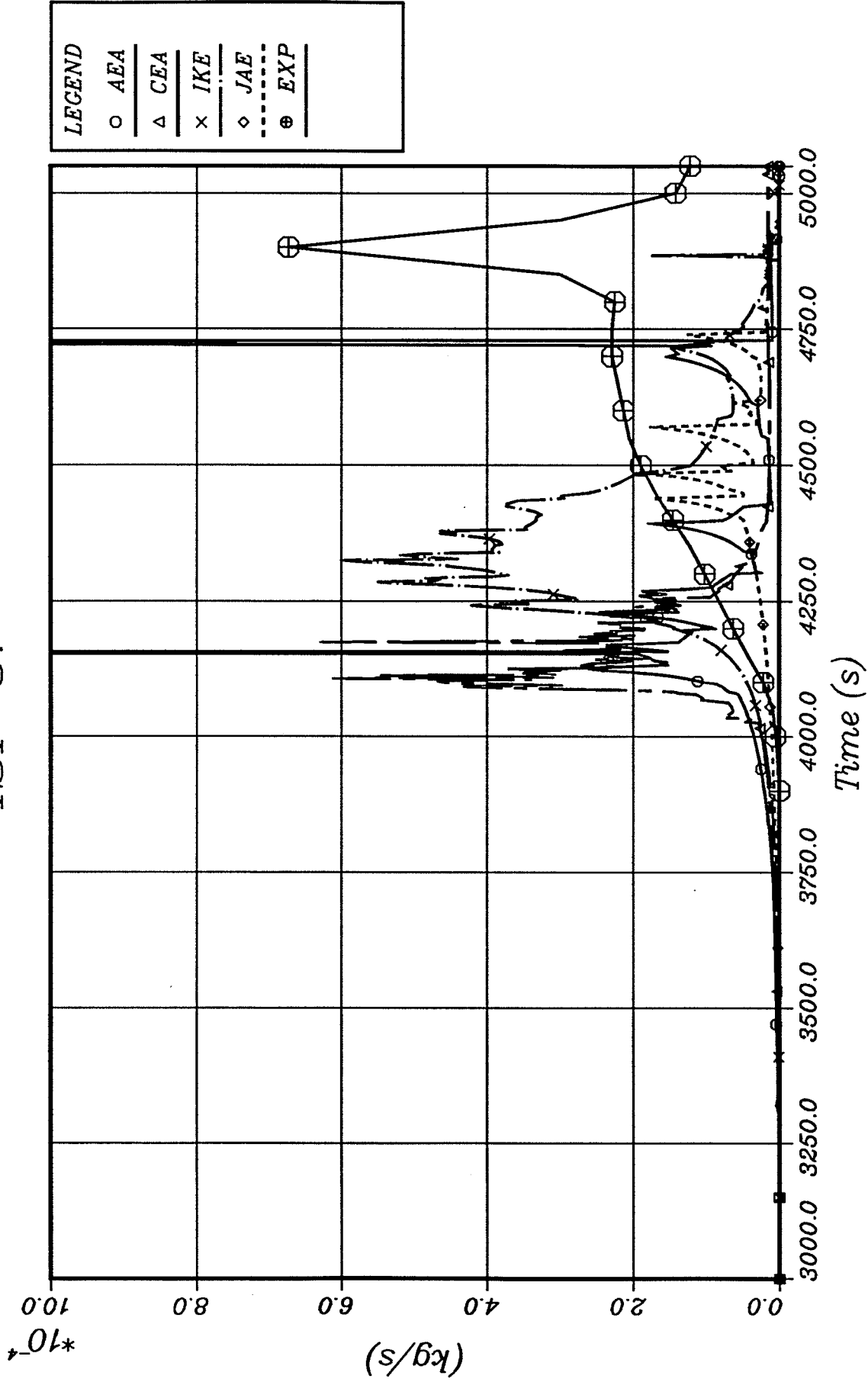


Figure 4.39: Hydrogen Generation Rate (Bundle + Shroud)

ISP 31

GRS

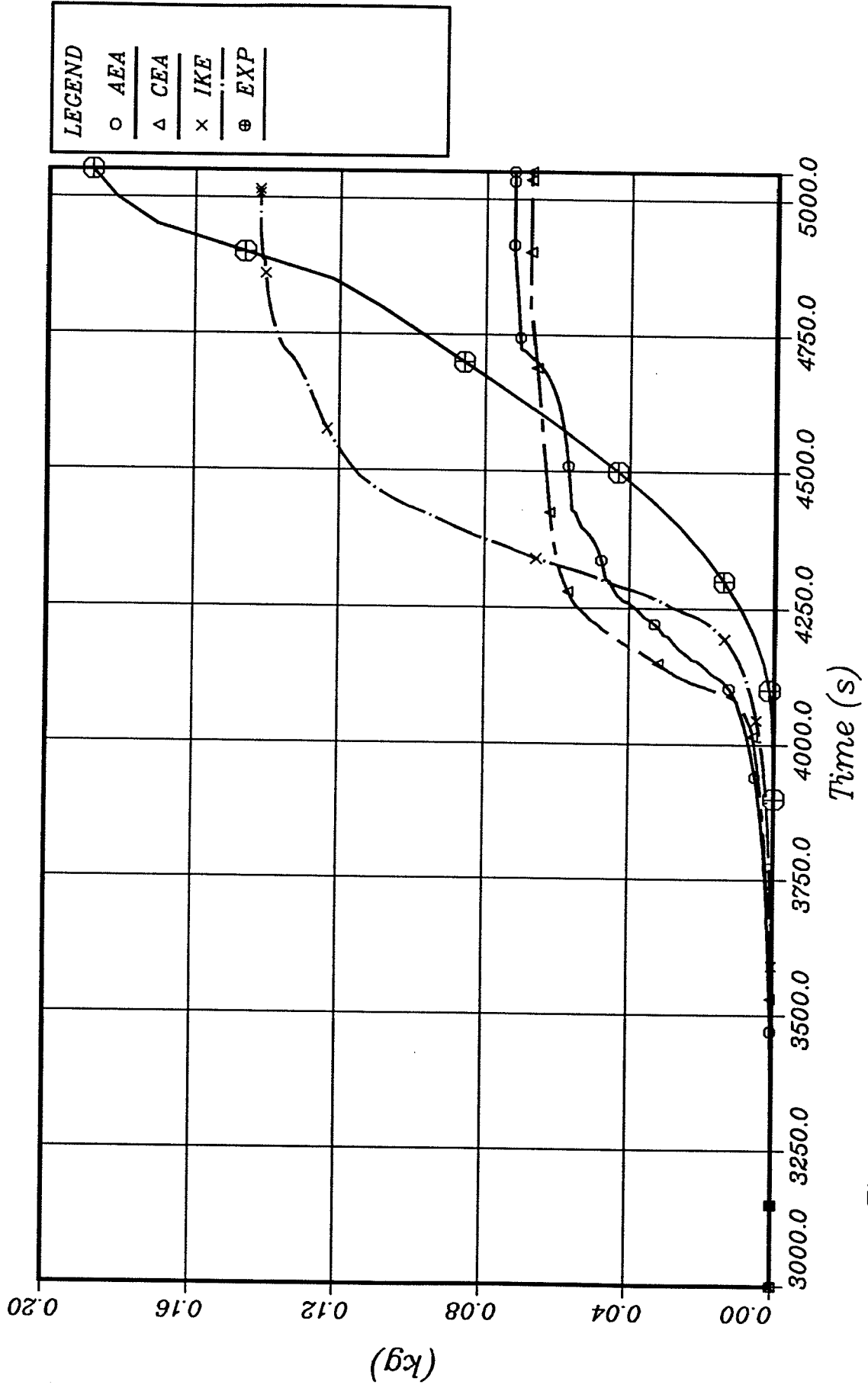


Fig. 4.40: Accumulated Hydrogen Generation(Bundle + Shroud)

## **9 Appendix**

"Open" contribution of two further participants

### **Recent SCDAP/RELAP5/MOD3 Analytical Results for International Standard Problem 31 - CORA-13**

J.K. Hohorst  
D.T. Hagman  
C.M. Allison

EG&G Ida, Inc.  
Idaho National Engineering Laboratory, Idaho Falls, Idaho

### **Contribution to ISP 31 - CORA 13 Calculations with ATHLET/CD and RELAP5/SCDAP**

J. Paulus  
Th. Steinrötter  
U. Brockmeier  
H. Unger

Ruhr-University of Bochum  
Department of Nuclear and New Energy Systems, FRG

# Recent SCDAP/RELAP5/MOD3 Analytical Results

for  
International Standard Problem 31 - CORA-13

J. K. Hohorst  
D. T. Hagrman  
C. M. Allison

EG&G Idaho, Inc.  
Idaho National Engineering Laboratory  
Idaho Falls, Idaho

## 1. Code Improvements

SCDAP/RELAP5/MOD3[8X], relative to MOD3[7af] and earlier versions of the code, contains 1) significant modeling improvements to allow the user to accurately model the early phases of a severe accident; 2) changes to the late-phase models so that predicted behavior accurately represents that which occurs during the late phase of an severe accident; 3) changes to improve the overall reliability and usability of the code. These changes include the addition of an Inconel spacer grid-Zircaloy cladding interaction model, a reflood model which limits the vapor diffusion of steam, RELAP5 style card numbers and input checking, a radial spreading of molten material model, radiative heat transfer time smoothing, time step repetition and many deficiency and error corrections.

## 2. Changes to the Input Model

Changes were made to the input model to better represent the conditions in the test facility during the test. Changes were made to the input, using only provided or published material property data, temperature and pressure histories provided by the experimenters,<sup>4</sup> bounding sensitivity studies of uncertainties in the test conditions, and the default variables to better represent materials and bundle conditions in the lower plenum during reflood. Localized hot spots in the bundle were modeled through the use of a representative hot rod.

## 3. Results of the Calculations

### 3.1 Influence of the Material Interaction Model

Results of calculations performed with SCDAP/RELAP5/MOD3 indicated that the inclusion of the grid spacer/material interaction model impacted the calculated core damage progression in the following manner: 1) initial fuel rod clad failure occurred near the Inconel grid spacer at a temperature substantially lower than calculated in earlier versions of the code; 2) cladding began to liquefy at temperatures near 1500 K due to eutectics being formed between Inconel from the grid spacer and the Zircaloy fuel rod clad; 3) a blockage region consisting of accumulated melted debris formed near the location of the grid spacer. Figure 1 compares the calculated unheated fuel rod temperature from the earlier calculation<sup>5</sup> using MOD3[7af] and MOD3[8X] with the measured data at the 750 mm elevation. The figure shows that the calculated temperature response of the bundle components was not adversely effected by the addition of the grid spacer model. The most notable improvement in the calculated results was the formation of a large blockage region near the Inconel grid spacer. Figure 2 shows an artist conception of the calculated and measured end-state of the bundle.

### 3.2 Vapor Limited Diffusion of Steam in Zircaloy

Early versions of the code prior to MOD3[8X] limited the oxidation of the fuel rod cladding by steam starvation which did not accurately model the interactions between the Zircaloy and gases flowing through the bundle. When the heat/mass transfer analogy based on vapor limited diffusion of steam to the Zircaloy surface was implemented in the code, heating rates in the bundle slowed considerably and the onset of hydrogen production was delayed several hundred seconds and occurred over a longer period of time than observed when steam starvation limits were imposed. Figures 3 and 4 compare the results of calculations performed using vapor limited diffusion of steam into the cladding and steam starvation limits with the measured data at two elevations and Figure 5 shows the rate of hydrogen production from both calculations. The predicted bundle heating when vapor diffusion limits on oxidation are used exclusively tend to be delayed considerably from the data in the upper bundle, whereas when steam starvation is used to limit oxidation, temperatures in the upper bundle agree well with the measured data. The predicted hydrogen production rate when vapor diffusion limits on oxidation are imposed agree quite well with the measured data. All calculations were performed using a  $ZrO_2$  failure temperature of 2250 K.

Although representative fuel rods are intended to describe the average behavior of fuel rods in an experimental bundle, in reality, local hot spots may exist due to local inhomogeneities in power generation, heat transfer or flow. Although these hot spots may not influence the overall behavior of the bundle or core, the local heat generation due to oxidation is strongly effected due to the exponential dependency of oxidation rates upon temperature. Consequently a more representative fuel bundle was tried which used one SCDAP fuel rod component to represent the local hot spots in the bundle, and another to represent the average rods in a region. Oxidation in the rod representing the hot spots was limited by steam starvation, and in the average rods by vapor diffusion. The predicted temperature response in the bundle using this approach, the reflood model activated, and a  $ZrO_2$  failure temperature of 2250 K agreed well with the measured data. The predicted rate of hydrogen production during the transient reflected the measured rate during the early stages of the experiment as well as the increased hydrogen production during reflood, though the total quantity produced was still underpredicted. Code to data comparisons of unheated fuel rod temperatures at various elevations in the bundle are shown in Figures 6 to 8 and a comparison of predicted hydrogen production with the measured is shown in Figure 9.

### 3.3 Effects of the Reflood Model

Changes to the input deck were made to accurately represent the lower plenum volumes and the reflood tank and to activate the reflood and oxide shattering model. Modeling changes were made to decrease the power in the lower plenum so that the lower heating rates attributable to the molybdenum and copper were reasonable, position the simulator and unheated fuel rods correctly in the lower plenum region, and allow RELAP5 to calculate the evaporation rate from the quench tank prior to the quenching phase of the experiment. Using these input changes and a  $ZrO_2$  failure temperature of 2450 K, the calculated temperature response in all areas of the bundle agrees well with the measured data. Figures 10 to 12 show the calculated temperatures at three elevations in the bundle compared to the measured values at the same elevations when the above described modeling changes were used and the reflood model activated.

As shown in the figures the predicted results showed good agreement with the data. The temperature in the lower quarter of the bundle is overpredicted but is improved over previous results. Further improvements will require more detailed modeling of the lower plenum and quench tank. The figures show the predicted temperatures in the upper three-quarters of the bundle agreeing well with the data.

### 3.3.1 Hydrogen Production

Figure 13 shows the predicted hydrogen production rate compared to the measured rate when the reflood model in the code has been activated, hot spots modeled, and the  $ZrO_2$  failure temperature set to 2450 K. The code is now accurately predicting the hydrogen spike at reflood and the percent of the total predicted hydrogen produced during reflood, although the total calculated amount produced during the experiment is still underpredicted. Table 1 shows the results of several sensitivity studies performed using the reflood model.

Although it must be confirmed by the experimenters underprediction of total hydrogen by the code may be explained as follows. The reported hydrogen data in ISP-31 reports<sup>67</sup> appears to have been taken at a distance of approximately 10 m from the core, after the gas had passed through a condenser and into a mixing tank. This could explain some of the time separation between the measured initiation of hydrogen production and that predicted by SCDAP/RELAP5/MOD3[8X]. More evidence of the effects of this delay is noticed in the temperature information. At 4000 s, the measured temperature indicates the onset of rapid oxidation, especially at the 750 and 950 mm elevations, in agreement with the code prediction. The measured rise in temperature associated with the onset of rapid oxidation occurs significantly before measurements indicate hydrogen production to occur during the experiment. The underprediction of hydrogen between  $t=4200$  s and  $t=4800$  s is due, in part, to melted material relocating. In the experiment the relocating materials continued to oxidize in the reflood tank until cooled, but in SCDAP/RELAP5 once relocated into the RELAP5 modeled areas they are no longer included in the SCDAP oxidation calculation. Another neglected item in the oxidation calculation is the oxidation of the outer surface of the shroud and the upper 0.5 m unheated portion of the bundle. Double sided oxidation was not initiated for the shroud liner in this calculation. The reflood calculation discussed in this appendix simply feeds water into the lower plenum region at a given mass flow rate with no modeling of the two state regions. The narrowness and height of the reflood hydrogen spike with respect to the data can be explained in two ways; 1) measured data is likely to be dispersed during the transport to the measurement location and 2) the reflood oxide shattering model instantly shatters the oxide over much of the length of the fuel rod whereas during the experiment the oxide layer may have shattered over a short time span.

### 3.3.2 End-state of the Bundle.

The end-state of the core as calculated by SCDAP/RELAP5[8x] and the final state of the core from the ISP-31 report are in good agreement. The end-state of the bundle determined from the metallurgical examination of the damaged bundle, showed the control rod missing above the 400 mm elevation and significant damage in the 300 to 400 mm range. SCDAP predicted control rod to completely disappear above the 200 mm elevation. The code and the metallurgical examination of the bundle show flow blockages at the second, Inconel, grid spacer location and relocated metallic melt at the bottom of the core.

### 3.3 Impact of the New Style Input

The RELAP5 card number style input was used for all calculations using SCDAP/RELAP5/MOD3[8X]. Replacing the free form input used in version 7af with the newer RELAP5 style cards caused no noticeable effects on the code predictions but does significantly decrease the time needed to prepare an input deck. The input checking routines clearly describe the errors detected and their location in the input deck. Card number style input increases the reusability of components by allowing the user to apply a cut and paste approach to deck design and since card order is no longer significant the major problems encountered during deck preparation have been eliminated. With the free form style of input used in version 7af, cards and numbers had to be in a required order and form and errors in input were not identified therefore a considerable amount of time could be required to develop and debug the deck.

#### 4. Conclusions

The code improvements, error correction, and changes to the input model to better describe the test facility and conditions significantly improved the code's ability to predict the test. When the test bundle and heated fuel rods are modeled to accurately describe their physical characteristics prior to the start of the test, the models and default values in the code do an excellent job of predicting the test with the exception of the total hydrogen production, which was underpredicted. Additional refinement of the input model to include the outer oxidation of the shroud liner and upper 0.5 m unheated portion of the bundle may be necessary to improve the prediction of hydrogen production. The use of a separate component to model areas in the core where hot spots could develop due to localized changes in flow rates, heat transfer or power generation and the activation of the reflood model improve the test results considerably with the measured and calculated values agreeing well.

#### 5. References

1. C. M. Allison and E. C. Johnson, Editors, SCDAP/RELAP5/MOD3 Code Manual, Volumes I to III, NUREG/CR-5273, EGG-2555, (draft), September, 1989.
2. P. Hofmann et. al. Dissolution of Solid UO<sub>2</sub> by Molten Zircaloy and its Modeling, International Symposium on Severe Accidents in Nuclear Power Plants, Sorrento, Italy, IAEA-SM-296/1, March, 1989.
3. C. M. Allison et. al. Code Usability Improvements, Interim Report (Draft) November, 1992.
4. M. Firnhaber, K. Trambauer, S. Hagen, and P. Hofmann, Specification of the International Standard Problem 31, CORA-13 Experiment on Severe Fuel Damage, August, 1991, Revision 1 October 1991.
5. R. W. Wright, presenter, J. K. Hohorst, preparer, Analysis of the OECD-CSNI International Standard Problem 31 using SCDAP/RELAP5, ISP-31 International Standard Problem Workshop, Karlsruhe, Germany, October, 1992.
6. S. Hagen, P. Hofmann, V. Noack, G. Schanz, G. Schumacher, and L. Sepold, Results of SFD Experiment CORA-13 (OECD International Standard Problem 31, KfK 5054, February, 1993.
7. M. Firnhaber, K. Trambauer, S. Hagen and P. Hofmann, International Standard Problem No. 31, CORA-13 Experiment on Severe Fuel Damage, OECD-CSNI Preliminary Comparison Report, (draft), August, 1992.

#### Tables

Table 1. Sensitivity Study Comparison for Hydrogen Production

	<i>grams H produced</i>	<i>% produced after reflood</i>
<i>Data</i>	210	48%
<i>Zr fail 2250</i>	87	32%
<i>Zr fail 2450</i>	118	38%
<i>Steam limited</i>	79	12%
<i>Diffusion limited</i>	83	1%

# Figures

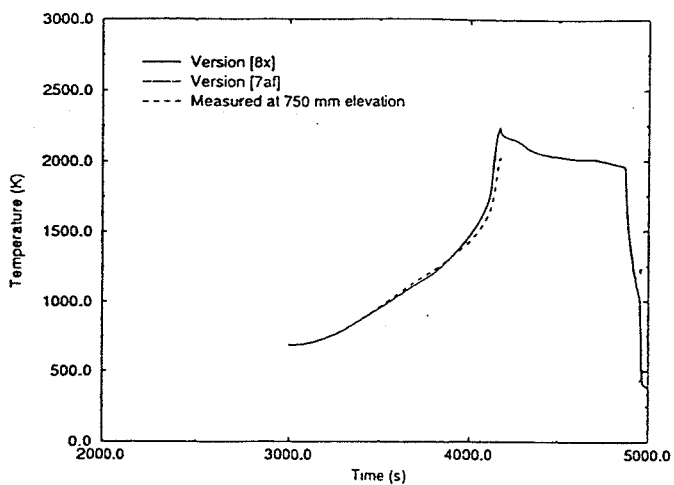


Figure 1. Comparison of calculated fuel rod temperatures from Version [7af] and [8x] with measured at 750 mm elevation.

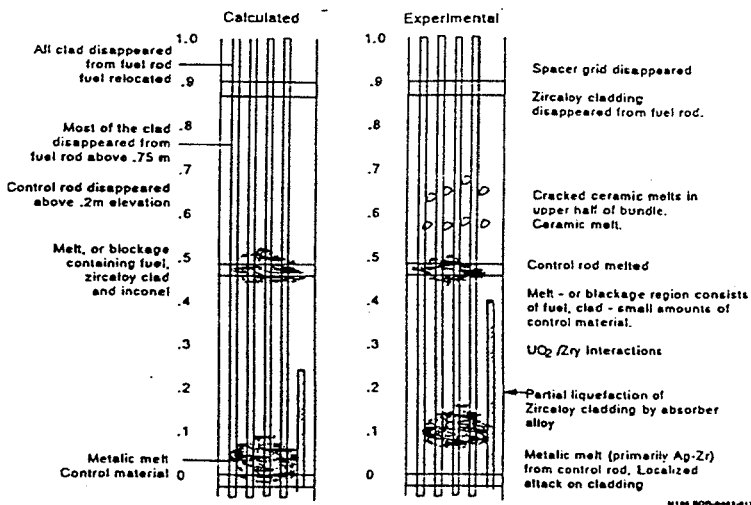


Figure 2. Artist rendition of the bundle showing the calculated and measured end-state.

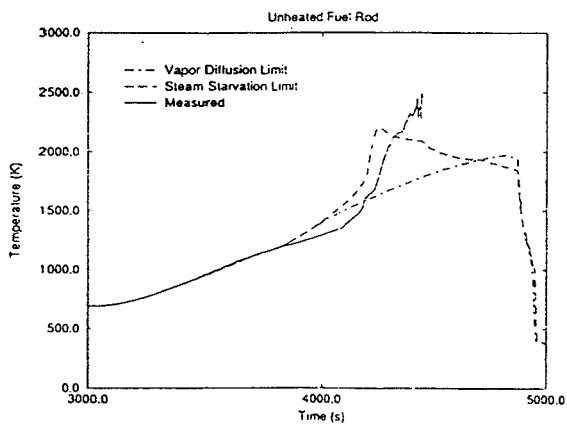


Figure 3. Calculated and measured temperatures at the 550 mm elevation - vapor diffusion and steam starved limitations.

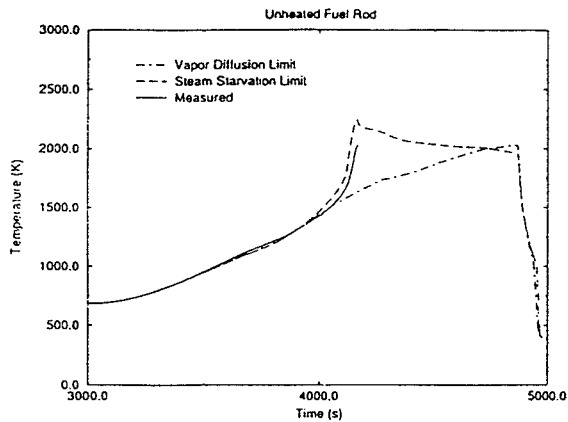


Figure 4. Calculated and measured temperatures at the 750 mm elevation - vapor diffusion and steam starved limitations.

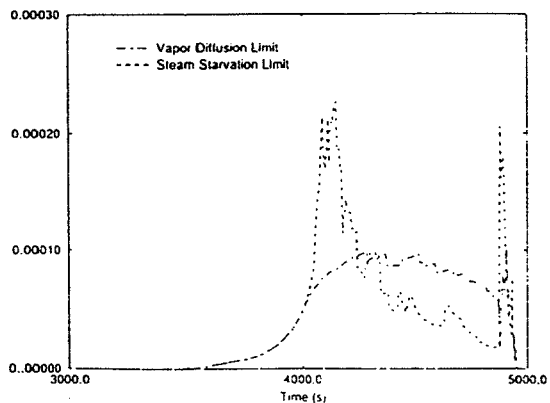


Figure 5. Hydrogen production rates from the steam starved and vapor diffusion limited cases.

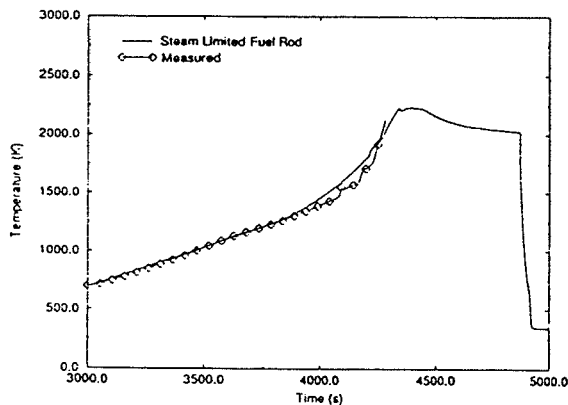


Figure 6. Calculated and measured temperatures at the 550 mm elevation when reflood hot spots in the bundle are modeled using a  $ZrO_2$  failure temperature of 2250 K.

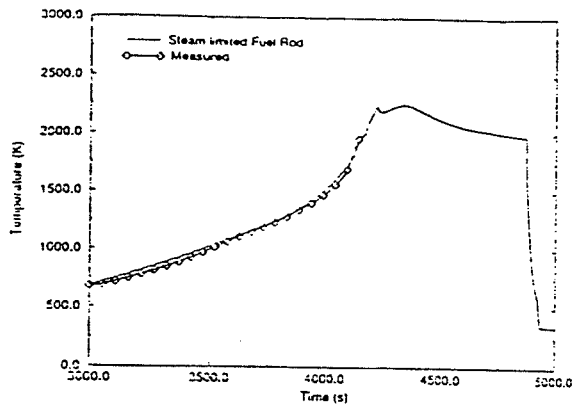


Figure 7. Calculated and measured temperatures at the 750 mm elevation when reflood and hot spots in the bundle are modeled using a  $ZrO_2$  failure temperature of 2250 K.

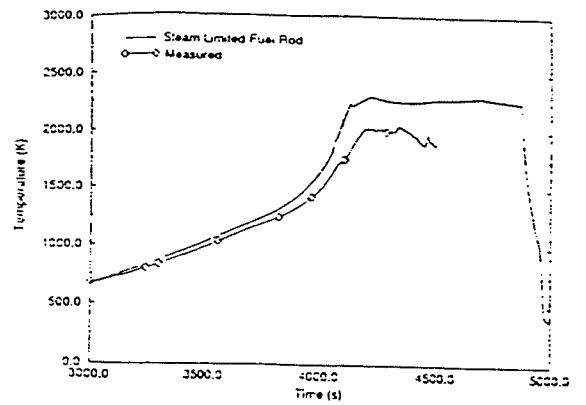


Figure 8. Calculated and measured temperatures at the 950 mm elevation when reflood and hot spots in the bundle are modeled using a  $ZrO_2$  failure temperature of 2250 K.

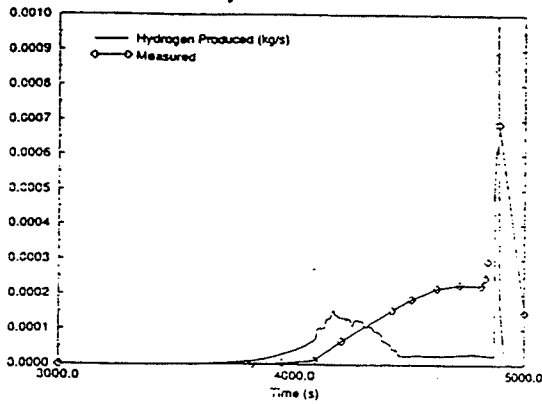


Figure 9. Hydrogen production in the bundle when reflood and the hot spots in the bundle using a  $ZrO_2$  failure temperature of 2250 K.

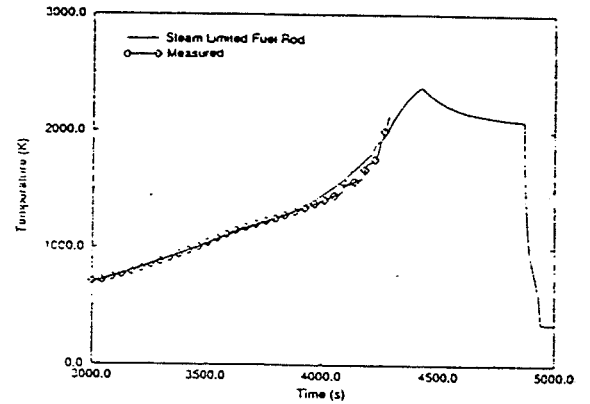


Figure 10. Calculated and measured temperatures at the 550 mm elevation when reflood and the hot spots in the bundle are modeled using a  $ZrO_2$  failure temperature of 2450 K.

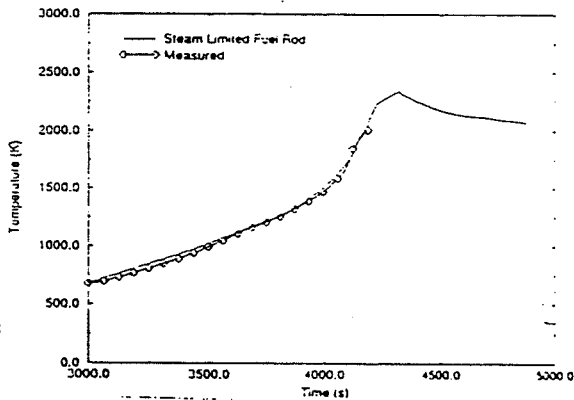


Figure 11. Calculated and measured temperatures at the 750 mm elevation when reflood and the hot spots in the bundle are modeled using a  $ZrO_2$  failure temperature of 2450 K.

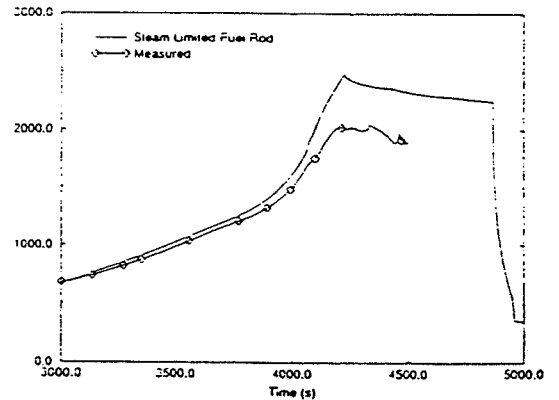


Figure 12. Calculated and measured temperatures in the bundle at the 950 mm elevation when reflood and hot spots in the bundle are modeled using a failure temperature of 2450 K.

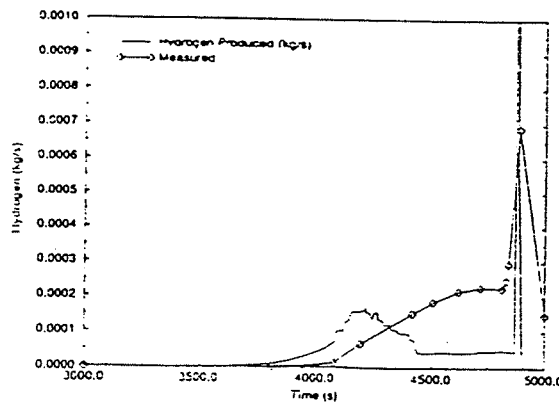


Figure 13. Calculated and measured hydrogen production rates when reflood and the hot spots in the bundle are modeled using a  $ZrO_2$  failure temperature of 2450 K.

# CONTRIBUTION TO ISP31 — CORA13 CALCULATIONS WITH ATHLET/CD AND RELAP5/SCDAP

J. Paulus, Th. Steinrötter, U. Brockmeier, H. Unger  
Ruhr-University of Bochum,  
Department of Nuclear and New Energy Systems, FRG

## INTRODUCTION

The comparative assessment of the severe accident analysis codes MELCOR, ICARE, ATHLET/CD and RELAP5/SCDAP is part of a study performed at the Ruhr-University of Bochum. The assessments are based on both, theoretical comparison of the physical models involved in the codes and comparison of computational and experimental results (see /1/ – /9/). The test CORA13 serves as an experimental basis for the code predictions presented here. CORA13 is a typical PWR test in terms of the geometrical arrangement of the test bundle (see /10/ – /13/). The bundle consists of 23 fuel and 2 absorber rods with grid spacers made of Inconel and Zircaloy. The absorber material is (Ag, In, Cd)-alloy. The heated rod length is 1000 mm. The flow of preheated argon through the bundle was adjusted to 8 g/s and a flow of 6 g/s steam was added during the transient of the test. The test was terminated by quenching at a problem time of 4870 s. The calculations reflect a satisfactory modeling of the governing phenomena, as there are heatup, oxidation (with the onset of a temperature excursion due to Zircaloy/steam reaction) and cooldown.

## CALCULATIONS WITH ATHLET/CD AND RELAP5/SCDAP

The major differences between the input decks for ATHLET/CD and RELAP5/SCDAP underlying the calculations presented here, are:

- In case of RELAP5/SCDAP, the bundle is modeled as to consist of 3 representative rods (SCDAP-components) – heated, unheated and absorber rods. The SCDAP-components “heated rods”, “unheated rods” and “absorber rods” are representing the 16 heated, 7 unheated and 2 absorber rods of the CORA13 test bundle. In case of ATHLET/CD, 4 representative rods have been defined (to represent 2 rings of heated and 2 rings of unheated rods) due to instructions given in the ISP-31 specification (see /10/),
- in case of RELAP5/SCDAP, the shroud and the shroud insulation are modeled as severe accident components (SCDAP-component, see /5/) while in case of ATHLET/CD both are modelled as “normal” heat structures (HECU-component, see /4/). The density of the shroud insulation in the RELAP5/SCDAP calculation was adjusted to a value of 350 kg/m<sup>3</sup> at 300 K instead of the physically correct value of 5800 kg/m<sup>3</sup> at 300 K (see /10/) to receive an energy distribution in the facility in accordance to the test (for details see /5/).
- due to the crossflow inlet of argon and steam the heat transfer Nusselt numbers are increased for the lower bundle region (0–350 mm) in the ATHLET/CD-calculation by a correction factor K. In reference to /14/ – /17/, the correction factor K in the bundle region between 0 mm and 350 mm is calculated as follows:

$$K = 2.86 - 5.3143 \cdot 10^{-3} \left[ \frac{1}{mm} \right] \cdot h[mm] \Big|_{0mm}^{350mm} .$$

At an elevation of 350 mm, the influence of the crossflow inlet on the heat transfer coefficients is assumed to be negligible (see /14/ – /17/),

- neither RELAP5/SCDAP nor ATHLET/CD are able to simulate the axial heat losses at the end of the rods. Therefore, the heat transfer coefficients at elevations between 0–150 mm are increased additionally in the ATHLET/CD-calculations (see /4/),
- in case of ATHLET/CD, the argon flow is simulated by an additional steam flow with adapted fluid properties (noncondensables are not taken into account in the current ATHLET/CD version).

Several other (minor) differences have to be taken into account, especially concerning the treatment of the initial and boundary conditions. For details see /4/ and /5/.

## RESULTS AND DISCUSSION

Sample calculations and experimental results of the CORA13 test are given in Figs. 1 – 5 in form of the cladding surface temperature history at elevations of 150 mm, 350 mm, 550 mm, 750 mm and 950 mm. In Fig. 6, the outer oxide layer thickness is depicted for the same elevations. The accumulated hydrogen production is shown in Fig. 7. The scope of this compact just allows some general remarks (for details see /4/, /5/, /7/ and /8/). The main points of interest of the calculations presented here are given in the following:

Three global phases are to be distinguished; the heatup phase, the escalation phase and the cooldown phase. It can be stated, that the heatup phase and the start of the escalation phase with the onset of the temperature excursion due to the Zircaloy/steam reaction (around 4200s) are well predicted by both codes.

Due to the unmodeled axial heat losses at the end of the rods, RELAP5/SCDAP overestimates the cladding surface temperatures at an elevation of 150 mm up to 200 K (see Fig. 1). As a result of the adaptations described above, ATHLET/CD estimates the cladding surface temperatures at an elevation of 150 mm well. In case of the ATHLET/CD calculation the material relocation model had to be turned off due to inadequate predictions of the relocation by the relatively simple ATHLET/CD stop-and-go model. Consequently, temperatures in the range between 4500 – 4870 s continue to increase (see Fig. 3 – 5). A more adequate modeling of this range will be possible with the new ATHLET/CD relocation model under development.

The start of the escalation phase at an elevation of 350 mm (see Fig. 2) is predicted – about 80 s – too early by ATHLET/CD: This is due to a feedback reaction from the 550 mm ATHLET/CD prediction (see Fig. 3) with its temperature overestimation due to the unmodelled latent heat of melting (relocation model turned off).

At an elevation of 950 mm (see Fig. 5) RELAP5/SCDAP overestimates the temperature gradients during the escalation phase due to a strong double-sided oxidation of the cladding with the according energy release and temperature increase: In the experiment single rods failed in a range between 4080 – 4150 s inducing their double-sided oxidation. In contrast to that, RELAP5/SCDAP predicts a simultaneous burst and consequent double-sided oxidation of all rods belonging to the SCDAP-components "heated rods" and "unheated rods" in a time window of 3910 – 3930 s.

The total amount of hydrogen released during the transient of CORA13 (see Fig. 7) is satisfactorily predicted by both codes. The accumulated hydrogen mass calculated by RELAP5/SCDAP shows an early and strong increase compared to the measurement. This is a result of the strong double-sided oxidation mentioned above. In case of ATHLET/CD, the mass of hydrogen produced due to the oxidation of the shroud is not directly calculated (see /18/ and /19/), and had to be concluded from the Zry-H<sub>2</sub>O-reaction energy (see /4/). The ATHLET/CD curve of the accumulated hydrogen mass shows a stronger increase than the measurement because steam starved situations for the shroud oxidation are not taken into account in the present ATHLET/CD version (see /18/ and /19/). From the comparison of the calculated and measured accumulated hydrogen mass it seems to be remarkable, that the measured accumulated hydrogen mass shows a nearly linear increase in the time span between 4500 – 4870 s (see Fig. 7), while a degressive course of the hydrogen mass had to be expected with respect to the measured temperature histories: In the time window 4500 – 4870 s, the measured temperatures at all elevations persist at a certain level (see Fig. 1 – 5). At constant temperatures, the oxidation rate should be expected to decrease with increasing oxide layer thickness. This should lead to a more convex form of the accumulated hydrogen mass as predicted by the codes than to the linear increase measured.

## ACKNOWLEDGEMENTS

This work was performed as part of the Research Project "Comparative Assessment of Different Computer Codes for Severe Accident Analysis, Contribution to the ATHLET/SA-Code Development". This project is cosponsored by the German Federal Administration Department for Research and Technology (BMFT) and the Ruhr University of Bochum. The authors are also pleased to acknowledge for their support by the Gesellschaft für Anlagen- und Reaktorsicherheit, Köln, as well as for much stimulating assistance and technical discussions with the staff of the Kernforschungszentrum Karlsruhe.

## REFERENCES

- [1] Brockmeier U., Unger H.: Modelle zur Beschreibung des Leichtwasserreaktorverhaltens bei schweren Störfällen für die Programme RELAP5/SCDAP, ATHLET/SA, CATHARE/ICARE,

MELCOR u.a., Erster Technischer Fachbereich zum Forschungsvorhaben BMFT 1500 831 7, Ruhr-Universität Bochum, Januar 1992

- [2] Paulus J., Brockmeier U., Unger H.: Nachrechnung des SFD-Versuches CORA-9 mit dem Schwerstörfallcode RELAP5/SCDAP, Zweiter Technischer Fachbericht zum Forschungsvorhaben BMFT 1500 831 7, Ruhr-Universität Bochum, Januar 1992
- [3] Paulus J., Brockmeier U., Unger H.: Darstellung der Programmstruktur des Computer-Codes MELCOR 1.8.1 und Analyse eines beispielhaften SWR-Problems anhand einer MELCOR-Simulation, Vierter Technischer Fachbericht zum Forschungsvorhaben BMFT 1500 831 7, Ruhr-Universität Bochum, Juli 1992
- [4] Paulus J., Brockmeier U., Unger H.: Nachrechnung des SFD-Versuches CORA13 mit dem Schwerstörfallcode ATHLET/CD, Siebter Technischer Fachbericht zum Forschungsvorhaben BMFT 1500 831 7, Ruhr-Universität Bochum, Juli 1992
- [5] Steinrötter Th., Paulus J., Brockmeier U., Unger H.: Nachrechnung des SFD-Versuches CORA13 mit dem Schwerstörfallcode RELAP5/SCDAP, Achter Technischer Fachbericht zum Forschungsvorhaben BMFT 1500 831 7, Ruhr-Universität Bochum, August 1992
- [6] Paulus J., Brockmeier U., Unger H., "Results of CORA-9 Post Test Calculations with ATHLET/SA and RELAP5/SCDAP, Proc. of NURETH-5, Vol. VI p 1843-1855, Salt Lake City, Sept, 21-24, 1992
- [7] Paulus J., Brockmeier U., Unger H., "Results of CORA-13 Post Test Calculations with ATHLET/SA and RELAP5/SCDAP, Int. ISP-31 Workshop 1992, KfK Karlsruhe, Oct. 7-8, 1992.
- [8] Paulus J., Brockmeier U., Unger H., "ISP-31 Calculations with different Severe Accident Analysis Codes - a Comparison", 2nd Int. ISP-31 Workshop 1993, Residence Inn Marriott, Bethesda, Maryland USA, Apr. 30, 1993.
- [9] Paulus J., Brockmeier U., Unger H., "Comparative Assessment of Severe Accident Analysis Codes - CORA Calculations with ATHLET/SA and RELAP5/SCDAP, Jahrestagung Kerntechnik 1993, Köln, May 25-27, 1993.
- [10] Firnhaber M., Trambauer K., Hagen S., Hofmann P.: Specification of the International Standard Problem ISP-31: CORA13 Experiment on Severe Fuel Damage, August 1991
- [11] Hagen S., et.al.: Results of SFD Experiment CORA-13. Kernforschungszentrum Karlsruhe, KfK 5054 Februar 1993
- [12] Firnhaber M., Trambauer K., Hagen S., Hofmann P.: International Standard Problem No. 31: Cora 13 Experiment on Severe Fuel Damage, Preliminary Comparison Report, 3. Description and Results of Experiment CORA-13, August 1992
- [13] Hofmann P., Hagen S., Noack V., "Description and Results of Experiment CORA13" Int. CORA Workshop 1992, KfK Karlsruhe, Oct. 5-7, 1992.
- [14] Basler M., Theoretische Analyse des Druck- und Geschwindigkeitsfeldes eines schrägdurchströmten Stabbüdels als Grundlage zur Quasi-Kontinuums-Theorie, Dissertation an der Fakultät für Maschinenbau der Ruhr-Universität Bochum, 1984.
- [15] Röß P., Untersuchung des Druck- und Geschwindigkeitsfeldes in einem Modell eines kastenlosen Schnellbrüterkerns, Dissertation an der Fakultät für Maschinenbau der Ruhr-Universität Bochum, 1989.
- [16] Böttgenbach H., Messungen von Strömungsfeldern in engen Stabbüdels zur Überprüfung einer anisotropen Strömungsfeldtheorie, Dissertation an der Fakultät für Maschinenbau der Ruhr-Universität Bochum, 1977.
- [17] Winter J., Experimentelle Ermittlung von Stromlinien in einem engen Brennstabgitter mit Schikanen zur Überprüfung einer anisotropen Widerstandshypothese, Dissertation an der Fakultät für Maschinenbau der Ruhr-Universität Bochum, 1978.
- [18] Trambauer K. et. al., Entwicklung und Verifikation des Programmsystems ATHLET-SA zur Analyse schwerer Störfälle. GRS-A-1689, Juni 1990
- [19] Trambauer K. et. al., Entwicklung des Rechenprogrammsystems ATHLET-SA zur Analyse schwerer Störfälle, Abschlußbericht. GRS-A-1937, Mai 1992

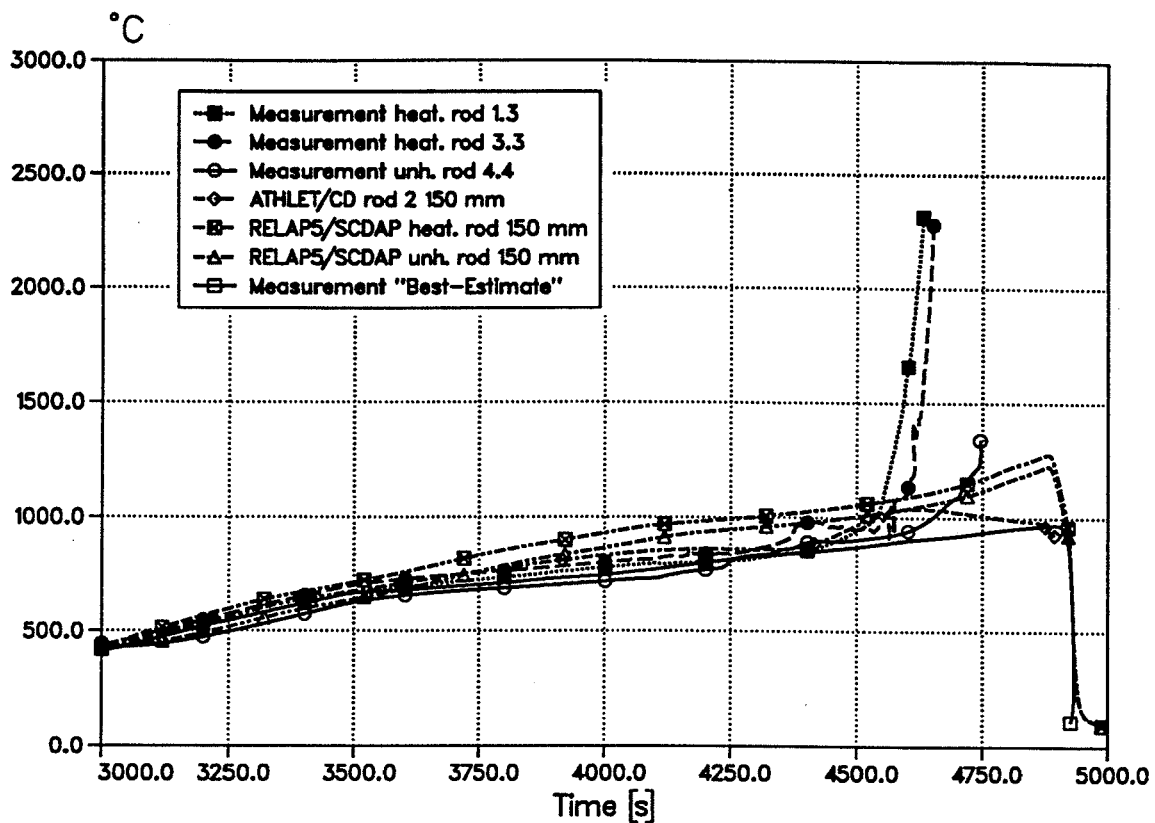


Fig. 1: History of the cladding surface temperature at an elevation of 150 mm for CORA13

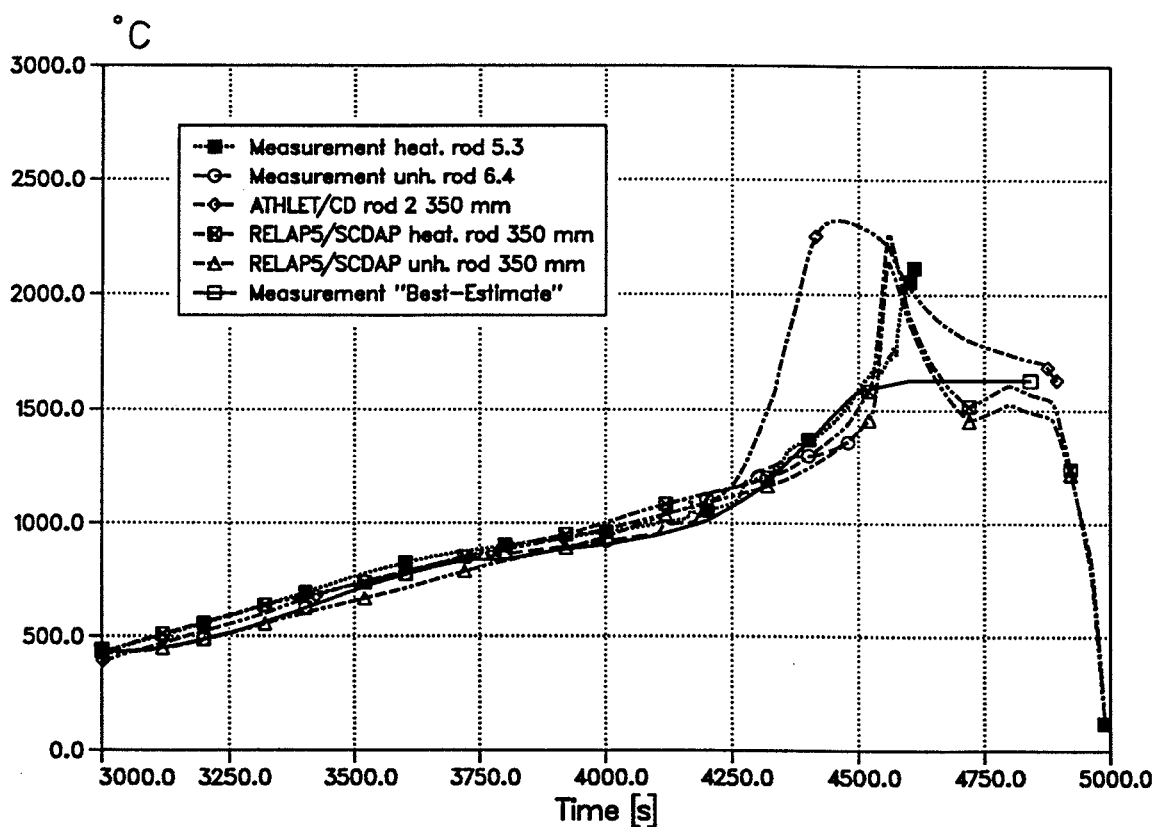


Fig. 2: History of the cladding surface temperature at an elevation of 350 mm for CORA-13

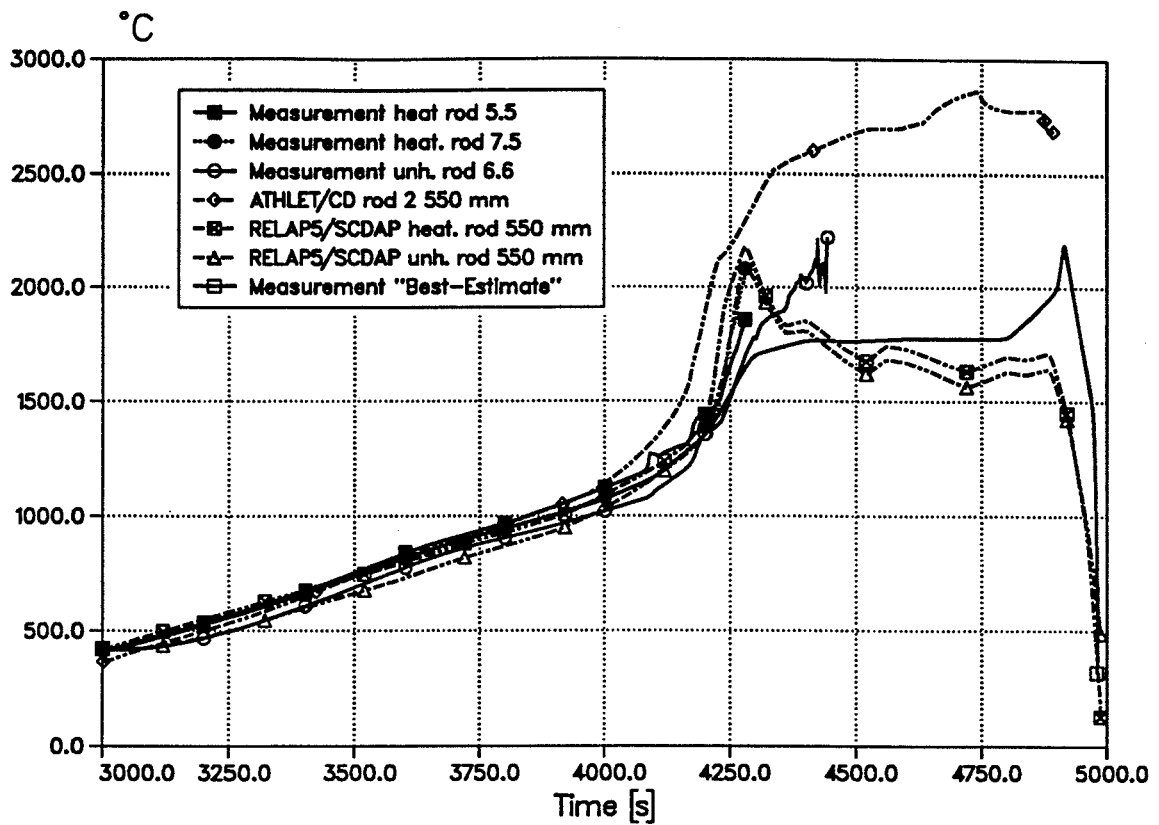


Fig. 3: History of the cladding surface temperature at an elevation of 550 mm for CORA13

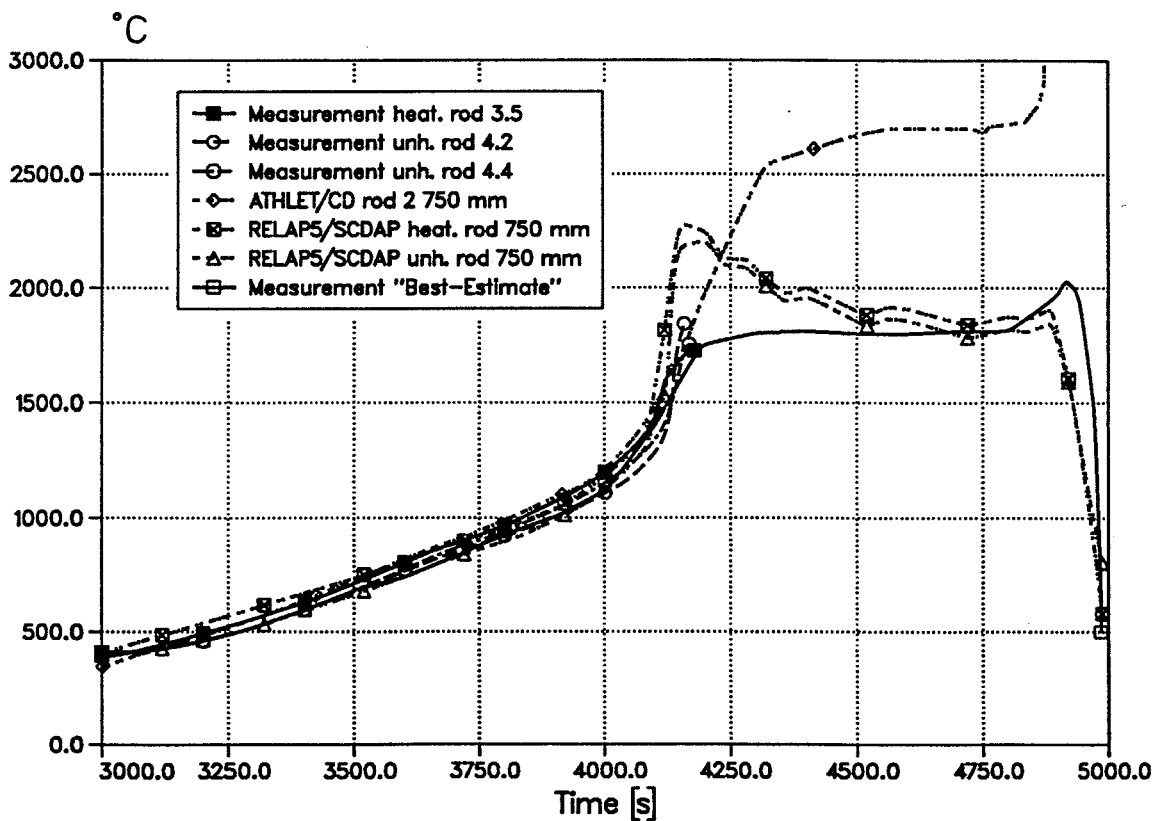


Fig. 4: History of the cladding surface temperature at an elevation of 750 mm for CORA-13

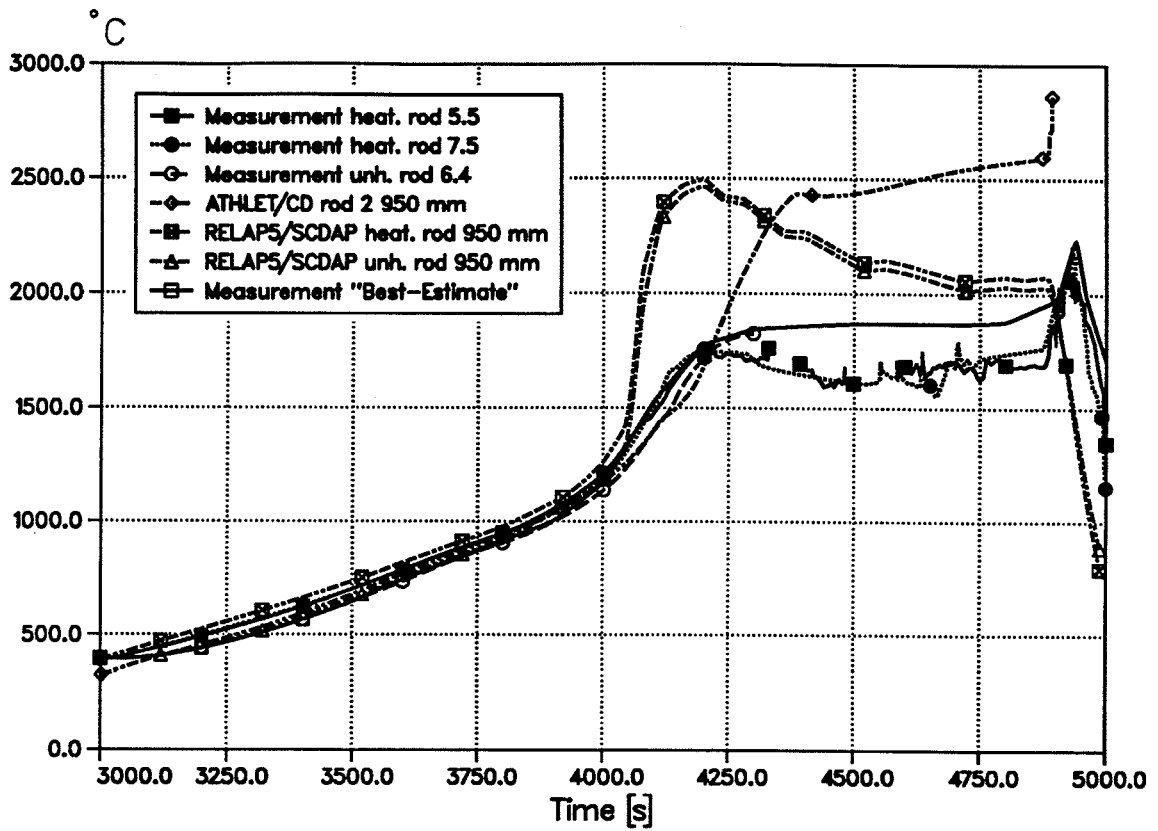


Fig. 5: History of the cladding surface temperature at an elevation of 950 mm for CORA13

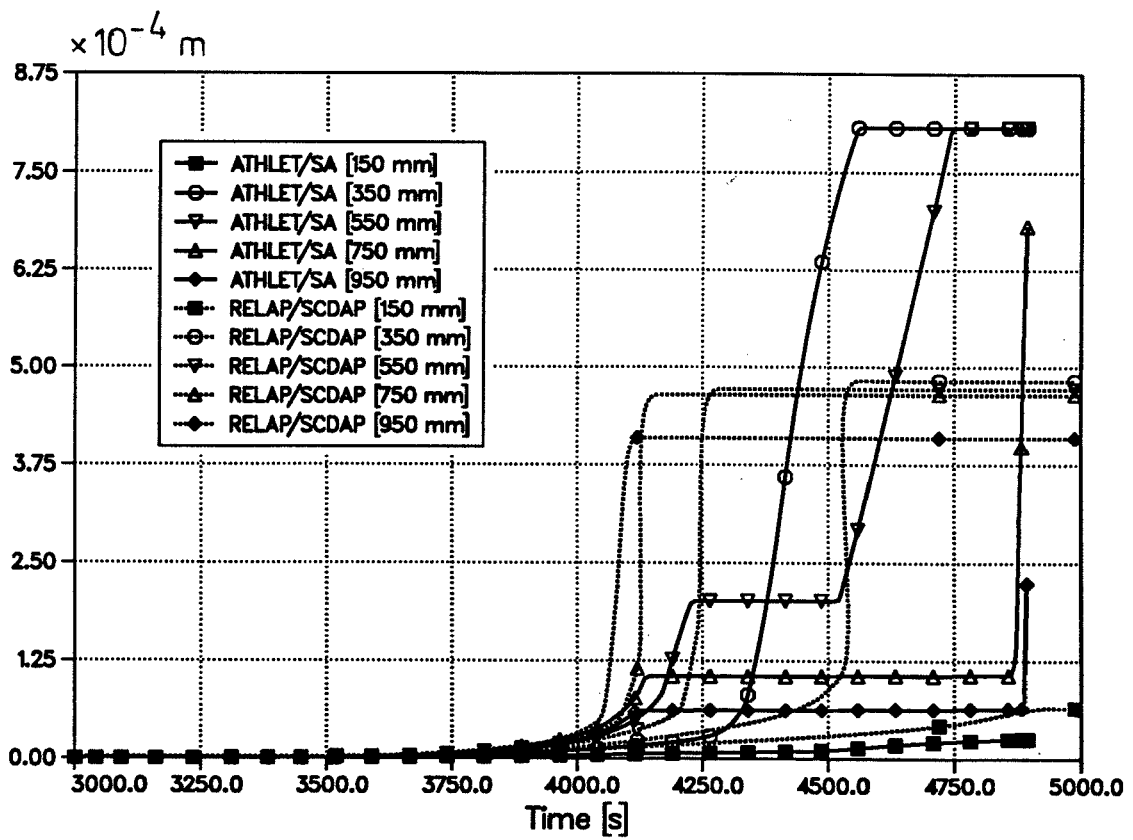


Fig. 6: History of the outer oxid layer thickness for CORA13

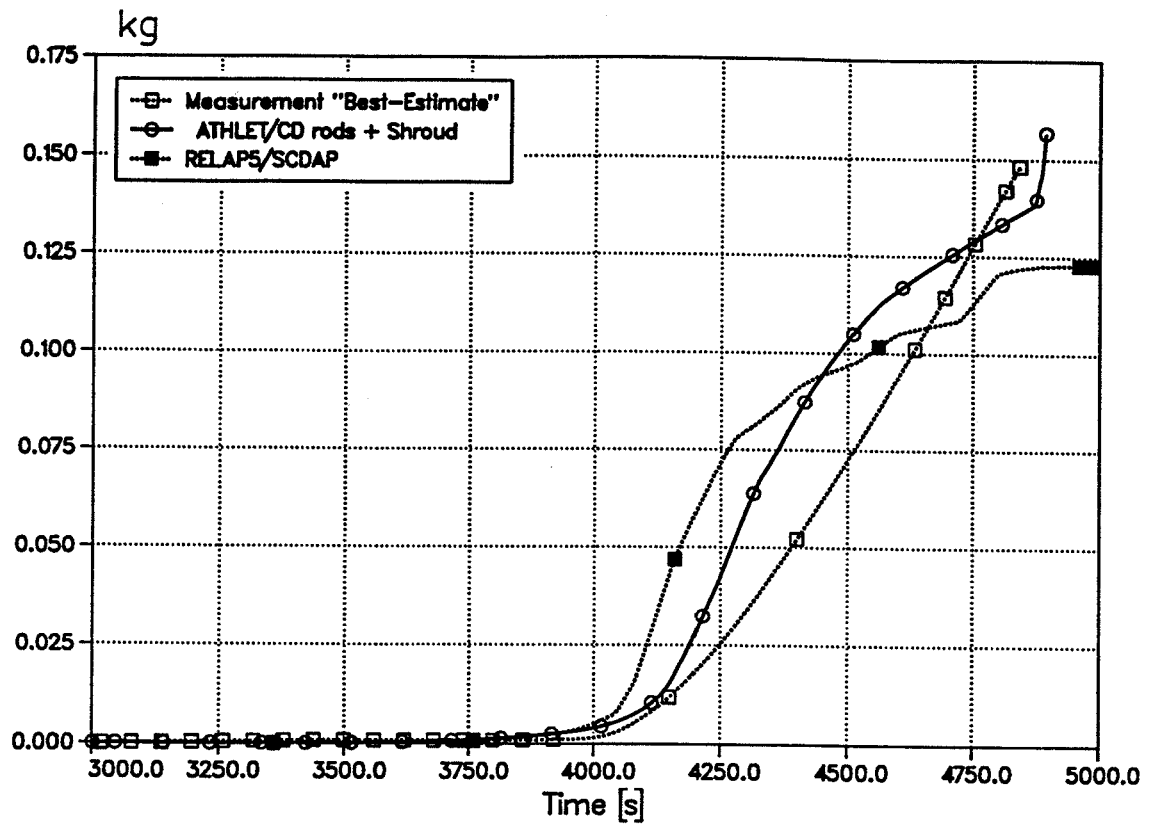


Fig. 7: History of the accumulated hydrogen production for CORA13

117

**Gesellschaft für Anlagen-  
und Reaktorsicherheit  
(GRS) mbH**

Schwertnergasse 1  
**50667 Köln**  
Telefon +49 221 2068-0  
Telefax +49 221 2068-888

Forschungsinstitute  
**85748 Garching b. München**  
Telefon +49 89 32004-0  
Telefax +49 89 32004-300

Kurfürstendamm 200  
**10719 Berlin**  
Telefon +49 30 88589-0  
Telefax +49 30 88589-111

Theodor-Heuss-Straße 4  
**38122 Braunschweig**  
Telefon +49 531 8012-0  
Telefax +49 531 8012-200

**[www.grs.de](http://www.grs.de)**

NEA/CSNI/R(93)17, GRS-106, KfK 5287      OECD/NEA-CSNI      International Standard Problem No. 31